Development of a CMRC cooled 10 kA current lead for HTS applications

zur Erlangung des akademischen Grades eines

DOKTORS DER INGENIEURWISSENSCHAFTEN (DR.-ING.)

von der KIT-Fakultät für Chemieingenieurwesen und Verfahrenstechnik des

Karlsruher Instituts für Technologie (KIT)

genehmigte

DISSERTATION

von

M. Sc. Eugen Shabagin

aus Giebelstadt

Tag der mündlichen Prüfung:	29.03.2022
Erstgutachter:	Prof. Dr.-Ing. Steffen Grohmann
Zweitgutachter:	Prof. Dr.-Ing. Mathias Noe

Dieses Werk ist lizenziert unter einer Creative Commons Namensnennung - Weitergabe unter gleichen Bedingungen 4.0 International Lizenz (CC BY-SA 4.0): https://creativecommons.org/licenses/by-sa/4.0/deed.de

Danksagung

Ich möchte an dieser Stelle die Gelegenheit nutzen und mich bei allen bedanken, die mich während meiner Promotion unterstützt und motiviert haben.

Meinem Doktorvater Prof. Dr.-Ing. Steffen Grohmann möchte ich besonders für die Betreuung dieser Arbeit, für das entgegengebrachte Vertrauen und die hilfreichen und konstruktiven Anregungen während der Promotion und besonders während der Korrekturarbeiten bedanken.

Weiterhin danke ich Herrn Prof. Dr.-Ing. Noe für die Möglichkeit die Promotion im Rahmen meiner Tätigkeit als wissenschaftlicher Mitarbeiter am Institut für Technische Physik (ITEP) durchzuführen. Die gemeinsamen wissenschaftlichen Untersuchungen und Veröffentlichungen zu supraleitenden Kabel in Ihrer Arbeitsgruppe haben mich thematisch sehr an meiner Promotion motiviert. An dieser Stelle möchte ich ebenfalls ganz besonders für die Zusammenarbeit, Motivation und Unterstützung der Kollegen der ITEP Kryogruppe danken.

Ebenfalls möchte ich mich bei meinem ehemaligen Kollegen des Instituts für Technische Thermodynamik und Kältetechnik (ITTK) bedanken, die mich über die ganze Zeit meiner experimentellen Arbeiten unterstützt haben.

Mein ganz besonderer Dank gilt meinen Eltern die während der Promotion stets an mich geglaubt haben. Insbesondere möchte ich meinem Bruder Alexander danken, der stets ein offenes Ohr für mich hatte und durch gemeinsame sportliche Aktivitäten einen Ausgleich zur Arbeit geschafft hat.

Schließlich möchte ich meiner Frau Mayya für die liebevolle und moralische Unterstützung danken. Du hast mich in schwierigen und mit Zweifel behafteten Zeiten immer wieder ermutigt und unterstützt. Doch am meisten danke ich dir dafür, dass du mir unseren wunderbaren Sohn Christian geschenkt hast und uns ein Zuhause erschaffen hast in dem wir immer wieder neue Kraft tanken können.

Abstract

Many high temperature superconducting (HTS) applications like superconducting cables, power rails, generators, fault current limiter, accelerators and magnets may require several kilowatts of cooling power at an operating temperature range of 50-80 K. The major cooling demand, depending on the application up to 70-90 %, is necessary for the cooling of resistive current leads (CL) that supply electric energy from the ambience at 300 K to the superconducting application at cryogenic temperatures. Therefore, a high thermal integration of the CL with the cooling system is required to provide an energy-efficient and a cost-efficient CL technology. The cryogenic mixed refrigerant cycles (CMRCs) are the optimal solution for the cooling of CLs, due to the possibility to generate cooling power at the required cryogenic temperatures by adjusting the composition of the mixture and cycle parameters to attain a high energy efficiency. The key in this technology is the direct implementation of the resistive current lead into the recuperative heat exchanger of the Linde-Hampson cycle, providing refrigeration power over the temperature range of the heat exchanger. Hereby, a mixed refrigerant is partly condensing and evaporating inside the heat exchanger and absorbing the Joule heat at the temperature it is generated in the current lead. Hereby, the economic efficiency of HTS applications in the energy technology can be considerably improved.

The aim of this work is the development of a 10 kA cryogenic mixed refrigerant cooled current lead (CMRC-CL). In order to enable a detailed investigation of the CL design, an existing numerical heat exchanger model is modified and implemented in the resistive current lead model that is developed in the frame of this work. Prior to that implementation, a literature review on the state-of-the-art CL solutions and cooling systems are conducted, numerically investigated and compared with each other. Based on this, a classical multi-tubes-in-tube CMRC-CL and a micro-structured CMRC-CL are developed and investigated numerically in this work. The first developed CMRC-CL design comprises a classical multi-tubes-in-tube heat exchanger which is wounded around a cylindrical CL made of copper. The second CMRC-CL prototype III is made of several micro-structured copper sheets that are connected together by a diffusion bonding process and is developed, patented and manufactured. Further, experimental investigation on the stainless steel micro-structured heat exchanger prototype II are conducted in the CMRC test stand at the Institute of Technical Thermodynamics and Refrigeration (ITTK) and the predictive qualities of the modified heat exchanger model are reviewed.

In section 2 five state-of-the-art CL solutions and design approaches are introduced and numerically investigated. The corresponding thermal loads at the cold end, the CL shape factors, the optimal refrigerant mass flows and the theoretical power consumptions of the systems are summarized in the design overview. According to the Wiedemann-Franz-Law, which describes the relation between the specific electrical resistance and thermal conductivity of metals, any metallic material can be used as a current lead. Each material leads to a different optimal geometry of the CL and therefore, the thermophysical properties of relevant resistive CL materials are evaluated and compared with each other.

The investigation of the CL types alone is not sufficient to evaluate the efficiency of the whole CL system and therefore, the state-of-the-art cooling systems for CLs are presented and discussed in section 3. Hereby, the total power consumptions P, including the required refrigeration power of the cooling system and the electric power losses of the respective current lead type, are calculated and discussed. A detailed analysis on the Linde-Hampson

refrigeration cycle, which is the basis of CMRCs is presented.

A numerical model for the calculation of CMRC-CLs is presented in section 4 which comprises the numerical investigations on the classical and the micro-structured CMRC-CLs. In order to identify an optimal refrigerant mixture, several parametric studies are performed with the classical CMRC-CL design. It was found that a refrigerant mixture with a larger composition of the low boiler methane, is an appropriate choice in the current design. In general, the classical CMRC-CL shows a significant reduction of the thermal load at the cold end and of the overall power consumption, compared to other state-of-the-art closed cycle cooling systems. The classical CMRC-CL designs in combination with a cryocooler at the cold stage, yields a specific thermal load at the 80 K cold stage of 14 W/kA at an overall power consumption of about 600 W/kA. Compared to a conventional conduction cooled current lead (CCCL) that is cooled by one cryocooler, this is a 67 % reduction of the thermal load at a 50 % reduced overall power consumption. Considerable smaller values are archived only with an optimized self-sufficient vapour cooled current lead (ss-VCCL) with a thermal load of 9 W/kA at a power consumption of 280 W/kA, however, comes with the disadvantage of an open system that requires a continuous supply of LN_2.

The classical heat exchanger design leads to several scalability problems that are described in Section 4.8 and the adjustment of this design to larger electric currents is related to relative large CL lengths and diameters. Therefore, a new micro-structured CMRC-CL design is developed, patented and manufactured (in IMVT) in the frame of this work. It consists of several micro-structured copper sheets of 0.5 mm thickness that comprise a certain amount of etched channels for the fluid flow. The total amount of the sheets depends on the electric current and the refrigerant mass flow that is needed to absorb a certain amount of Joule heating, thermal radiation and thermal load due to thermal conduction from the ambience. All sheets are stacked together by a specific stacking pattern, then covered by the top and bottom plates and irreversibly connected in a diffusion bonding process. The new design, allows a simple adjustment of the amount of sheets, the amount of channels per sheet, the CL length and the refrigerant mass flow for a desired electric current. The respective numerical model is developed and CLs for electric currents of 10 kA and 20 kA are designed and numerically investigated. One of the investigated CMRC-CL designs **C**, yields a thermal load of 6.5 W/kA at a temperature of 85 K. Compared to a CCCL that is working in this temperature range, this is an 85 % reduction of the thermal load and therefore, the largest reduction compared to the state-of-the-art solutions. To follow the concept of the CL comparison that is presented in this work, the CMRC-CL design **C** is extended by an additional cooling machines (GM-AL60) at the cold end to absorb the remaining thermal load. With a total power consumption of 490 W/kA, the micro-structured CMRC-CL system is the most efficient closed-cycle system. However, it is to denote that it is realistic to develop CMRC-CL systems that do not need an additional cryocooler and temperatures below 85 K are possible by an adjustment of the refrigerant mixture and/or the refrigerant cycle. Further, the developed and manufactured micro-structured CMRC-CL is a solid and important design milestone in the development of future CL types.

Experimental results that are obtained with the micro-structured heat exchanger prototype II, which is made of stainless steel, are discussed in section 5. The operating characteristics and the performance of this prototype are evaluated and the measurement data are compared with the results obtained from the numerical model. The conducted

experiments showed a temperature decrease to about 85 K with a hydrocarbon based refrigerant mixture. The numerical model showed a good agreement with the measured temperature data along the heat exchanger at temperatures above 170 K, however, a deviation of the temperature gradients is present at lower temperatures and is investigated in this work. Experiments with mixtures containing neon showed no further cool down of the system and the temperature at the cold end increased instead, because of the reduced specific cooling power of this mixture with neon. Further experiments with LRS mixtures, that have a considerable larger specific cooling power, may be performed to overcome this effect.

In conclusion, the numerical and experimental results on the micro-structured heat exchanger designs provide evidence that it is possible to develop a CMRC system that can cool down a superconducting application at least to the temperature of liquid nitrogen without the need of additional cryocoolers as the last cold stage. Furthermore, the new micro-structured CMRC-CL design allows a simple adjustment of its geometric and hydraulic parameters for a predefined electric current and it may be possible to design CLs even for the large electric currents of aluminium plants that are typically operated at 200-500 kA.

Zusammenfassung

HTS-Anwendungen in elektrischen Netzwerken wie supraleitende Stromkabel und Stromschienen einerseits, sowie Motoren, Generatoren und Transformatoren hoher Leistung anderseits benötigen einige Kilowatt Kälteleistung bei Betriebstemperaturen von ca. 50-78 K. Ein Großteil der Kälteleistung, je nach Anwendung bis zu ca. 90 %, wird dabei zur Kühlung der Stromzuführung benötigt, die zwischen Umgebungstemperatur (300 K) und der kryogenen Arbeitstemperatur der Supraleiter betrieben werden. Zur Kühlung solcher Stromzuführungen sind kryogene Gemischkreisläufe (Cryogenic Mixed Refrigerant Cycle - CMRC) die optimale Lösung, da die Wärmeströme über den gesamten Temperaturbereich bei Temperaturdifferenzen von nur wenigen Kelvin abgeführt werden können. Die Anpassung der optimalen Temperaturniveaus erfolgt über die Zusammensetzung weitsiedender Kältemittelgemische, deren Komponenten entlang des Hauptwärmeübertragers auf der Hochdruckseite jeweils partiell kondensieren und auf der Niederdruckseite in Gegenstrom jeweils partiell verdampfen. Die Druckniveaus liegen in Bereichen, in denen kostengünstige Standardkomponenten aus der Kältetechnik verfügbar sind. Durch die hohe thermische Integration ist zu erwarten, dass die Gesamteffizienz von CMRCs in der Anwendung trotz deutlich niedriger Komplexität und Kosten durch den Verzicht auf kalte Expansionsmaschinen bzw. Kaskadenschaltungen im Bereich der Effizienz der Turbo-Brayton Prozesse liegt. Daraus ergibt sich ein hohes Potenzial, künftig eine neue Klasse geschlossener, effizienter, skalierbarer und kostengünstiger Kältemaschinen für HTS-Anwendungen zur Verfügung zu stellen. Die Wirtschaftlichkeit von HTS Anwendungen in der Energietechnik wird damit wesentlich verbessert.

Das Ziel dieser Arbeit ist die Entwicklung einer 10 kA kryogenen Stromzuführung, welche mit einer kryogenen Gemischkälteanlage gekühlt wird (CMRC-CL). Um eine detaillierte Untersuchung des CL-Designs zu ermöglichen, wird ein bestehendes numerisches Wärmeübertragermodell modifiziert und in das im Rahmen dieser Arbeit entwickelte Berechnungsmodel für resistive Stromführungen implementiert. Vor der Implementierung wird eine Literaturrecherche zu den aktuellen Stromzuführungsdesigns und Kühlsystemen durchgeführt, welche numerisch untersucht und miteinander verglichen werden. Darauf aufbauend werden in dieser Arbeit eine klassische Rohr-in-Rohr und eine mikrostrukturierte CMRC Stromzuführung entwickelt und numerisch untersucht. Die erste entwickelte Stromzuführung besteht aus einem klassischen Rohr-in-Rohr-Wärmeübertrager, der um eine zylindrische Stromzuführung aus Kupfer gewickelt ist. Der zweite CMRC-CL Prototyp III besteht aus mehreren mikrostrukturierten Kupferblechen, die durch ein Diffusionsschweißverfahren miteinander verbunden sind. Der Prototyp III wurde im Rahmen dieser Arbeit numerisch untersucht, patentiert und am Institut für Mikroverfahrenstechnik (IMVT) hergestellt. Darüber hinaus wurden im CMRC-Prüfstand am Institut für Technische Thermodynamik und Kältetechnik (ITTK) experimentelle Untersuchungen am mikrostrukturiertem Wärmeübertrager aus Edelstahl (Prototyp II) durchgeführt und die Vorhersagequalitäten des modifizierten Wärmeübertragermodells wurde überprüft.

In Kapitel 2 werden fünf verschiedene Stromzuführungsarten, die den Stand der Technik wiedergeben, vorgestellt und numerisch untersucht. Die entsprechenden Wärmeeinträge am kalten Ende, die sogenannten CL-Formfaktoren, die optimalen Kältemittelmassenströme und die theoretische Leistungsaufnahme der Systeme sind in dem Kapitel zusammengefasst. Nach dem Wiedemann-Franz-Gesetz, das den Zusammenhang zwischen dem spezifischen elektrischen Widerstand und der Wärmeleitfähigkeit von Metallen beschreibt, kann jeder metallische Werkstoff als Stromleiter verwendet werden. Jedes Material führt

zu einer anderen optimalen Geometrie der Stromzuführung und daher werden die thermophysikalischen Eigenschaften relevanter Materialien bewertet und miteinander verglichen.

Die Untersuchung der Stromzuführung allein reicht nicht aus, um die Effizienz des gesamten Systems zu bewerten, daher werden verschiedene Kühlsysteme die den Stand-der-Technik wiedergeben in Kapitel 3 vorgestellt und diskutiert. Dabei wird der jeweilige Gesamtstromverbrauch inklusive der benötigten Kälteleistung des Kühlsystems und der elektrischen Verlustleistung der Stromleitung berechnet und diskutiert. Es wird eine detaillierte Analyse des Linde-Hampson-Kältekreislaufs, der den CMRCs zugrunde liegt, vorgestellt.

Ein numerisches Modell zur Berechnung von CMRC-CLs wird in Kapitel 4 präsentiert und beinhaltet die numerischen Untersuchungen des klassischen und des mikrostrukturierten Designs. Um ein optimales Kältemittelgemisch zu identifizieren, werden mehrere Parameterstudien mit dem klassischen CMRC-CL Design durchgeführt. Es hat sich gezeigt, dass in der Auslegung des CMRC-CL ein Kältemittelgemisch mit einer höheren Zusammen-setzung des Tiefsieders Methan eine geeignete Wahl ist. Die klassische CMRC-CL führt zu einer deutlichen Reduzierung des Wärmestromes am kalten Ende und des Gesamtstromverbrauchs im Vergleich zu anderen Kühlsystemen die in einem geschlossenen Kühl-kreislauf arbeiten. Das klassische CMRC-CL Design in Kombination mit einem Kryokühler ergibt einen spezifischen thermischen Wärmestrom an der 80 K kalten Stufe von 14 W/kA bei einer Gesamtleistungsaufnahme von etwa 600 W/kA. Im Vergleich zu einer konventionellen, kontaktgekühlten Stromzuführung (CCCL), die von einem Kryokühler gekühlt wird, bedeutet dies eine 67 % Reduzierung der thermischen Last bei einer um 50 % reduzierten Gesamtleistungsaufnahme. Deutlich kleinere Werte werden nur bei einer optimierten, autarken gasgekühlten Stromzuführung (ss-VCCL) erreicht. Der Wärmestrom am kalten Ende beträgt hier etwa 9 W/kA bei einer Leistungsaufnahme von 280 W/kA, hat jedoch den Nachteil eines offenen Systems, das eine kontinuierliche Versorgung mit LN_2 erfordert.

Das klassische Wärmeübertragerdesign führt zu mehreren Skalierbarkeitsproblemen die in Kapitel 4.8 beschrieben sind. Die Anpassung dieses Designs an größere elektrische Ströme führt zu relativ großen geometrischen Abmessungen. Daher wurde im Rahmen dieser Arbeit ein neues mikrostrukturiertes CMRC-CL Design entwickelt, patentiert und ein Prototyp in IMVT hergestellt. Es besteht aus mehreren mikrostrukturierten Kupferblechen mit einer Dicke von 0.5 mm, die eine gewisse Anzahl von geätzten Kanälen für den Fluidstrom aufweisen. Die Gesamtanzahl der Platten hängt von der elektrischen Stromstärke und dem Kältemittelmassenstrom ab, welche für die Aufnahme der Joule'schen Wärme, Wärmestrahlung und Wärmestrom durch Wärmeleitung aus der Umgebung benötigt wird. Alle Bleche werden nach einem bestimmten Stapelmuster zusammengestapelt, dann von einer oberen und einer unteren Platte bedeckt und in einem Diffusionsschweißverfahren irreversibel verbunden. Das neue Design ermöglicht eine einfache Anpassung der Blechanzahl, der Anzahl der Kanäle pro Blech, der Stromzuführungs-länge und des Kältemittelmassenstroms für einen gewünschten elektrischen Strom. Das entsprechende numerische Modell wurde entwickelt und Stromzuführungen für elektrische Ströme von 10 kA und 20 kA entworfen und numerisch untersucht. Eines der untersuchten CMRC-CL Designs **C**, ergibt einen Wärmeeintrag von 6.5 W/kK bei einer Temperatur von 85 K. Im Vergleich zu einem CCCL, das in diesem Temperaturbereich arbeitet, ist dies eine 85 % Reduzierung des Wärmestromes am kalten Ende und damit die größte Reduzierung gegenüber den Lösungen aus dem Stand der Technik. Eine Erweiterung des CMRC-CL-Designs **C**

um eine zusätzliche Kältemaschine (GM-AL60), damit am kalten Ende die verbleibende thermische Last absorbiert und die Temperatur weiter abgesenkt werden kann, führt zu einer Gesamtleistungsaufnahme von 490 W/kA und ist somit das effizienteste geschlossene Stromzuführungssystem. Es ist jedoch anzumerken, dass es realistisch ist, CMRC-CL Systeme zu entwickeln die keinen zusätzlichen Kryokühler benötigen und Temperaturen unterhalb von 85 K durch eine Anpassung des Kältemittelgemisches und/oder des Kältemittelkreislaufs möglich sind. Darüber hinaus ist die entwickelte und gefertigte mikrostrukturierte CMRC Stromzuführung ein solider und wichtiger Design-Meilenstein in der Entwicklung zukünftiger Stromzuführungen.

Experimentelle Ergebnisse, die mit dem mikrostrukturierten Wärmeübertrager Prototyp II aus Edelstahl durchgeführt wurden, werden in Kapitel 5 vorgestellt und diskutiert. Die Betriebseigenschaften und die Leistung des Prototyps werden bewertet und die Messdaten mit den Ergebnissen des numerischen Modells verglichen. Die durchgeführten Experimente zeigten einen Temperaturabfall auf etwa 85 K mit Kältemittelgemisch auf Kohlenwasserstoffbasis. Das numerische Modell zeigte eine gute Übereinstimmung mit den gemessenen Temperaturdaten entlang des Wärmeübertragers bei Temperaturen über 170 K, jedoch liegt eine Abweichung der Temperaturgradienten bei niedrigeren Temperaturen vor und wird in dieser Arbeit untersucht. Versuche mit neonhaltigen Mischungen zeigten keine weitere Abkühlung des Systems, stattdessen erhöhte sich die Temperatur am kalten Ende aufgrund der durch die Beimischung von Neon geringer gewordenen spezifischen Kälteleistung. Um diesen Effekt zu überwinden, können weitere Versuche mit sogenannten LRS-Mischungen durchgeführt werden, die eine erheblich größere spezifische Kälteleistung aufweisen.

Zusammenfassend belegen die numerischen und experimentellen Ergebnisse zu den mikrostrukturierten Wärmeübertragerdesign, dass es möglich ist ein CMRC-System zu entwickeln, das eine supraleitende Anwendung mindestens auf die Temperatur von flüssigem Stickstoff herunterkühlen kann, ohne dass zusätzliche Kryokühler benötigt werden. Darüber hinaus ermöglicht das neue mikrostrukturierte CMRC-CL Design eine einfache Anpassung seiner geometrischen und hydraulischen Parameter für einen vordefinierten elektrischen Strom und es wäre möglich, Stromzuführungen sogar für die großen elektrischen Ströme von Aluminiumwerken auszulegen, die typischerweise bei 200-500 kA arbeiten.

Table of Contents

List of Figures

List of Tables

I List of symbols, indices and abbreviations

Symbols

Symbol	Unit	Description
A	m^2	Area
COP	(-)	Coefficient of performance
c_p	$\mathrm{J/(kg\,K)}$	Isobaric heat capacity
d, D	m	Diameter
err	(-)	Numerical error
f	(-)	Factor for the heat transfer area
g	$\mathrm{m/s^2}$	Gravitational constant
h	J/kg	Specific enthalpy
Δh_v	J/kg	Specific heat of vaporisation
I	A	Electric current
k	$\mathrm{W/(m^2\,K)}$	Thermal transmittance
k_u	(-)	Coverage factor for the measurement uncertainty
l	kJ/kg	Specific work
L	m	Length
$\dot{m}$	kg/s	Mass flow
$\dot{m}''$	$\mathrm{kg/(s\,m^2)}$	Mass flux
n, N	kg/s	Number/Amount
P	W	Power
P_total	W	Total power dissipation of all refrigeration units
$P_\mathrm{total,el}$	W	Total power dissipation of all refrigeration units + electric power losses of the current leads
q	J/kg	Specific thermal energy
q'	$\mathrm{J/(kg\,m)}$	Specific thermal energy per unit length
$\dot{q}'$	W/m	Heat transfer rate per unit length
$\dot{Q}$	W	Heat transfer rate
RRR	(-)	Residual-resistivity-ratio
s	$\mathrm{J/(kg\,K)}$	Specific entropy
$\Delta s_{\Delta c}$	$\mathrm{J/(kg\,K)}$	Specific entropy due to concentration gradients
$\Delta s_{\Delta p}$	$\mathrm{J/(kg\,K)}$	Specific entropy due to pressure gradients
$\Delta s_{\Delta T}$	$\mathrm{J/(kg\,K)}$	Specific entropy due to temperature gradients
$\dot{S}_\mathrm{II}$	W/K	Entropy production rate caused by gradients
t	s	Time
T	K	Temperature
U	m	Circumference
x	m	Coordinate of the current lead

$\tilde{x}$	(-)	Mole fraction
y	(-)	Liquid fraction
$y^\star$	(-)	Heat transfer ratio
z	m	Coordinate of the heat exchanger
α	$\mathrm{W/(m^2\,K)}$	Heat transfer coefficient
α_S	V/K	Seebeck coefficient
γ	$\mathrm{K^-1}$	Volumetric coefficient of thermal expansion
ε	(-)	Void fraction
$\tilde{\eta}$	(-)	Efficiency
$\tilde{\eta}_\mathrm{Carnot}$	(-)	Carnot efficiency
θ	°	Flow angle
λ	$\mathrm{W/(m\,K)}$	Thermal conductivity
ν	$\mathrm{m^3/kg}$	Specific volume
ρ	$\Omega\,\mathrm{m}$	Specific electrical resistance

Indices

a	Ambience
af.cool	Aftercooler
c	Cold end
comp	Compressor
C	Carnot
CCCL	Conduction cooled current lead
CL	Current lead
Cu	Copper
el	Electric
evap	Evaporating
ext	External
f	Friction
ff	Forced-flow
G	Gas
h	Hot
HP	High pressure
hx	Heat exchanger
i	Inner
I	Due to electric current
in	Inlet
inf	Infinity
int	Internal
l	Liquid
liq	Liquefaction
LP	Low pressure
m	Mean
max	Maximum
min	Minimum
num	Numerical
o	Outer

opt	Optimum
out	Outlet
PE	Peltier element
rad	Thermal radiation
ref	Refrigeration
ss	Self-sufficient
t	Technical
th	Theoretical
thr	Throttling device
tp	Triple point
v	Vapour
w	Windings
λ	Due to thermal conductivity

Physical Constants

Symbol	**Value**	**Unit**	**Description**
L_0	2.44×10^{-8}	V^2/K^2	Lorentz number

List of Abbreviations

AAD	Average absolute deviation
ARD	Average relative deviation
CCCL	Conduction cooled current lead
CryoPHAEQTS	Cryogenic Phase Equilibria Test-Stand
EoS	Equation of state
FBG	Fibre Bragg grating
GERG-EoS	GERG-2008 equation of state
GM	Gifford-McMahon
HCM	Hydrocarbon mixture
HTS	High-temperature superconductor
IMVT	Institute for Micro Process Engineering Institut für Mikroverfahrenstechnik
ITTK	Institute of Technical Thermodynamics and Refrigeration Institut für Technische Thermodynamik und Kältetechnik
LN_2	Liquid nitrogen
MCCL	Multi-stage cooled current leads
MHE	Micro-structured heat exchanger
PCL	Peltier current lead
PR-EoS	Peng-Robinson equation of state
PT	Pulse tube
REFPROP	Reference Thermodynamic and Transport Properties
SBG	Silver-Bell-Ghally
SRM	Synthetic refrigerant mixture
VCCL	Vapour cooled current lead
VCPCL	Vapour cooled Peltier current lead

1 Introduction

High temperature superconducting (HTS) applications like superconducting cables, power rails, generators, fault current limiter, accelerators and magnets may require several kilowatts of cooling power at an operating temperature range of 50-80 K. The major cooling demand, depending on the application up to 70-90 % [1], is necessary for the cooling of resistive current leads (CL) that supply electric energy from the ambience at 300 K to the superconducting application at cryogenic temperatures. Especially in high electric current applications a large demand on cooling power is needed for the CLs, like in the 1 km long, 10 kV superconducting cable system AmpaCity [2, 3], which require in total six 10 kA CL terminals that are cooled by an open liquid nitrogen system. Further industrial applications that require large electric currents are the chlorine electrolysis that are typically operated at 20 kA and the aluminium production plants with 200-500 kA [1].

The cryogenic mixed refrigerant cycles (CMRCs) are the optimal solution for the cooling of CLs, due to the possibility to generate cooling power at the required cryogenic temperatures by adjusting the composition of the mixture and cycle parameters to attain a high energy efficiency [4], especially in comparison to refrigeration cycles that are operated with pure refrigerants. The key in this technology is the direct implementation of the resistive current lead into the recuperative heat exchanger of the Linde-Hampson cycle, providing refrigeration power over the temperature range of the heat exchanger. Hereby, a mixed refrigerant is partly condensing and evaporating inside the heat exchanger and absorbing the Joule heat at the temperature it is generated in the current lead. The high thermal integration of the CL and the cooling medium in a close cooling system, the relative low complexity of the set-up and in particular the scalability of CMRC-CLs, have the potential to provide a new cost-efficient CL technology. Hereby, the economic efficiency of HTS applications in the energy technology can be considerably improved.

The present work builds on two major preliminary works at the Institute of Technical Thermodynamics and Refrigeratioon - Institut für Technische Thermodynamik und Kältetechnik (ITTK). In the first work conducted by Kochenburger [4], an experimental CMRC test stand was built to investigate the thermophysical properties of refrigerant mixtures and the efficiency of heat exchanger prototypes. Investigations on hydrocarbon based mixtures (HCM) and non-flammable synthetic refrigerant mixtures (SRM) were performed in [4]. In the second preliminary work conducted by Gomse [5], a numerical heat exchanger model for the two-phase heat transfer and pressure drop of HCM and SRM refrigerant mixtures was developed, validated and experimentally verified in the CMRC test stand. It comprises parasitic heat loads, like the thermal radiation, and fluid property variations of mixed refrigerants can be implemented into the algorithm.

The aim of this work is the development of a 10 kA cryogenic mixed refrigerant cooled

current lead (CMRC-CL). In order to evaluate the possibility of this technology, the numerical heat exchanger model of Gomse [5] is modified and implemented in the developed numerical calculation model for resistive CL in the frame of this work. The first developed CMRC-CL design comprises a classical multi-tubes-in-tube heat exchanger which is wounded around a cylindrical CL made of copper. The second CMRC-CL prototype III is made of several micro-structured copper sheets that are connected together by a diffusion bonding process and is developed and manufactured, however, could not be experimentally tested in the time frame of this work. Nevertheless, experimental investigation on the stainless steel micro-structured heat exchanger prototype II are conducted in the CMRC test stand and the predictive qualities of the modified heat exchanger model are reviewed.

Within the scope of this work, five state-of-the-art CL solutions and design approaches are introduced and numerically investigated in section 2. The corresponding thermal loads at the cold end, the CL shape factors, the optimal refrigerant mass flows and the theoretical power consumptions of the systems are summarized in the design overview. Further, the thermophysical properties of relevant resistive CL materials are evaluated and compared with each other.

In the section 3, the state-of-the-art cooling systems for CLs are evaluated and discussed. Hereby, the total power consumptions P, including the required refrigeration power of the cooling system and the electric power losses of the respective current lead type, are calculated and discussed. A detailed analysis on the Linde-Hampson refrigration cycle, which is the basis of CMRCs, is presented.

Section 4 describes the mainly investigated classical CMRC-CL, the respective test stand and the new micro-structured CMRC-CL prototype III. The numerical CMRC-CL models for both prototypes are presented and the respective CLs performances are discussed in several parametric studies. Furthermore, an appropriate refrigerant mixture composition for resistive CL is identified. Conclusively, the geometric dimensions of CMRC-CLs, that are build with the superior micro-structured design, are presented for electric currents of 10 kA and 20 kA.

Experimental results that are obtained with the micro-structured heat exchanger prototype II, which is made of stainless steel, are discussed in section 5. The operating characteristics and the performance of this prototype are evaluated and the measurement data are compared with the results obtained from the numerical model.

Finally, the essential results of the present work are summarized and the outlook for future developments is presented in section 6.

2 State-of-the art Current leads

Current leads in superconducting systems are the links between the power supply at room temperature and the superconducting application at the cryogenic temperature. These links are used to supply electric energy to the superconducting application in the form of alternate current (AC) or direct current (DC). Most superconducting applications require a continuous supply of electric energy and therefore a continuous supply of cooling power to remove the heat leakage and ensure the operating temperature of the superconductor. Except for NMR and MRI systems that normally work in persistent mode, where the power supply can be turned off and the current leads be thermally decoupled from the cold body [6], the heat leakage of the system consists mainly of two permanent contributions. The first contribution is electric power losses, due to the transport of electric current through the current lead that induce the so-called Joule or ohmic heating

$$P_{\mathrm{el}} = \dot{Q}_{\mathrm{I}} = R\,(T) \cdot I^2 = \frac{\rho\,(T) \cdot L}{A} \cdot I^2 \tag{2.1}$$

where ρ is the specific electrical resistance, I the amperage, L the length and A the cross section area of the current lead. The Joule heating is minimized by increasing the cross section area ($A \uparrow$) and by reducing the current lead length ($L \downarrow$). On the other hand, the second contribution to the heat load, i.e. thermal conduction due to Fourier's Law

$$\dot{Q}_{\lambda} = -\frac{A}{L} \cdot \int \lambda\,(T)\,\mathrm{d}T \tag{2.2}$$

with the thermal conductivity λ of the current lead material, requires a long current lead ($L \uparrow$) with a smaller cross section area ($A \downarrow$). For the reduction of the thermal load into the cryogenic system, both contributions have to be balanced by the selection of an appropriate ratio of length to cross section area. Nevertheless, the electric requirements consequently lead to a significant thermal load into an otherwise well isolated cryogenic system.

Minimizing the thermal load at the cold end of the cryogenic/superconducting system is the usually used optimization method for current leads. By selecting an appropriate geometry, the contribution of the Fourier's Law (2.2) at the warm terminal can be reduced to zero, yielding an adiabatic boundary condition [7]. From an energetic point of view, this is reasonable for one stage conducting cooled current leads (CCCL) that are cooled only by one refrigeration machine at the cold end or by the boil off of a cryogenic fluid in an open system. However, from the thermodynamic point of view, the thermal integration of the cooling system at the coldest part in a CCCL is the least efficient in comparison to any other type of current lead. Therefore, together with CCCL four other types of

current leads are presented in the following for a temperature range of 300 K to 77.4 K.

The material used for the resistive part of the current lead is usually copper, which makes the lead a good electrical and thermal conductor. However, according to the Wiedemann-Franz-Lorenz law [8–10] and its relation to the design of a current lead, any metallic material can be used. The detailed analysis of metallic material properties for current leads is discussed in Sec. 2.7. For the comparison of different current lead types in the following, copper with a residual-resistivity-ratio $RRR = 50$ is used.

2.1 Conduction cooled current leads

Conduction cooled current leads are cooled only by one refrigeration unit, for example a cryocooler, at the cold end. The design goal of CCCLs is the minimization of the thermal load $\dot{Q}_\mathrm{c}$ at the coldest part of the lead. Therefore, the heat load has to be analysed by the following energy balance of an infinitesimal length of the current lead according to Fig. 1, yielding

$$\dot{Q}_\lambda(x) = \dot{Q}_\lambda(x + \mathrm{d}x) + \mathrm{d}\dot{Q}_\mathrm{I} \tag{2.3}$$

$$\mathrm{d}\dot{Q}_\lambda = \mathrm{d}\dot{Q}_\mathrm{I} \tag{2.4}$$

The infinitesimal amount of ohmic heating $\mathrm{d}\dot{Q}_\mathrm{I}$, can be combined with the Fourier's Law (2.2) to

$$\mathrm{d}\dot{Q}_\mathrm{I} = I^2 \cdot \frac{\rho\,(T)}{A}\,\mathrm{d}x = -I^2 \cdot \frac{\rho\,(T) \cdot \lambda\,(T)}{\dot{Q}_\lambda}\,\mathrm{d}T \tag{2.5}$$

and (2.4) becomes

$$\int_{\dot{Q}_\mathrm{c}}^{\dot{Q}_\mathrm{h}} \dot{Q}_\lambda\,\mathrm{d}\dot{Q}_\lambda = -I^2 \int_{T_\mathrm{c}}^{T_\mathrm{h}} \rho\,(T) \cdot \lambda\,(T)\;\mathrm{d}T \tag{2.6}$$

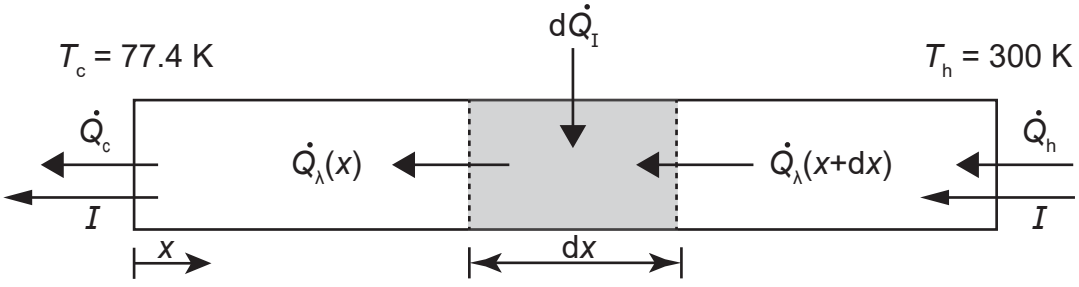

Figure 1: Energy balance for the conduction cooled current lead.

Integrating (2.6) yields the equation for the thermal load at the cold end of the current lead

$$\dot{Q}_{\mathrm{c}} = \sqrt{\left(\dot{Q}_{\mathrm{h}}\right)^2 + 2 \cdot I^2 \int_{T_{\mathrm{c}}}^{T_{\mathrm{h}}} \rho\left(T\right) \cdot \lambda\left(T\right) \, \mathrm{d}T} \tag{2.7}$$

The thermal load $\dot{Q}_{\mathrm{c}}$ can only be minimized, when $\dot{Q}_{\mathrm{h}}$ from the ambience into the cryogenics system becomes zero, yielding an adiabatic boundary condition at the warm end $(x = L)$

$$\dot{Q}_{\mathrm{h}} \stackrel{!}{=} 0 = -\lambda \cdot A \cdot \cancelto{0}{\left.\frac{\mathrm{d}T}{\mathrm{d}x}\right|_{x=L}} \tag{2.8}$$

The thermal load at the cold end in an optimized CCCL is then minimized to

$$\dot{Q}_{\mathrm{c,min}} = I \sqrt{2 \cdot \int_{T_{\mathrm{c}}}^{T_{\mathrm{h}}} \rho\left(T\right) \cdot \lambda\left(T\right) \, \mathrm{d}T} \tag{2.9}$$

The optimum heat flow $\dot{Q}_{\mathrm{c,opt}}$ through the current lead is calculated by replacing the parameter T_{c} in the lower bound of the integral (2.9) by the variable T, and is used for the calculation of the optimum geometry ratio of the length versus the cross section area according to the Fourier's law (2.2)

$$\left(\frac{L}{A}\right) = -\int \frac{\lambda\left(T\right)}{\dot{Q}} \, \mathrm{d}T = -\int \frac{\lambda\left(T\right)}{-\dot{Q}_{\mathrm{c,opt}}} \, \mathrm{d}T \tag{2.10}$$

$$\left(\frac{I \cdot L}{A}\right) = \int_{T_{\mathrm{c}}}^{T_{\mathrm{h}}} \frac{\lambda\left(T\right)}{\sqrt{2 \cdot \int_{T}^{T_{\mathrm{h}}} \rho\left(T\right) \cdot \lambda\left(T\right) \, \mathrm{d}T}} \, \mathrm{d}T \tag{2.11}$$

The expression on the left-hand side of (2.11) in (A/m) is called shape-factor and is used in the design of conduction cooled current leads. It should be noted that the minimal heat load at the cold end (2.9) and the shape-factor (2.11) are linked to the material properties of the lead. The comparison of different materials is presented in Sec. 2.7. For commercial copper with a residual-resistance-ratio of $RRR = 50$, the design parameters are presented in Tab. 1. The minimum heat load per amperage $\dot{Q}_{\mathrm{c,min}}/I$ is about 42.5 W/kA for the shape-factor of 3515 kA/m. For a designed current of 10 kA, this is equal to a thermal

load at the cold end of 425 W. This can be realised by the selection of an appropriate length and cross section area of the current lead according to the relation $\left(L/A\right)$ in Tab. 1.

The adiabatic boundary condition at the warm end (2.8) can be shown with the temperature profile of an optimized current lead, which can be calculated with the partial differential form of (2.4) with respect to x and the simplification of no temperature gradient perpendicular to x, yielding

$$\left(\frac{\partial \dot{Q}_{\lambda}}{\partial x}\right) \mathrm{d}x - \left(\frac{\partial \dot{Q}_{\mathrm{I}}}{\partial x}\right) \mathrm{d}x = 0 \tag{2.12}$$

which gives the following expressions

$$\frac{\partial}{\partial x}\left(-\lambda\left(T\right) \cdot A \cdot \frac{\partial T}{\partial x}\right) - \frac{\partial}{\partial x}\left(I^2 \cdot \frac{\rho\left(T\right)}{A} \cdot \mathrm{d}x\right) = 0 \tag{2.13}$$

$$\frac{\partial}{\partial x}\left(\lambda\left(T\right) \cdot A \cdot \frac{\partial T}{\partial x}\right) + I^2 \cdot \frac{\rho\left(T\right)}{A} = 0 \tag{2.14}$$

Equation (2.14) is a steady state one-dimensional, second-order differential equation and describes the temperature distribution in axial direction with a temperature-dependent internal heat source, i.e. the Joule heating. Two boundary conditions at $x = 0$ and $x = L$ are needed to solve (2.14). For current leads usually the following Dirichlet boundary conditions are used,

$$T_{(x=0)} = T_{\mathrm{c}} \overset{(e.g.)}{=} 77.4\,\mathrm{K} \tag{2.15}$$

$$T_{(x=L)} = T_{\mathrm{h}} \overset{(e.g.)}{=} 300\,\mathrm{K} \tag{2.16}$$

which describe a fixed temperature at the cold ($x = 0$) and warm ($x = L$) end of the lead. Solutions of (2.14) are shown in Fig. 2 for three different current lead lengths (a,b,c) at

Table 1: Design parameters of a conduction cooled current lead with a residual-resistance-ratio $RRR = 50$. L and d are example values and can be changed according to the ratio $\left(L/A\right)$.

Material	$\dot{Q}_{\mathrm{c,min}}/I$ W/kA	$\left(I \cdot L/A\right)$ kA/m	I kA	$\dot{Q}_{\mathrm{c,min}}$ W	$\left(L/A\right)$ m/m^2	L m	$d^{\star}$ mm
Copper	42.5	3515	10	425	351.5	0.69	50

* Cross section diameter of a cylindrical current lead

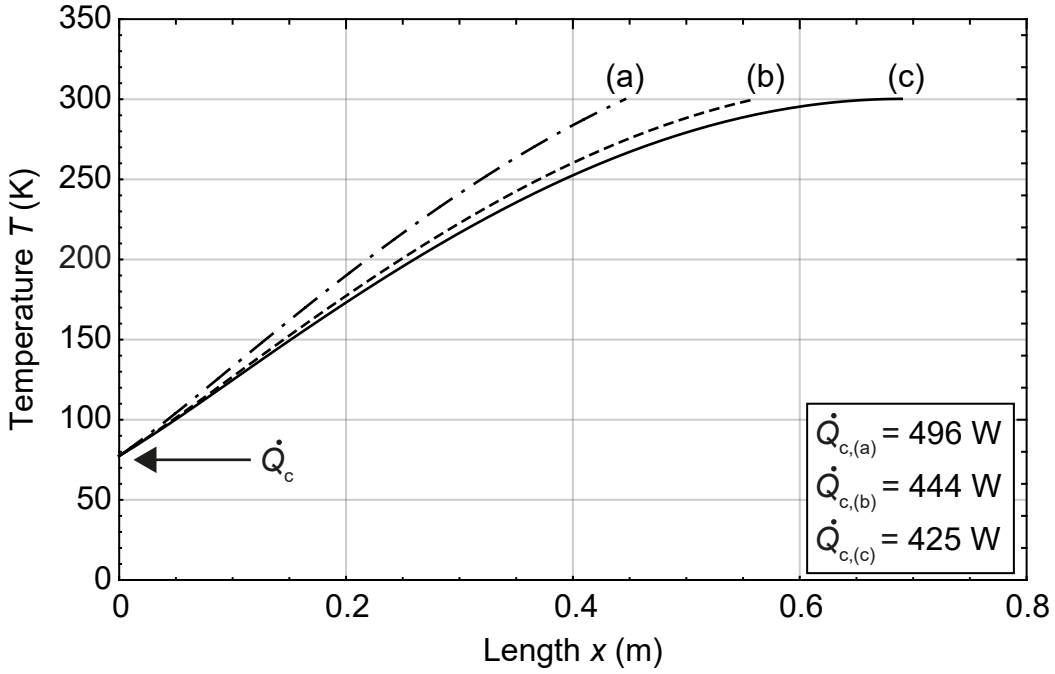

Figure 2: Temperature profiles of three (a,b,c) cylindrical 10 kA conduction cooled current leads with fixed cross section diameter of 50 mm, but with different lead lengths of 0.44 m, 0.56 m and 0.69 m, respectively.

fixed cross section diameter and amperage. The thermal load at the cold end $\dot{Q}_c$ is the largest for the shortest current lead (a) and the smallest for case (c). Among the three cases, only (c) was designed with the shape-factor $\left(I \cdot L/A\right) = 3515\,\mathrm{kA/m}$ from Tab. 1 of an optimized conduction cooled current lead. Therefore, only the temperature profile of (c) complies with the adiabatic boundary condition at the warm end in accordance with (2.8) and minimizes the thermal load according to (2.9). The adiabatic boundary condition is detected by the zero temperature gradient at the warm end. Despite the shorter current lead lengths (a,b) and therefore a smaller Joule heating (2.1), the heat loads at the cold end are higher in comparison to (c). Evidence for this is shown in the following Fig. 3, evaluated with equation (2.14) for current lead lengths ranging between 0.1 m and 0.8 m.

In Fig. 3, the heat loads in a current lead for two different modes are presented. The first mode represents the heat loads $\dot{Q}_c$ at the cold end, when electric current is applied. The second mode describes the heat load at the cold end $\dot{Q}_{c,0}$, when no electric current is applied. For small current lead lengths, the contribution to $\dot{Q}_c$ is higher due to the thermal conduction than to the Joule heating. At (a) both contributions are equal and the relation changes to higher Joule heating when a larger current lead length is used. Thermal conduction from the ambience into the cryogenic system decreases linearly with length to point (c), at which the heat load becomes zero, due to the zero temperature

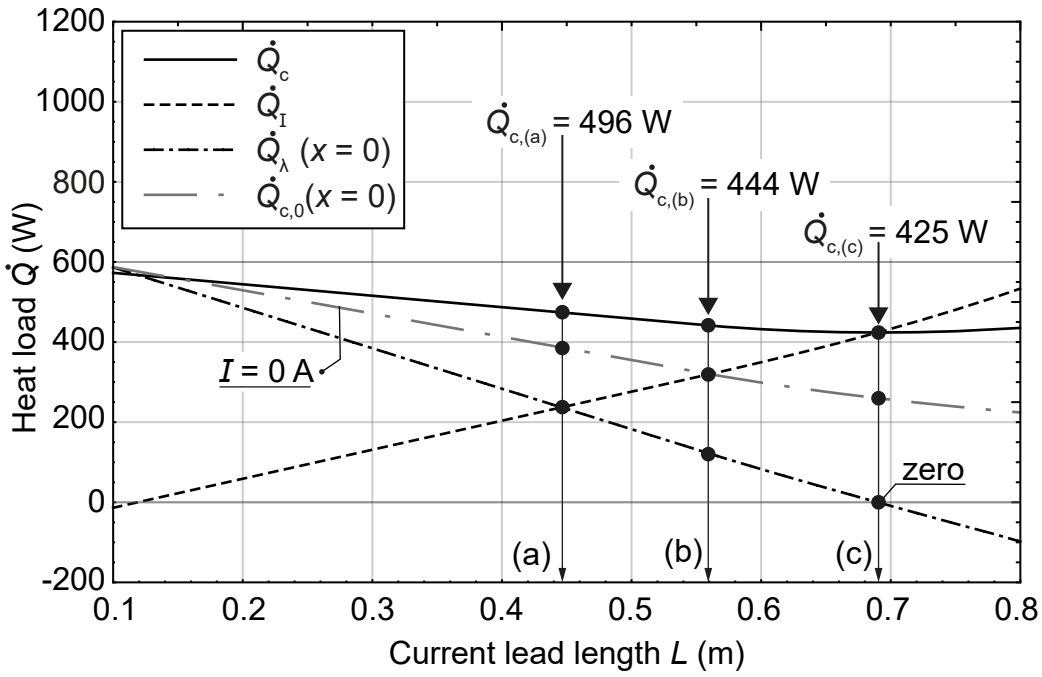

Figure 3: Heat loads in a cylindrical ($d = 50\,\mathrm{mm}$), 10 kA conduction cooled current lead as a function of the current lead length L. Whereby $\dot{Q}_\mathrm{c}$ describes the heat load at the cold end, which compromises the Joule heating $\dot{Q}_\mathrm{I}$ and the heat load due to the thermal conduction $\dot{Q}_\lambda$. The heat load $\dot{Q}_{\mathrm{c},0}$ describes the heat load at the cold end without electric current. The points (a,b,c) are linked to the three investigated current leads in Fig. 2.

gradient at the warm end. At this point, the function of the overall heat load at the cold end $\dot{Q}_\mathrm{c}$ has a minimum and thus represents an optimized CCCL.

Joule heating of the current lead (b) shows an intersection with the heat load $\dot{Q}_{\mathrm{c},0}$ at zero current. It was found that for (b), with a 20% smaller shape-factor compared to (c), the ratio of the overall heat load to the Joule heating $\dot{Q}_\mathrm{c}/\dot{Q}_\mathrm{I}$ is about[1] $1.38 \approx \sqrt{2}$. This value may be used for the conceptual design of an under-current type current lead. Under-current design signifies a lead with a smaller length, a higher cross section area or a smaller optimum electric current compared to the optimum values determined from the shape factor. The opposite applies for over-current design. The three different design variations are shown in Fig. 4 for exemplary geometric dimensions. The under-current design leads to a high heat load due to the thermal conduction from the ambience and can lead to the freeze out of air humidity on the top flange of the cryostat. To prevent freezing, an electric heater [11] or a dry box filled with nitrogen gas [12, 13] can be used at the warm part of the current lead right above the cryostat top flange.

[1] Ratio investigated for the materials copper, aluminium and 90/10 brass and should be approximately-equal for all metallic materials according to the Wiedemann-Franz-Lorenz law [8, 9].

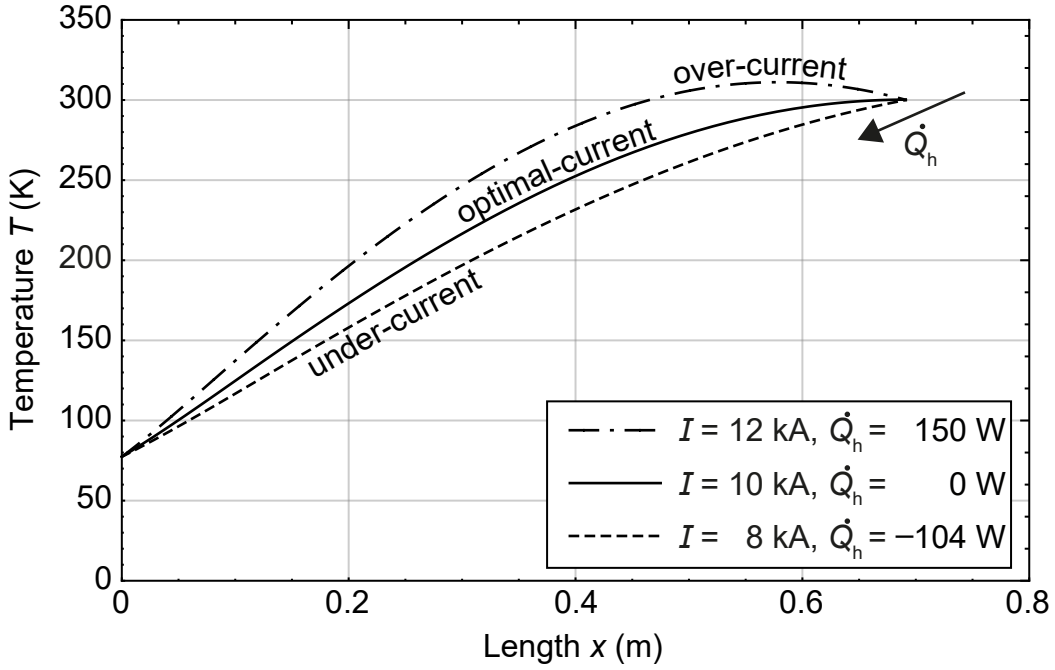

Figure 4: Temperature profiles of conduction cooled current leads working at over-current 12 kA, optimal-current 10 kA and under-current 8 kA mode. Geometric design values taken from Tab. 1. The negative sign for a heat load translates to a flow to the cold end of the current lead according to the used coordinate system in Fig. 1.

Over-current design is characterized by a peak in the temperature profile, which yields a heat load towards the warm end. In this design, a water cooling system [14, 15] has to be used to remove the heat load $\dot{Q}_h$ for the stabilisation of the temperature at the warm end.

For systems that are installed in an electric transmission grid, such as high-temperature superconducting (HTS) power systems, including HTS cables, transformers or fault current limiters, the electric current can change considerably over time [16]. The current lead has to be designed for the peak current, which yields an under-current design and safe operation, but implies a larger cooling load like for the case (b) in Fig. 2. Alternatively, the economically more reasonable way, a transient optimization method described in [16] can be used.

2.2 Multi-stage cooled current leads

Multi-stage conduction cooled current leads (MCCL), archive a smaller heat load at the cold end in comparison to CCCL by the application of several cooling stages at intermediate temperatures [1, 17–27]. According to the first and the second law of thermodynamics, the power requirement of a refrigeration machine is higher at lower temperatures. Therefore, the intermediate refrigeration stages absorb the incoming heat from the warmer part,

yielding in a smaller thermal load at the cold end. However, reducing the thermal load at the cold end [1] is not the only optimization method of a current leads. It is possible to design a lead, which minimizes the power input of all refrigeration stages [1, 18, 28] used in a MCCL. Furthermore, a second optimization method, which was first presented by Agsten [29] and recently adapted for MCCL and vapour cooled current leads by Schreiner [1], can be used to minimize the overall power requirements including the so-called double effect [29] of the electric power losses. Electric power losses induce Joule heating, which has to be removed by a refrigeration machine, and additionally represents the loss of energy in the electric circuit. Both effects are considered in the second optimization method for MCCL. In the following, the optimization methods for a two-stage conduction cooled current lead (2-MCCL) are presented.

In Fig. 5, a sketch of a MCCL with two refrigeration stages is presented and is used in the analysis of the optimization methods. The intermediate refrigeration stages in the optimization methods are defined as ideal refrigeration stages, i.e. Carnot stages. The Carnot cycle absorbs a heat load at a constant refrigeration temperature and rejects a heat load at ambient temperature. According to the first and the second law of thermodynamics, the power input needed for this process can be expressed as

$$P_{\mathrm{Carnot}} = T_{\mathrm{h}} \cdot \cancelto{0}{\Delta \dot{S}_{\mathrm{II}}} + \dot{Q}_{\mathrm{c}} \cdot \left(\frac{T_{\mathrm{h}}}{T_{\mathrm{c}}} - 1 \right) \tag{2.17}$$

with zero entropy increase $\Delta \dot{S}_{\mathrm{II}}$ caused by gradients, due to the energy transfer across the system boundaries and the convective transport of the fluid inside the cycle. The theoretical absence of any temperature gradient $\Delta T = 0\,\mathrm{K}$ in the transfer of finite amount of heat, would require a process that take infinite time Δt, or infinite heat transfer area A

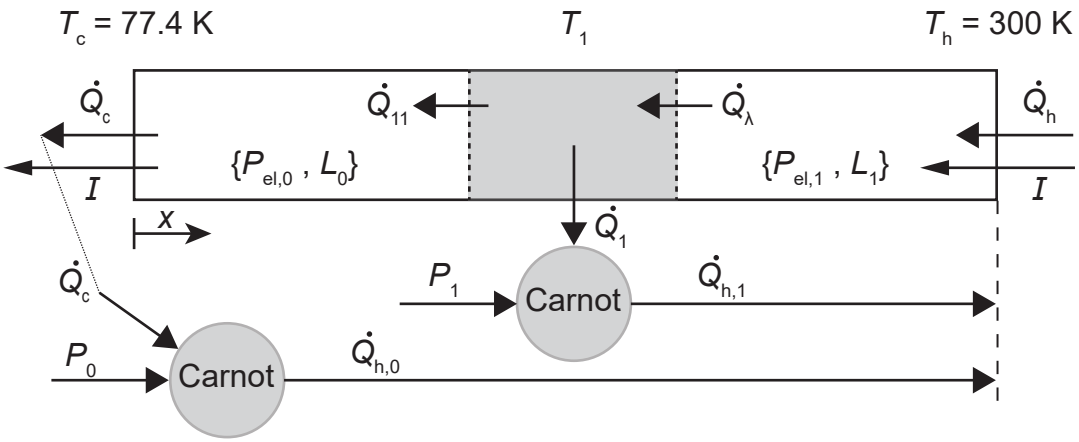

Figure 5: Sketch of a MCCL with two refrigeration stages, defined as Carnot stages. The variables $\{P_{\mathrm{el}}, L\}$ represent the electric power loss and the length of the corresponding current lead parts, before and after the intermediate stage.

[30]. According to the heat transfer theory between two bodies, the amount of heat energy is proportional to the temperature difference ΔT, the time taken Δt and the contact area A with

$$Q \propto A \cdot \Delta T \cdot \Delta t \tag{2.18}$$

Whereas $A \to \infty$ will lead to an infinite volume inside the cycle and therefore to an infinite power rating, $\Delta t \to \infty$ will take infinite time to absorb the finite amount of heat energy and the power density of the process will tend to zero. Therefore, it is more common to evaluate the so-called coefficient of performance COP of the Carnot cycle and compare it with the real power consumption of a refrigerator machine, yielding the Carnot efficiency[2] $\tilde{\eta}_{\mathrm{C}}$

$$COP_{\mathrm{Carnot}} = \frac{\dot{Q}_{\mathrm{c}}}{P_{\mathrm{Carnot}}} = \left(\frac{T_{\mathrm{h}}}{T_{\mathrm{c}}} - 1\right)^{-1} \tag{2.19}$$

$$\tilde{\eta}_{\mathrm{C}} = \frac{COP_{\mathrm{real}}}{COP_{\mathrm{Carnot}}} = \frac{\dot{Q}_{\mathrm{c}} \cdot \left(\frac{T_{\mathrm{h}}}{T_{\mathrm{c}}} - 1\right)}{P_{\mathrm{real}}} \tag{2.20}$$

Data for Carnot efficiencies of real refrigeration machines can be found in [1, 31]. It should be mentioned that the coefficient of performance decreases with decreasing refrigeration temperature. Nevertheless, (2.17) can be used as an appropriate optimization function for cooling at a constant temperature, since in this case, the Carnot cycle can be used as the thermodynamic reference cycle and the real refrigeration power, according to (2.20), is only a multiple thereof.

The thermal heat loads to the refrigeration stages are calculated with the energy balance equation analogous to the procedure in Sec. 2.1, yielding

$$\dot{Q}_1 = \sqrt{\left(\dot{Q}_{\mathrm{h}}\right)^2 + 2 \cdot I^2 \int_{T_1}^{T_{\mathrm{h}}} \rho\left(T\right) \cdot \lambda\left(T\right) \,\mathrm{d}T \cdot \left(1 - y^{\star}\right)} \tag{2.21}$$

$$\dot{Q}_{\mathrm{c}} = \sqrt{\left(\sqrt{\left(\dot{Q}_{\mathrm{h}}\right)^2 + 2 \cdot I^2 \int_{T_1}^{T_{\mathrm{h}}} \rho\left(T\right) \cdot \lambda\left(T\right) \,\mathrm{d}T \cdot y^{\star}}\right)^2 + 2 \cdot I^2 \int_{T_{\mathrm{c}}}^{T_1} \rho\left(T\right) \cdot \lambda\left(T\right) \,\mathrm{d}T} \tag{2.22}$$

[2] Carnot efficiency $\widehat{=}$ Figure of Merit $\widehat{=}$ Percent of Carnot $\widehat{=}$ $COP_{\mathrm{real}}/COP_{\mathrm{Carnot}}$

and

$$y^{\star} = \dot{Q}_{11}/\dot{Q}_{\lambda} = \dot{Q}_{11}/\sqrt{\left(\dot{Q}_{\mathrm{h}}\right)^2 + 2 \cdot I^2 \int_{T_1}^{T_{\mathrm{h}}} \rho\left(T\right) \cdot \lambda\left(T\right) \, \mathrm{d}T} \tag{2.23}$$

with three unknown variables, i.e. the temperature of the intermediate stage T_1, the heat load at the warm end $\dot{Q}_{\mathrm{h}}$ and the heat load towards the cold end $\dot{Q}_{11}$, which is expressed as the ratio $y^{\star}$. The input power of the refrigeration stages are then calculated with the first and the second law of thermodynamics to

$$P_1 = \dot{Q}_1 \cdot \left(\frac{T_{\mathrm{h}}}{T_1} - 1\right) \tag{2.24}$$

$$P_0 = \dot{Q}_{\mathrm{c}} \cdot \left(\frac{T_{\mathrm{h}}}{T_{\mathrm{c}}} - 1\right) \tag{2.25}$$

$$P_{\mathrm{total}} = P_0 + P_1 = f\left(\dot{Q}_{\mathrm{h}}, T_1, y^{\star}\right) \tag{2.26}$$

The optimum values for $\left(\dot{Q}_{\mathrm{h}}, T_1, y^{\star}\right)$ are found in the derivatives of the total Carnot power in (2.26) for all three unknown variables simultaneously, which have to be zero according to

$$\left(\frac{\partial P_{\mathrm{total}}}{\partial \dot{Q}_{\mathrm{h}}}\right) = \left(\frac{\partial P_{\mathrm{total}}}{\partial T_1}\right) = \left(\frac{\partial P_{\mathrm{total}}}{\partial y^{\star}}\right) = 0 \tag{2.27}$$

For the optimization of the total Carnot power, the derivatives of P_{total} in (2.26) for T_1 and $y^{\star}$ has to be determined. According to (2.21), $\dot{Q}_{\mathrm{h}}$ results in a higher refrigeration power at the intermediate stage and also in a higher Carnot power. Therefore, $\dot{Q}_{\mathrm{h}}$ is set to zero in this optimization method, yielding an adiabatic boundary condition at the warm end. The corresponding refrigeration powers of the the intermediate stage and at the cold end, as well as the Carnot powers and the electric power losses of the current leads are listed in Tab. 2 for the two optimization methods. In this case, the ratio $y^{\star} \approx 0.16$ and the intermediate temperature $T_1 = 157\,\mathrm{K}$ are found. It is to denote, that $y^{\star}$ does not approaches zero and means that the intermediate stage absorbs only a certain fraction of the incoming heat from the warmer part of the lead. This method reduces the electric power losses of the lead (see Tab. 2), due to the steeper temperature gradient at the intermediate stage and is also depicted in [28].

The second optimization method, minimizes the total Carnot power and the electric power

losses together and is characterized by the following minimization function

$$P_{\text{total,el}} = P_0 + P_1 + P_{\text{el},1} + P_{\text{el},0} = f\left(\dot{Q}_\text{h}, T_1, y^\star\right) \tag{2.28}$$

with the electric power losses of the upper part $P_{\text{el},1}$ and the lower part $P_{\text{el},0}$, which are calculated with the equation for the Joule heating (2.1), where the length to cross-section area $\left(L/A\right)$ is substituted with the Fourier's Law (2.2). The optimum heat flow in the lead, which is required for the calculation of the electric power losses, is derived from (2.21) and (2.22) analogous to the procedure in (2.11), yielding

$$P_{\text{el},1} = I^2 \int_{T_1}^{T_\text{h}} \frac{\rho\left(T\right) \cdot \lambda\left(T\right)}{\sqrt{\left(\dot{Q}_\text{h}\right)^2 + 2 \cdot I^2 \int_{T}^{T_\text{h}} \rho\left(T\right) \cdot \lambda\left(T\right)\, \mathrm{d}T}}\, \mathrm{d}T \tag{2.29}$$

$$P_{\text{el},0} = I^2 \int_{T_\text{c}}^{T_1} \frac{\rho\left(T\right) \cdot \lambda\left(T\right)}{\sqrt{\left(\sqrt{\left(\dot{Q}_\text{h}\right)^2 + 2 \cdot I^2 \int_{T_1}^{T_\text{h}} \rho\left(T\right) \cdot \lambda\left(T\right)\, \mathrm{d}T \cdot y^\star}\right)^2 + 2 \cdot I^2 \int_{T}^{T_1} \rho\left(T\right) \cdot \lambda\left(T\right)\, \mathrm{d}T}}\, \mathrm{d}T \tag{2.30}$$

Here, all three unknown variables $\left(\dot{Q}_\text{h}, T_1, y^\star\right)$ have to be found for the overall minimum of $P_{\text{total,el}}$ and yield $(-209\,\text{W}, 150\,\text{K}, 0.24)$. The negative sign for the heat load $\dot{Q}_\text{h}$, translates to a flow to the cold end of the current lead according to the used coordinate system in Fig. 5, and can lead to the freeze out of air humidity on the top flange. The results are presented in Tab. 2.

The first optimization method requires the adiabatic boundary condition at the warm end. This method requires a longer current lead to hold the adiabatic boundary condition and therefore results in higher electric power dissipation. The restriction to realize the adiabatic boundary condition makes this methods contradictory in terms of minimizing

Table 2: Comparison of the two optimization methods for a MCCL with two refrigeration stages.

Optimization method	$\dot{Q}_1/I$ W/kA	$\dot{Q}_\text{c}/I$ W/kA	P_total/I W/kA	P_el/I W/kA	$P_\text{total,el}/I$ W/kA
① P_Carnot	32.0	19.6	85.8	51.6	137.3
② $P_\text{Carnot} + P_\text{el}$	33.5	20.4	92.1	33.7	125.8

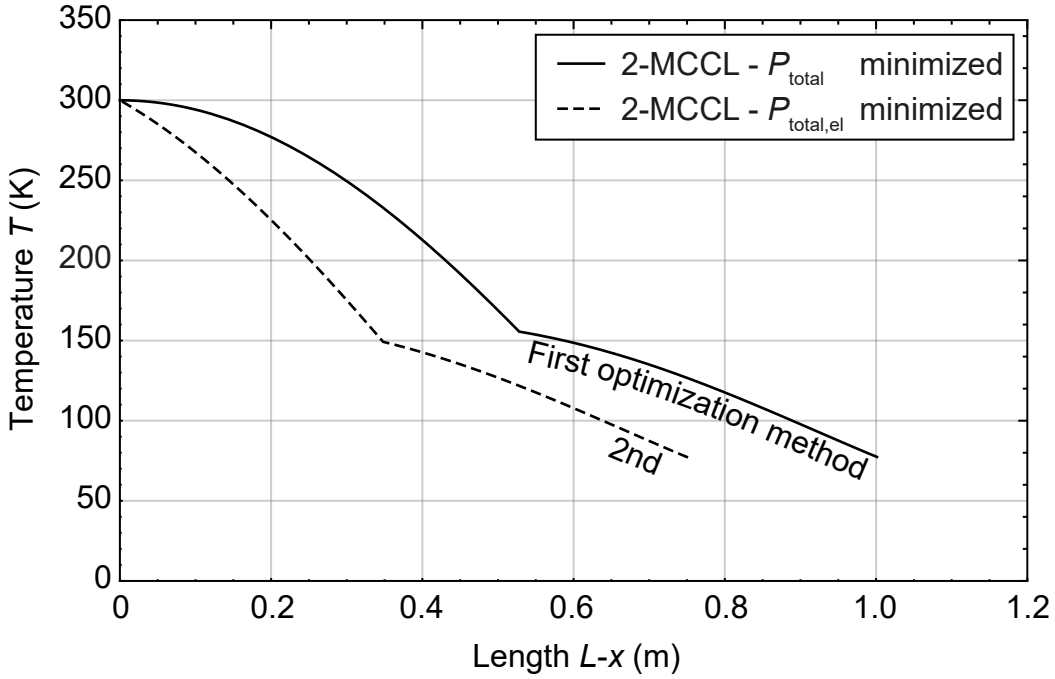

Figure 6: Temperature profiles of three cylindrical ($d = 50\,\mathrm{mm}$), 10 kA MCCLs with two refrigeration stages designed with three different optimization methods.

the overall energy consumption $P_{\mathrm{total,el}}$ according to (2.28). Furthermore, as mentioned in the previous Sec. 2.1, the electric current in HTS power systems that are installed in electric transmission grids changes with time and the current lead has to be designed for the peak current. This will result in an under-current design and a non-adiabatic boundary condition at the warm end. Therefore, it becomes unnecessary to adjust the geometry L/A for the adiabatic condition at the warm end of a current lead that is implemented in an electric grid.

The most efficient and compact way to design a MCCL is the second optimization method, where the overall energy consumption $P_{\mathrm{total,el}}$ of the system is minimized. The corresponding temperature profiles of MCCLs designed with the investigated optimization methods are presented in Fig. 6. The MCCL designed with the first optimization method requires the longest lead, due to the restriction of two adiabatic boundary conditions at the warm end and at the intermediate stage. One adiabatic condition is required for the second optimization method, which makes the current lead shorter compared to the first method. However, the shortest current lead and without any restrictions to the temperature gradient is designed with the 3rd optimization method. The design parameters for the geometry (shape factors) are shown in Tab. 3 for the three optimization methods and for each part of the MCCL. The calculation is performed analogous to the equations (2.10) and (2.11).

Table 3: Shape factors for two differently optimized MCCLs with two refrigeration stages. The subscript 1 refers to the upper part of the lead and the subscript 0 to the lower and colder part.

Shape factors kA/m	1st optimization	2nd method
$\left(I \cdot L/A\right)_1$	2675	2675
$\left(I \cdot L/A\right)_0$	3164	2429

2.3 Continuously cooled current leads

Multi-stage current leads with more than two refrigeration stages are possible and already demonstrated in [27] for a three-stage 20 kA 3-MCCL, but comes with a higher complexity of the system design. The addition of more refrigeration stages reduces the thermal load at the cold end and minimizes the overall Carnot power [28] and the overall electric power consumption [1] of the system. In the following, the theoretical minima of the first and the second optimization methods from Sec. 2.2 for an infinite number of refrigeration stages are presented.

The first optimization method minimizes the total Carnot power of all refrigeration stages and can be described with the following function to minimize, when an infinite number of stages is used (described first by Hilal [32])

$$P_{\text{total,inf}} = \dot{Q}_\text{c} \cdot \left(\frac{T_\text{h}}{T_\text{c}} - 1\right) + \int_{T_\text{c}}^{T_\text{h}} \mathrm{d}\dot{Q}_\text{ref} \left(\frac{T_\text{h}}{T} - 1\right) \mathrm{d}T \tag{2.31}$$

with the infinitesimal small refrigeration power $\mathrm{d}\dot{Q}_\text{ref}$ that absorbs the incoming heat due to the thermal conduction and the Joule heating

$$\mathrm{d}\dot{Q}_\text{ref} = \mid \mathrm{d}\dot{Q}_\text{I} \mid + \mid \mathrm{d}\dot{Q}_\lambda \mid \tag{2.32}$$

$$\mathrm{d}\dot{Q}_\text{ref} = I^2 \cdot \frac{\rho\left(T\right) \cdot \lambda\left(T\right)}{\dot{Q}_\lambda} \mathrm{d}T + \left(\frac{\partial \dot{Q}}{\partial T}\right) \mathrm{d}T \tag{2.33}$$

Combining (2.33) with (2.31) yields the Carnot power for an infinite number of Carnot stages as

$$P_{\text{total,inf}} = \int_{T_\text{c}}^{T_\text{h}} \underbrace{\left(T_\text{h} \cdot \frac{\dot{Q}_\lambda(T)}{T^2} + I^2 \cdot \frac{\rho(T) \cdot \lambda(T)}{\dot{Q}_\lambda(T)} \cdot \left(\frac{T_\text{h}}{T} - 1 \right) \right)}_{\mathcal{L}\left(T, \dot{Q}_\lambda(T)\right)} \mathrm{d}T \tag{2.34}$$

as a function of the optimal heat flow through the current lead $\dot{Q}_\lambda$, which in turn is a function of the current lead temperature. To find the minimum of (2.34), it is necessary to find the optimal function of $\dot{Q}_\lambda(T)$, which makes $P_{\text{total,inf}}$ a functional and has to be solved with the Euler-Lagrange equation from the *calculus of variations*

$$\frac{\partial \mathcal{L}}{\partial \dot{Q}_\lambda} - \frac{\mathrm{d}}{\mathrm{d}T} \cdot \left(\frac{\partial \mathcal{L}}{\partial \dot{Q}'_\lambda} \right) = 0 \tag{2.35}$$

where $\mathcal{L}$ is the term inside the round brackets in (2.34). In this case, no derivative of $\dot{Q}_\lambda$ is present in $\mathcal{L}$ and the solution of (2.35) becomes accessible, yielding for the optimal heat flow through the lead

$$\dot{Q}_{\lambda,\text{inf}} = I \cdot T \cdot \sqrt{\left(\frac{1}{T} - \frac{1}{T_\text{h}} \right) \cdot \rho(T) \cdot \lambda(T)} \tag{2.36}$$

which is used for the calculation of the optimal shape factor of the lead according to (2.11) and the temperature profile of the lead with the Fourier's Law (2.2). In this case, it is not necessary to solve the differential equation described in (2.14), because the optimal heat flow through the lead is already known.

In the second optimization method, where additionally to the Carnot power the electric power dissipation is taken into account (described first by Agsten [29]), (2.34) is expanded to

$$P_{\text{total,inf,el}} = P_{\text{total,inf}} + P_\text{el} \tag{2.37}$$

$$P_{\text{total,inf,el}} = \int_{T_\text{c}}^{T_\text{h}} \left(T_\text{h} \cdot \frac{\dot{Q}_\lambda(T)}{T^2} + I^2 \cdot \frac{\rho(T) \cdot \lambda(T)}{\dot{Q}_\lambda(T)} \cdot \left(\frac{T_\text{h}}{T} - 1 \right) + I^2 \cdot \frac{\rho(T) \cdot \lambda(T)}{\dot{Q}_\lambda(T)} \right) \mathrm{d}T \tag{2.38}$$

and minimized with the Euler-Lagrange equation (2.35) for an optimum heat flow of

$$\dot{Q}_{\lambda,\text{inf,el}} = I \cdot \sqrt{\rho(T) \cdot \lambda(T) \cdot T} \tag{2.39}$$

The results for the two optimization methods with an infinite amount of refrigeration

Table 4: Comparison of the first and second optimization method, according to Sec. 2.2, for a MCCL with an infinite amount of refrigeration stages.

Optimization method for ∞	$(I \cdot L/A)$ kA/m	$\dot{Q}_\infty/I$ W/kA	$\dot{Q}_c/I$ W/kA	$P_{\text{total,inf}}/I$ W/kA	P_{el}/I W/kA	$P_{\text{total,inf,el}}/I$ W/kA
① P_{Carnot}	7415	67.7	8.5	73.1	76.1	149.2
② $P_{\text{Carnot}} + P_{\text{el}}$	4044	67.9	9.8	82.8	32.1	114.9

stages is presented in Tab. 4. Both methods show a theoretical minimum for the thermal load at the cold end of about 9 W/kA, but generate two different shape-factors, which makes the current lead designed with the second optimization method shorter.

The use of an infinite number of refrigeration stages to reduce the specific power consumption to the theoretical minimum cannot be realized. Nevertheless, it can be approximated with six intermediate refrigeration stages according to [1]. However, six refrigeration stages make the system complex and the investment costs can play a significant role. It may be more practicable to use two refrigeration stages. In this case, the specific power consumption $P_{\text{total,inf}}/I$ in the first optimization method is about 17 % higher and $P_{\text{total,inf,el}}/I$ in the second method about 10 % higher compared to the optimal values in Tab. 4. In Fig. 7 the temperature profiles of the first and the second optimization method from Fig. 6 are compared with the temperature profiles of the theoretical current leads with an infinite amount of refrigeration stages. The MCCL with two refrigeration stages, where the total Carnot power and the electric power losses $P_{\text{total,el}}$ are minimized (second method), shows a good agreement with the temperature profile of the corresponding current lead with infinite stages. While the current lead which is designed with the first optimization method, shows a significant difference to the temperature profile and the length of the current lead with an infinite amount of refrigeration stages. According to [1] and [28] more than five stages are needed to archive a similar current lead length.

The above theoretical investigations for a current lead with an infinite amount of refrigeration stages are performed with Carnot stages, the thermodynamic reference cycle for refrigeration machines that supply cooling power at a constant temperature and at zero power density. It is more efficient, however, to cool current leads with a refrigeration machine, which supplies cooling power at a temperature glide between the cryogenic and ambient temperature, with vapour flow along the lead, providing additional cooling power from its sensible heat.

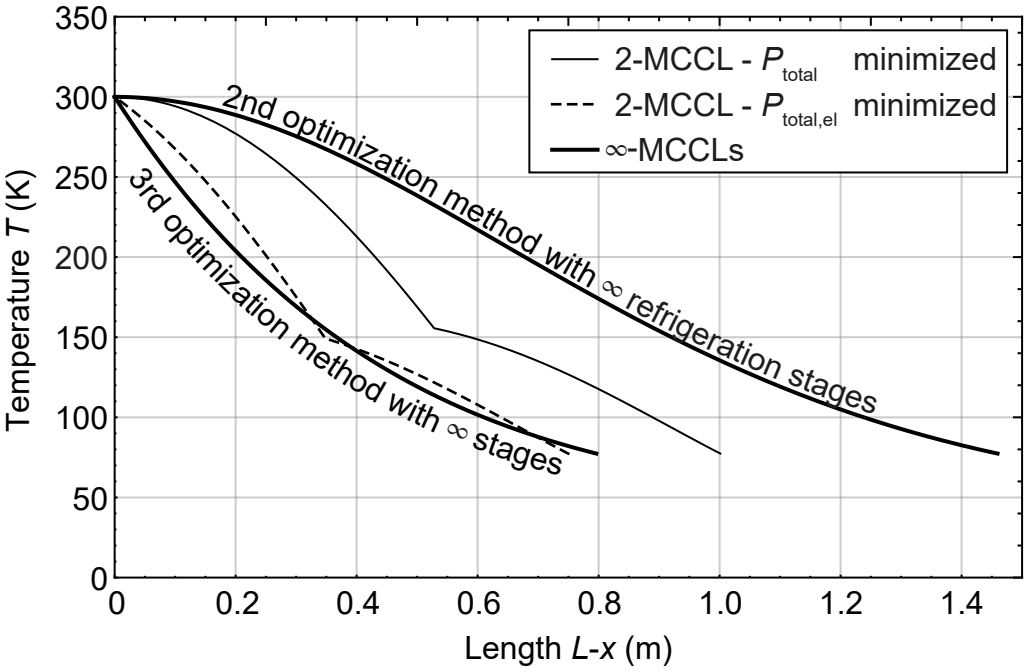

Figure 7: Comparison of the temperature profiles of cylindrical ($d = 50\,\mathrm{mm}$), 10 kA MCCLs with two and with an infinite amount of refrigeration stages, designed with the second and third optimization method.

2.4 Vapour cooled current leads

Vapour cooled current leads (VCCL) use the latent and the sensible heat of a cryogenic fluid entering at the cold end of the lead. The current lead, submerged in the cryogenic liquid, evaporates the fluid due to the incoming thermal load on account of the Joule heating and the thermal conduction from the warmer part. When enough heat transfer area between the current lead and the generated vapour is available, the sensible heat of the gas is used for further convective cooling of the lead. In fact, this design option is one of about nine major design possibilities of VCCLs [33]. VCCL can either be part of an open cooling system, especially in case of liquid nitrogen cooling, or of a closed cooling system, which is typical for helium-cooled VCCL.

Vapour cooled current leads were first designed for helium-cooled applications [34]. One of the key components is the heat exchanger in the resistive part of the current lead for the cold helium vapour flow. For a high heat transfer area between the lead and the vapour, various design approaches are used. For example, Efferson [34] first introduced a heat exchanger design, where the lead consist of parallel porous tubes for the helium flow. A spiral-fin 10 kA design was introduced by Shu [35] for the Superconducting Super Collider (SSC). The SSC project, however, was cancelled and instead the Large Hadron Collider (LHC) project at CERN used about 3300 high-temperature superconducting

(HTS) current leads with a current rating ranging from 60 A to 13 kA, which have a zig-zag fin design for the resistive part [36]. At the Forschungszentrum Karlsruhe (now Karlsruhe Institute of Technology, KIT), a 30 kA helium-cooled copper lead surrounded by perforated copper plates for a high heat transfer area was used for the POLO Model Coil [37]. This design was also used in the development of the 60 kA ITER Toroidal Field Coils [38], which later was expanded to a current lead operation up to 80 kA [39]. For the projects JT60SA [40] and Wendelstein 7-X [41], KIT changed the heat exchanger design of the resistive current leads from a perforated to a meander flow path fin type [42, 43] with the amperage of about 25 kA and 20 kA, respectively.

With the discovery of HTS, binary current leads with liquid nitrogen as an intermediate coolant for temperatures between 77 K and 300 K were developed, adapting the heat exchanger designs from previous work with helium. In [44], a 1 kA HTS current lead with a liquid nitrogen bath and a vapour cooled heat exchanger for the upper resistive part of the lead is used. The lower part, operating from 77 K to 4 K, is designed as a helium bath conduction cooled HTS current lead. The design of the resistive current lead is similar to the parallel porous tubes design introduced in [34]. A different design approach for the heat exchanger is used in [45, 46], where a so-called jelly-roll is used. It is a pierced copper sheet rolled on a central stainless-steel tube that acts as a structural spine for the lead assembly.

Methods for design calculation and optimization of VCCLs are presented in several references, for instance the method used for the development of the helium-cooled current leads for the SSC is presented in [47, 48]. A computer code named *Curlead*, developed at the former Forschungszentrum Karlsruhe by Heller, is published in [49]. For binary HTS vapour-cooled current leads, Wesche [50] introduced a numerical simulation model, where the thermal behaviour of Bi-2223/Ag and Bi-2212 bulk material as the HTS component are compared. Further, basic analysis on binary HTS helium-cooled current leads are performed by Hull [51].

Generally, VCCLs can be divided into self-sufficient [28, 33, 52] and forced-flow [28, 53] vapour-cooled current leads. Self-sufficient current leads are only cooled with latent and sensible heat of the evaporating mass flow, generated by the thermal load dissipated from the cold end into a cooling bath. In a closed vapour filled system with a cryocooler as a re-condensing unit inside a cryostat, Chang [54] performed investigations on the effect of natural convection on the current lead. Accordingly, the CCCL optimization method can be used for VCCLs in cryostats with a wide vapour space and should be modified for leads surrounded by a narrow vapour-filled neck. Two practical design cases of self-sufficient current leads in an open system are investigated in [55]. In the following, the calculation method for self-sufficient nitrogen vapour cooled current leads is presented.

The temperature profile of a self-sufficient VCCL is described with a differential equation of second order based on (2.14) with an additional term for the convective cooling of the gas flow

$$\frac{\partial}{\partial x}\left(\lambda\left(T\right)\cdot A\cdot\frac{\partial T}{\partial x}\right)+I^2\cdot\frac{\rho\left(T\right)}{A}-\alpha\cdot f\cdot U\cdot\left(T-T_{\mathrm{G}}\right)=0 \tag{2.40}$$

where T_{G} is the temperature of the gas flow, whose temperature change is described with a differential equation of first order

$$\frac{\partial T_{\mathrm{G}}}{\partial x}=\frac{\alpha\cdot f\cdot U\cdot\left(T-T_{\mathrm{G}}\right)}{\dot{m}\cdot c_{\mathrm{p}}\left(T\right)} \tag{2.41}$$

where α is the convective heat transfer coefficient between the current lead surface and the gas flow, $U=\pi\cdot d$ is the wetted perimeter of a cylindrical current lead multiplied by a factor f, $\dot{m}$ is the mass flow and $c_{\mathrm{p}}\left(T\right)$ the temperature dependent isobaric heat capacity of the nitrogen gas [56, 57]. According to the VDI Heat Atlas [58], the convective heat transfer coefficient α is a function of the flow characteristics and the fluid properties and can be expressed by the right correlations of the dimensionless *Nusselt number*. However, the real flow characteristics and the heat transfer area can only be derived after the selection of an appropriate heat exchanger design for the vapour cooled current lead. Therefore, a conservative value of $\alpha=25\,\mathrm{W/(m^2\,K)}$ [58] for a forced convection flow in gases and a certain multiplying factor f for the heat transfer area are assumed in this analysis.

The mass flow of a self-sufficient VCCL is determined by the heat load at the cold end $\dot{Q}_{\mathrm{c}}$ and the heat of evaporation Δh_{v} of the cryogenic fluid, with

$$\dot{m}=\frac{\dot{Q}_{\mathrm{c}}}{\Delta h_{\mathrm{v}}\left(T\right)}=\frac{\left(-\lambda\cdot A\cdot\frac{\mathrm{d}T}{\mathrm{d}x}\right)_{x=0}}{\Delta h_{\mathrm{v}}\left(T\right)} \tag{2.42}$$

Hereby, $\dot{Q}_{\mathrm{c}}$ has to be first derived from an interim solution of the coupled differential equation system and recalculated inside an iteration loop until a predefined convergence is reached. For the numerical solution of a boundary value problem (2.40) linked to an initial value problem (2.41), the use of the shooting method [59] is recommended but is not imperatively required. Alternatively, the numerical problem can be solved using a standard Finite-Difference-Method (FDM) for (2.41) and the control volume approach for (2.40) inside the Gauss-Seidel iteration [60].

In Fig. 8, four different nitrogen vapour-cooled current leads are shown in comparison to an optimal designed CCCL with the length L_0. The two VCCLs located in the middle of

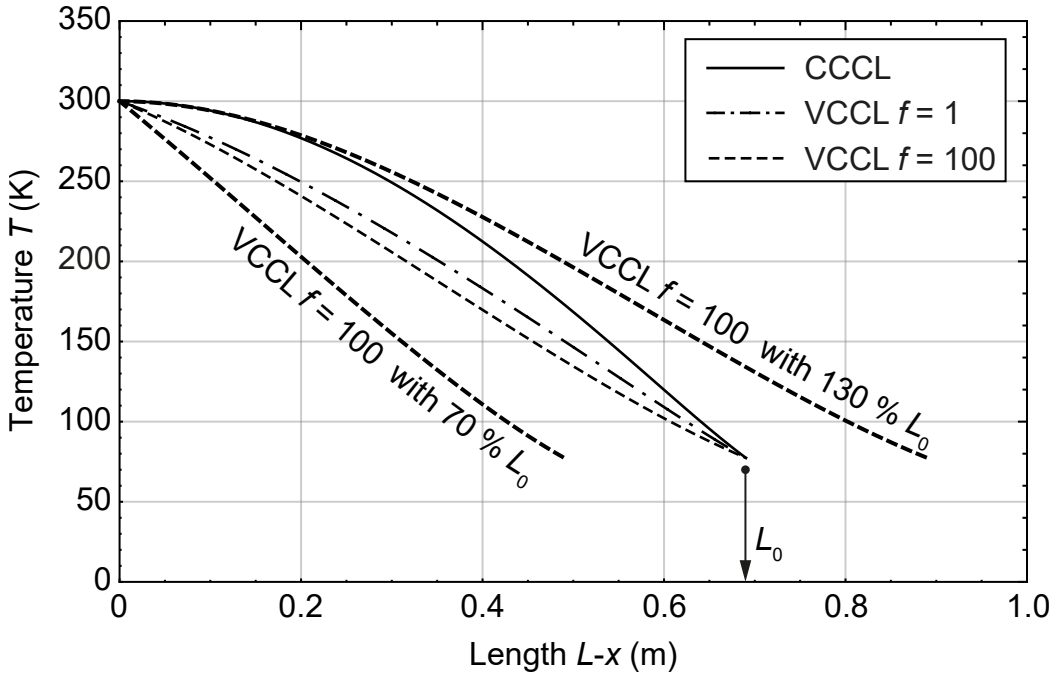

Figure 8: Temperature profiles of four cylindrical ($d = 50\,\mathrm{mm}$), 10 kA VCCLs and one CCCL. The profiles located in the center have a current lead length of L_0 and the lateral profiles 130 % greater or 70 % smaller length. The heat transfer area multiplier f is described in (2.37).

the figure have the same current lead length L_0 as the CCCL and are designed with two different heat transfer multipliers $f = \{1, 100\}$. The VCCL with $f = 1$ has only the outer surface of a cylinder with $d = 50\,\mathrm{mm}$ for the heat transfer and the VCCL with $f = 100$ a 100 times larger heat transfer area. The calculated values of the mass flow, the heat load, the liquefaction work, the electrical power loss and the total power loss of the current lead are summarized in Tab. 5 in comparison to a CCCL and a VCCL with ideal heat transfer. In the VCCL with $f = \infty$, the temperature difference between the current lead and the gas is minimized, yielding a single differential equation

$$\frac{\partial}{\partial x}\left(\lambda\left(T\right)\cdot A\cdot\frac{\partial T}{\partial x}\right)+I^2\cdot\frac{\rho\left(T\right)}{A}-\dot{m}\cdot c_{\mathrm{p}}\left(T\right)\cdot\frac{\partial T}{\partial x}=0 \tag{2.43}$$

The results in Tab. 5 show that by increasing the heat transfer area by $f = 100$, the ideal heat transfer case can be nearly reached. Second, a self-sufficient current lead reduces the heat load at the cold end down to $24.5\,\mathrm{W/kA}$ $\left(57\ \%\right)$ and also reduces the electric and total power losses compared to CCCL. The minimal required power for a refrigeration machine for the case of self-sufficient current leads is not referred to the Carnot power, but rather to the minimal liquefaction work specified in Sec. 3.2.

Table 5: Numerical results of three different VCCLs in comparison to a CCCL. The VCCL with $f = \infty$ represents an ideal case of infinite heat transfer area and zero temperature difference between the current lead and the nitrogen gas.

Current lead design	$\dot{m}$ kg/(h kA)	$\dot{Q}_c/I$ W/kA	P_{total}/I W/kA	P_{el}/I W/kA	$P_{total,el}/I$ W/kA
CCCL	0	42.5	122.2*	42.5	164.7
VCCL $f = 1$	0.584	32.3	125.0*	37.6	162.6
VCCL $f = 100$	0.444	24.6	95.1*	35.7	130.8
VCCL $f = \infty$	0.443	24.5	94.7*	35.7	130.5

* Carnot power

* Minimal liquefaction work (Sec. 3.2)

The lateral temperature profiles in Fig. 8 of VCCLs with $f = 100$ describe current leads with different lengths of 70 % and 130 % compared to a VCCL with L_0. The corresponding calculated results are shown in Tab. 6. For shorter self-sufficient VCCLs, the thermal load at the cold end increases due to the higher contribution of the Fourier's Law, but reduces the electrical power losses and reverse for longer current leads. The optimum for the total power consumption of the system can be found for current lead lengths in-between the two lateral cases. According to the optimization approach for vapour cooled current leads in [1], the optimum value for $P_{total,el}$ is 129.7 W/kA and close to the ideal VCCL, where the shape factor of an optimized CCCL is used. Therefore, the shape factor of an optimized CCCL can be practically used for a self-sufficient current lead that optimizes the total power consumption $P_{total,el}$.

Forced-flow vapour/gas cooled current leads introduce a forced fluid mass flow into the system to increase the convective cooling effect. It is possible to cool such a lead with a forced liquid flow that can be controlled by a valve, or with a pressurised cold gas at intermediate temperatures [23, 33, 36, 53]. Likewise, a forced vapour flow into the system can be applied with a certain liquid portion y (Sec. 3.2) that contains enough liquid for the

Table 6: Numerical results of three different $f = 100$ VCCLs with different current lead lengths L_0.

Current lead design		$\dot{m}$ kg/(h kA)	$\dot{Q}_c/I$ W/kA	P_{total}/I W/kA	P_{el}/I W/kA	$P_{total,el}/I$ W/kA
VCCL $f = 100$,	70 % L_0	0.532	29.4	113.8*	23.6	137.4
VCCL $f = 100$,	100 % L_0	0.444	24.6	95.1*	35.7	130.8
VCCL $f = 100$,	130 % L_0	0.424	23.4	90.6*	51.2	141.9

* Minimal liquefaction work (Sec. 3.2)

Table 7: Design parameter of two forced-flow (ff) vapour-cooled current leads.

Current lead design	$(I \cdot L/A)$ kA/m	$\dot{m}$ kg/(h kA)	$\dot{Q}_c/I$ W/kA	P_{total}/I W/kA	P_{el}/I W/kA	$P_{total,el}/I$ W/kA
Goloubev ff-VCCL [28]	7626	1.05	8.6	79.5*	73.7	153.2
Schreiner ff-VCCL [1]	4048	1.03	9.0	82.3*	31.9	114.2

* Carnot power
* Minimal liquefaction work (Sec. 3.2)

heat load at the cold end. Schreiner [1] and Goloubev [28] evaluated an optimum liquid portion of nitrogen-cooled, forced-flow VCCLs of about $y = 15\,\%$, but for different shape factors of 4048 kA/m and 7626 kA/m, respectively. The difference is based on different optimization methods of the total power consumption and is depicted in Tab. 7. While in [28], the Carnot cycle as the reference cycle is used, in [1] the minimal liquefaction work and the electric losses for the total power consumption are applied. The ff-VCCL design of Goloubev [28] is approaching the design values of a MCCL with an infinite amount of refrigeration stages, according to the first optimization method presented in Tab. 4. While the ff-VCCL design of Schreiner [1], is based on the second optimization method. Compared to an ideal self-sufficient VCCL with $f = \infty$ in Tab. 5, the specific heat loads at the cold end $\dot{Q}_c/I$ in Tab. 7 are smaller, mainly due to the more than a factor two higher specific mass flow.

2.5 Peltier current leads

A Peltier current lead (PCL) is a combination of the metallic part of the lead and a semiconductor, like bismuth telluride Bi_2Te_3 or bismuth antimony BiSb, materials that exhibit a large thermoelectric effect. At the junction between a metal and a semiconductor, heat is generated or absorbed when electric current is applied, the so-called Peltier effect [61]. The amount of generated heat at the warm end, and absorbed heat at the colder end of the Peltier element, is described with the Seebeck coefficient α_S, also known as the thermoelectric power and yields

$$\dot{Q}_{Peltier} = \pm\, \alpha_S \left(T_{junction}\right) \cdot I_{PE} \cdot T_{junction} \tag{2.44}$$

with the electric current passing through the Peltier element I_{PE}, and the temperature at the junction $T_{junction}$ between a metal and a semiconductor. The Seebeck coefficient α_S for Bi_2Te_3, amounts to about 140-220 µV/K in the range of 200-300 K, and is negative for n-type semiconductors. However, absolute values are used for the Seebeck coefficient in the following calculations.

A schematic view of two Peltier current leads in an electric circuit is shown in Fig. 9. For

the Peltier effect, the semiconductors have to de doped with electron donors (n-type) or with electron acceptors (p-type). The n-type semiconductors are placed at the warm end of the current lead, in which the flow of electrons is directed towards the cold end (physical direction of electric current), and vice versa for p-type. Hereby, the cooling effect of the Peltier elements is always located at the colder junction. At the warmer junction, heat is generated and has to be removed from the system with an additional air or water cooling system.

The use of Bi_2Te_3 Peltier elements in a current lead was first investigated by Okumura and Yamaguchi in Japan in 1997 [62]. Compared to a CCCL, a reduction of the heat load at 77 K of 20-30 % was found from numerical calculations, and confirmed experientially for electric currents up to 700 A. Subsequent, the working group started to develop numerical investigations regrading the performance of Peltier current leads at liquid helium temperatures [63, 64], with the result of a 30 % reduction of the thermal load at 4.2 K. Additionally, measurements of the temperature dependent material properties, Seebeck coefficient $\alpha_S(T)$, specific electrical resistance $\rho(T)$ [65] and thermal conductivity $\lambda(T)$ [66] of Bi_2Te_3 Peltier elements were carried out. Further, numerical investigations of multi-stage HTS Peltier current leads for helium-free magnet systems [67], of a PCL with a polarity change switch for polarity-reversible superconducting magnets [68], and of a PCL operating in alternating current mode [69] were carried out. The principle of a

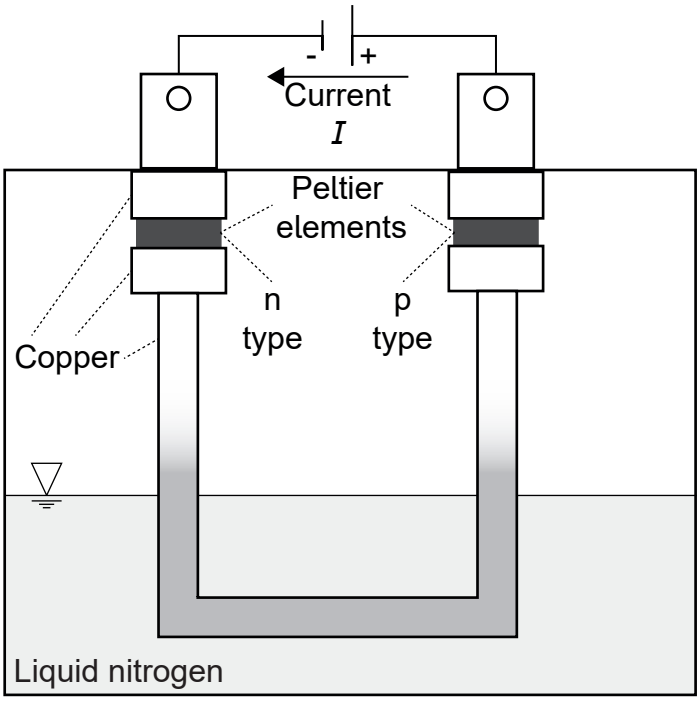

Figure 9: Schematic view of a liquid nitrogen cooled Peltier current lead. The electric current flow I is referred to the physical electric current direction.

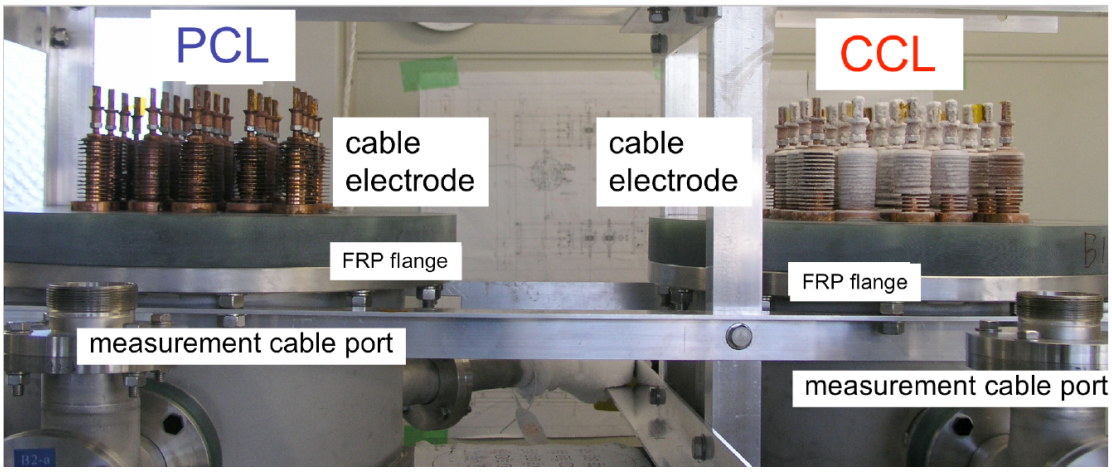

Figure 10: Terminals of the 20 m, 2.2 kA and 20 kV DC high-temperature superconducting power transmission line in Chubu University [74]. The terminal on the left-hand side of the photo, comprises Peltier current leads, and standard conduction cooled current leads on the right-hand side.

150 A PCL-HTS current lead with a multi-stage concept, connected to a magnet at liquid helium temperatures, was experimentally proven in [70, 71], yielding a reduction of the thermal load by 35 % compared to a CCCL. Experimental investigations on a cryogen-free magnet system with a 75 A PCL are presented in [72], and yield a reduction of the thermal load at the cold end by 30 %, and by 16 % for zero current. The reduction of the heat load at zero current is explained by the low thermal conductivity, typically 2-3 W/(m K) [66], of the implemented Peltier elements. This effect was also observed experimentally in the 200 A PCL application at the University of Tübingen [73] and in the 20 m long high-temperature superconducting cable system at the Chubu University [74]. The terminals of the HTS cable system [74] are shown in Fig. 10. Both terminals consist of twenty electric current feedthroughs on a fiber-reinforced polymer flange. The terminal on the left-hand side of the photo comprises Peltier current leads, and standard conduction cooled current leads on the right-hand side. In contrast to the PCL terminal, at the terminal without Peltier elements a clear formation of water ice can be seen. According to the Fourier's law (2.2) that concludes to a higher thermal load into the CCCL terminal, and therefore to the freeze out of air humidity. The additional fins that can be seen on the current leads in Fig. 10 increase the heat transfer area for the convective cooling that is necessary to remove the heat load, due to the Peltier heating effect. If this heat load is not removed completely, the temperature at both metal-semiconductor junctions of the Peltier elements will rise and lead to a system failure. Further experimental investigations on PCLs were made in the 500 m, 20 kV and 5 kA HTS cable project [75–77], where in total 144 Peltier current leads (72 for each terminal) were used. The heat leak into the cold system due to the current lead was measured to 30 W/kA [75].

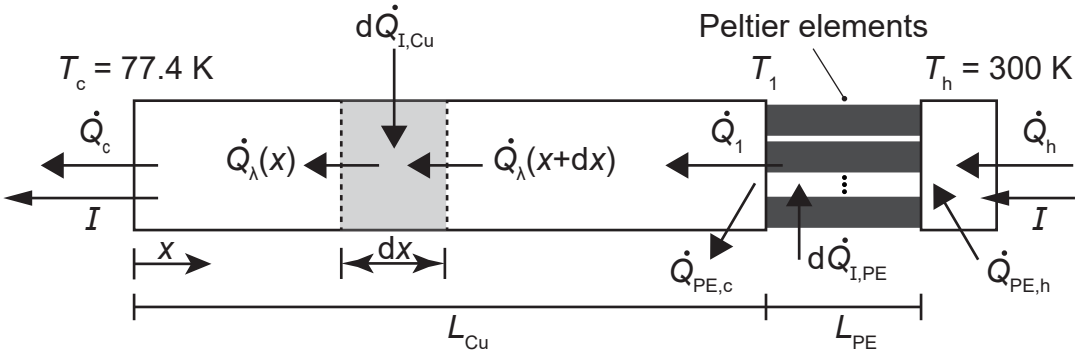

Figure 11: Energy balance for the conduction cooled Peltier current lead.

In the following, the analytical and the numerical calculation methods for Peltier current leads are presented. The material properties of Bi_2Te_3 Peltier elements, used in this work, are derived from [78, 79], yielding

$$\alpha_{\mathrm{S}}(T) = 3.1 \cdot 10^{-7} \cdot T + 9.2 \cdot 10^{-5} \tag{2.45}$$

$$\rho_{\mathrm{PE}}(T) = 3.5 \cdot 10^{-8} \cdot T - 1.5 \cdot 10^{-6} \tag{2.46}$$

$$\lambda_{\mathrm{PE}}(T) = 1.7\,\mathrm{W/(m\,K)} \tag{2.47}$$

with the specific electrical resistance ρ_{PE} and the thermal conductivity λ_{PE}. The heat loads in a PCL are depicted in Fig. 11, comprising the heat loads due to the Peltier effect at the metal-semiconductor junctions $\left(\dot{Q}_{\mathrm{PE,h}}, \dot{Q}_{\mathrm{PE,c}}\right)$ at the warm and the cold end, respectively. The energy balance for the Peltier element is derived analogous to (2.3-2.6) for the CCCL, yielding

$$\int_{\dot{Q}_1+\dot{Q}_{\mathrm{PE,c}}}^{\dot{Q}_{\mathrm{h}}+\dot{Q}_{\mathrm{PE,h}}} \dot{Q}_\lambda \,\mathrm{d}\dot{Q}_\lambda = -I_{\mathrm{PE}}^2 \int_{T_1}^{T_{\mathrm{h}}} \rho(T) \cdot \lambda(T)\,\mathrm{d}T \tag{2.48}$$

Integrating (2.48), yields the equation for the thermal load at the cold end of one Peltier element

$$\dot{Q}_1 = \sqrt{\left(\dot{Q}_{\mathrm{h}} + \dot{Q}_{\mathrm{PE,h}}\right)^2 + 2 \cdot I_{\mathrm{PE}}^2 \int_{T_1}^{T_{\mathrm{h}}} \rho_{\mathrm{PE}}(T) \cdot \lambda_{\mathrm{PE}}(T)\,\mathrm{d}T} - \dot{Q}_{\mathrm{PE,c}} \tag{2.49}$$

The thermal load $\dot{Q}_1$ is minimized, when $\dot{Q}_{\mathrm{h}}$ and the Peltier heat $\dot{Q}_{\mathrm{PE,h}}$ at the warm junction becomes zero, yielding an adiabatic boundary condition at the warm end. With

(2.44), the minimal heat load at the cold end of all n_{PE} Peltier elements amounts to

$$\dot{Q}_{1,\min} = n_{\mathrm{PE}} \cdot \left(\sqrt{2 \cdot I_{\mathrm{PE}}^2 \int_{T_1}^{T_\mathrm{h}} \rho_{\mathrm{PE}}(T) \cdot \lambda_{\mathrm{PE}}(T)\, \mathrm{d}T} - \alpha_{\mathrm{S}}(T_1) \cdot I_{\mathrm{PE}} \cdot T_1 \right) \tag{2.50}$$

and is used in the calculation of the following heat load at the cold end of a copper lead

$$\dot{Q}_{\mathrm{c}} = \sqrt{\dot{Q}_1^2(T_1) + 2 \cdot I^2 \int_{T_\mathrm{c}}^{T_1} \rho(T) \cdot \lambda(T)\, \mathrm{d}T} \tag{2.51}$$

with the total amperage I of all Peltier elements connected in parallel to the lower copper lead

$$I = n_{\mathrm{PE}} \cdot I_{\mathrm{PE}} \tag{2.52}$$

The thermal load at the cold end of the current lead in (2.51) is minimized, when the temperature at the cold junction between copper and Peltier element becomes $T_1 = 219\,\mathrm{K}$ (cf. Fig. 12). This temperature is found numerically in the global minima of $\dot{Q}_{\mathrm{c}}$. This junction temperature can be realized by the selection of an appropriate geometry for the copper lead and the Peltier elements according to the corresponding shape factors, calculated analogous to the equations (2.10) and (2.11). The shape factors for copper and Peltier elements are 2583 kA/m and about 5.7 kA/m, respectively. The temperature difference along the Peltier element of about $\Delta T = 80\,\mathrm{K}$ is generated due to the Peltier cooling effect of $\dot{Q}_{\mathrm{PE,c}} = 35.1\,\mathrm{W/kA}$ at the cold junction, and is only valid if the heat at the warm junction of $\dot{Q}_{\mathrm{PE,h}} = 55.5\,\mathrm{W/kA}$ is removed from the system completely. Such Peltier current lead reduces the heat load an the cold end to $\dot{Q}_{\mathrm{c}} = 31.0\,\mathrm{W/kA}$, a 27 % reduction compared to a CCCL.

The temperature profile of a PCL is calculated by solving a system of two differential equations according to (2.14) for the Peltier element and the copper lead with the following boundary conditions that refer to the used coordinate system in Fig. 11

$$T_{\mathrm{PE}}(x = L_{\mathrm{Cu}} + L_{\mathrm{PE}}) \stackrel{!}{=} T_\mathrm{h} \tag{2.53}$$

$$T_{\mathrm{PE}}(x = L_{\mathrm{Cu}}) \stackrel{!}{=} T_{\mathrm{Cu}}(x = L_{\mathrm{Cu}}) \tag{2.54}$$

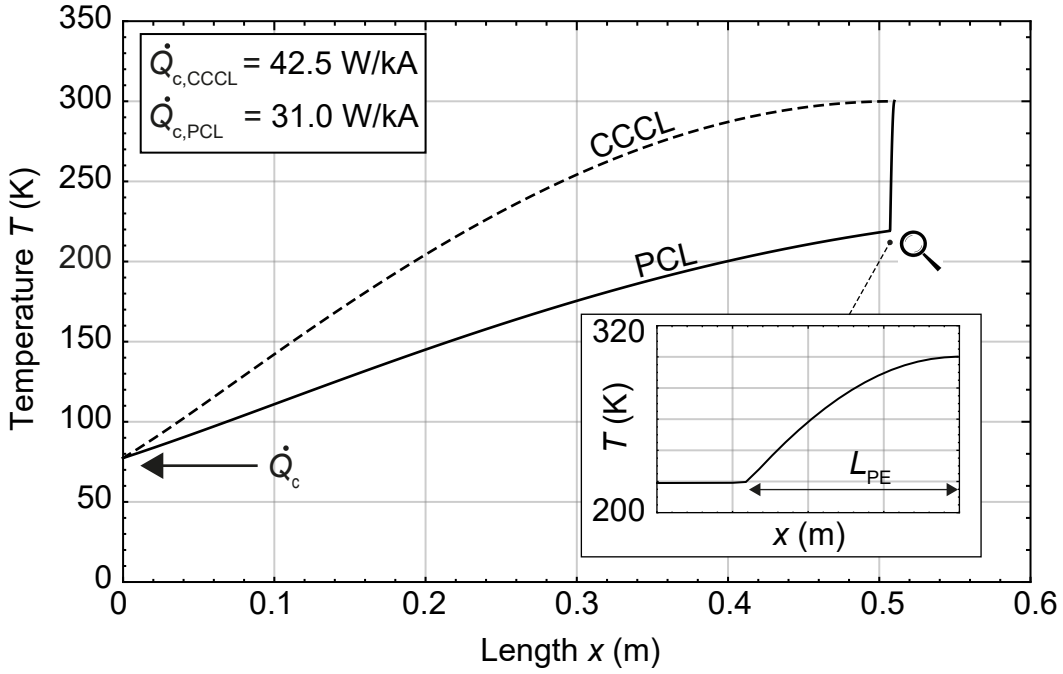

Figure 12: Temperature profiles of a 10 kA CCCL and a PCL with ten 1 kA Peltier elements at the warm end. The steep temperature gradient of a PCL at warm end represents the part with the Peltier elements, which is zoomed in below. The diameter and the length of the Peltier elements are 25 mm and 2.8 mm, respectively. The diameter of the copper lead is 50 mm.

$$n_{\mathrm{PE}} \cdot \left(\lambda_{\mathrm{PE}} \cdot A_{\mathrm{PE}} \cdot T'_{\mathrm{PE}}(x) - \alpha_{\mathrm{S}} \cdot I_{\mathrm{PE}} \cdot T_{\mathrm{PE}}(x)\right)\Big|_{x=L_{\mathrm{Cu}}} \stackrel{!}{=} \lambda_{\mathrm{Cu}}\left(T_{\mathrm{Cu}}(x)\right) \cdot A_{\mathrm{Cu}} \cdot T'_{\mathrm{Cu}}(x)\Big|_{x=L_{\mathrm{Cu}}} \tag{2.55}$$

$$T_{\mathrm{Cu}}(x=0) \stackrel{!}{=} T_{\mathrm{c}} \tag{2.56}$$

The boundary condition (2.55) describes the energy flow at the cold metal-semiconductor junction, where the Peltier cooling effect is implemented on the left hand side of the equation. The Dirichlet boundary condition at the warm end of the Peltier element (2.53) can also be substituted by a Neumann boundary condition, if the cooling heat flux of the water or air cooling system is known. The corresponding temperature profile of a PCL in comparison to a CCCL, is shown in Fig. 12. As shown in this figure, there is a steep temperature gradient at the warm end of the lead. This results from the implemented Peltier elements in the current lead, which decrease the temperature at the cold junction due to the Peltier cooling effect. The adiabatic boundary condition that is shown in the zoomed region, however, can only be archived, when the Peltier heat $\dot{Q}_{\mathrm{PE,h}}$ is removed at the top of the current lead completely, and the geometries are in accordance to the

Table 8: Numerical results of a 10 kA Peltier current lead.

Current lead design	$\dot{Q}_{\mathrm{PE,h}}$ W/kA	$\dot{Q}_{\mathrm{PE,c}}$ W/kA	$\dot{Q}_{\mathrm{c}}/I$ W/kA	P_{total}/I W/kA	P_{el}/I W/kA	$P_{\mathrm{total,el}}/I$ W/kA
PCL	55.5	35.1	31.0	89.3*	66.1	155.4

* Carnot power. Cooling system at the warm end not included.

optimal shape factors. To archive an adiabatic boundary condition at all warm, metal-semiconductor junctions in a real application will be a challenging task, taking contact resistance and manufacturing uncertainties in the fabrication of doped Peltier elements into account. Rather, a slightly under-current design with a small thermal load from the ambience into the system will be present. The electric power dissipation of the Peltier elements of 45.7 W/kA is larger compared to the copper part, and has to be taken into account in the calculation of the overall power dissipation $P_{\mathrm{total,el}}/I$ presented in Tab. 8. It is to mention that the intermediate temperature T_1 is not predefined in the calculation of the temperature profile, it results numerically from the boundary condition (2.55) and corresponds to the value of $T_1 = 219\,\mathrm{K}$, which is also found in the global minima of $\dot{Q}_{\mathrm{c}}$ in (2.51). This agreement of results indicates that the correct energy flow boundary condition (2.55) between copper and Peltier elements was used. The use of ten 1 kA Peltier elements for a 10 kA current lead is a theoretical approach in this work and was not experimentally proven so far. However, same specific results and temperature profiles can be calculated for Peltier current leads at lower and currently feasible amperages.

The implementation of Peltier elements into a vapour-cooled current lead can further reduce the thermal load at the cold end to about 20.6 W/kA. Numerical investigations of vapour cooled Peltier current leads (VCPCL) are presented in the appendix (A).

2.6 Design overview

The following shall give a short overview of the investigated current lead designs. The numerical results of 10 kA conduction (CCCL), multi-stage (2-MCCL), self-sufficient vapour (VCCL $f = 100$) and Peltier (PCL) cooled current leads are summarized in Tab. 9. The corresponding temperature profiles are presented in Fig. 13. The 2-MCCL is designed with two refrigeration stages and the second optimization method, which minimizes the overall specific power consumption $P_{\mathrm{total,el}}/I$. Ten 1 kA Peltier elements, 25 mm in length and 2.8 mm in diameter, are used in the PCL current lead. The metal parts of the current leads are made of copper with a diameter of 50 mm. The double entries for the shape factor $\left(I \cdot L/A\right)$ of the MCCL and the PCL are referred to the warmer and colder parts of the current leads.

According to Tab. 9, the two-stage 2-MCCL, compared to the other design options, yield

Table 9: Numerical results of 10 kA conduction (CCCL), multi-stage (2-MCCL), self-sufficient vapour (VCCL) and Peltier (PCL) cooled current leads.

Current lead design	$(I \cdot L/A)$ kA/m	$\dot{m}$ kg/(h kA)	$\dot{Q}_c/I$ W/kA	P_{total}/I W/kA	P_{el}/I W/kA	$P_{total,el}/I$ W/kA
CCCL	3515	0	42.5	122.2*	42.5	164.7
2-MCCL	2675/2429	0	20.4	92.1	33.7	125.8
VCCL $f = 100$	3515	0.444	24.6	95.1*	35.7	130.8
PCL	5.7/2583	0	31.0	89.3*	66.1	155.4

* Carnot power
* Minimal liquefaction work (Sec. 3.2)

the least overall specific power consumption of $P_{total,el}/I = 125.8\,\mathrm{W/kA}$. Further, the specific thermal load at the cold end is minimized to $\dot{Q}_c/I = 20.4\,\mathrm{W/kA}$, but comes with the implementation of a second refrigeration machine at the intermediate temperature of 150 K. The conventional conduction cooled current lead CCCL shows the largest values for the thermal load and the overall power consumption. However, with just one refrigeration stage it is the simplest system configuration, especially compared to the PCL that requires ten Peltier elements. Compared to the 2-MCCL, the self-sufficient VCCL is a part of an open system and shows slightly larger values, with a difference of about 5 W/kA for the overall power consumption and the thermal load.

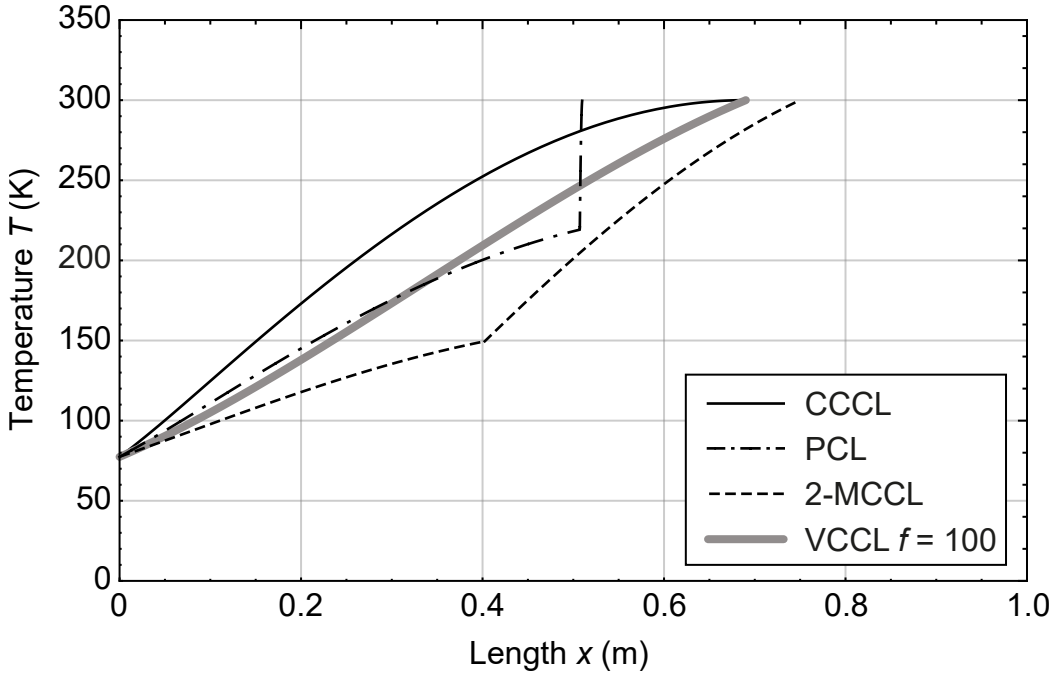

Figure 13: Temperature profiles of 10 kA conduction (CCCL), multi-stage (2-MCCL), self-sufficient vapour (VCCL $f = 100$) and Peltier (PCL) cooled current leads.

2.7 Material properties

Materials used for the resistive part of the current leads are metals, usually copper that is also used in the calculations above. According to the Wiedemann-Franz-Law [8–10] (WFL), which describes the relation between the specific electrical resistance and thermal conductivity of metals by

$$\lambda(T) \cdot \rho(T) = L_0 \cdot T \tag{2.57}$$

where $L_0 = 2.44 \times 10^{-8}\,\mathrm{V^2/K^2}$ is the Lorentz number, any metallic material can be used as a current lead. With (2.57), the minimal thermal load at the cold end of a conduction cooled current lead according to (2.9) becomes

$$\dot{Q}_{\mathrm{c,min}} = I\sqrt{2 \cdot \int_{T_\mathrm{c}}^{T_\mathrm{h}} L_0 \cdot T \,\mathrm{d}T} = 45.4\,\mathrm{W/kA} \tag{2.58}$$

without the need of any thermal properties of the material. However, the WFL only applies near room temperature[2] and shows significant deviations at lower temperatures for all metallic materials. In Fig. 14a, the minimal specific thermal loads $\dot{Q}_c/I$ at the cold end of a conduction cooled current lead for different metallic materials are presented. The first entry, labelled with number 1, is the thermal load according to the WFL with 45.4 W/kA. Other materials are labelled according to Tab. 10. For example, the thermal load of a copper or an aluminium current lead is smaller in comparison to the WFL, but is considerably larger for stainless steel and cupronickel. Similar results are obtained with phosphor bronze (CuSn 5) and brass. Two materials show a significant lower heat load compared to WFL and other common current lead materials, number 5 Beryllium and number 29 Nb_3Sn. Nb_3Sn is a superconductor with a critical temperature of 18.3 K, and is used as a superconducting insert wire in helium-cooled current leads [82]. However, not every material is suitable for high amperage current leads, because of their small shape factors compared to copper or aluminium that are depicted in Fig. 14b. According to (2.11), the optimal shape factor of a current lead is a function of the thermal conductivity. A high shape factor leads to a longer or a thinner current lead and vice versa. While it is practical to use copper for a 10 kA current lead, with a length of 700 mm and a diameter of 50 mm, for a manganin current lead, the length has to be about 25 mm at the same diameter (see Tab. 10). With this geometric dimensions of a manganin current lead, it would be impossible to handle the relatively large heat load of 461 W at 77.4 K. On the other hand, the optimum diameter becomes larger as the conductivity of the

[2] WFL also works at very low temperatures approximately below 10 K, where only conduction electrons contribute to the thermal conductivity [80].

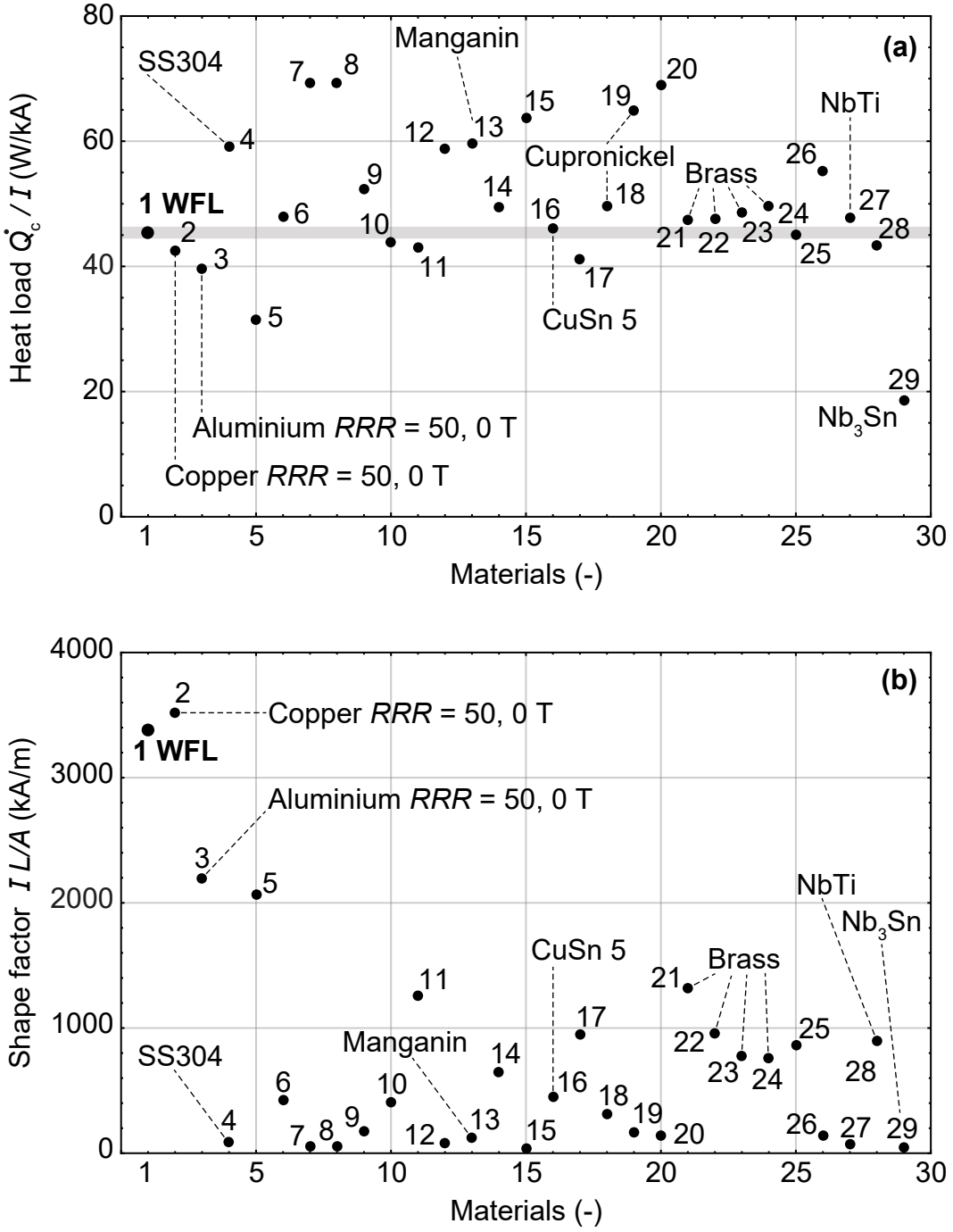

Figure 14: Minimal specific thermal loads (a) at the cold end and shape factors (b) of conduction cooled current leads (CCCL) made of different materials, numbers according to Tab. 10. The current lead works between 300 K and 77.4 K. Material properties are derived from *CryoComp* [81].

materials drops, and can be used as an advantage for low current instrumentation leads [10]. The diameters of 1 mA, 1.5 m long instrumentation leads made of different materials, are presented in Fig. 15. For a manganin instrumentation lead, with its low thermal conductivity of 22 W/(m K), an optimal diameter of 123 µm is calculated. This is about

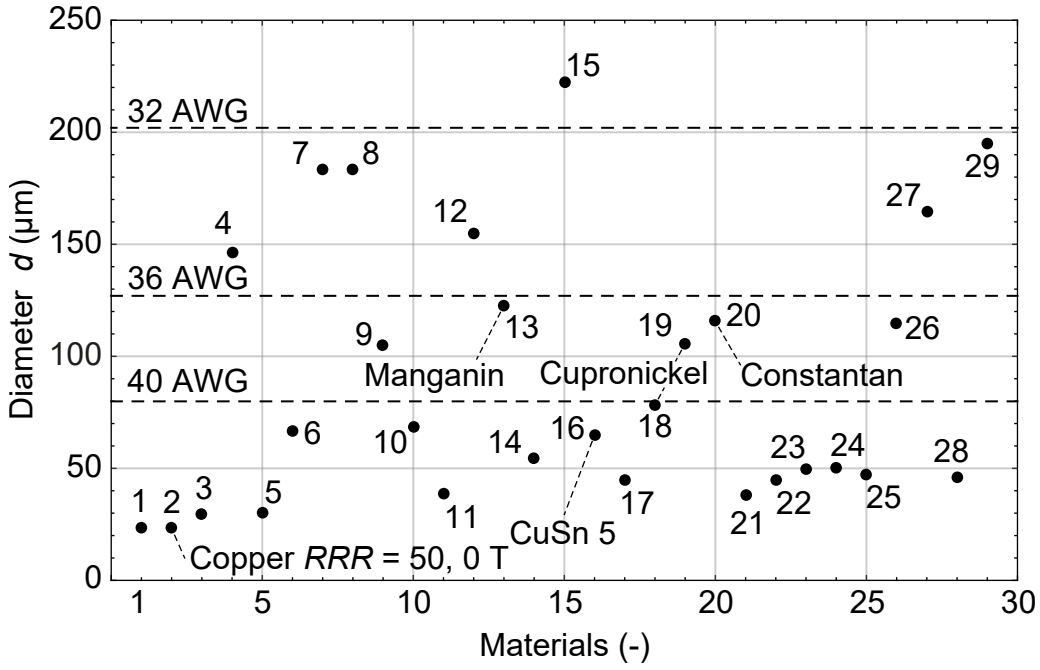

Figure 15: Optimal diameters of 1 mA, 1.5 m long instrumentation leads made of different materials, numbers according to Tab. 10. The instrumentation leads work between 300 K and 77.4 K. Material properties are derived from *CryoComp* [81].

a 36 American Wire Gauge (AWG), which is commonly used in cryogenic engineering. A copper instrumentation lead would have a diameter of 23.2 µm, a factor four smaller diameter than a 40 AWG wire and difficult to handle [10]. For currents below 1 kA, and especially for the use in high magnetic fields, a phosphor bronze lead can be used. At any fixed temperature between 2 K and 300 K, it shows a high magnetoresistance up to 14 T [83]. According to the last column in Tab. 10, a 1 kA phosphor bronze lead with a length of 200 mm has an optimal diameter of 75 mm. The dimensions are well suited for the connection to the first stage of a two-stage cryocooler.

The thermal conductivity of all materials decreases towards lower temperatures, but some materials show an intermediate increase between about 10 K and 30 K that can reach about two orders of magnitude larger values compared to room-temperature. This peak is observed for crystals, but also for some pure metals like copper and aluminium, which is shown in Fig. 16a for copper together with the specific electrical resistance. For the latter materials, the quantity of the effect can be classified with the so-called residual-resistivity-ratio (RRR value). RRR is defined as the ratio of the specific electrical resistance of the material at room temperature and at liquid helium temperature. The specific electrical resistance at low temperatures, has a strong dependence on purity and the amount of lattice vibrations, yielding to larger RRR values for metals of high purity.

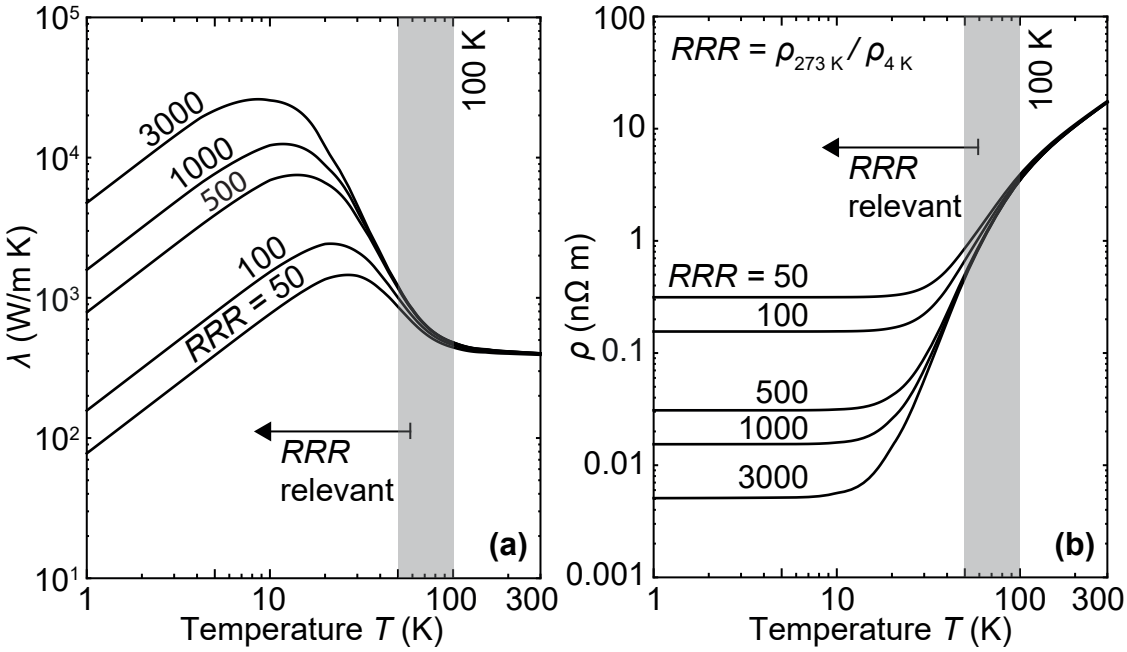

Figure 16: Thermal conductivity (a) and specific electrical resistance (b) of copper for different RRR values. Material properties are derived from *CryoComp* [81].

For the resistive part of a current lead that has a low end temperature of 50 K to 77.4 K, the effect of impurity has practically no influence on the thermal load at the cold end. Comparing the thermal loads of copper current leads with $RRR = 50$ and $RRR = 3000$ working between room temperature and 77.4 K or 50 K yields

$$\left(\frac{\dot{Q}_c}{I}\right)_{\text{RRR 50}} - \left(\frac{\dot{Q}_c}{I}\right)_{\text{RRR 3000}} = \begin{cases} 0.16\,\text{W/kA}, & T_\text{c} = 77.4\,\text{K} \\ 0.24\,\text{W/kA}, & T_\text{c} = 50\,\text{K} \end{cases} \tag{2.59}$$

with differences in the thermal load as low as 0.4 % compared to $\dot{Q}_c/I$.

Metallic materials like copper or aluminium show a significant magnetoresistance effect, which decreases the thermal conductivity and increases the specific electrical resistance at high magnetic fields, which is presented in Fig. 17. This effect can be compensated by using high purity materials with a large RRR value, exemplary presented for copper with $RRR = 500$ in Fig. 17. However, the magnetoresistance effect yields about one order of magnitude smaller thermal load contributions compared to the values presented in (2.59), and is therefore not relevant in this temperature range.

In the material selection for resistive current leads, the thermal behaviour during an over-current should be considered as well. During an over-current scenario that is shown in Fig. 4, a temperature increase near the warm end of the current lead can be detected.

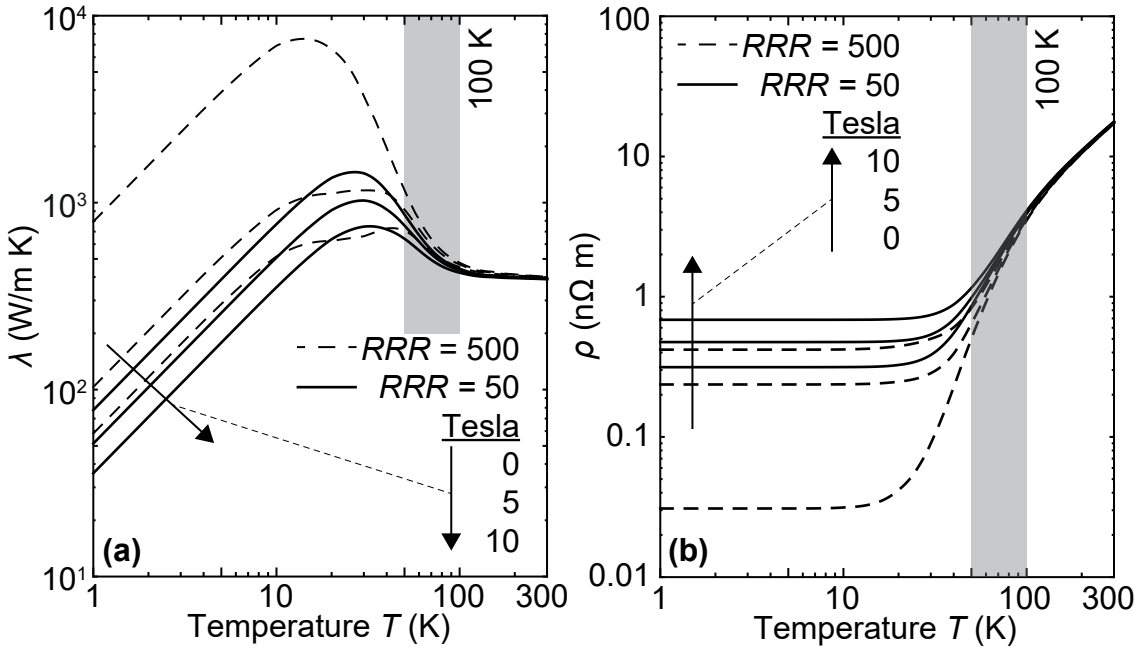

Figure 17: Thermal conductivity (a) and specific electrical resistance (b) of copper at different magnetic fields in Tesla and for two different RRR values. Material properties are derived from *CryoComp* [81].

The maximum overshoot temperature, the temperature at the peak of conduction cooled current leads made of copper and its alloys are shown in Fig. 18 as a function of the over-current ratio I/I_{opt}. The overshoot temperature of the copper current lead is significantly higher compared to its alloys above $I/I_{\mathrm{opt}} > 120\%$. Therefore, for a stable operation even during an over-current event, it is preferable to use a copper alloy as a resistive current lead instead of the pure metal. However, according to the corresponding shape factors in Tab. 10, the copper alloy current lead lengths are more than three times smaller compared to the pure copper. A 10 kA current lead made of phosphor bronze results in eight times smaller length of about 90 mm. Current leads made of copper alloys are therefore an appropriate choice for currents of about 1 kA and below. For high amperage current leads, pure copper is the material of choice.

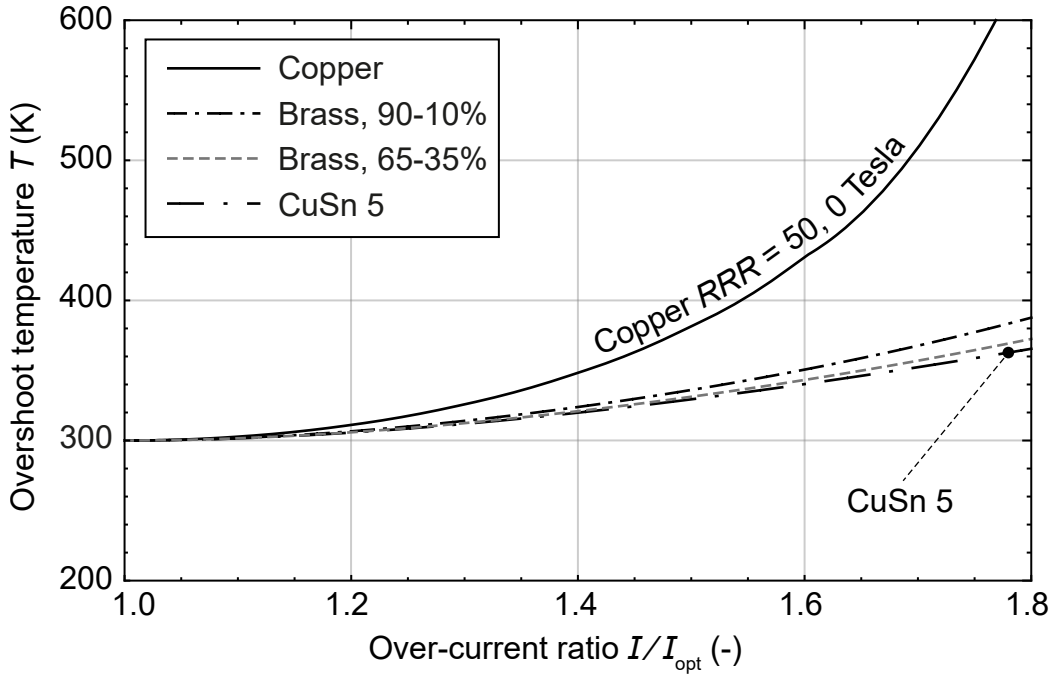

Figure 18: Over-shoot temperature of a conduction cooled current lead as a function of the over-current ratio $\left(I/I_{\mathrm{opt}}\right)$ for copper with RRR 50 at zero magnetic field and its alloys Brass 90-10%, Brass 65-36% and Phosphor bronze CuSn5.

Table 10: Schedule of investigated metallic materials used for a 10 kA conduction cooled current lead (CCCL) with the calculated results of thermal load at the cold end, shape factor, lead length and lead diameter for a special case♦ between 300 K and 77.4 K. Material properties are derived from *CryoComp* [81]. A cylindrical CCCL with a diameter of 50 mm is used in the calculation of the optimal length L.

Material number	Material name	$\dot{Q}_c/I$ W/kA	$(I \cdot L/A)$ kA/m	L mm	d♦ mm
1	WFL⋆	45.4	3380■	664	27
2	Copper*	42.5	3515	691	27
3	Aluminium*	39.7	2197	431	34
4	304 Stainless steel	59.1	89	17	170
5	Beryllium	31.4	2068	406	35
6	Niobium	47.9	427	84	77
7	Inconel 718, annealed	69.3	57	11	212
8	Inconel 718, cold worked	69.3	56.9	11	212
9	Titanium	52.4	173	34	122
10	Pb-Sn soft solder	43.9	408	80	79
11	6061-T6 Aluminum	43.0	1260	247	45
12	Invar-36	58.8	80	16	179
13	Manganin (84Cu, 12Mn, 4Ni)	59.7	127	25	142
14	Beryllium copper (2% Be)	49.5	646	127	63
15	Titanium alloy (Ti-6Al-4V)	63.7	39	8	256
16	Phosphor bronze (94Cu, 5Sn, .2P)	46.1	453	89	75
17	Nickel, 4N5	41.2	950	187	52
18	Copper Nickel, 90-10	49.6	313	62	90
19	Copper Nickel, 70-30	64.8	171	34	122
20	Constantan, Cu-Ni 57-43%, 70-30	69.0	143	28	134
21	Brass, 90-10% Cu-Zn - CDA 22000	47.4	1320	260	44
22	Brass, 80-20% Cu-Zn - CDA 24000	47.7	956	188	52
23	Brass, 70-30% Cu-Zn - CDA 26000	48.7	779	153	57
24	Brass, 65-35% Cu-Zn - CDA 27000	49.6	757	149	58
25	5083-T0 Aluminum alloy, annealed	45.0	866	170	54
26	K Monel, annealed (67Ni, 30Cu,...)	55.3	145	28	133
27	NbTi alloy	47.7	70	14	190
28	7075-T6 Aluminum alloy	43.4	896	176	53
29	Nb3Sn	18.5	50	10	225

⋆ Wiedemann-Franz-Lorenz law

* Residual-Resistance-Ratio (RRR) 50, 0 Tesla

♦ Optimal diameter for a 1 kA current lead with a length of 200 mm

■ Calculated with the thermal conductivity of RRR 50 copper at zero magnetic field

3 Cooling systems for current leads

3.1 Cryocooler

Cryocoolers are regenerative gas compression machines, where Helium-4 gas is almost always used as the working fluid. All cryocooler types are based on the Stirling refrigeration process, and are working with an oscillating mass flow and pressure of the fluid. The oscillation is controlled by a rotary valve and a displacer drive in the so-called Gifford-McMahon (GM) cryocooler, or by a gas piston without any mechanically moving parts in the so-called Pulse Tube (PT) cryocooler. The cooling effect is archived by an appropriate phase shift of pressure and mass flow in the cold head of the cryocooler. The internal heat transfer between the low and high pressure gas, is archived with a regenerator that consist of a porous material. In cryocoolers that work above 10 K, the regenerator material consists mainly out of small lead (Pb) spheres, or includes additional rare earth materials that enable refrigeration at 4.2 K [84, 85]. The helium is pressurized to about 20 bar in a compressor box that is connected via two flexible lines to the cryocooler cold head. The compressor box consists of a scroll compressor, an oil removal system to prevent the contamination of oil in the cold head, and an air or water cooling system for the compressed gas and the compressor. Because of an oil adsorber in the compressor box and several o-ring seals inside the cold head (seals not applicable in PT coolers), the refrigerator system requires a periodic maintenance.

Crycoolers can be acquired with one, two or also with three refrigeration stages that provide refrigeration at different temperature levels. Three examples of crycooler cold heads are presented in Fig. 19. In the middle (b), a cryocooler with a single refrigeration stage (cold head) is shown. Single stage machines can provide refrigeration down to 25 K, however, in most cases the operating range is certificated only down to 50 K. This machines are mainly used for the liquefaction of liquid nitrogen, thermal shield cooling of cryogenic cryostat systems, or may be used for the cooling of high amperage resistive current leads. At the time of this publication, a refrigeration power of maximal 600 W at 80 K and an input power of 11.5 kW are archived with these machines [87]. This corresponds to the cooling power needed for one pair of conduction cooled current leads with an amperage of 7 kA, or a single 14 kA current lead. On the left-hand side of Fig. 19, a 10 K two stage Gifford-McMahon cryocooler (a) is shown. It has two cold heads, one that has a working temperature of about 50 K and a smaller one that has a working temperature of about 10 K. Two stage cryocoolers have a cooling power at the first stage of about 30 to 60 W at 50 K that only partly can be used for the resistive current leads, due to other heat loads into the cryogenic system that are typically covered with these machines. Considering the case that half of the cooling power of the first stage with maximal 30 W can be used for a pair of resistive CCCL current leads, with a required refrigeration power of 43 W/kA at 50 K, the maximum current would yield 350 A.

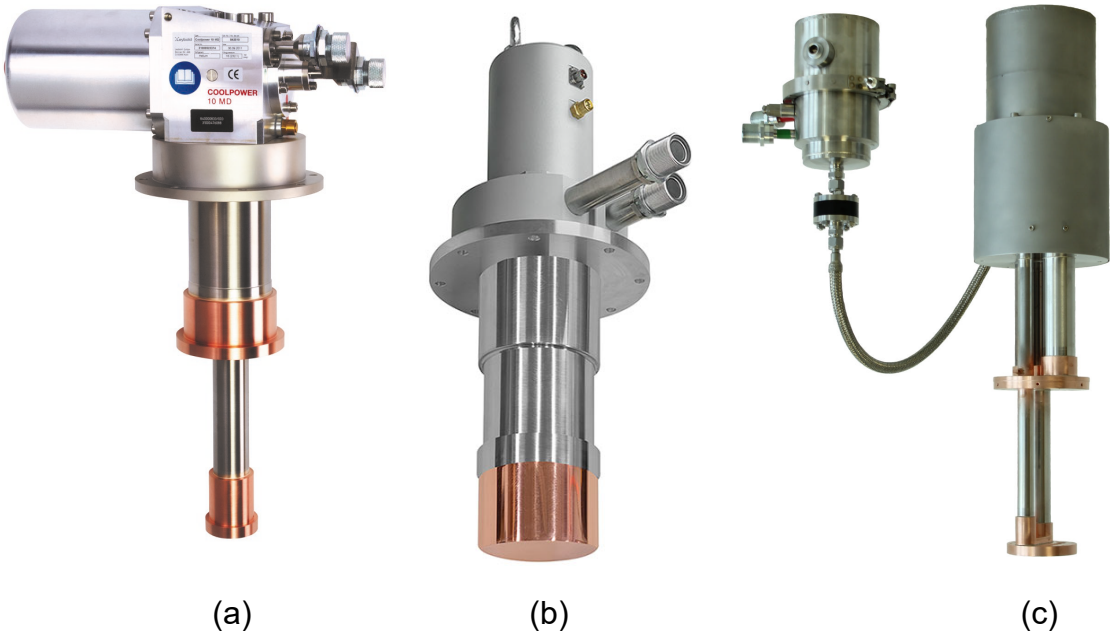

Figure 19: Overview of three different cryocooler cold heads. Where (a), is a two stage 10 K Gifford-McMahon (CP 10 MD) from Leybold [86], (b) is a 80 K single stage Gifford-McMahon (AL600) from Cryomech [87] and (c) is a two stage 4.2 K GM-type Pulse Tube cryocooler (TransMIT PTD 406C) from cryo.TransMIT [88]. A list of present cryocooler manufacturers can be found in [89].

The cryocooler (c) on the right-hand side of Fig. 19 is a 4.2 K two stage Gifford-McMahon type Pulse Tube cryocooler. This cryocooler does not require a mechanically driven displacer to move the regenerator inside the cold head, and works with an almost vibration free moving gas piston that is controlled by the phase shift of pressure waves and mass flow of the fluid, in combination with a buffer volume and an orifice or a capillary. The advantage of a GM type PT cooler over a GM cooler is that the cold head is maintenance free, however, the compressor box maintenance is still required. However, the refrigeration power of the first stage is on a same level as of the two stage GM cryocoolers. Further, PT coolers show a strong dependence on gravity orientation. The performance of PT coolers at angles, with respect to the gravity, above 90° will strongly decrease [90]. With the preposition, "Gifford-McMahon type", the compressor box of a PT cryocooler is classified. In this case, a standard scroll compressor is used in the compressor box, like in GM cryocoolers. If instead a valveless compressor is used, also called a pressure oscillator, the cryocooler is called a Stirling type PT cryocooler.

Stirling type PT cryocoolers have a single refrigeration stage at a working temperature of 78 K, but can have a high refrigeration power up to 3000 W [91]. However, this relatively high refrigeration power for a regenerative working refrigeration machine, comes with a considerable large input power of about 40 kW. A larger refrigeration power of about 5000 W can be archived with a Stirling cryogenerator, which is based on the Stirling cycle

Table 11: Overview of several single stage cryocoolers from different manufacturers with the corresponding refrigeration powers $\dot{Q}_{\mathrm{ref}}$ at 80 K, the input powers P at 50 Hz, the Carnot efficiencies*, as well as the amperages and the specific power consumptions of single CCCL current leads, with a required cooling power of 42.5 W/kA.

Single stage cryocoolers	$\dot{Q}_{\mathrm{ref}}$ W	P W	$\tilde{\eta}_{\mathrm{C}}$ %	I_{CCCL} kA	P/I_{CCCL} W/kA
Leybold [86] - Gifford-McMahon					
COOLPOWER (CP) 50	50	2300	6.0	1.18	1949
CP 140 T	140	7500	5.1	3.29	2280
CP 250 MD	175	7500	6.4	4.12	1820
SHI Cryogenics Group [93] - Gifford-McMahon					
RD-125D 77 K	34	1300	7.2	0.80	1625
CH-104 77 K	40	2600	4.2	0.94	2766
RDK-400B 40 K	150	7200	5.7	3.53	2040
RDK-500B 20 K and CH-110LT 40 K	175	7200	6.7	4.12	1748
CH-110 77 K	190	7200	7.3	4.47	1611
Cryomech [87] - Gifford-McMahon					
AL10	14	1000	3.9	0.33	3030
AL60	60	1700	9.7	1.41	1206
AL125	120	3300	10.0	2.82	1170
AL200	190	4200	12.4	4.47	940
AL300	320	7000	12.6	7.53	930
AL600	600	11500	14.3	14.12	814
AFCryo [91] - Stirling type Pulse Tube					
PTC 90	120	3100	10.6	2.82	1100
PTC 330	480	12000	11.0	11.29	1063
PTC 1000	1450	25000	16.0	34.12	733
PTC 1500	3000	40000	20.6	70.59	567
Stirling cryogenics [92] - Reversed-Stirling					
SPC-1	1250	10625	32.4	29.41	360
SPC-4	5000	42500	32.4	117.65	360
RIX Industries [94] - Stirling type Pulse Tube					
2s226K	150	2750	15,0	3.53	779
2s241K	220	4500	13.4	5.18	869
2s362K	1000	22000	12.5	23.53	935

* Carnot efficiency $\widehat{=}$ Figure of Merit $\widehat{=}$ Percent of Carnot $\widehat{=}$ $\mathrm{COP}_{\mathrm{real}}/\mathrm{COP}_{\mathrm{Carnot}}$

and requires an input power of 42.5 kW [92].

An overview of single stage cryocoolers is depicted in Tab. 11. For each cryocooler, the corresponding refrigeration power $\dot{Q}_{\mathrm{ref}}$ at 80 K, the electric input power P at 50 Hz, the Carnot efficiency $\tilde{\eta}_{\mathrm{C}}$ according to (2.20), as well as the amperage I_{CCCL} and the specific power consumption P/I_{CCCL} of a single CCCL current lead with 42.5 W/kA are depicted. The GM cryocoolers from SHI and Leybold show values below 10 % for the Carnot efficiencies and the specific power consumptions of about 2000 W/kA (Carnot

yields 122 W/kA Tab. 9), while the coolers from Cryomech show slightly improved values. However, some manufacturers use same compressors for a number of cold heads at different cooling powers in their product line, yielding a not optimized power consumption for some cryocoolers. The Carnot efficiencies are higher for cryocoolers with a cooling power above 1000 W, e.g the Stirling cryocooler from Stirling Cryogenics [92] with an efficiency of about 32.5 %, a cooling power of 1250 W and a specific power consumption of 360 W/kA. However, large Stirling cryocoolers and Stirling type Pulse Tube cryocoolers [91] can not be mounted into a cryostat like GM or GM type PT cryocoolers, and are mainly used as a nitrogen liquefaction and re-condensation units.

3.2 Liquid nitrogen

Liquid nitrogen can be used to cool down resistive current leads to the temperature of its normal boiling point at about 78 K. In the vapour cooled current lead VCCL design, the current lead is submerged in the liquid nitrogen. Due to the thermal load at the cold end of 24.6 W/kA (Tab. 9), the liquid nitrogen evaporates and the sensible heat of the nitrogen gas should be used for further convective cooling. Nitrogen cooled current leads can be either part of an open system, with a continuous supply of the cryogenic liquid, or of a closed cooling system in combination with a cryocooler as a liquefaction unit. For the comparison of electric power consumptions of different current lead designs, the cooling with liquid nitrogen should not be referred to the Carnot cycle but rather to the minimal liquefaction work $l_{\min}$, which is outlined in the following.

In Fig. 20, the temperature entropy diagram of nitrogen is depicted with the state points of the ideal cycle process for liquefaction with

1. $(1) \rightarrow (4^*)$ Isothermal compression and heat rejection
2. $(4^*) \rightarrow (4)$ Isentropic (idealized adiabatic) expansion
3. $(4) \rightarrow (2)$ Isobaric and isothermal latent heat absorption
4. $(2) \rightarrow (1)$ Isobaric and non-isothermal sensible heat absorption

The minimal required power to liquefy nitrogen, the following minimal liquefaction work $l_{\text{min,1-4}}$ in $\left(\text{kJ/kg}\right)$ is used

$$l_{\text{min,1-4}} = q_1 - q_0 \tag{3.1}$$

$$l_{\text{min,1-4}} = T_1 \cdot (s_1 - s_4) - (h_1 - h_4) \tag{3.2}$$

with the absorbed energy q_0, the rejected energy q_1, the ambient temperature T_1, the mass specific entropies s and the mass specific enthalpies h of the fluid. With the ther-

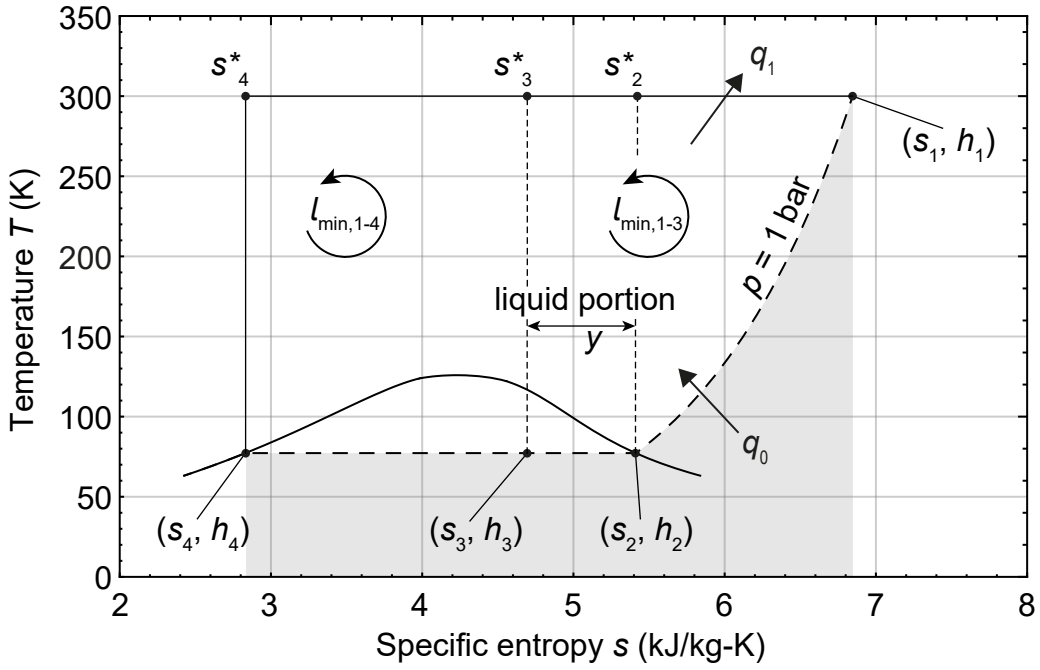

Figure 20: Temperature entropy diagram of nitrogen, that is used for deriving the minimal liquefaction work. $l_{\text{min,1-4}}$ is used to describe the minimal liquefaction work of a self-sufficient vapour cooled current lead and $l_{\text{min,1-3}}$ the forced flow VCCL.

modynamic properties of nitrogen from REFPROP [56], the minimal liquefaction work is calculated to

$$l_{\text{min,1-4}} = 300\,\text{K} \cdot 4.01\,\text{kJ/(kg K)} - 433.12\,\text{kJ/kg} \tag{3.3}$$

$$l_{\text{min,1-4}} = 770\,\text{kJ/kg} = 0.21\,\text{kWh/kg} \tag{3.4}$$

and is used in the calculation of the specific power consumption P_{liq} of vapour cooled current leads in Sec. 2.4. For ideal self-sufficient VCCLs with a mass flow of $\dot{m}_{\text{VCCL,ss}} = 0.443\,\text{kg/(h kA)}$, a minimum liquefaction power of about 94.7 W/kA is required. However, liquefaction of nitrogen is mainly done in large air separation plants, which have approximately a power consumption of about 0.56 kWh/kg [95], and therefore a figure of merit of about

$$\eta_{\text{FoM}} = COP_{\text{real}}/COP_{\text{min}} = 38,5\% \tag{3.5}$$

which is used in the calculation of the real power consumption that is needed for the cooling of an ideal self-sufficient VCCL, yielding

$$P_{\mathrm{liq,real,ss}}/I = \frac{770\,\mathrm{kJ/kg} \cdot 0.443\,\mathrm{kg/(h\,kA)}}{0.385 \cdot 3.6} = 246.1\,\mathrm{W/kA} \tag{3.6}$$

Combining this value with the electric power dissipation of the current lead, presented in Tab. 9, yields for the total power consumption

$$P_{\mathrm{total,el,ss}}/I = P_{\mathrm{liq,real,ss}}/I + P_{\mathrm{el,ss}}/I = 246.1\,\mathrm{W/kA} + 35.7\,\mathrm{W/kA} = 281.8\,\mathrm{W/kA} \tag{3.7}$$

Compared to the most efficient refrigeration machine presented in Tab. 11, the SPC-1 that may be used for the cooling of a CCCL with a total power consumption of 402.5 W/kA, $P_{\mathrm{total,el,ss}}/I$ yield a considerable smaller value. However, as mentioned in the previous Sec. 3.1, these large refrigeration machines can not be used as typical cold heads, and are mainly used for the liquefaction of nitrogen. Therefore, the cooling power of these machines has first to be used to liquefy nitrogen, yielding a maximum amperage of 23.4 kA and a total power consumption necessary for an ideal self-sufficient VCCL of

$$P_{\mathrm{SPC\text{-}1,ss}}/I = \frac{P_{\mathrm{SPC\text{-}1}} \cdot (h_1 - h_4) \cdot \dot{m}_{\mathrm{VCCL,ss}}}{\dot{Q}_{\mathrm{ref,SPC\text{-}1}}} + P_{\mathrm{el,ss}}/I = 488.7\,\mathrm{W/kA} \tag{3.8}$$

A difference of about 200 W/kA between a VCCL that is cooled with the SPC-1 refrigerator in closed system and liquid nitrogen in an open system. This overall power consumption, the high investment cost of this refrigerators and the low price of liquid nitrogen are the main reasons why high amperage current leads for HTS applications are mainly cooled with liquid nitrogen in an open system.

A forced-flow vapour cooled current lead, compared to a self-sufficient VCCL, requires an additional vapour mass flow that reduces the heat load at the cold end to 9 W/kA [1]. This can be accomplished with two different refrigeration machines, whereby one machine is producing the thermal load at the cold end corresponding amount of liquid, and a second that only generates the required amount of additional cold vapour. Further, it is possible to install a heater into the liquid nitrogen bath and provide the additional forced mass flow. However, it is also possible to use only one refrigeration machine that can liquefy nitrogen until a certain liquid portion y, which is depicted in Fig. 20. The

minimal liquefaction work for this case, yield

$$h_3 = h_4 + (h_2 - h_4) \cdot (1 - y) \tag{3.9}$$

$$s_3 = s_4 + (s_2 - s_4) \cdot (1 - y) \tag{3.10}$$

$$l_{\text{min,1-3}} = T_1 \cdot (s_1 - s_3) - (h_1 - h_3) \tag{3.11}$$

$$l_{\text{min,1-3}} = 283\,\text{kJ/kg} \approx 0.08\,\text{kWh/kg} \tag{3.12}$$

with the optimal liquid portion of about $y = 15\,\%$, according to Schreiner [1] and Goloubev [28]. The liquefaction work in (3.12), in combination with the optimal mass flow of $\dot{m}_{\text{VCCL,ff}} = 1.03\,\text{kg/(h\,kA)}$ and the electric power dissipation of 31.9 W/kA (outlined in Tab. 7), yields for the specific power consumption of an overall electrical optimized forced-flow VCCL

$$P_{\text{not-total,ff,el}}/I = l_{\text{min,1-3}} \cdot \dot{m}_{\text{VCCL,ff}} + P_{\text{el,ff}}/I \approx 113\,\text{W/kA} \tag{3.13}$$

A factor 2.5 reduction, compared to the total power consumption of an ideal self-sufficient VCCL in (3.7). However, in contrast to a self-sufficient VCCL, a forced-flow design requires an additional device to provide the necessary mass flow of nitrogen and its power consumption has to be considered in (3.13) as well. Provided that the previous refrigeration machine SPC-1 from Tab. 11 is used to liquefy the nitrogen until the mass fraction of $y = 15\,\%$ (point 3 in Fig. 20), a maximum amperage of 16.5 kA is calculated and the corresponding total power consumption is given by

$$P_{\text{SPC-1,ff}}/I = \frac{P_{\text{SPC-1}} \cdot (h_1 - h_3) \cdot \dot{m}_{\text{VCCL,ff}}}{\dot{Q}_{\text{ref,SPC-1}}} + P_{\text{el,ff}}/I = 673\,\text{W/kA} \tag{3.14}$$

Compared to the self-sufficient VCCL in (3.8), the forced-flow VCCL leads to a 184 W/kA larger specific power consumption and a significant smaller amperage, despite the smaller electric power dissipation and the smaller minimal liquefaction work. It becomes apparent that the use of a refrigeration device providing cooling power at a fixed temperature, like the SPC-1, is not suitable for the forced-flow VCCL design.

In an open system with a continuous supply of liquid nitrogen, a bath heater can be installed to provide the additional mass flow that is necessary for the forced-flow VCCL with

$$P_{\text{heater}}/I = (h_2 - h_4) \cdot (1 - y) \cdot \dot{m}_{\text{VCCL,ff}} = 48.4\,\text{W/kA} \tag{3.15}$$

Analogous to (3.6) and (3.7), the total power consumption of an ideal forced-flow VCCL in combination with a heater in an open system is given by

$$P_{\text{total,el,ff}}/I = P_{\text{liq,real,ff}}/I + P_{\text{el,ff}}/I + P_{\text{heater}}/I = 652\,\text{W/kA} \tag{3.16}$$

with the real power consumption $P_{\text{liq,real,ff}}$, analogous to (3.6), which is needed to liquefy nitrogen according to the optimal mass flow $\dot{m}_{\text{VCCL,ff}}$. $P_{\text{total,el,ff}}$ in (3.16), yields a slightly smaller power consumption compared to the closed system of a SPC-1 cooled forced-flow VCCL (3.14). Therefore, it is more efficient to use liquid nitrogen with a heater for the cooling of the forced-flow VCCL design, instead of a cryocooler. Comparing this power consumption with the self-sufficient cases in (3.7) and in (3.8) leads to the conclusion that the force-flow VCCL concept does not provide a reduction of the overall power consumption. Conversely, this design leads to a significant larger overall power consumption. Nevertheless, a further approach to the forced-flow design option in a closed system, is the direct implementation of the current lead into a recuperative refrigeration system, like the Linde-Hampson cycle.

3.3 Linde-Hampson cycle

The Linde-Hamson cycle is a recuperative refrigeration cycle that, in contrast to a cryocooler, moves the refrigerant in a circuit in one direction. Schematic representations of a Linde-Hampson refrigerator (a) and a Linde-Hamson gascooler (b) are given in Fig. 21.

The cooling cycle of a Linde-Hampson refrigerator (a) proceeds in the following steps. Initially, the gaseous refrigerant is compressed ($1 \rightarrow 2$), and the resulting compression heat q_{a} is rejected in the aftercooler at ambient temperature T_{a}. In the counter-flow heat exchanger, known as a recuperative heat exchanger, the high pressure (HP) gas ($3 \rightarrow 4$) is cooled by the low-pressure (LP) gas ($6 \rightarrow 7$). Further, the HP fluid is expanded in the throttling device and fed to the evaporator ($5 \rightarrow 6$), where a certain cooling load q_0 at cryogenic temperature is absorbed. At the following, the LP fluid flows through the heat-exchanger back to the compressor.

The Linde-Hampson gascooler (b) does not have an evaporator and the thermal load q_0 is distributed over the entire recuperative heat-exchanger. Therefore, providing refrigeration over a certain temperature range. This cycle may be used for the cooling and liquefaction of gases, in combination with a three-pass heat exchanger, or for the cooling of resistive current leads. The latter case is investigated in this work in Sec. 4.

The refrigeration powers of a Linde-Hampson refrigerator (a) and a gascooler (b) are

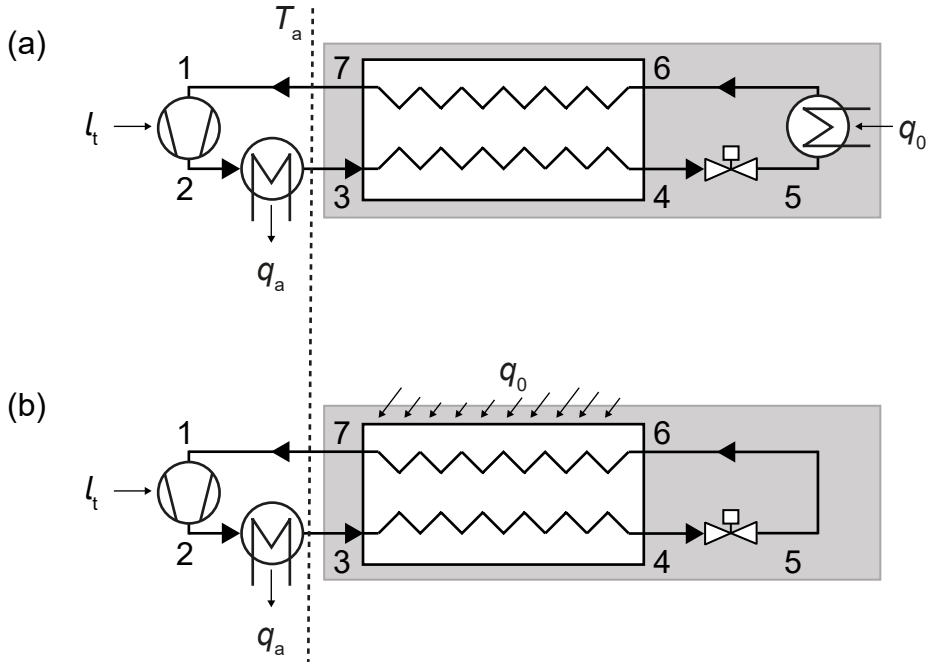

Figure 21: Schematic representations of a Linde-Hampson refrigerator (a) and of a Linde-Hampson gascooler (b).

given by the respective energy balance around the heat exchanger, the evaporator and the throttling device and yield in both cases

$$q_0 = (h_7 - h_3) \tag{3.17}$$

where $(h_7 - h_3)$ is the mass specific enthalpy difference at the warm end of the heat exchanger and q_0 is the specific refrigeration load at the evaporation temperature in the refrigerator (a), or the integrated refrigeration load over the whole temperature range in the heat exchanger in the gascooler (b). Assuming an ideal heat exchanger with a minimum temperature approach at the warm end, yield the maximum refrigeration load $q_{0,\max}$ of

$$q_{0,\max} = -\int_{p_7}^{p_3} \left(\frac{\partial h}{\partial p}\right)_T \mathrm{d}T = \int_{p_7}^{p_3} \left(\frac{\partial h}{\partial T}\right)_p \left(\frac{\partial T}{\partial p}\right)_h \mathrm{d}p = \int_{p_7}^{p_3} c_\mathrm{p} \cdot \mu_\mathrm{JT}\, \mathrm{d}p \tag{3.18}$$

which is related to the integral of the specific isobaric heat capacity c_p and the Joule-Thomson coefficient μ_JT of the refrigerant with respect to the pressure p. The Joule-Thomson coefficient describes the temperature change of a real fluid during a decompression that occurs through a throttling device at constant enthalpy, which is defined

Table 12: Molar compositions of three different hydrocarbon-based refrigerant mixtures.

Refrigerant mixtures	Nitrogen	Methane	Ethane	Propane	Butane
			mole - %		
LRS mixture 1	10	15	15	25	35
LRS mixture 17	20	30	20	15	15
GRS mixture 1	30	25	15	30	0

as

$$\mu_{\mathrm{JT}} = \left(\frac{\partial T}{\partial p}\right)_h = \frac{\nu}{c_{\mathrm{p}}} \cdot (\gamma \cdot T - 1) \tag{3.19}$$

where ν is the specific volume and γ is the volumetric thermal expansion coefficient. In the case of an ideal gas, with $\gamma = 1/T$, the Joule-Thomson coefficient is zero at all temperatures. A pressure decrease of a real fluid with a positive Joule-Thomson coefficient leads to a temperature decrease, i.e the Joule-Thomson cooling effect.

Linde-Hampson cycles that are operated with zeotropic refrigerant mixtures, e.g. mixtures in Tab. 12, can be classified into two types [96]. The gas refrigerant supply (GRS) type, where the temperature of the high pressure stream at the heat exchanger inlet (point 3 in Fig. 21) is above the dew point temperature of the refrigerant mixture, as shown in the temperature enthalpy (T-h) diagram of the GRS mixture 1 in Fig. 22a. In the case of a minimal temperature approach at the warm end of the heat exchanger, the maximum specific refrigeration power (3.18) for the GRS mixture 1 is equal to $q_{0,\max} = 40\,\mathrm{kJ/kg}$. The second type is the liquid refrigerant supply (LRS) type, in which partial condensation of the HP stream occurs in the aftercooler. Consequently, the dew point temperature of the LRS mixture at the heat exchanger inlet is below the dew point of the refrigerant, as shown in Fig. 22b for the LRS mixture 17, where the point 3 lies inside the two-phase area. The refrigerant mixtures LRS mixture 1, LRS mixture 17 and GRS mixture 1 show this transition at a temperature of 293.15 K and high pressures of about 5 bar, 12 bar and 33 bar respectively. The maximum specific refrigerant power of LRS mixture 17 is $q_{0,\max} = 140\,\mathrm{kJ/kg}$ which is more than three times larger compared to the GRS mixture 1,. Therefore, larger energy efficiencies can be obtained with LRS Linde-Hampson cycles, compared to GRS systems. Based on that, the LRS system is chosen in the investigation of cryogenic mixed refrigerant cooled current leads in this work (Sec. 4).

The specific refrigeration power of an ideal Linde-Hampson cooler $q_{0,\max}$, as a function of the high pressure p_3, is presented in Fig. 23 for six different working fluids. The pure refrigerants argon, nitrogen and methane show significant smaller specific refrigeration

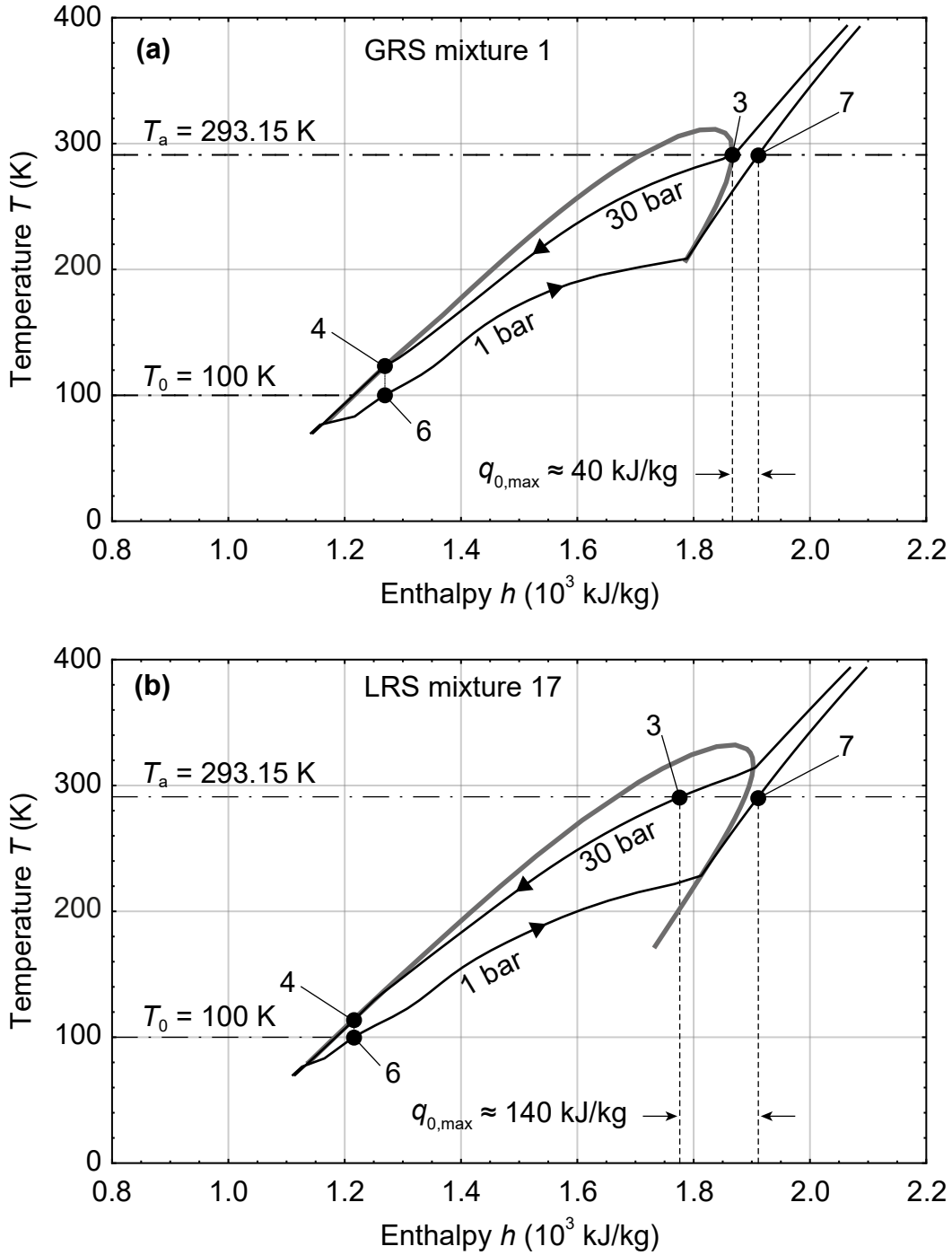

Figure 22: Temperature-enthalpy diagrams of a GRS (a) and a LRS (b) refrigerant mixture. The molar compositions of the mixtures are presented in Tab. 12. The points 3, 7, 4 and 6 relate to the state points of the Linde-Hampson gascooler presented in Fig. 21. Points 4 and 6 represent an example calculation for $T_6 = 100\,\mathrm{K}$ and zero pressure losses along the heat exchanger. Phase envelope and isobars are predicted with the Peng-Robinson equation of state [97, 98].

powers in comparison to the presented mixed refrigerants, whose molar compositions are listed in Tab. 12. To archive the same specific refrigeration power of the mixed refrigerant

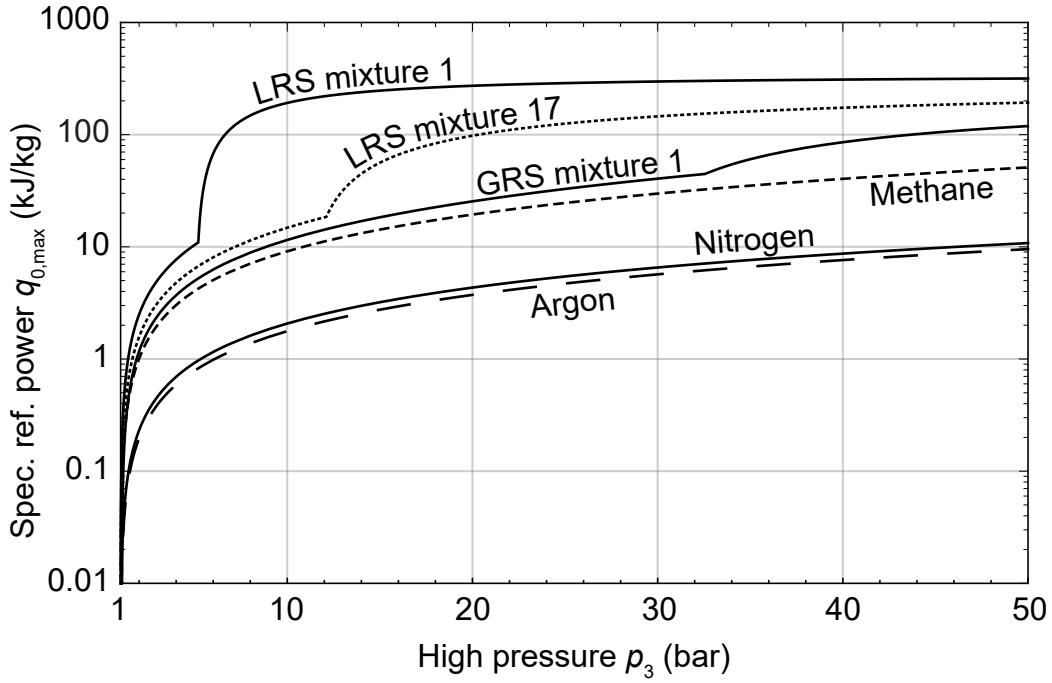

Figure 23: Specific refrigeration powers of an ideal Linde-Hampson refrigerator or a gascooler ($T_7 = T_3 = 293.15\,\mathrm{K}, p_7 = 1\,\mathrm{bar}$), for six different refrigerants. The molar compositions of the LRS and GRS mixtures are presented in Tab. 12. Calculated with the thermodynamic properties derived from REFPROP [56].

GRS mixture 1 at 30 bar, a Linde-Hampson cooler with nitrogen requires a high pressure of about 295 bar, and consequently leads to a larger technical work l_t of the compressor. Therefore, pure refrigerants may rather be liquefied in a pre-cooled Linde high-pressure cycle with an intermediate pressure stage, or with a Claude, or a Heylandt cycle [99]. The low energy efficiency of a Linde-Hampson cycle, when operated with a pure refrigerant, can be identified in the analysis of the first and the second law of thermodynamics around the refrigeration cycle, yielding the general thermodynamic work function for the process work [100]

$$l_\text{in-out} = (h_\text{in} - h_\text{out} + l_\mathrm{t}) - T_\mathrm{a} \cdot (s_\text{in} - s_\text{out}) \tag{3.20}$$

with the mass specific enthalpies h and the entropies s of a fluid at inlet and outlet of a control volume element or a system component and with the technical work l_t that is introduced into this component. Equation (3.20) is generally valid for all thermodynamic processes. The sum of all process work $l_\text{in-out}$ in a thermodynamic cycle, describes the technical work l_t that is necessary to preserve its stationary energy transformation and yield for the Linde-Hamson gascooler

$$l_\mathrm{t} = \sum l_\mathrm{i\text{-}j} = l_\mathrm{comp} + l_\mathrm{af.cool} + l_\mathrm{hx} + l_\mathrm{thr} \stackrel{!}{=} (h_2 - h_1) \tag{3.21}$$

with the technical work l_t and the work function l_comp of the compressor, the work functions of the aftercooler $l_\mathrm{af.cool}$, of the heat exchanger l_hx and of the throttling device l_thr. According to (3.20), these work functions are given by

$$l_\mathrm{comp} = l_{1-2} = (h_1 - h_2 + l_\mathrm{t}) - T_\mathrm{a} \cdot (s_1 - s_2) \tag{3.22}$$

$$l_\mathrm{af.cool} = l_{2-3} = (h_2 - h_3) - T_\mathrm{a} \cdot (s_2 - s_3) \tag{3.23}$$

$$l_\mathrm{hx} = l_{3-4,6-7} = (h_3 - h_4 + h_6 - h_7) - T_\mathrm{a} \cdot (s_3 - s_4 + s_6 - s_7) \tag{3.24}$$

$$l_\mathrm{thr} = l_{4-5} = (h_4 - h_5) - T_\mathrm{a} \cdot (s_4 - s_5) \tag{3.25}$$

The corresponding enthalpies and entropies can be determined from the respective fluid properties with respect to pressure and temperature, as well as from the energy balance equations of the components.

The numerical results of the efficiency analysis of a Linde-Hampson gascooler, working between the temperatures of $T_7 = T_3 = T_\mathrm{a} = 293.15\,\mathrm{K}$ and $T_6 = 100\,\mathrm{K}$ and pressures of $p_7 = 3\,\mathrm{bar}$ and $p_3 = 30\,\mathrm{bar}$, are summarized in Tab. 13. Three mixtures, whose molar compositions are depicted Tab. 12, and pure nitrogen are investigated. The technical work l_t of a Linde-Hampson gascooler that is operated with nitrogen, shows the highest value compared to the mixed refrigerants. Furthermore, the maximum refrigeration load $q_\mathrm{0,max}$ is a factor of 45 smaller compared to the LRS mixture 1. The reasons for the considerable worse performance of a pure fluid like nitrogen in comparison to a mixture is first the

Table 13: Numerical results of the efficiency analysis of a Linde-Hampson gascooler ($T_7 = T_3 = T_\mathrm{a} = 293.15\,\mathrm{K}, T_6 = 100\,\mathrm{K}, p_7 = 3\,\mathrm{bar}, p_3 = 30\,\mathrm{bar}$) for three refrigerant mixtures and for pure nitrogen. The molar compositions of the mixtures are depicted in Tab. 12. The technical work is calculated with an isentropic efficiency of 0.7.

Refrigerant mixtures	l_comp	$l_\mathrm{af.cool}$	l_hx	l_thr $\left(\mathrm{kJ/kg}\right)$	$\sum l_\mathrm{i\text{-}j}$	l_t	$q_\mathrm{0,max}$
LRS mixture 1	44.5	68.5	78.3	13.9	205.3	205.3	276.8
LRS mixture 17	58.9	72.7	146.0	13.7	291.3	291.3	123.2
GRS mixture 1	61.7	79.8	156.5	17.9	315.9	315.9	38.6
Nitrogen	57.8	148.9	33.6	166.2	406.5	406.5	6.1

smaller refrigeration effect according to (3.18) that is explained by the smaller Joule-Thomson coefficient of pure refrigerants which are operating at supercritical temperatures. In general, the Joule-Thomson coefficient of a fluid gets larger near its critical temperature [96]. A mixed refrigerant has a certain number of components, whose critical temperatures lie inside the operating temperature range, providing by this a high refrigeration effect. Second, the high entropy productions in the throttling device and in the aftercooler, yielding large values for the work functions in this components. The largest process work in the case of mixed refrigerant is found in the counter-flow heat exchanger, however, mainly due to the significant larger external thermal load $q_{0,\max}$ that is described by the enthalpies in (3.24). A further and deeper view on the entropy production of a particular component is possible in the investigation of the temperature, pressure and concentration gradients inside the components. This contributions are all described by the thermodynamic work function (3.20) and can be expressed as

$$l_{\text{in-out}} = T_{\text{a}} \cdot \left(\Delta s_{\Delta T} + \Delta s_{\Delta p} + \Delta s_{\Delta c} \right) \tag{3.26}$$

with the specific entropy production $\Delta s_{\Delta T}$ due to internal temperature gradients which is defined as

$$\Delta s_{\Delta T} = \int \frac{(T_{\text{h}} - T_{\text{c}})}{T_{\text{h}} \cdot T_{\text{c}}} \, \mathrm{d}q \tag{3.27}$$

where q is the transferred energy in the form of heat between a hot and a cold part inside the component. The increase of entropy $\Delta s_{\Delta T}$ scales with the increasing temperature difference between the parts (or between the fluid streams inside the heat exchanger) and the decreasing product of this temperatures. Applying (3.27) on the recuperative heat exchanger of a Linde-Hampson gascooler yields the entropy production due to the internal heat transfer process between the high pressure and low pressure fluid

$$\Delta s_{\text{hx-int},\Delta T} = \int \frac{(T_{\text{HP}} - T_{\text{LP}})}{T_{\text{HP}} \cdot T_{\text{LP}}} \, \mathrm{d}h_{\text{HP}} = \int_0^{\text{L}} \frac{(T_{\text{HP}} - T_{\text{LP}})}{T_{\text{HP}} \cdot T_{\text{LP}}} \cdot \left(\frac{\partial h}{\partial z} \right)_{\text{HP}} \mathrm{d}z \tag{3.28}$$

with the transferred thermal load that is equal to the specific enthalpy change $\mathrm{d}h_{\text{HP}}$ of the HP fluid and is integrated along the heat exchanger coordinate z from zero to the total length L. Additional entropy production in the heat exchanger due to the heat transfer is caused by the external thermal load q_0 into the system. If the temperature of the external source is known, the entropy production can be calculated according the corresponding temperature difference with

$$\begin{aligned}\Delta s_{\text{hx-ext},\Delta T} &= \int \frac{(T_{\text{ext}} - T_{\text{LP}})}{T_{\text{ext}} \cdot T_{\text{LP}}} \left(\mathrm{d}h_{\text{LP}} - \mathrm{d}h_{\text{HP}}\right) \\ &= \int_0^{\text{L}} \frac{(T_{\text{ext}} - T_{\text{LP}})}{T_{\text{ext}} \cdot T_{\text{LP}}} \cdot \left[\left(\frac{\partial h}{\partial z}\right)_{\text{LP}} - \left(\frac{\partial h}{\partial z}\right)_{\text{HP}}\right] \mathrm{d}z\end{aligned} \tag{3.29}$$

with the transferred heat load $(\mathrm{d}h_{\text{LP}} - \mathrm{d}h_{\text{HP}})$ according to the energy conservation around the heat exchanger. In this case the external thermal load is applied to the LP stream. For an idealized heat transfer with a infinitesimal small temperature difference between the LP stream and the external source, (3.29) can be converted into

$$\Delta s_{\text{hx-ext},\Delta T} = \int_0^{\text{L}} \frac{1}{T_{\text{LP}}^2} \cdot \left(\frac{\partial T}{\partial z}\right)_{\text{LP}} \cdot (h_{\text{LP}} - h_{\text{HP}}) \, \mathrm{d}z \tag{3.30}$$

In the case of mixed refrigerants, the entropy production $\Delta s_{\Delta T}$ can be minimized by reducing the respective temperature difference by an adjustment of the mixture composition, yielding a change of the enthalpy profiles and therefore, a change of the isobaric heat capacities $c_{\text{p}} = \left(\mathrm{d}h/\mathrm{d}T\right)_p$ of the fluid streams. For pure fluids, the specific isobaric heat capacities are considerably larger at high pressures than at low pressures, leading to different temperature gradients along the heat exchanger. Furthermore, the c_{p} of pure fluids at high pressures is increasing with decreasing temperature[3] and contributes to a larger temperature difference at the cold end of the heat exchanger. According to (3.27), this leads to a large entropy increase in the heat exchanger. For more information about the entropy production, due to the heat transfer of a pure and a mixed refrigerant in a Linde-Hampson refrigerator (Fig. 21a), the author refers to the figures 2.10 and 2.13 proposed by Kochenburger in [4].

The second entropy production term $\Delta s_{\Delta p}$ in (3.26) is caused by the pressure loss of the fluid streams. This can be caused by friction losses inside the component or by the throttling in the Joule-Thomson valve. According to the fundamental thermodynamic relation of the enthalpy, the entropy production of an isenthalpic expansion is defined as

$$\Delta s_{\Delta p} = \int -\frac{\nu}{T} \, \mathrm{d}p \tag{3.31}$$

where the mass specific entropy increase scales with decreasing temperature, increasing specific volume ν, and increasing pressure difference. In general, the specific volume of fluids is smaller at higher pressures, therefore, a larger LP and HP in the refrigeration

[3] The specific isobaric heat capacity of pure fluids at pressures above the critical pressure is increasing with temperature up to the point, where the enthalpy of the fluid is equal to the enthalpy of the critical point. From this point on, the specific isobaric heat capacity is decreasing with decreasing temperature.

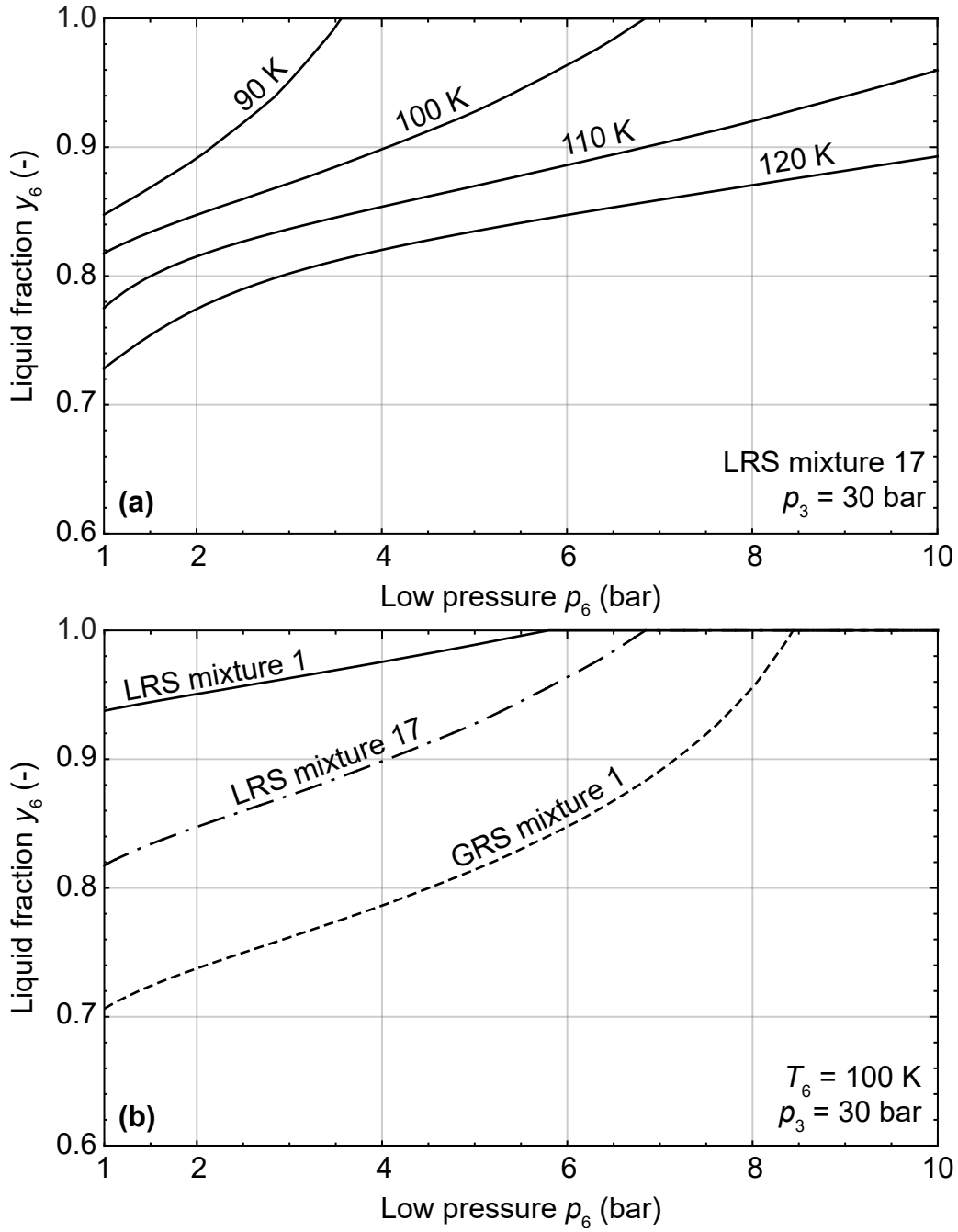

Figure 24: Liquid fractions as a function of the low pressure p_6 for different design temperatures (a) and refrigerant mixtures (b). The molar compositions of the mixtures are presented in Tab. 12. Calculated with the thermodynamic properties derived from PR-EoS [97, 98].

cycle lead to a smaller entropy production, due to the pressure drop and the expansion in the valve. Additionally, the specific volume is decreasing with increasing liquid fraction y of the refrigerant mixture in the cycle. Towards the cold end of the heat exchanger, the liquid fractions in both the HP and the LP streams of a mixed refrigerant are increasing, hereby reducing the entropy production $\Delta s_{\Delta p}$. The liquid fractions y_6 of the LP stream at the inlet to the heat exchanger (point 6 in Fig. 21) are presented in Fig. 24a for the

LRS mixture 17 at different operating temperatures. It follows that at different design temperatures, the liquid fractions are generally increasing with increasing low pressure p_6. Additionally, the liquid fractions at a fixed low pressure are larger for a lower design temperature T_6. The comparison of the investigated refrigerant mixtures in Fig. 24b shows that the LRS mixtures, especially LRS mixture 1, lead to larger liquid fractions compared to the GRS mixture and therefore to a reduction of the entropy production according to (3.31).

A further contribution to the entropy increase is the entropy of mixing $\Delta s_{\Delta c}$, due to the concentration changes in the phases in the case of a mixed refrigerant. This entropy production can be evaluated by subtracting the process work (3.26) of the component by the above contributions from (3.27) and (3.31).

The percentage compositions of the process works of a Linde-Hampson gascooler are also depicted in Fig. 25 for LRS mixture 1, GRS mixture 1 and nitrogen. The LRS mixture 17 shows similar results to the GRS mixture 1 and is therefore not presented in this chart. On the left-hand side of Fig. 25, the pie charts (a,b,c) correspond to the investigation with a low pressure of $p_6 = 3\,\text{bar}$ and the charts (a*,b*,c*) on the right-hand side correspond to $p_6 = 7\,\text{bar}$. The LRS mixture 1 shows a slightly different process work composition to the investigated GRS mixture 1. With 50 %, the heat exchanger process work of the GRS mixture 1 has the largest contribution to the overall entropy production of the cycle. Comparing this value with the respective contribution from LRS mixture 1, shows a significant reduced share of l_{hx}. Furthermore, the technical work of the LRS mixture 1 is about 35 % smaller at a seven times larger refrigeration load.

The process work compositions do not change significantly between the two operating pressures in Fig. 25, however, the technical work is approximately halved for the cases of larger low pressure $p_6 = 7\,\text{bar}$. In general, the technical work l_{t} of Linde-Hampson cycle is decreasing with increasing low pressure p_6 for all refrigerants and is presented in Fig. 26a. Pure nitrogen shows the largest technical work compared to the investigated refrigerant mixtures, at all pressures up to 10 bar. The least amount of work is needed with the LRS mixture 1. The differences of the pure component in the technical work compared to the mixtures are not large, however, taking the corresponding refrigeration loads into account, yields a significant difference in the coefficient of performance (COP) and is presented in Fig. 26b. The COP describes the ratio between the specific refrigeration load q_0 to the technical work l_{t} analogous to (2.19). Compared to the LRS mixture 1, the COP values for nitrogen, yield one order of magnitude smaller results. Linde-Hampson gascoolers that are operated with LRS mixtures archive larger COP values compared to GRS systems. It is interesting to denote that the COP function of the LRS mixture 1 becomes uniform from a low pressure of about 7 bar. This is explained by the transition of the LP stream at the outlet of the heat exchanger into the two-phase region. From this

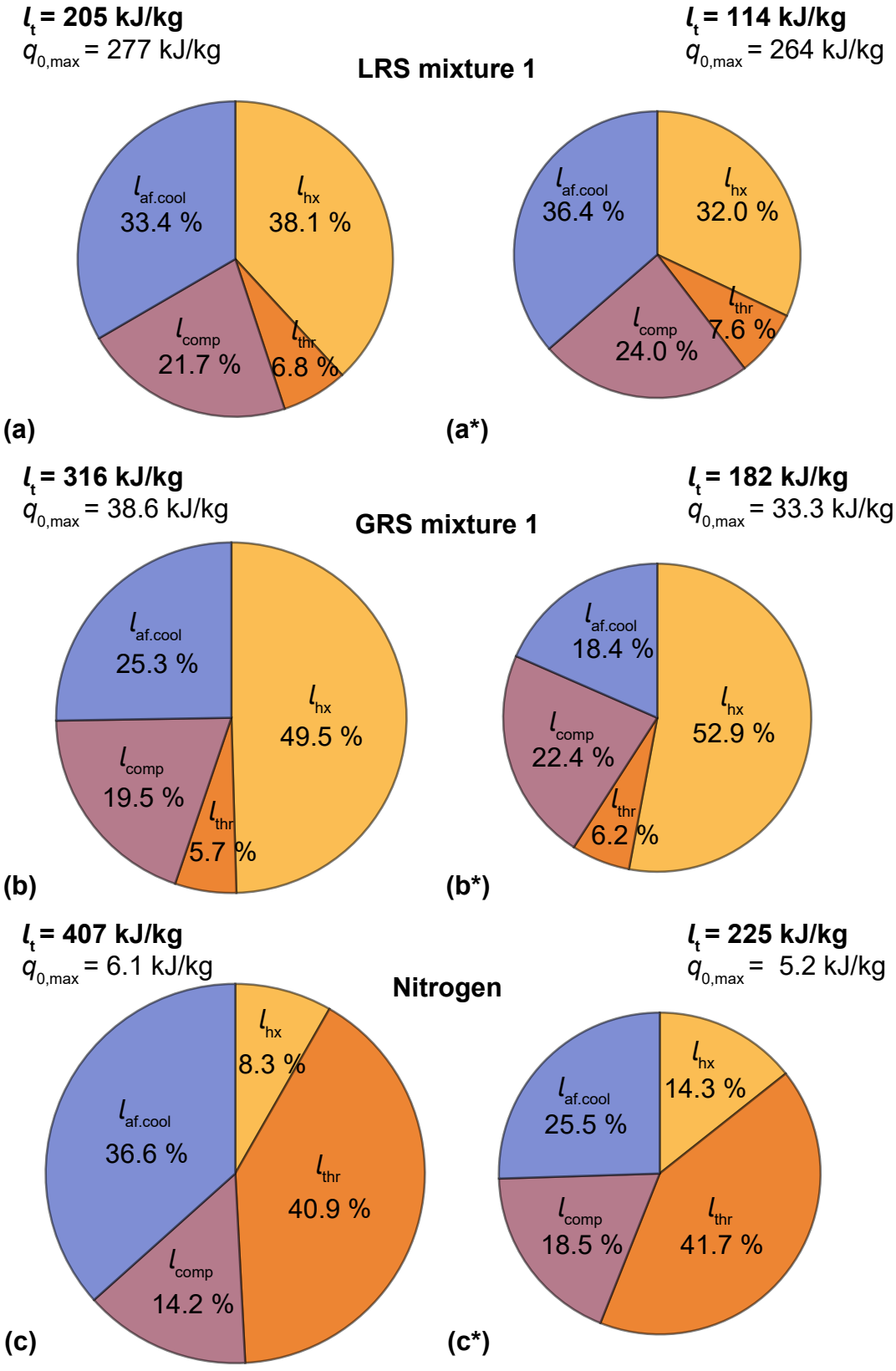

Figure 25: Percentage compositions of the process work in a Linde-Hampson gascooler working with the LRS mixture 1, the GRS mixture 1 and with pure nitrogen at a high pressure of $p_6 = 30\,\mathrm{bar}$, at a low pressures of $p_6 = 3\,\mathrm{bar}$ for (a,b,c) and at $p_6 = 7\,\mathrm{bar}$ for (a*,b*,c*). The refrigeration temperature is set to $T_6 = 100\,\mathrm{K}$.

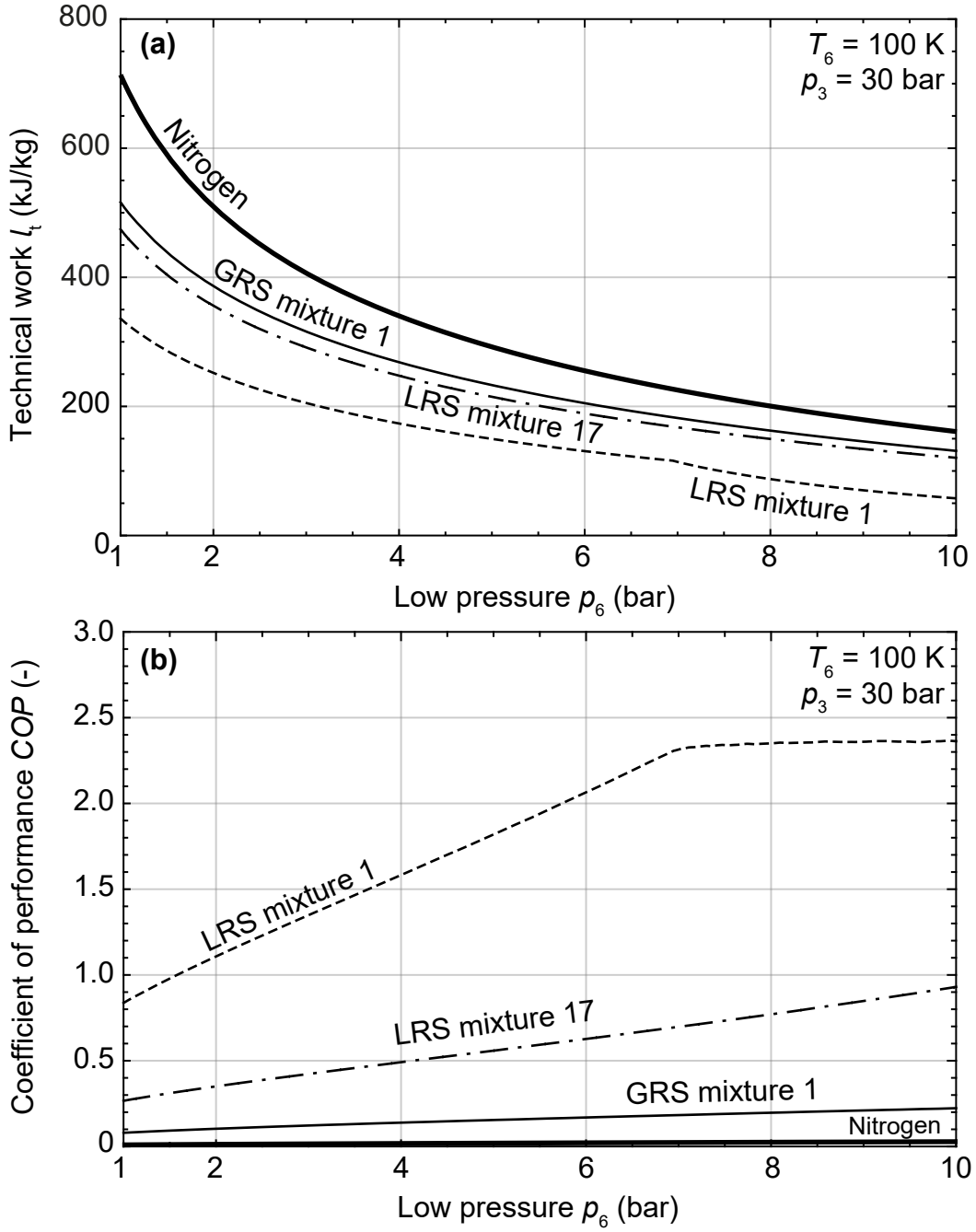

Figure 26: Technical work (a) and coefficient of performace (b) of a Linde-Hampson gascooler ($T_7 = T_3 = 293.15\,\mathrm{K}, T_6 = 100\,\mathrm{K}, p_7 = 3\,\mathrm{bar}, p_3 = 30\,\mathrm{bar}$) as functions of the low pressure p_6 for three refrigerant mixtures and for pure nitrogen (depicted in Tab. 12). The technical work is calculated with an isentropic efficiency of 0.7.

point on, the maximum refrigeration effect $q_{0,\max}$ is decreasing with decreasing pressure at almost the same rate as the technical work l_t, thus leading to uniform COP values.

The lowest temperature that can be archived with a Linde-Hampson cycle is limited by the freezing point of the refrigerant. The freezing point of a refrigerant mixture can be estimated according to the mole fraction-weighted average of the triple point temperatures

T_{tp} of the mixture components [101], yielding

$$T_{\mathrm{freeze}} = \sum_{i=1}^{N} \widetilde{x}_i \cdot T_{\mathrm{tp},i} \tag{3.32}$$

where N represents the total number of components and $\widetilde{x}_i$ is the mole fraction of component i. This estimation corresponds to a linear approximation between the freezing points of the respective components. Due to the freezing point depression of multicomponent mixtures, (3.32) slightly overestimates the actual freezing point. Therefore, this equation may be used in the estimation of the lowest possible design temperature for a refrigeration cycle. According to (3.32), the freezing points of the GRS mixture 1 and the LRS Mixture 17 are approximately 88 K and 81 K, respectively. The LRS Mixture 1 that with the largest specific refrigeration effect has a freezing point of about 95 K.

In conclusion, the technical work l_{t} of a refrigeration cycle is only the sum of all work functions in the cycle that describes the entropy production rates of the individual components and is generally decreasing with increasing low pressure p_6 of the LP stream for all refrigerants. The efficiency (COP value) of a Linde-Hamspon cycle can be increased by the use of a mixed refrigerant instead of a pure refrigerant, because of

1. the internal and external heat loads that are absorbed always at the highest possible temperature, yielding to a minimization of the entropy production according to (3.27)
2. the increasing liquid fractions in both the HP and LP streams towards the counter-flow heat exchanger cold end which are minimizing the entropy production due to the pressure drop and expansion according to (3.31)
3. the significant larger refrigeration load $q_{0,\max}$ that can be archived with a mixed refrigerant and is depicted in Fig. 23.

An additional advantage of mixed refrigerants over pure fluids is the considerable larger heat transfer coefficients [5], due to condensation and evaporation processes inside the heat exchanger. Thus, leading to a reduction of the required heat transfer area to absorb a certain amount of heat. However, the fluid properties of zeotropic refrigerant mixtures, especially the capacity rates, vary along the counter-flow heat exchanger and the use of standard heat exchanger design methods [58] is inadequate. Therefore, a two-phase heat transfer calculation method for heat exchangers was developed by Gomse [5], which is used in this work for the investigation of the Linde-Hampson cycle in combination with a resistive current lead and is presented in Sec. 4.

3.4 System comparison

The following shall give a short comparison of the required specific power consumptions that are needed to cool a resistive current lead with the presented cooling systems, except for Linde-Hampson cooling system that is presented in the following Sec. 4.

The total power consumptions $P_{\mathrm{total,el}}$, including the required refrigeration power of the cooling system and the electric power losses of the respective current lead type, are presented in Tab. 14. The amperage I represents the maximum operating current that is possible with the respective cooling system and current lead type. A straightforward system configuration is a single stage GM cryocooler AL600 in combination with a conduction cooled current lead, which results in a maximum amperage of 14.1 kA. However, the AL600 with a Carnot efficiency of $\tilde{\eta}_{\mathrm{C}} = 14.3\,\%$ (Tab. 11) and the large electric power losses of a CCCL, leads to a relative large specific power consumption of 858 W/kA. Nevertheless, using the same cryocooler and additional Peltier elements at the warm end of the current lead, yields a considerable larger amperage of 19.3 kA and a smaller specific power consumption. However, at the time of this publication, a PCL at this amperage level has not been developed yet. Larger amperages and smaller power consumptions can be archived with the more efficient Stirling cryogenerators, which may work as nitrogen re-condensation units in combination with vapour cooled current leads. Compared to the self-sufficient systems, the forced-flow VCCL leads to a considerable smaller electric current and to a larger power consumption, despite the smaller thermal load at the cold

Table 14: Cooling systems for resistive current leads at 77 K. Cryocooler description refers to the refrigeration machines presented in Tab. 11. The amperage I represents the maximum possible current, derived from the cooling power of the refrigeration machines.

Cooling system	Description	Current lead type	I kA	$\dot{Q}_{\mathrm{c}}/I$ W/kA	$P_{\mathrm{total,el}}/I$ W/kA
GM cryocooler	AL600	CCCL	14.1	42.5	858
GM cryocooler	AL600	PCL	19.3	31.0	660[a]
Reversed-Stirling	SPC-1	ss-VCCL[b]	23.4	24.6	489
	SPC-1	ff-VCCL	16.5	9.0[c]	673[d]
	SPC-1	ss-VCPCL[e]	27.8	20.6	443[a]
Cryocoolers	[1]	MCCL	20.0	21.5	950
LN_2	(3.7)	ss-VCCL[b]	∞	24.6	282
LN_2	(3.16)	ff-VCCL[f]	∞	9.0[c]	652

[a] cooling system at the warm end for the Peltier heat rejection is not included
[b] with the heat transfer area multiplier $f = 100$
[c] according to [1]
[d] power consumption of the nitrogen gas circulation device is not included
[e] presented in the appendix (A) - VCPCL $f = \infty$ copper
[f] in combination with a bath heater

Table 15: Cooling systems for a 10 kA current lead at 77 K. Cryocooler description refers to the refrigeration machines presented in Tab. 11.

Cooling system	Description	Current lead type	$\dot{Q}_c$ W	$\dot{Q}_{ex}$ W	$P_{total,el}$ kW	$P_{total,el}/I$ W/kA
GM cryocooler	AL600	CCCL	425	175	11.9	1190
GM cryocooler	AL300	PCL	310	10	7.7	770
PT cryocooler	PTC 330	ss-VCCL[a]	262[b]	4	12.4	1240
	PTC 330	ss-VCPCL[c]	206	12.6	31	3100
Reversed-Stirling	SPC-1	ss-VCCL[a]	246	717	10.7	1070
	SPC-1	ff-VCCL	90[a]	495	10.7	1070
	SPC-1	ss-VCPCL[c]	206	977	10.7	1070
Cryocoolers	[1]	MCCL	335	-	17.6	1760
LN_2	(3.7)	ss-VCCL[a]	246	-	2.8	280
LN_2	(3.16)	ff-VCCL	90	-	6.5	650

[a] with the heat transfer area multiplier $f = 100$
[b] with the mass flow of $\dot{m} = 0.396\,\mathrm{kg/(h\,kA)} < \dot{m}_{VCCL,ss}$
[c] presented in the appendix (A) - VCPCL $f = \infty$ copper

end. The state-of-the-art multi-stage cooled current lead system described in [1], where in addition to a AL600 cryocooler two intermediate cooling stages and a water cooling system are used, leads to a specific power consumption of 950 W/kA at a current of 20 kA. A comparable amperage may be archived with the SPC-1 cooler in combination with a ss-VCCL, however, at nearly half of the energy consumption. The smallest energy consumption is archived with a ss-VCCL and nitrogen boil-off in an open system, at all amperages.

The refrigeration systems for the cooling of a 10 kA current lead are presented in Tab. 15. In addition to the cooling load at the cold end $\dot{Q}_c$ and the overall power consumption $P_{total,el}$, the excess refrigeration power $\dot{Q}_{ex}$ is given. $\dot{Q}_{ex}$ describes the remaining cooling power at 77 K of the respective refrigeration machine. The smallest power consumption in a closed system of 7.7 kW, is archived with the combination of a AL300 GM cryocooler and a Peltier current lead, followed by a ss-VCCL in combination with the SPC-1 reversed Stirling cryogenerator, with a power consumption of 10.7 kW. In the latter case, the excess refrigeration power is sufficient for the cooling of an additional 10 kA current lead. Smaller power consumption can be accomplished with a ss-VCCL and LN_2 boil-off in an open system, yielding 2.8 kW. The MCCL system [1] leads to the largest power consumption in Tab. 15, however, it is to denote that this system is not optimized for an electric current of 10 kA. Further improvements in the cooling system comparison, may be archived by the implementation of the investment and additional costs of the investigated refrigeration systems.

4 Cryogenic mixed refrigerant cooled current leads

Based on the investigations of designs and cooling systems for resistive current leads working at a temperature of 78 K that are presented in Sec. 2 and Sec. 3, the forced-flow vapour cooled current lead design has yet no practical solution. Despite the fact that this design leads to the lowest thermal load at the cold end, compared to the investigated designs in Tab. 14, it yields in combination with a closed nitrogen liquefier system to relatively large specific power consumptions. The main reason for this is that the refrigeration systems that are used for the liquefaction of nitrogen are mainly cold head systems, i.e. providing cooling power at a fixed temperature, yielding a large entropy production in the system according to (3.27). Furthermore, it is more convenient to use LN_2 and a bath heater instead (c.f. Sec. 3.2). In order to overcome this disadvantages of ff-VCCLs, another refrigeration concept is introduced, i.e. the cryogenic mixed refrigerant cooled current lead (CMRC-CL). The key in this technology is the direct implementation of the resistive current lead into the recuperative heat exchanger of the Linde-Hampson cycle, providing refrigeration power over the temperature range of the heat exchanger. Hereby, a mixed refrigerant is partly condensing and evaporating inside the heat exchanger and absorbing the Joule heat at the temperature it is generated in the current lead. This chapter introduces the state of the art of CMRC technology and its implementation to resistive current leads, followed by the conceptual classical design that is investigated in Sec. 4.2. In order to enable a reliable prediction of the current lead performance, a numerical calculation model is developed and described in Sec. 4.3, which includes the heat exchanger model and heat transfer correlations investigated by Gomse [5]. The numerical results of the investigated refrigerant mixtures in combination with a 10 kA current lead are presented in Sec. 4.4. Finally, conclusions are made for further CMRC-CL technology developments.

4.1 State of the art of CMRC technology

At the time of this publication, there are only a view commercially available cryocoolers that are working with the CMRC technology. The company MMR Technology Inc. provides liquid nitrogen generators with a liquefaction rate of approximately 8 L/d, which corresponds to about 15 W at 77 K. The required input power of this machines is about 950 W, which yields according to (2.20) a Carnot efficiency of 4.6 %. Another CMRC based cold head system is the Polycold® PCC cooler [102], provided by the company Edwards. It has a cooling power of 8 W at 78 K at an input power of 960 W and therefore a Carnot efficiency of 2.3 %. However, this refrigeration systems are not suitable for the cooling of high amperage resistive conduction cooled current leads, due to their low cooling power at 78 K.

Goloubev [28] suggested the combination of a Linde-Hampson CMRC refrigeration cycle and a closed nitrogen compression circuit for the cooling of forced-flow vapour cooled

current leads ff-VCCL. In the experimental investigations, the compressed nitrogen gas (12 bar) is cooled by a CMRC refrigeration machine to a temperature of about 100 K and then throttled in a valve to a pressure of 1.13 bar, yielding liquefaction of nitrogen at a temperature of about 78 K, due to the Joule-Thomson cooling effect. The LN_2 with a liquid fraction of about $y = 68$ % is then accumulated in a collector, where a heater is used to simulate the thermal load of a resistive current lead. No experiments with a real current lead were performed in this study. Afterwards, the nitrogen gas is heated up to room temperate and then compressed and circulated by a compressor in a closed circuit. Overall, three 3-way recuperative heat exchangers are used in the CRMC cycle, and an additional 3-way heat exchanger for the precooling of the mixed refrigerant and the nitrogen gas to a temperature of about 244 K with an R507 refrigeration machine. For the CMRC circuit, a hydrocarbon mixture of nitrogen, methane, ethylene and propane is used with the molar concentrations of 32.8 %, 33.6 %, 10.4 % and 23.2 % respectively. The mixture showed a solidification at a temperature range of 80 K to 85 K. This refrigeration system liquefies nitrogen at a rate of $\dot{m} = 0.291$ g/s and has an overall power consumption of 2287 W, including the CMRC, nitrogen compressor and the R507 compression cycle. Goloubev performed theoretical investigation regarding the cooling of forced-flow VCCL with a liquid fraction of $y = 68\%$, yielding a liquid mass flow of $\dot{m} = 0.166\,\mathrm{g/(s\,kA)}$. Unfortunately, the corresponding shape factor of the optimum VCCL is not mentioned in [28]. However, Goloubev used the Carnot power optimization (c.f. Sec. 2.2) and assumes an adiabatic boundary condition at the warm end, yielding relative large shape factors. The nitrogen mass flow in the experiment would therefore yield an electric current of about 1.75 kA and a specific power consumption of 1307 W/kA. This corresponds to a 40 % larger specific refrigeration power consumption compared to the design with the largest $P_{\mathrm{total,el}}/I$ value presented in Tab. 14.

Nellis et al. [103] suggested to combine the recuperative heat exchanger of a Linde-Hampson CMRC with a resistive current lead directly, without an intermediate nitrogen compression cycle. In [103] a numerical calculation model of the recuperative heat exchanger performance is presented, which is based on the effectivness-NTU method presented in [104]. Generally, the effectivness-NTU relations that are reported in many books, e.g [58], are inadequate for mixed refrigerants, where fluid properties vary along the heat exchanger length. However, using small elements of the heat exchanger in the numerical calculation, this method can also be applied to CMRCs. Further, no explicit information about the heat exchanger design and heat transfer kinetics are given. In [103], a genetic optimization algorithm (PIKAIA 1.2) for the identification of the optimum composition of the investigated refrigerant mixtures is used. In Tab. 16, three mixtures are presented that are optimized in [103] for the temperatures of 100 K, 90 K and 80 K and providing specific refrigeration power of 69 kJ/kg, 67 kJ/kg, 54 kJ/kg, respectively. However, these

Table 16: Molar compositions of refrigeration mixtures that are investigated by Nellis et.al. in [103]

Refrigerant mixtures	Nitrogen	Methane	Ethane	Propane	Isobutane	Isopentane	Argon
	mole - %						
Nellis 100 K	15.3	35.4	15.5	5.6	5.7	7.0	15.6
Nellis 90 K	28.6	29.4	20.8	2.5	7.0	6.5	5.4
Nellis 80 K	45.1	23.6	16.5	5.4	2.2	7.1	0

mixtures are optimized for the case where the distributed thermal load along the heat exchanger is equal to the thermal load at the cold end in the evaporator. This system corresponds to a combination of a Linde-Hampson gascooler and a refrigerator, which are depicted in Fig. 21. In a subsequent experimental investigation presented in [105], a CMRC with a Hampson type recuperative heat exchanger and a heating wire, with a heating power up to 1.5 W, is used to simulate the effect of the distributed thermal load along the heat exchanger. However, the experiments showed a flow management problem, due to the insufficient inertia of the low flow rates to entrain the liquid that forms on both sides of the orifice [105]. Therefore, the coldest temperature that was recorded in this experiment was 110 K in closed cycle operation.

4.2 Conceptual design with classical heat exchanger

The conceptual cryostat system for the investigation of resistive CMRC cooled current leads is presented in Fig. 27. Inside the cryostat / vacuum chamber, two resistive current leads made of copper are connected via flexible copper braids. In the middle of this copper connection, a Cryomech AL600 cryocooler (c.f. Tab. 11) is attached via additional copper braids in combination with an electric insulation made of sapphire. The cryocooler has a cooling power of 600 W at 80 K and its cold head is attached to a 600 W heater. The cryogenic valves at the lower part of the system are used as throttling devices of the Linde-Hampson cycle for the circulating mixed refrigerant. The conceptual drawing of the CMRC cooled current lead is shown in Fig. 28. The resistive current lead (without the copper bands) is about 670 mm long and has an outer diameter of 80 mm. The core diameter of the current lead, which represents the effective cross section area for the flow of electrical current, is about 56 mm. The counterflow heat exchanger (hx) of the Linde-Hampson cylce is wounded around the current lead core. This current lead concept is designated as the classical design concept, mainly due to the implementation of a classical multi-tubes-in-tube heat exchanger, whose geometries are presented in Tab. 17 and in the lower part of Fig. 28. It consists of seven stainless steel capillaries inside an outer copper tube, with a total length of 5.9 m, wound with an axial height of about 580 mm along the current lead. To prevent the bunching of the capillaries inside the heat exchanger, a centring ring in regular intervals can be placed. Alternatively, a so-called wire finned

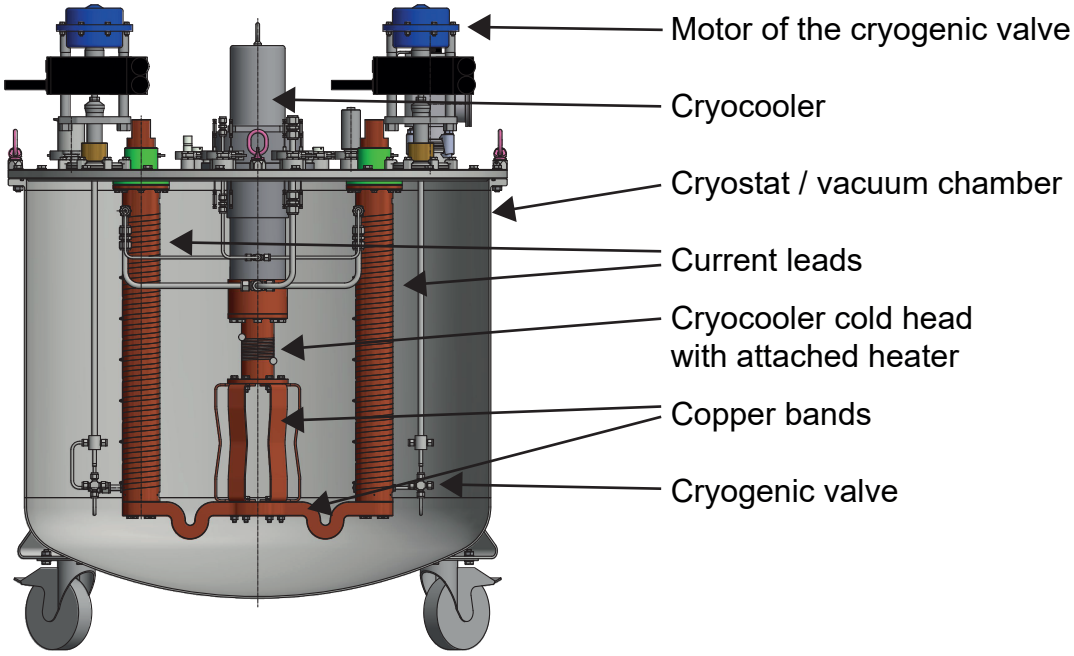

Figure 27: Cryostat system for the investigation of resistive CMRC cooled current leads.

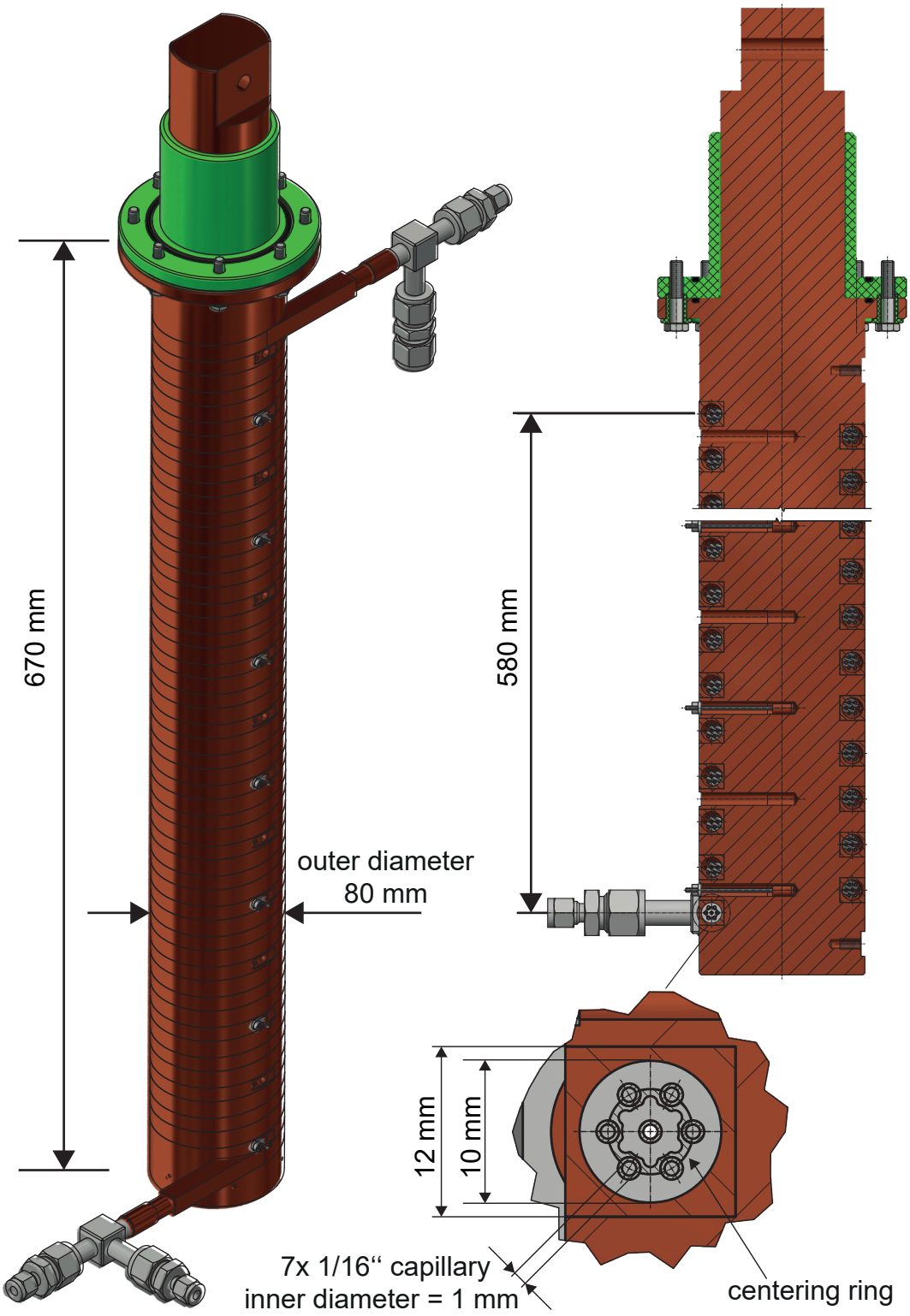

Figure 28: Conceptual drawings of the classical design current lead.

tubes-in-tube heat exchanger [106, 107] can be used, in which a silvered copper wire is wound around all capillaries. The latter method increases the turbulence and thereby the heat transfer on the shell side and the wires act like fins [107]. However, the wire

fins reduce the hydraulic diameter of the shell which increases the pressure drop of the stream in the shell. In this study, a wire finned tubes-in-tube heat exchanger, with a wire diameter of $d_\mathrm{f} = 0.8\,\mathrm{mm}$ and a pitch of $p_\mathrm{f} = 10\,\mathrm{mm}$, is used. Inside the capillaries, the high pressure stream of the mixed refrigerant is flowing until it is throttled in the respective cryogenic valve. After the throttling, the low pressure stream enters the heat exchanger and is flowing in the area around the capillaries through the heat exchanger.

The length of the heat exchanger L_hx that is given in Tab. 17 is calculated with the following expression

$$L_\mathrm{hx} = n_\mathrm{w} \cdot \pi \cdot \sqrt{d_\mathrm{coil}^2 + \left(\frac{h_\mathrm{coil}}{\pi}\right)^2} \tag{4.1}$$

with

$$n_\mathrm{w} = \frac{L_1 - D_\mathrm{hx,o}}{h_\mathrm{coil}} \tag{4.2}$$

$$d_\mathrm{coil} = d_1 + D_\mathrm{hx,i} = \sqrt{\frac{I \cdot L_1 \cdot 4}{\pi \cdot \left(I \cdot L/A\right)_1}} + D_\mathrm{hx,i} \tag{4.3}$$

where n_w is the number of windings, d_coil is the mean coil diameter, h_coil is the coil pitch and the inner $D_\mathrm{hx,i}$ and the outer $D_\mathrm{hx,o}$ diameters of the copper tube, where the LP stream is flowing. The diameter d_1, the length L_1 and the shape factor $\left(I \cdot L/A\right)_1$ refer to the CMRC part of the current lead and are presented in Tab. 18. The heat transfer areas

Table 17: Geometry of the helical multi tubes-in-tube heat exchanger.

	HP	LP
Inner diameter $\left(d_\mathrm{hx,i}\ ,\ D_\mathrm{hx,i}\right)$	1.09 mm	10 mm
Outer diameter $\left(d_\mathrm{hx,o}\ ,\ D_\mathrm{hx,o}\right)$	1.59 mm	12 mm
Number of tubes $\left(n_\mathrm{tube,HP}\ ,\ n_\mathrm{tube,\ LP}\right)$	7	1
Heated circumference (HP-LP)	23.97 mm	34.97 mm
Length (L_hx)	5.9 m	
Heat transfer area - streams ($A_\mathrm{HP}\ ,\ A_\mathrm{LP}$)	0.1414 m^2	0.2063 m^2
Heat transfer area - CL ($A_\mathrm{CL\text{-}LP}$)	0.139 m^2	
Hydraulic diameter	1.09 mm	2.91 mm
Number of windings (n_w)	28	
Mean coil diameter (d_coil)	66 mm	
Coil pitch (h_coil)	20 mm	
Outer CMRC-CL diameter D_1	80 mm	

Table 18: Geometry of the CMRC cooled current lead.

Current lead parts	d_j (mm)	L_j (mm)	A_j (mm^2)	$\left(I \cdot L/A\right)_j$ ($\mathrm{kA/m}$)
CMRC ($j = 1$)	56	580	2463	2355
Copper connection ($j = 2$)	-	400	3000	1333

between the HP stream and the LP stream that are given in Tab. 17 and are defined as

$$A_{\mathrm{HP}} = \pi \cdot d_{\mathrm{hx,i}} \cdot n_{\mathrm{tube,HP}} \cdot L_{\mathrm{hx}} \tag{4.4}$$

$$A_{\mathrm{LP}} = \pi \cdot d_{\mathrm{hx,0}} \cdot n_{\mathrm{tube,HP}} \cdot L_{\mathrm{hx}} \tag{4.5}$$

with $d_{\mathrm{hx,i}}$ is the inner and $d_{\mathrm{hx,0}}$ is the outer diameter of the HP capillary and $n_{\mathrm{tube,HP}}$ the number of capillaries/tubes of the HP stream.

A 10 kA conduction cooled current lead that is operated between 300 K and 78 K will result in a thermal load at the cold end of about $\dot{Q}_{\mathrm{c}} = 425\,\mathrm{W}$. Early results of this study showed that it is possible to reduce the thermal load with a CMRC cooled current lead by more than 30 % [108] compared to a CCCL. However, with a CMRC that has a refrigeration temperature above 120 K. Therefore, an additional cryocooler with a refrigeration power of about 600 W at 78 K is necessary to absorb the remaining thermal load of a 10 kA current lead pair at the cold end. Its refrigeration power and therefore, the cold end temperature can be regulated with a heater. The additional cryocooler is preliminary installed to gain experimental flexibility in the CMRC-CL system development and is therefore used as a intermediate solution, i.e. it is realistic to develop CMRC-CLs that do not need the cryocooler. However, to compare the state-of-the-art CL solutions at a temperature of about 78 K with the developed 10 kA CMRC-CL in this work, a cryocooler is used as the additional refrigeration stage at the cold end of the CMRC.

The geometries of the upper CMRC part and the lower copper connection part of the current lead are chosen such that the thermal load at the cold end, without the circulating refrigerant mixture $\left(\dot{m} = 0\,\mathrm{g/s}\right)$, is equal to the value of a conventional CCCL. This will ensure the investigation of the CMRC current lead and the circulating refrigerant mixture in the experiments, assuming a minimal reduction of the thermal load at the cold end to about 30 W/kA [108]. The corresponding temperature profile is presented in Fig. 29. At the end of the CMRC part, the electric current flows through the copper connection into the second current lead. The relevant geometry parameters are summarised in Tab. 18.

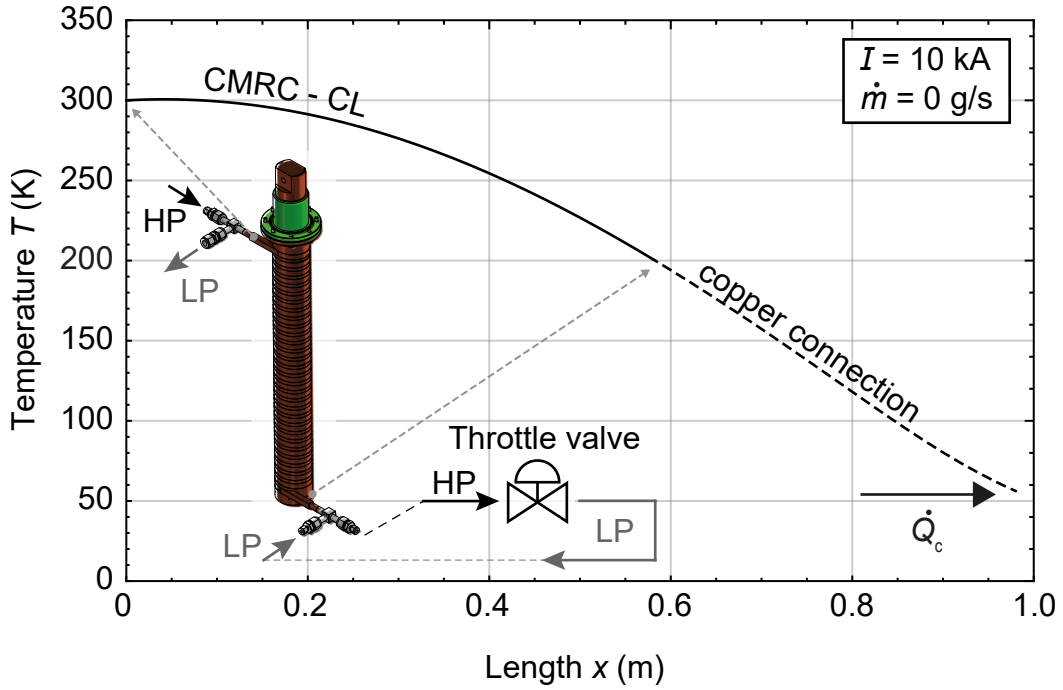

Figure 29: Temperature profile of the CMRC cooled current lead at zero mass flow.

The schematic representation of the refrigeration cycle is illustrated in the piping and instrumentation diagram (P&ID) in Fig. 30. The low pressure stream of the refrigerant mixture is initially compressed in the compressor (K 220). The resulting compression heat is rejected in the aftercooler (NK 210) at ambient temperature. Afterwards, the compressed and recooled gas flows through an oil separator, two coalescers with different filters and an activated charcoal trap. These components are part of the oil removal system that are placed in the HP stream and are needed to remove the entrained oil in the gas via the connections to the suction line of the compressor. The following buffer tank (PF 200), is used to regulate the amount of refrigerant charge in the cycle, which can be adjusted with the respective valves. Moreover, the connections around the buffer tank are used to separate the cold and hot parts of the CMRC cycle. This procedure is necessary in the initial start-up of the cycle, due to the high oil carry over of the compressor. After the spliting of the HP stream, the flow meters (F201 and F203) are used to measure the refrigerant mass flows. The inlet pressures of the resistive current leads are adjusted by the respective electronic expansion valves. The current lead connections at the top flange of the vacuum chamber are actively cooled with water to remove the heat load due to the Joule heating of the connecting cables at room temperature and to ensure a stable temperature.

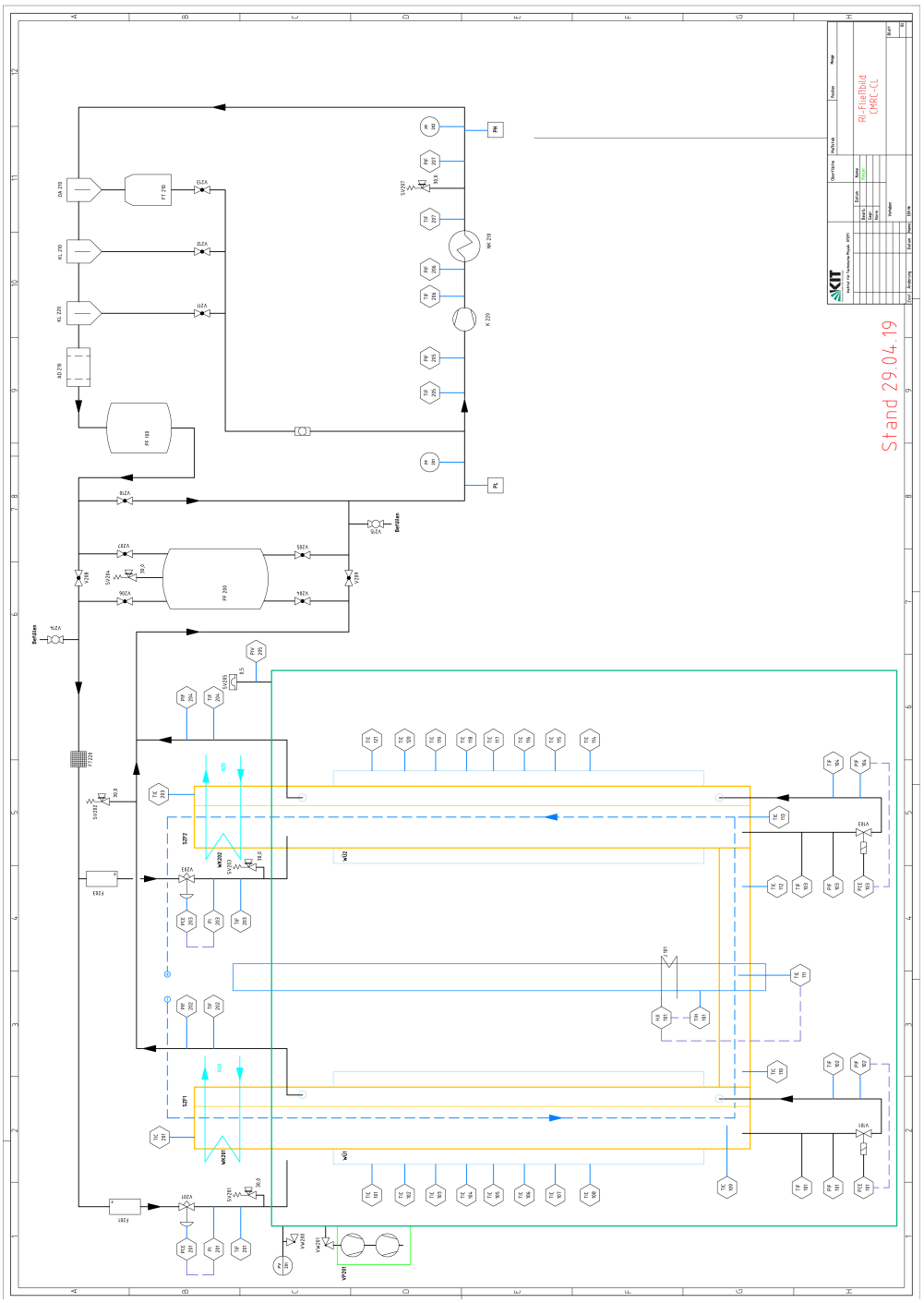

Figure 30: Piping and instrumentation diagram (P&ID) of the conceptual CMRC cooled current lead test stand.

4.3 Modelling framework

The calculation method for CMRC cooled current leads is implemented in the modelling framework developed by Gomse [5]. It comprises a numerical heat exchanger model that takes the two-phase heat transfer and pressure drop of the LP and the HP streams into account. Furthermore, parasitic heat loads, like the thermal radiation and the ohmic heating of a current lead, and fluid property variations of mixed refrigerants can be implemented into the algorithm. This model follows the concept of using the wall temperature of the capillaries inside the heat exchanger as the iterative variable. Hereby, the individual fluid streams are only coupled with the wall temperature and not with each other. This coupling method reduced the computational effort in the calculation of the complex boiling and condensation kinetics in the individual fluid streams. In the following, the general concept of the implementation of resistive current leads into the heat exchanger model is introduced. Further, necessary modifications of the algorithm are discussed.

The coordinate systems for the numerical investigation of the CMRC-CL are shown in Fig. 31. The coordinate of the current lead starts at the height of the counter flow heat exchanger at $x = 0$, with the assumption of an uniform temperature of 300 K above this level, due to the water cooling system. The coordinate x ends at the total length of the current lead at $L_{\mathrm{CL}} = 0.98\,\mathrm{m}$ (c.f. Tab. 18). The heat exchanger coordinate z starts at the fluid entrance into the current lead and follows the helically wound channels until the

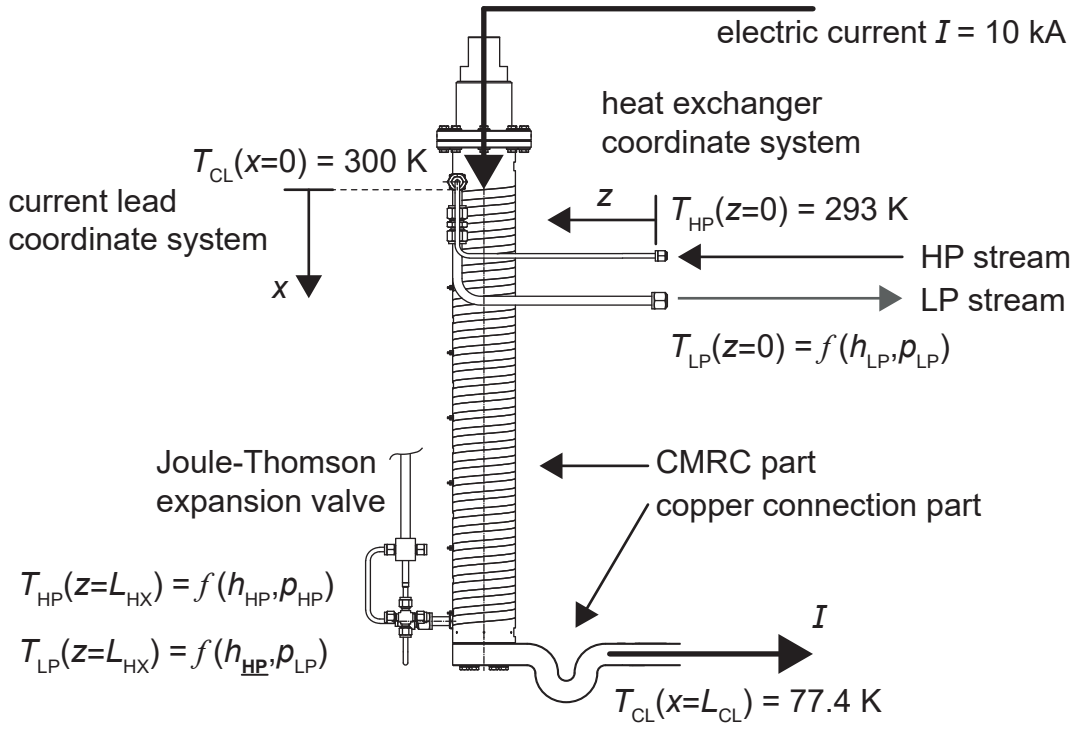

Figure 31: Coordinate systems and temperature boundary conditions of the modelling framework of the CMRC-CL.

connection to the Joule-Thomson valve at $L_{\mathrm{hx}} = 5.9\,\mathrm{m}$. For the correct implementation of the heat transfer area into the numerical model, a conversion of the coordinates is necessary and is given by

$$z = \left(\frac{L_{\mathrm{hx}}}{L_{\mathrm{CL}}}\right) \cdot x \tag{4.6}$$

The calculation of the temperature profile of the CMRC current lead $T_{\mathrm{CL}}(x)$ is performed based on a system of two one-dimensional differential equations of second order. The temperature profile of the upper CMRC part, with the index ($j = 1$), is given by

$$\underbrace{\lambda_1(T_{\mathrm{m}}) \cdot \frac{\partial}{\partial x}\left(A_1 \cdot \frac{\partial T_1}{\partial x}\right)}_{\text{Heat conduction}} + \underbrace{I^2 \cdot \frac{\rho_1(T_1)}{A_1}}_{\text{Joule heating}} - \underbrace{\alpha_{\mathrm{LP}}(T_{\mathrm{LP}}) \cdot U_1 \cdot (T_1 - T_{\mathrm{LP}})}_{\text{Convection cooling}} = 0 \tag{4.7}$$

where λ_1 is the thermal conductivity at a fixed mean temperature of $T_{\mathrm{m}} = (300 + 120)/2\,\mathrm{K}$, I the amperage, ρ_1 the specific electrical resistance, A_1 the cross-section area, U_1 the heated circumference and α_{LP} the heat transfer coefficient between the current lead and the low pressure stream inside the shell of the heat exchanger.

The temperature profile of the copper connection part ($j = 2$) is described with

$$\frac{\partial}{\partial x}\left(\lambda_2(T) \cdot A_2 \cdot \frac{\partial T_2}{\partial x}\right) + I^2 \cdot \frac{\rho_2(T_2)}{A_2} = 0 \tag{4.8}$$

This differential equation system is a boundary value problem (BVP) and requires four different boundary conditions. The first condition is the fixed temperature at the warm end of the CMRC part

$$T_1(x = 0) = 300\,\mathrm{K} \tag{4.9}$$

The boundary conditions for the conservation of energy and the temperature at the joint between the two current lead parts at $L_1 = 0.58\,\mathrm{m}$, yielding

$$T_1(x = L_1) \overset{!}{=} T_2(x = L_1) \tag{4.10}$$

$$\lambda_1(T_{\mathrm{m}}) \cdot A_1 \cdot T_1'(x)\Big|_{x=L_1} \overset{!}{=} \lambda_2\big(T_2(x)\big) \cdot A_2 \cdot T_2'(x)\Big|_{x=L_1} \tag{4.11}$$

and the boundary condition for the temperature at the cold end of the current lead at

$L_{\mathrm{CL}} = 0.98\,\mathrm{m}$, defined as

$$T_1\left(x = L_{\mathrm{CL}}\right) = 77.4\,\mathrm{K} \tag{4.12}$$

The thermal conductivity λ_1 in (4.7) is placed outside the derivation with respect to x in the heat conduction term, because this temperature dependent property caused numerical problems in the evaluation of the differential equation system. It was found that this problem occurs only in the combination with the complex function of the heat transfer coefficient $\alpha_{\mathrm{LP}}\left(T_{\mathrm{LP}}\right)$, which links the single-phase and two-phase heat transfer functions of the low pressure fluid. The implementation of a regularisation by means of the Gauss error function for vapour qualities between 0 to 0.02 and 0.98 to 1 by Gomse [5], to archive a smooth transition between the correlations, did not resolved this problem. However, Gomse [5] resolved with the error function numerical oscillations in the location of the phase transition and used it in the energy balance equation and the conservation of momentum. Nevertheless, according to Fig. 16a the thermal conductivity of copper in the temperature range of 300 K to 120 K remains nearly constant, yielding therefore a conservative simplification in (4.7). The thermal conductivity of the lower copper connection part, however, is a function of the respective temperature and the typical increase of the property with decreasing temperature is implemented. The numerical solutions of the temperature profiles in (4.7) and (4.8) are transformed into a single function for the current lead temperature, yielding

$$T_{\mathrm{CL}}\left(x\right) = \begin{cases} T_1\left(x\right) & \text{for} \quad 0 < x \leq L_1 \\ \\ T_2\left(x\right) & \text{for} \quad L_1 < x \leq L_{\mathrm{CL}} \end{cases} \tag{4.13}$$

The heat exchanger model presented in [5] follows the approach of the stream evolution method, which is based on solving the steady-state mass, momentum and energy balances for the HP and LP streams. The following main assumptions are used in this model:

1. one-dimensional and steady fluid flow,
2. thermodynamic equilibrium between vapour and liquid,
3. separated flow and
4. negligible axial heat conduction in the fluids.

The conservations of mass for the LP and HP streams are defined in such a way that the total mass flow $\dot{m}$ does not change in the axial direction z. The one dimensional energy balance for the LP stream in combination with a resistive current lead yields

$$\frac{\partial h_{\mathrm{LP}}}{\partial z} = \underbrace{\frac{1}{\dot{m}} \cdot k_{\mathrm{LP}} \cdot U_{\mathrm{LP}} \cdot (T_{\mathrm{W}} - T_{\mathrm{LP}})}_{\text{heat transfer W } \rightarrow \text{ LP}} + \underbrace{\alpha_{\mathrm{LP}} \cdot U_1^{\star} \cdot (T_{\mathrm{CL}} - T_{\mathrm{LP}})}_{\text{heat transfer CL } \rightarrow \text{ LP}}$$

$$- \underbrace{\frac{1}{2} \cdot \dot{m''}^2 \frac{\partial}{\partial z} \left[\frac{x_{\mathrm{LP}}^3}{\varepsilon_{\mathrm{LP}}^2 \cdot \rho_{\mathrm{LP,v}}^2} + \frac{(1 - x_{\mathrm{LP}})^3}{(1 - \varepsilon_{\mathrm{LP}})^2 \cdot \rho_{\mathrm{LP,l}}^2} \right]}_{\text{kinetic}} - \underbrace{g \cdot \sin(\theta)}_{\text{potential}} \tag{4.14}$$

$$+ q'$$

with the specific enthalpy of the LP fluid h_{LP}, the overall heat transfer coefficient k_{LP} between the wall T_{W} and the LP stream, the heated circumference U_{LP} of the LP stream, the modified heated circumference of the current lead $U_1^{\star}$, the vapour quality x_{LP}, the void fraction $\varepsilon_{\mathrm{LP}}$, the vapour $\rho_{\mathrm{LP,v}}$ and liquid $\rho_{\mathrm{LP,l}}$ densities, the gravitational constant g, the flow angle θ and the specific thermal energy per unit length q' for a possible heat of reaction in the fluid. However, q' is zero in the investigation of the CMRC-CL. The thermodynamic properties are implemented as a function of the enthalpy and pressure $f(h, p)$. The modification of the heated circumference $U_1^{\star}$ is based on the conversion of the coordinate systems according to (4.6) and ensures the correct implementation of the heat transfer area $A_{\text{CL-LP}}$, between the LP stream and the CL, which is defined as

$$A_{\text{CL-LP}} = U_1^{\star} \cdot L_{\mathrm{hx}} = U_1 \cdot L_{\mathrm{CL}} = 0.139\,\mathrm{m}^2 \tag{4.15}$$

$$U_1^{\star} = 75\% \cdot \pi \cdot D_{\mathrm{i}} \tag{4.16}$$

conservatively assuming that 75 % of the circumference of the LP stream is actively used in the heat transfer. The energy balance for the HP stream is derived analogous to (4.14), however, without the heat load due to the current lead. Further, the conservation of momentum is needed to predict the pressure drop of the streams $j = \mathrm{LP,HP}$ and yields

$$\frac{\partial p_j}{\partial z} = \underbrace{\left(\frac{p_j}{z} \right)_{\mathrm{f}}}_{\text{friction}} \underbrace{- \dot{m''}^2 \frac{\partial}{\partial z} \left[\frac{x_j^3}{\varepsilon_j^2 \cdot \rho_{j,\mathrm{v}}^2} + \frac{\left(1 - x_j\right)^3}{\left(1 - \varepsilon_j\right)^2 \cdot \rho_{j,\mathrm{l}}^2} \right]}_{\text{accelaration}} \tag{4.17}$$

$$- \underbrace{\left[\varepsilon_j \cdot \rho_{j,\mathrm{v}} + \left(1 - \varepsilon_j\right) \cdot \rho_{j,\mathrm{l}} \right] \cdot g \cdot \sin(\theta)}_{\text{hydrostatic}}$$

with the three contributions to the pressure drop: the friction losses, the acceleration losses and the hydrostatic losses. The boundary conditions that are needed to solve the equations (4.14) and (4.17) for the LP and HP streams are the constant inlet temperature and pressures with

$$T_{\mathrm{HP}} = 293\,\mathrm{K} \tag{4.18}$$

$$p_{\mathrm{HP}} = p_3 \tag{4.19}$$

$$p_{\mathrm{LP}} = p_6 \tag{4.20}$$

whereby the pressures p_3 and p_6, according to the schematic representation of the Linde-Hampson gascooler in Fig. 21, are variables, whose influence is investigated in the parametric study of this work. The temperature of the LP stream after the Joule-Thomson expansion valve at the heat exchanger inlet is controlled by the algorithm, according to the isenthalpic change of state in the throttling device.

The wall temperature in [5] is calculated with the so-called cell method, using a control volume and the energy balance of the conductive and convective energy flows (including the thermal radiation) in the heat exchanger wall segment (here the capillaries) between the HP and the LP stream. The cold and hot ends of the wall are considered as open ends as defined in [5]. This method shows similarities to a standard Finite-Difference-Method (FDM) with a control volume approach, which may be implemented inside a Gauss-Seidel iteration [60]. However, the wall temperature in the heat exchanger algorithm of [5] is not calculated in an internal iteration loop until a certain convergence is reached, therefore, an additional while loop with a temperature convergence criterion of 10^{-5} is implemented in this code.

Heat transfer, pressure drop and void fraction correlations used in the computation of the classical multi tubes-in-tube heat exchanger are listed in Tab. 19. Further information on the kinetics and the multi tubes-in-tube heat exchanger may be found in [5], especially in the appendix A.2.

The numerical investigation of the CMRC current lead in this work is focused on hydrocarbon based mixtures (HCM) and not on synthetic refrigerant mixtures (SRM). Gomse [5] investigated different heat transfer and pressure drop correlations in multi tubes-in-tube heat exchanger and found that the predictions of the kinetics, compared to HCM mixtures, are considerably worse in the case of the SRMs. The average relative deviations (ARD) of the pressure drop of the SRMs, showed over-predictions (ARD>0) ranging from

Table 19: Correlations used in the numerical calculation of the multi tubes-in-tube heat exchanger according to [5]. The correlations are valid for hydrocarbon-based mixtures.

Mechanism	Correlation
Single phase heat transfer	
HP stream $f\,(Re)$	VDI Heat Atlas - G3 [109]
LP stream $f\,(Re)$	Kruthiventi [107]
Two-phase heat transfer	
Pure boiling	Liu and Winterton [110]
Nucleat boiling correction factor F_c	Thome and Shakir [111]
Mixture boiling (modified SBG)	Sardesai [112]
Pure condensation	Cavallini [113]
Mixture condensation (SBG)	Cavallini [113]
Frictional pressure drop	
Single phase flow $f\,(Re)$	VDI Heat Atlas - L1 (1.4) [109]
Two-phase flow $f\,(Re)$	Lockhart and Martinelli [114]
Void fraction	
Separated flow	Chrisholm [115]

SBG - Silver-Bell-Ghally
Re - Reynolds number

-26 % to -60 %. This over-prediction of the pressure drop may lead to an exclusion of relevant SR mixtures in the investigation of the CMRC-CL. The pressure drop ARDs of HCMs, however, were under-predicted (ARD<0) in all relevant investigated correlation with a deviation of about 4.3 %, when using the Lockhart-Martinelli [114] correlation. Nevertheless, for most of the heat transfer correlations investigated in [5] for HCMs and SRMs, the average absolute deviations of the measured temperatures along the heat exchanger were found to be below 5 %.

The thermodynamic properties of hydrocarbon based mixtures (HCM) can be predicted with the GERG-2008 equation of state [116] (GERG-EoS), where mixing rules are implemented in the reference of thermodynamic and transport properties [56] (REFPROP). However, according to the investigations made by Gomse [5], GERG-2008 shows unreliable rendering of the phase envelope for the mixture compositions used in this work. Therefore, the use of the cubic Peng-Robinson equation of state [97] (PR-EoS) is suggested by [5], which is a simple and robust EoS and is used in this work for HCMs.

The flowchart of the numerical solution algorithm of a CMRC-CL is depicted in Fig. 32, which is based on [5]. The main solution strategy can be divided into three steps: initialization, main loop and the verification of the results. The input parameters are the geometries of the heat exchanger and the current lead as well as the operating conditions

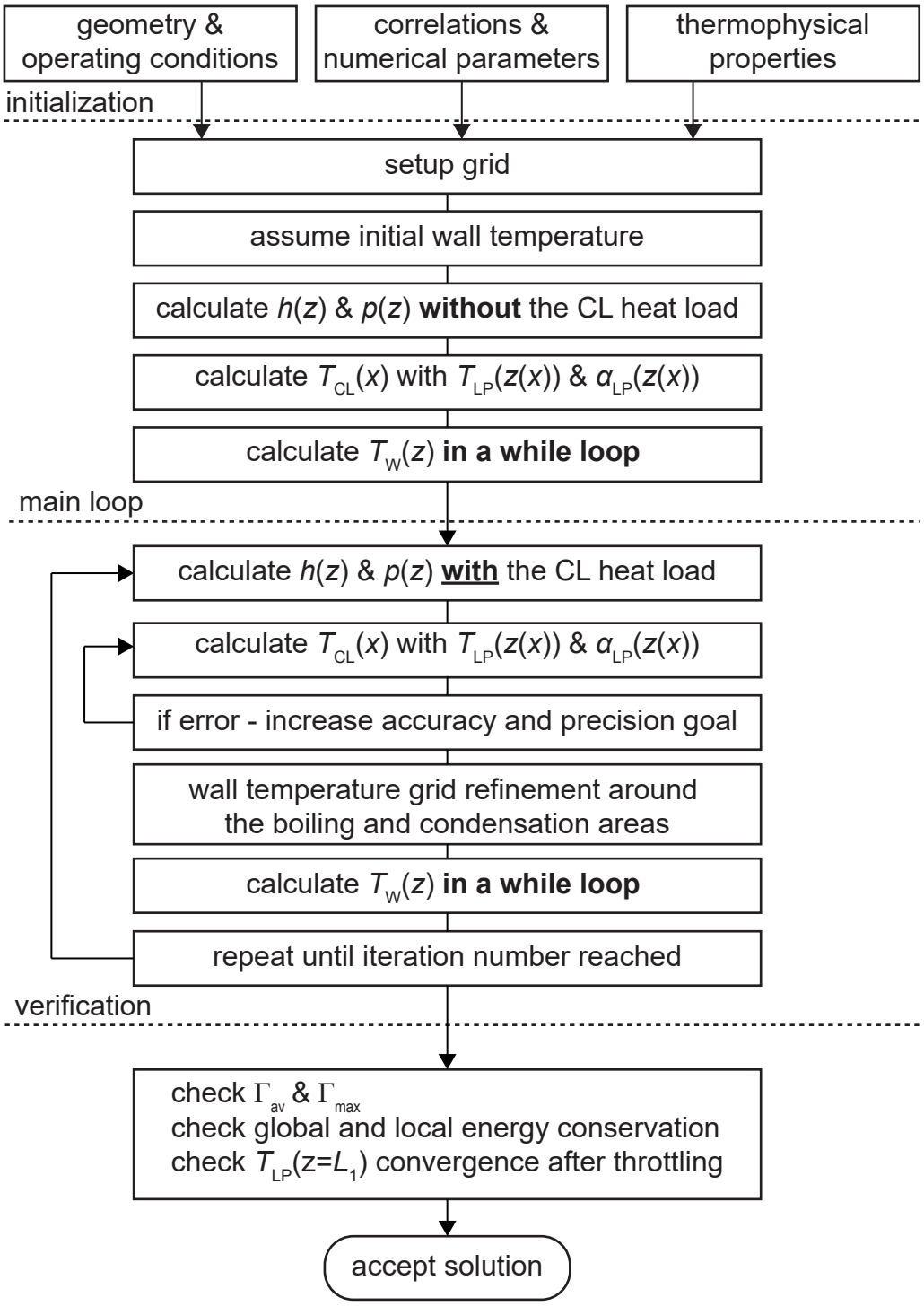

Figure 32: Flowchart of the numerical solution algorithm

like temperatures, pressures, mass flow of the refrigerant and the amperage. The thermophysical properties of the refrigerant mixture and of the solid materials are implemented as interpolated functions into the algorithm. In the initialization process, the differential equations of the heat exchanger and the current lead are not linked, however, the initial temperature profile of the LP stream that is calculated without the current lead heat

load, is used to generate the initial temperature profile of the CMRC-CL. Compared to the algorithm that is described in [5], the heat exchanger wall temperature T_W calculation is performed in an internal while loop. In the main loop, the heat load due to the current lead is introduced into the energy balance equation (4.14) of the LP stream, generating hereby a link to the differential equation (4.7) of the CMRC part of the CL.

This solution method does not solve the differential equations of the hx and of the CL simultaneously, rather it is a consecutive calculation method that requires a common convergence of the global energy conservation that can be reached after a certain amount of iteration loops. This energy criterion is accompanied by the wall temperature convergence, which is described by the normalized average residuum Γ_{av} and the normalized maximum residuum Γ_{max} according to the equations (4.25) and (4.26) presented in [5]. The convergence of the current lead temperature is controlled by the accuracy and precision goals of the numerical explicit midpoint method that is implemented in Mathematica [117]. Furthermore, it was found that the temperature $T_{LP}(z = L_{HX}$, T_6 according to the Linde-Hampson gascooler in Fig. 21a) of the LP stream after the expansion valve can be used as the general convergence criterion of this numerical system. When this temperature has converged, the minimum values for residuals and errors in the energy conservation can be found. Example convergence plots are presented in Fig. 33 for a LRS mixture 11 that is investigated in Sec. 4.4. The normalized average Γ_{av} and maximum residuals Γ_{max} of the wall temperature T_W inside the heat exchanger together with the fluid temperature T_6 after the expansion device are presented as a function of the iteration number in the main loop in Fig. 33a and Fig. 33b, respectively. Threshold values of 10^{-4} for the residuals were found to be good indicators for the convergence. Smaller residuals may be found by increasing the iteration number, however, the maximum iteration number was mainly limited by the internal memory of the computer. The progress towards convergence of the temperature after the expansion valve T_6 and of the joint temperature according to (4.10) as the function of the iteration number is depicted in Fig. 33c. The fluid temperature T_6 converges at about 125 K. It is interesting to denote that the residuals have a high dispersion near the overall convergence of the numerical model. This may result from the implemented expansion valve in the model, that defines the boundary condition for the LP temperature T_6 at the inlet of the heat exchanger/current lead and is calculated with the fluid property data. Consequently, this dispersion may be caused by the lower accuracy of the property data at low temperatures. Depending on the investigated mixture and boundary conditions, iteration numbers between 400 and 1000 could be evaluated. Therefore, in addition to the numerical convergence parameters, the overall energy conservation error is calculated and indicated in each investigation.

The energy conservation of the numerical CMRC-CL model is evaluated with respect to the system boundary around the cryogenic mixed refrigerant cycle and the current lead,

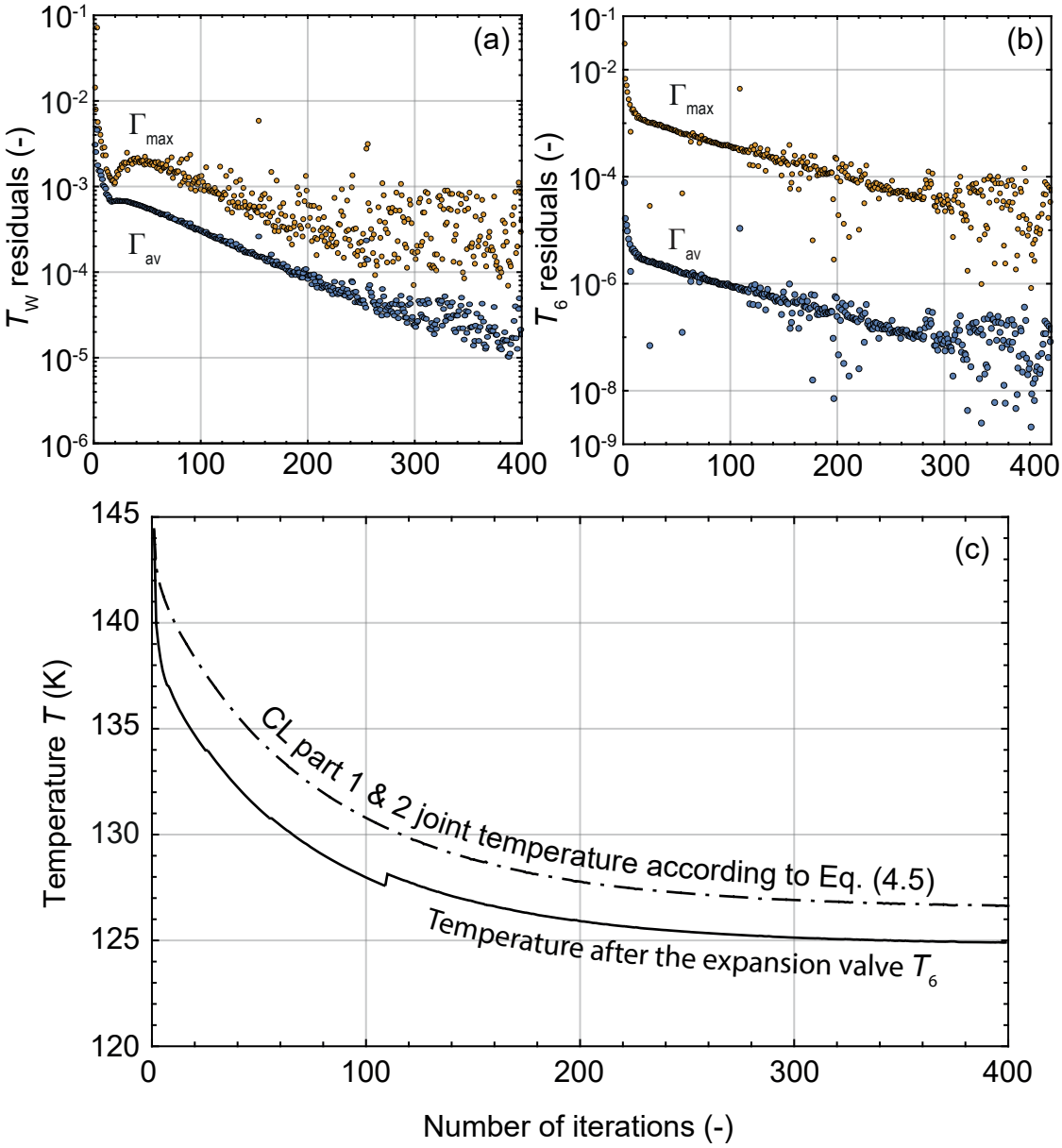

Figure 33: Convergence parameters of the numerical model for the LRS mixture 11 ($T_7 = T_3 = 293.15\,\mathrm{K}, p_7 = 3\,\mathrm{bar}, p_3 = 30\,\mathrm{bar}$, $I = 10\,\mathrm{kA}$). The wall temperature residuals in (a), the fluid temperature residuals after the expansion valve in (b) and the temperatures T_6 and the joint temperature according to (4.10) as the function of the iteration number in (c). The molar compositions of the LRS mixtures 11 are presented in Tab. 20. The numerical error of the energy conservation is 1.18 %.

which is presented in Fig. 34. On the left-hand side of Fig. 34, a Linde-Hampson gascooler is depicted and on the right-hand side the investigated current lead with an upper CMRC cooled part and a lower conduction cooled part. The corresponding energy conservation equation is defined as

$$P_{\mathrm{comp}} - \dot{Q}_{\mathrm{a}} - \dot{Q}_{\mathrm{h}} + P_{\mathrm{el},1} + P_{\mathrm{el},2} - \dot{Q}_{\mathrm{c}} \stackrel{!}{=} 0 \tag{4.21}$$

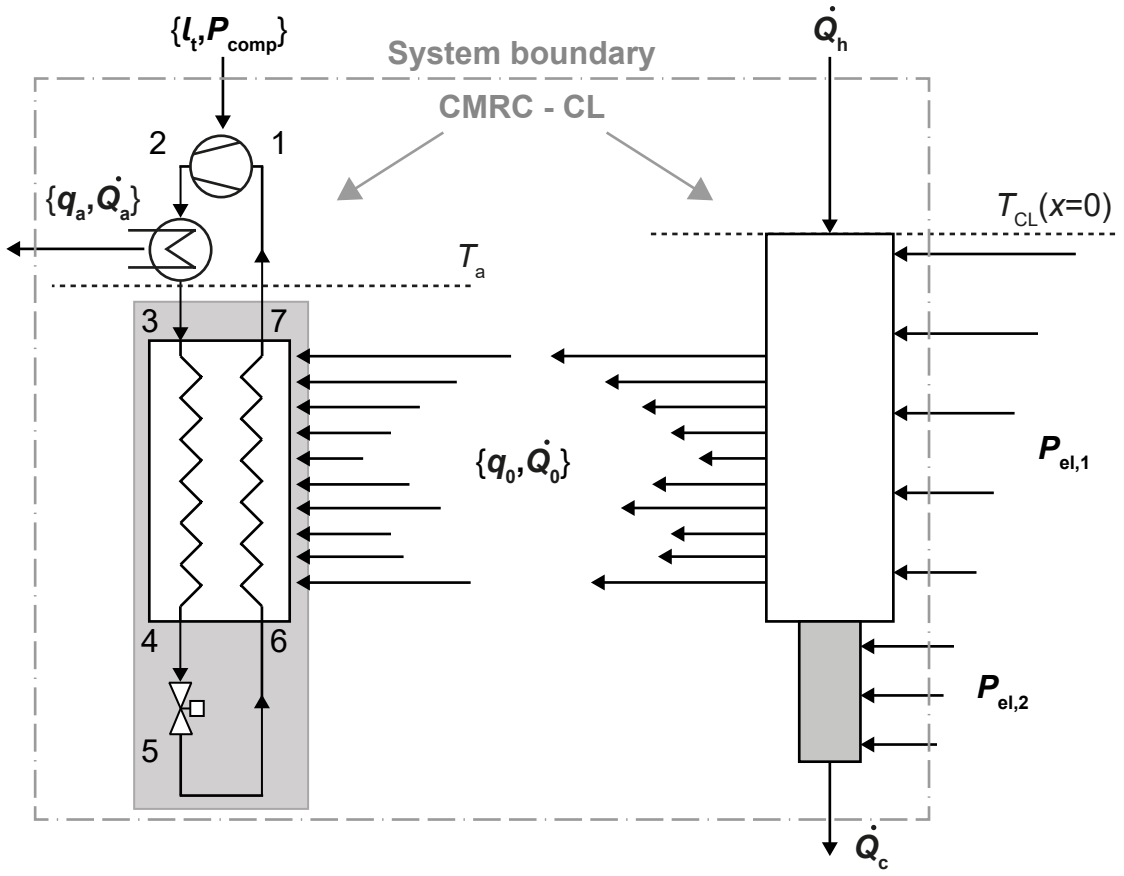

Figure 34: System boundary for the energy conservation of a CMRC-CL.

with the input power of the compressor P_{comp}, the dissipated heat in the aftercooler $\dot{Q}_{\mathrm{a}}$, the electric power dissipations of the CL $\left(P_{\mathrm{el},1}, P_{\mathrm{el},2}\right)$, the thermal load at the warm end $\dot{Q}_{\mathrm{h}}$ and at the cold end $\dot{Q}_{\mathrm{c}}$ of the CL. The cooling load of the CMRC gascooler $\dot{Q}_0$ is transferred internally from the CL to the CMRC and is evaluated internally in both subsystems of the CMRC-CL. The numerical error of the energy conservation *err* is presented as the ratio of the right hand side of (4.21) to the sum of all energy rates with

$$err = \frac{P_{\mathrm{comp}} - \dot{Q}_{\mathrm{a}} - \dot{Q}_{\mathrm{h}} + P_{\mathrm{el},1} + P_{\mathrm{el},2} - \dot{Q}_{\mathrm{c}}}{P_{\mathrm{comp}} + \dot{Q}_{\mathrm{a}} + \dot{Q}_{\mathrm{h}} + P_{\mathrm{el},1} + P_{\mathrm{el},2} + \dot{Q}_{\mathrm{c}}} \cdot 100\% \tag{4.22}$$

4.4 Baseline study with 10 kA

In the following chapter, the computation results of the CMRC-CL numerical model are presented for an electric current of 10 kA and for different refrigerant mixtures that are working at different operating pressures and mass flow rates. In total, seventeen mixtures with different component compositions are investigated and are given in Tab. 20. The molar compositions of the high boiling components propane and butane are decreasing from mixture 1 to mixture 17 and vice versa for the compositions of the low boilers nitrogen and methane. According to (3.32), the freezing point temperatures of the mixtures are ranging from 86.8 K to 94.6 K.

The following boundary conditions are used in the first parametric study:

1. electric current of $I = 10\,\mathrm{kA}$
2. fluid mass flow of $\dot{m} = 3\,\mathrm{g/s}$
3. fluid high pressure of $p_3 = 19\,\mathrm{bar}$
4. fluid low pressure of $p_3 = 4\,\mathrm{bar}$
5. ambient and fluid HP inlet temperatures of $T_\mathrm{a} = T_3 = 293.15\,\mathrm{K}$

Table 20: Molar compositions and with (3.32) approximated freezing point temperatures T_freeze of the investigated hydrocarbon-based refrigerant LRS mixtures. The molar concentrations of the high boilers butane and propane are decreasing from mixture 1 to 17.

Refrigerant mixtures	Nitrogen	Methane	Ethane	Propane	Butane	T_freeze (3.32) (K)
			mole - %			
LRS mixture 1	10	15	15	25	35	94.6
LRS mixture 2	10	15	15	35	25	91.8
LRS mixture 3	10	15	25	25	25	92.3
LRS mixture 4	20	20	10	15	35	92.4
LRS mixture 5	20	20	10	25	25	89.6
LRS mixture 6	20	20	15	20	25	89.8
LRS mixture 7	20	20	20	15	25	90.1
LRS mixture 8	20	20	10	35	15	86.8
LRS mixture 9	30	20	10	10	30	88.7
LRS mixture 10	20	20	20	20	20	88.7
LRS mixture 11	10	25	25	25	15	90.0
LRS mixture 12	30	20	10	15	25	87.3
LRS mixture 13	30	20	15	10	25	87.6
LRS mixture 14	30	20	15	15	20	86.2
LRS mixture 15	10	25	35	15	15	90.5
LRS mixture 16	10	30	25	25	10	88.9
LRS mixture 17	20	30	20	15	15	87.8

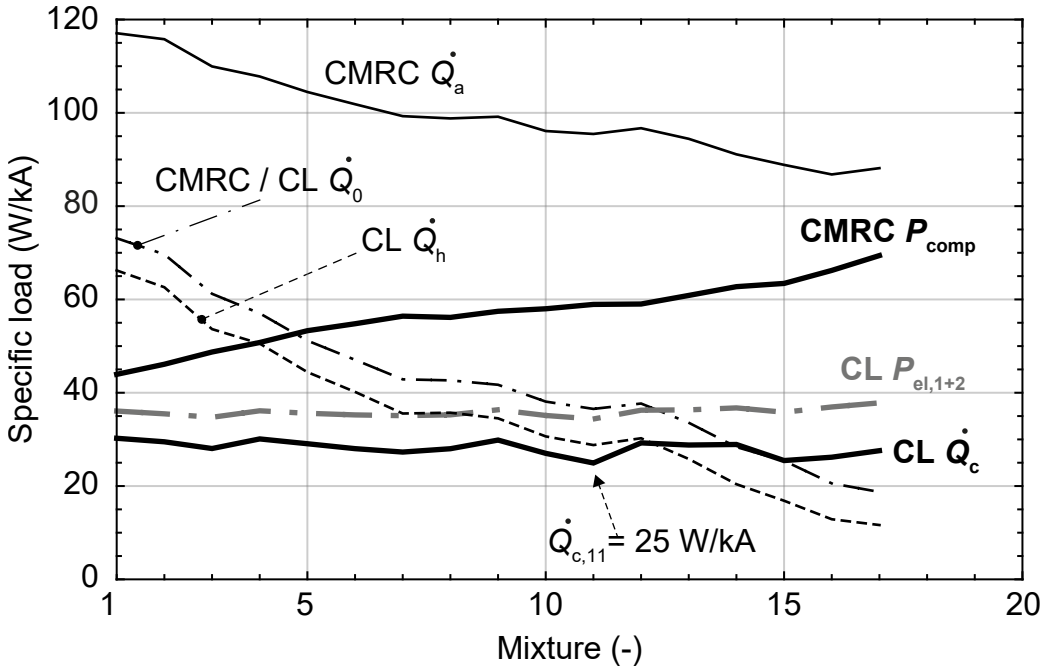

Figure 35: Specific loads in $\left(\mathrm{W/kA}\right)$ of the $I = 10\,\mathrm{kA}$ CMRC-CL as the function of the investigated mixture according to Tab. 20. Boundary conditions of the first parametric study are used. The tabulated results are given in the appendix Tab. 35.

6. current lead temperature at $x = 0$ of $293.15\,\mathrm{K}$
7. current lead temperature at $x = L_{\mathrm{CL}}$ of $77.4\,\mathrm{K}$
8. isentropic efficiency of the compressor is set to 0.7

The specific loads in $\left(\mathrm{W/kA}\right)$ of a CMRC-CL, according to the system boundary depicted in Fig. 34, are presented in Fig. 35 for the seventeen investigated refrigerant mixtures. The numerical results of the specific loads are tabulated in the appendix in Tab. 35 as well as the temperatures T_6 after the throttling device, which are ranging from $161\,\mathrm{K}$ to $142\,\mathrm{K}$. The electrical power dissipation of the whole current lead $P_{\mathrm{el},1+2}$ and the thermal load at the cold end $\dot{Q}_{\mathrm{c}}$ at $77.4\,\mathrm{K}$ show no clear trend regarding the composition of the refrigerant mixtures. Nevertheless, minimum values of $\dot{Q}_{\mathrm{c}} = 24.9\,\mathrm{W/kA}$, $P_{\mathrm{el},1+2} = 34.4\,\mathrm{W/kA}$ and a minimal temperature after the throttling device of $T_6 = 142\,\mathrm{K}$ are found with the mixture 11. The largest compositions in mole % of mixture 11 are the intermediate-boiling refrigerants propane, ethane and methane and have an equal molar composition of 25 %. However, a clear trend is evident in the thermal load at the warm end of the current lead $\dot{Q}_{\mathrm{h}}$, which is decreasing from the mixture 1 to 17 and therefore with decreasing molar compositions of the high boiling components, such as butane and propane. This is explained with the larger refrigeration power $\dot{Q}_0$ for mixtures with a larger amount of high boilers, especially butane. The use of mixtures with a lower amount of high boilers tend to

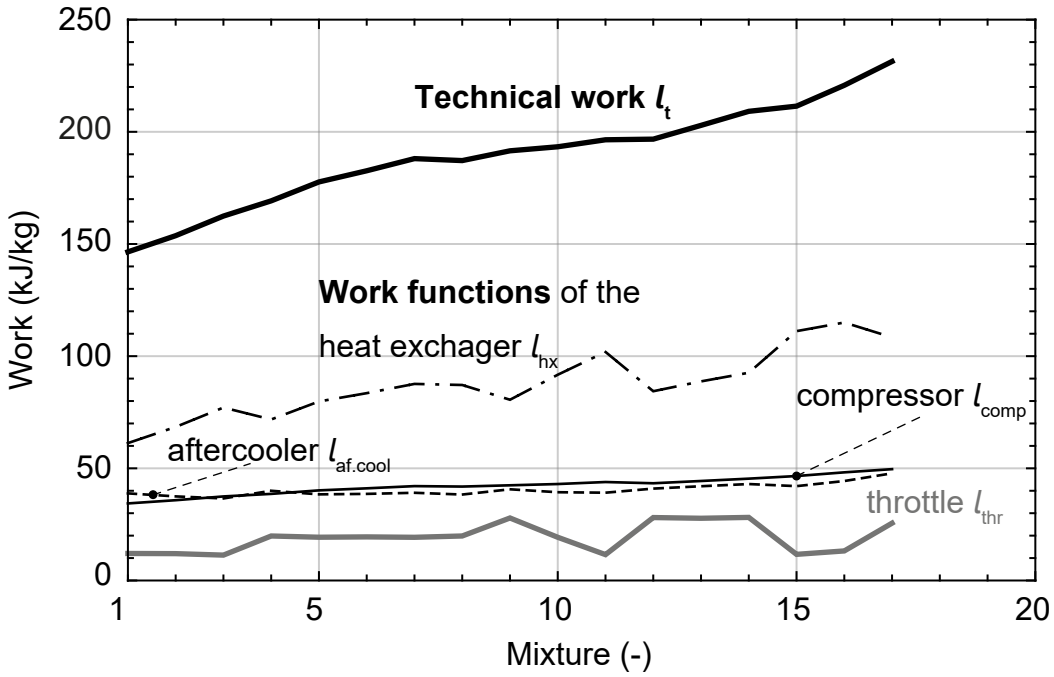

Figure 36: Technical work of the CMRC cycle and the work functions of the cycle components of the first parametric study. The tabulated results are given in the appendix Tab. 36

the adiabatic boundary condition at the warm end $\left(\dot{Q}_\mathrm{h} \to 0\right)$ in the temperature profile of the CL that is discussed in Sec. 2.1. This adiabatic boundary condition, however, comes with a higher compression power P_comp of the fluid and therefore with a larger overall power consumption of the system. The maximum power input of the compressor is found with the mixture 17 and is the lowest with the mixture 1. The cause of the larger compression power for mixtures with a lower amount of high boilers can be explained in the analysis of the respective work functions inside the CMRC, according to the method described in Sec. 3.3 and is presented in the following.

The technical work[4] of the compressor l_t and the work functions of the CMRC components are presented in Fig. 36 for the investigated mixtures. The sum of all work functions in a CMRC according to (3.21) describes the technical work l_t that is necessary to preserve the stationary energy transformation in this thermodynamic cycle. Here, the work functions of the heat exchanger l_hx, of the compressor l_comp and of the aftercooler $l_\mathrm{af.cool}$ show an upward trend to mixtures with a smaller molar concentration of high boilers, whereby the work function of the heat exchanger shows the most significant influence on the technical work. The work function of the throttling device l_thr lead to the smallest contribution to l_t. However, mainly due to the large liquid fraction y of the refrigerant mixture before

[4] The conversion between the power for the compression and the technical work is $l_\mathrm{t} = P_\mathrm{comp}/\dot{m}$.

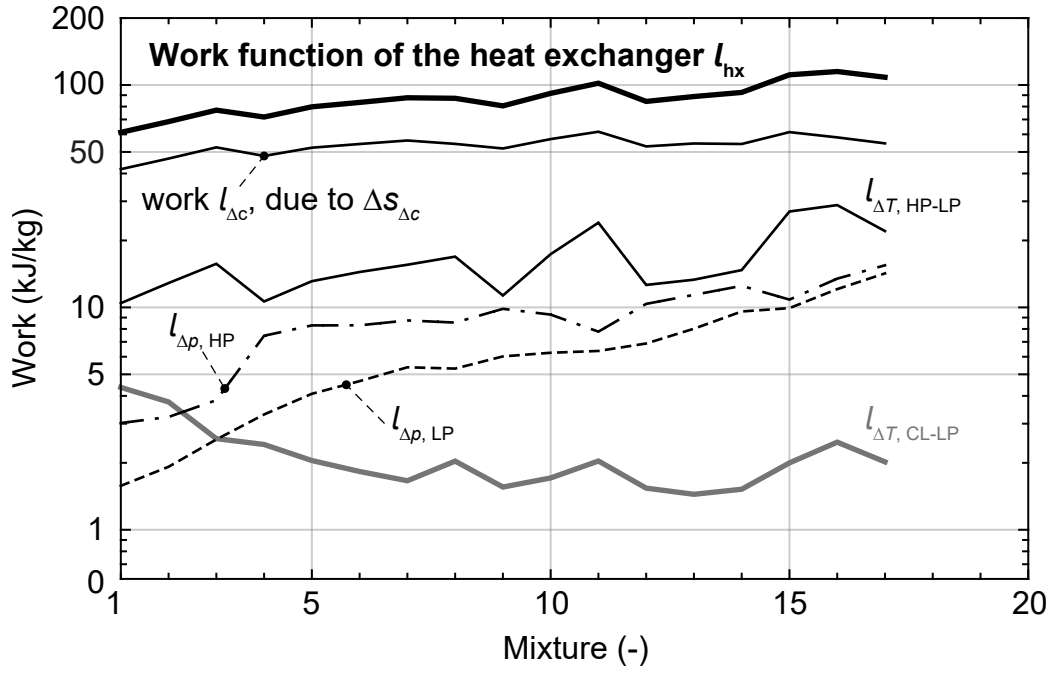

Figure 37: Work function of the heat exchanger and the required work due to the entropy production rates that are caused by gradients for the investigated mixtures in the first parametric study. The sum of all entropy production rates presented here in the form of work is equal to the work function of the heat exchanger l_{hx}. The tabulated results are given in the appendix Tab. 37

the throttle and the small pressure difference during the throttling process which is one of the major benefits of a mixed refrigerant cycle over Linde-Hampson systems that are working with pure refrigerants.

A detailed view on the process work of the heat exchanger is possible in the investigation of its entropy production, due to temperature $\Delta s_{\Delta T}$ (3.27), pressure $\Delta s_{\Delta p}$ (3.31) and concentration $\Delta s_{\Delta c}$ (3.26) gradients. With the mass flow of the fluid $\dot{m}$ and the ambient temperature T_{a}, this entropy productions yield the mass specific work and are presented in Fig. 37. The corresponding tabulated results are given in the appendix Tab. 37. According to (3.26) the sum of all entropy production rates in the heat exchanger presented here in the form of work are equal to the process work of this component, i.e. l_{hx}. The least contribution to the work function of the heat exchanger is caused by the transfer of the heat from the current lead to the low pressure stream $l_{\Delta T,\ \mathrm{CL\text{-}LP}}$, due the corresponding temperature difference. The maximum value of $l_{\Delta T,\ \mathrm{CL\text{-}LP}}$ is found with the mixture 1 and the minimal value with the mixture 13. In contrast to $l_{\Delta T,\ \mathrm{CL\text{-}LP}}$, the entropy production in the form of work that is caused by the transfer of heat between the HP and LP stream $l_{\Delta T,\ \mathrm{HP\text{-}LP}}$, is increasing towards mixtures with a smaller composition of high boilers. It shall be noted that $l_{\Delta T,\ \mathrm{HP\text{-}LP}}$ is larger compared to $l_{\Delta T,\ \mathrm{CL\text{-}LP}}$, which is mainly due to the

larger thermal load that is transferred between the HP and LP stream and the smaller overall temperature difference between the CL and the LP and is discussed in the further course of this chapter. A clear upward trend from mixture 1 to 17 is observed in the work contributions, due to the pressure gradients in the HP $l_{\Delta p,\,\mathrm{HP}}$ and LP $l_{\Delta p,\,\mathrm{LP}}$ streams inside the heat exchanger. The pressure losses of the HP and LP streams for all investigated mixtures, except for mixtures 1 to 3, are calculated to nearly constant values of about 8 bar and 0.8 bar, respectively. The pressure losses of mixtures 1 to 3 are at about 5 bar for the HP stream and 0.5 bar for the LP stream. Except the steep rise of $l_{\Delta p,\,\mathrm{HP}}$ after the first 3 mixtures, the upward trend of $l_{\Delta p,\,\mathrm{HP}}$ and $l_{\Delta p,\,\mathrm{NP}}$ from mixture 1 to 17 is not evident with the investigation of the pressure losses only. Therefore, it is explained by smaller liquid fractions of the fluid streams in the heat exchanger for mixtures with a smaller molar concentration of high boilers, resulting in a larger specific volume ν of the fluid and according to (3.31) to a larger entropy production, due to pressure gradients. The corresponding tabulated data for the pressure losses and the liquid fractions in the heat exchanger are given in the appendix Tab. 38. Further, it should be noted that the work due to the concentration gradients in the mixture $l_{\Delta c}$, yields to the major contribution to l_{hx} and shows an upward trend from mixture 1 to 17. However, $l_{\Delta c}$ is calculated with (3.26) and not with an explicit equation like the contributions due to the temperature and pressure gradients, therefore, no further information on this entropy production term can be provided here.

A further possibility to investigate the results of the parametric CMRC-CL study and to analyse the influence of different mixtures is to evaluate the efficiency $\tilde{\eta}$ of the Linde-Hampson process. The efficiency of a thermodynamic cycle, especially of refrigeration machines, is described by the ratio of the coefficient of performance COP_{real} of a real refrigeration machine to the COP_{ideal} value of the ideal reference process, typically the Carnot cycle (cf. (2.20)). In this work, no experimental data of a CMRC-CL are given and the numerical coefficient of performance COP_{num} is used instead of a COP_{real}. Further, the COP value of the Carnot cycle can not be used for Linde-Hamson gascoolers, because the Carnot cycle is the reference cycle for refrigeration machines that provide cooling power at a constant temperature and not an integrated cooling load over the whole temperature range of the recuperative heat exchanger. Kochenburger [4] derived the theoretical COP_{th} value for Linde-Hamson gascoolers, which is given by

$$COP_{\mathrm{th}} = \frac{(T_6 - T_{\mathrm{a}})}{T_{\mathrm{a}} \cdot \left[1 - \log_e\left(T_{\mathrm{a}}/T_6\right)\right] - T_6} \tag{4.23}$$

and is used in this work as the reference value. Further, there is the possibility to derive two different efficiencies for the Linde-Hampson cycle, yielding

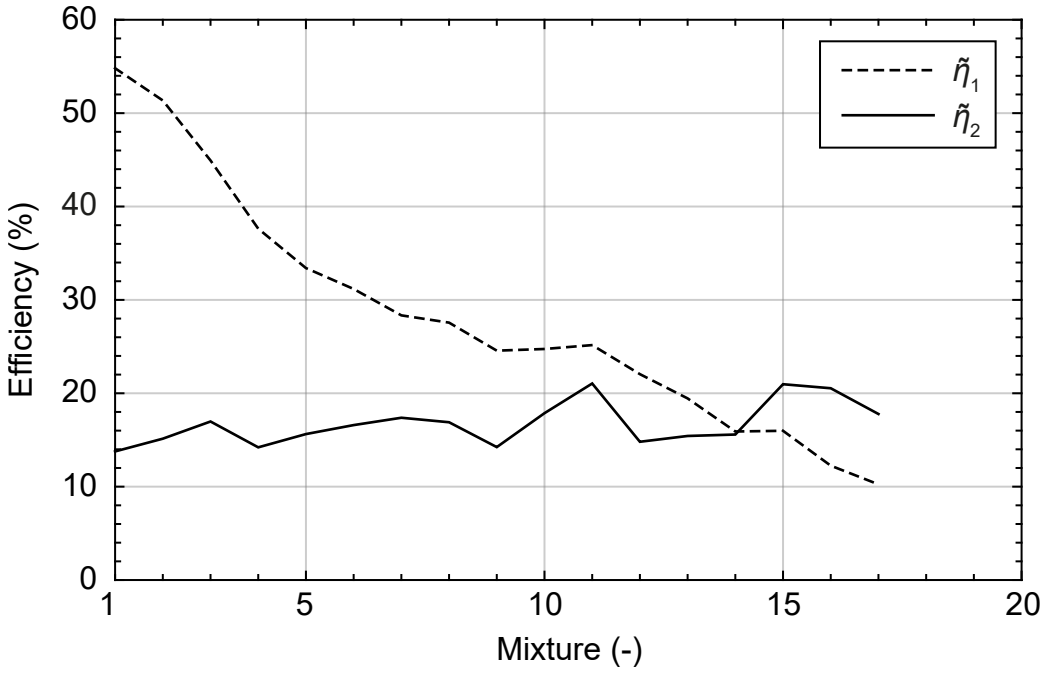

Figure 38: Comparison of two different efficiencies as a function of the investigated mixtures in the first parametric study.

$$\tilde{\eta}_1 = \frac{COP_{\mathrm{num}}}{COP_{\mathrm{th}}} = \frac{\dot{Q}_0}{P_{\mathrm{comp}} \cdot COP_{\mathrm{th}}} = \frac{q_0}{l_{\mathrm{t}} \cdot COP_{\mathrm{th}}} \tag{4.24}$$

$$\tilde{\eta}_2 = \frac{COP^{\star}_{\mathrm{num}}}{COP_{\mathrm{th}}} = \frac{l_{\mathrm{min}}}{l_{\mathrm{t}} \cdot COP_{\mathrm{th}}} = \frac{l_{\mathrm{hx}}}{l_{\mathrm{t}} \cdot COP_{\mathrm{th}}} \tag{4.25}$$

first the classical efficiency approach $\tilde{\eta}_1$, which uses the ratio of the cooling load q_0 to the technical work l_{t} as the numerical COP_{num} value. Second, the new efficiency approach $\tilde{\eta}_2$ derived from [100] which uses the minimal required work l_{min} in the numerator of the new $COP^{\star}_{\mathrm{num}}$ value and describes the absolute minimal work that is needed for the thermodynamic cycle. For Linde-Hampson gascoolers and refrigerators, the minimal work is the process work of the component in which the external heat load q_0 is applied, hence, the process work of the heat exchanger l_{hx} for a gascooler. The corresponding efficiencies $\tilde{\eta}_1$ and $\tilde{\eta}_2$ are presented in Fig. 38. The largest value for the efficiency $\tilde{\eta}_1$ of about 55 % is found with the mixture 1, which has in comparison to other mixtures a larger amount of high boilers and requires the minimum technical work. This efficiency function shows a clear down trend towards mixtures with a larger molar concentration of low boilers in the refrigerant mixture. Accordingly, a CMRC-CL working with the mixture 17 has the lowest efficiency of about 10 %. On the other hand, the second efficiency $\tilde{\eta}_2$ shows a

counter-current trend from mixture 1 to 17 and has a narrower efficiency range of 14 % to 21 %. The largest efficiencies of $\tilde{\eta}_2 = 21\%$ are found with mixtures 11 and 15. According to the tabulated results that are presented in the appendix Tab. 35, CMRC-CLs that are working with mixture 11 and 15 lead to the smallest thermal load at the cold end of the CL $\dot{Q}_\mathrm{c}$ and the coldest temperature after the throttling device T_6.

As a conclusion of the first parametric study, three significant mixtures are identified and are used for further investigations in the course of this chapter:

- mixture 1 that leads to the minimal technical work l_t, however, yields the maximum thermal load at the cold end of the CL $\dot{Q}_\mathrm{c}$ and the maximum temperature after the throttling device T_6
- mixture 11 that leads to minimal $\dot{Q}_\mathrm{c}$ and T_6 values and the largest efficiency $\tilde{\eta}_2$
- mixture 17 that leads to the maximal l_t value and to minimal thermal load at the warm end of the CL $\dot{Q}_\mathrm{h}$ and tend to the CL concept of an adiabatic boundary condition

The CMRC-CL temperature profiles of the selected refrigerant mixtures 1 (a), 11 (b) and 17 (c) are presented in Fig. 39 as a function of the current lead length. Fig. 39a is divided in the CMRC part ranging from 0 m to 0.58 m and the copper connection part that is connected to the 77.4 K cold stage at 0.98 m. The temperature profiles of the HP and the LP streams are depicted in the CMRC part of the CL. Compared to the conduction cooled current lead profiles shown in Fig. 4, the temperature of the CMRC-CL (a) may be described as a CL in an under-current design mode with a quasi-linear temperature profile. In the zoomed region at the warm end of the CL in Fig. 39a, two notable changes in the LP temperature profile are labelled with an exclamation mark. First, the crossing over of the HP and the LP streams near the inlet and outlet of the heat exchanger. In typical Linde-Hampson refrigerator applications, such temperature crossing is not present and is non-physical. However, in a Linde-Hampson gascooler in combination with a CL that has a hotter temperature at the warm end than the inlet temperature of the HP stream, here 300 K and 293.15 K respectively, this temperature crossing is possible. Consequently, an additional thermal load from the CL is absorbed by the LP stream, yielding a crossing over of the HP-LP temperature profiles. Second, the change of the gradient in the temperature profile of the LP stream. This is explained by the two-phase to gaseous change of state of the refrigerant, yielding a zero liquid fraction at the heat exchanger outlet of the LP stream. Similar behaviour of the HP stream is not observed, because the Linde-Hampson cycle of the first parametric study in combination with the investigated mixtures (Tab. 20) is classified as the liquid refrigerant supply (LRS) type and the HP stream enters the heat exchanger already in its two-phase state. The phase transition of the LP stream is shifted to larger CL lengths and to smaller temperatures for the mixtures 11 and 17, which

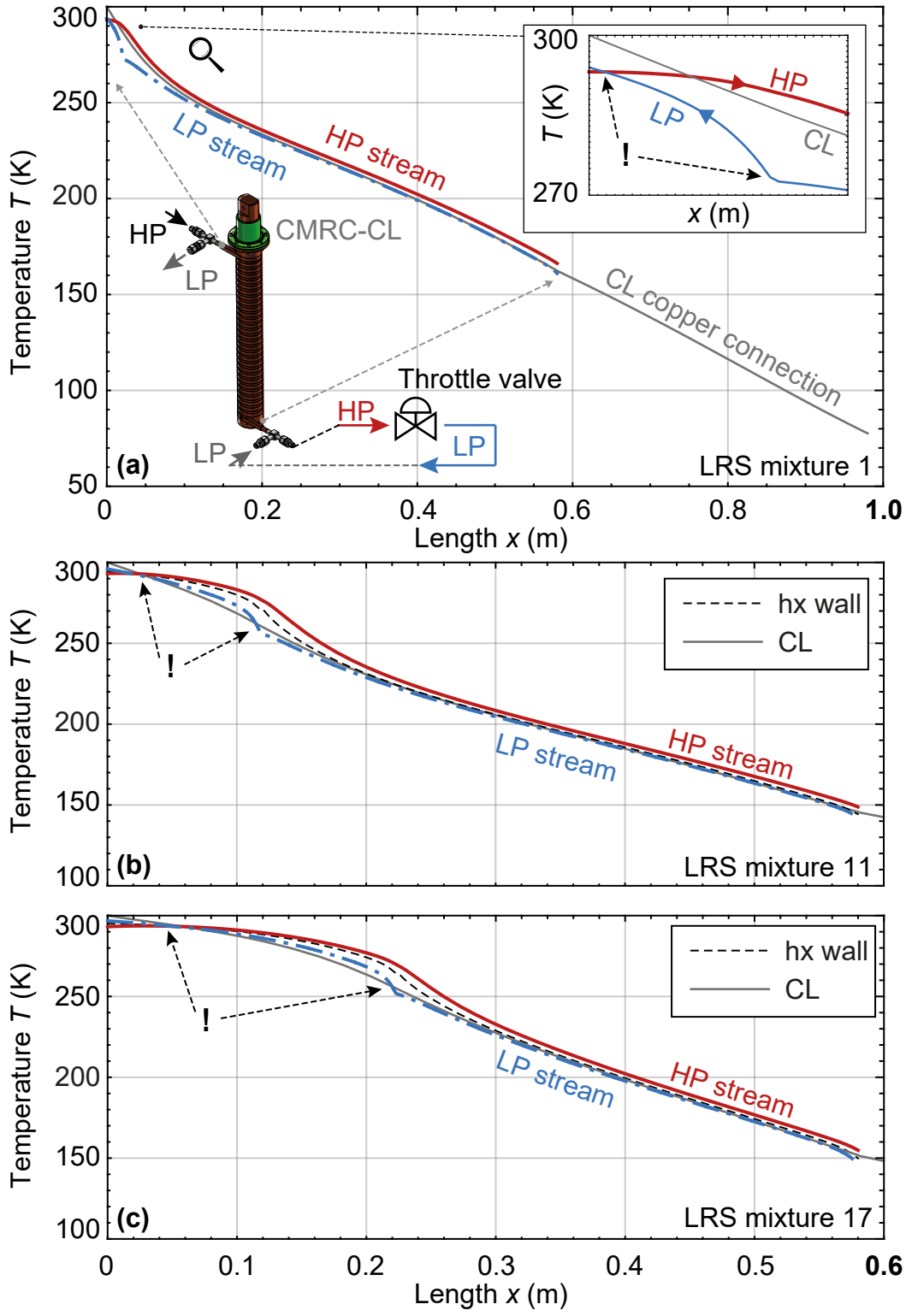

Figure 39: Temperature profiles of CMRC-CLs working with mixtures 1 (a), 11 (b) and 17 (c) as a function of the current lead coordinate x. Boundary conditions of the first parametric study are used. The x axes of (b) and (c) are limited to the length of the CMRC part of the CL.

have a smaller amount of high boilers and therefore have a smaller specific refrigeration power at higher temperatures. Consequently, the thermal load at the warm end, due to

thermal conduction $\dot{Q}_{\mathrm{h}}$, decreases for mixtures with a lower amount of high boilers and may converge to zero for mixtures with a larger amount of low boilers, especially with GRS mixtures. In particular, there is hardly any cooling of the CL in the first 0.2 m with mixture 17 (c.f. Fig. 39c). According to the temperature difference profiles between the HP and LP streams of the investigated mixtures that are depicted in Fig. 40a, the maximum temperature differences are found at the phase change points of the respective LP streams. The transitions to negative values of $\Delta T_{\mathrm{HP\text{-}LP}}$ indicates the crossing over of the streams.

In Fig. 40b the temperature differences between the CL and the LP stream are presented for the investigated mixtures as a function of the CL length. The largest temperature difference of about 13 K is found with mixture 11 at the warm end of the CL. The increasing temperature difference at the cold end of the CL is due to the throttling valve and the associated Joule-Thomson effect that reduces the temperature of the refrigerant after its expansion. Pinch points (except the crossing over points) are found for all investigated mixtures at about 70 % to 93 % of the CL length. It is interesting to denote that the temperature difference profile of mixture 1 has no negative values along the CL length, while the mixtures 11 and 17 show two changes of sign. This means, that the CL is cooled by the LP stream of mixture 1 over the whole CL length, but is partly heated with the LP stream when mixture 11 and 17 are used. For the latter cases, this means that the dominating cooling mechanism in the first 0.1 m to 0.2 m of the CL is caused by the longitudinal thermal conduction of the CL and not by the LP stream of the mixture. The local longitudinal thermal conduction, due to Fourier's Law, is presented in Fig. 41 for the three investigated mixtures. The local thermal conduction in the case of mixture 1 has a maximum at the warm end of the CL and a minimum at about 0.25 m. The opposite applies for the mixtures 17, where the minimum longitudinal thermal conduction value is at the warm end and the maximum value at about 0.2 m. In the case of mixture 11, the CMRC part of the CL has its maximum longitudinal thermal conduction at a length of about 0.1 m and a minimum value at about 0.35 m. The maxima of the longitudinal thermal conduction of mixture 11 and 17 are found at the same positions as the corresponding crossings of the CL and LP stream temperatures (c.f. Fig. 39 and Fig. 40). Further explanation for the behaviour of the fluid and CL temperatures is provided by the consideration of the heat transfer kinetics between the streams and between the CL and the LP stream and is provided in the following.

In Fig. 42 the heat transfer coefficients of the LP stream α_{LP}, the HP stream α_{LP} and the corresponding thermal transmittance between the streams $k_{\mathrm{HP\text{-}LP}}$ are presented for the investigated mixtures 1, 11 and 17. The thermal transmittance $k_{\mathrm{HP\text{-}LP}}$ describes the kinetic relation between the temperatures and the transferred heat between the streams. It comprises the heat transfer coefficients α_{HP} and α_{LP} of the streams, as well as all

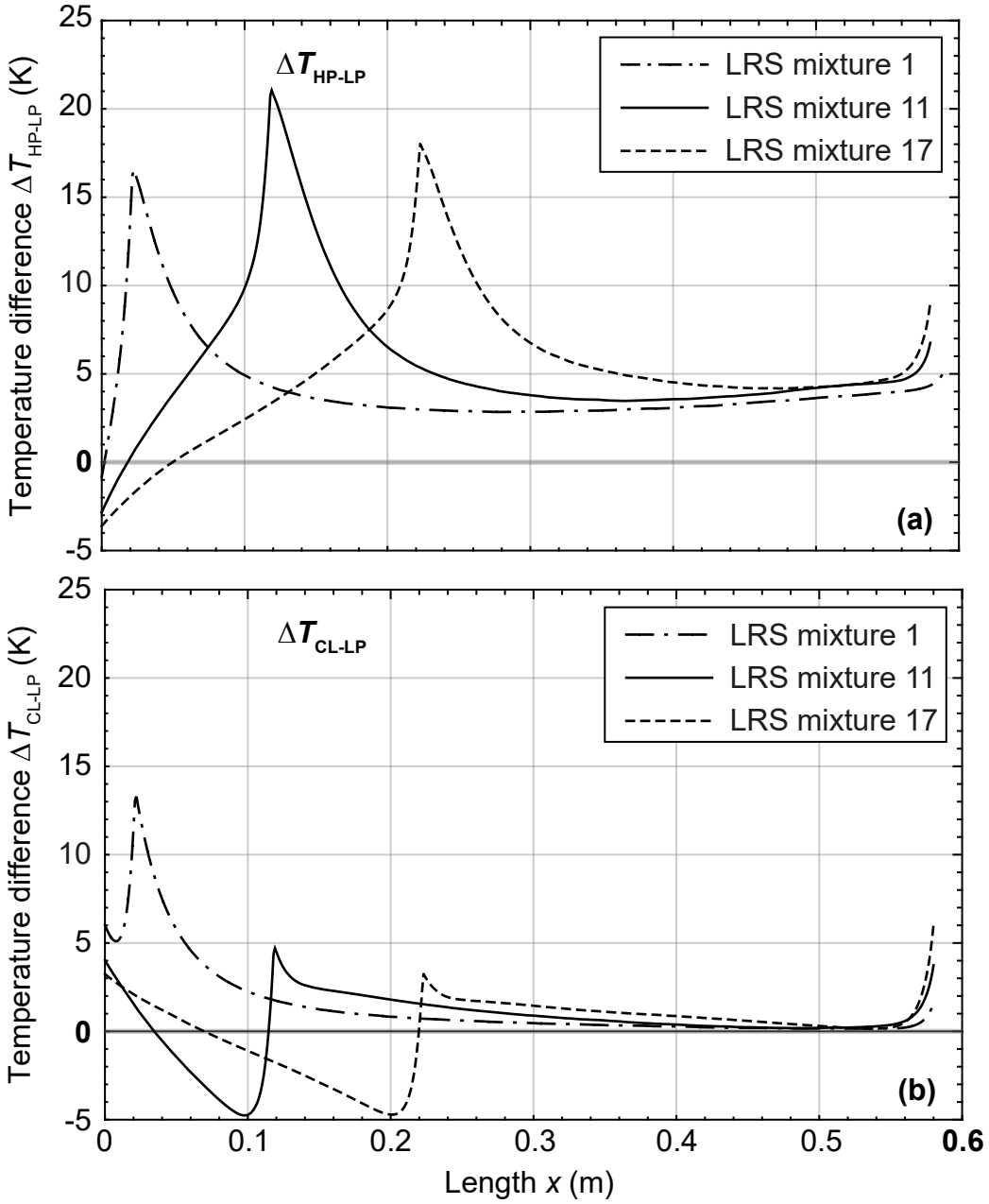

Figure 40: Temperature differences between the HP and LP stream as a function of the heat exchanger coordinate z (a) and temperature differences between the CL and LP stream as a function of the current lead coordinate x (b) of CMRC-CLs working with mixture 1, 11 or 17. Boundary conditions of the first parametric study are used.

thermal resistances between them. Typically, $k_{\text{HP-LP}}$ is used in design procedures (e.g ϵ-NTU method [109]) of single-phase heat exchangers together with its integral value kA. However, in the case of two-phase flow of zeotropic mixtures, the classical design procedures are inadequate [5], but the thermal transmittance $k_{\text{HP-LP}}$ is used to explain the negative temperature differences in Fig. 40b. The points in Fig. 42 that are identified with the exclamation mark show significant changes in the kinetics of the heat transfer between the streams $k_{\text{HP-LP}}$ and between the current lead and the LP stream that is

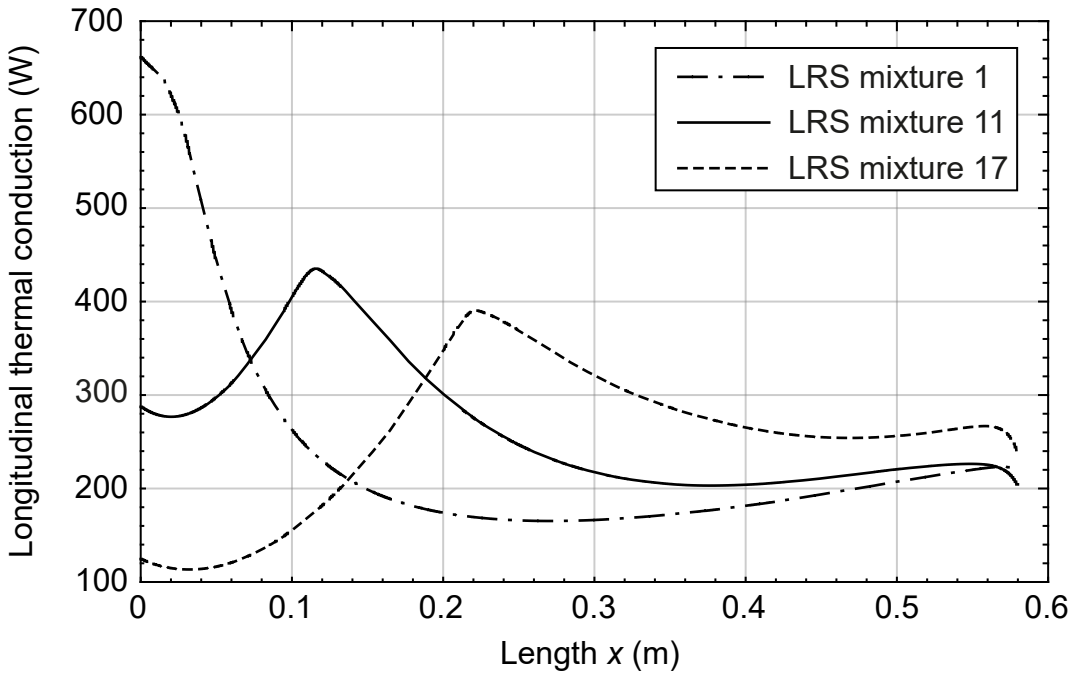

Figure 41: Local longitudinal thermal conduction of the CMRC part of the current lead as a function of the CL length for mixtures 1, 11 and 17. Boundary conditions of the first parametric study are used.

described with α_{LP} only, according to (4.7) and (4.14). Following the flow direction of the LP stream in reversal direction of the x axes of Fig. 42c for the mixture 17 as an example, the largest values for the thermal transmittance are found in the range of 0.24 m to 0.58 m. In this range, the HP and the LP stream are in their two-phase state. The first steep reduction of $k_{\mathrm{HP\text{-}LP}}$ at $x = 0.23\,\mathrm{m}$ is caused by the two-phase to gaseous change of state of the LP stream, therefore, increasing the thermal resistance between the streams. Further, the heat capacity of the LP stream is significantly smaller in its gaseous state compared to the two-phase condition and lead to a steep temperature increase, due to the heat load from the HP stream (c.f. Fig. 39c). This effect induces the first crossing over of the CL-LP temperature difference to negative values at 0.23 m. The second crossing over of $\Delta T_{\mathrm{CL\text{-}LP}}$, however, is mainly due to the above-mentioned different temperatures of the CL and the HP stream at $x = 0\,\mathrm{m}$. For $x < 0.05\,\mathrm{m}$ the LP stream is heated up by the CL, but is also cooled by the HP stream. Nevertheless, the second steep change of the thermal transmittance of mixture 11 and 17 at the beginning of the CL, is explained by the steep reduction of the heat transfer coefficient α_{HP} of the HP stream. Consequently, the thermal resistance between the streams strongly increases. The HP stream does not change its state, however, the two-phase heat transfer show relative poor transfer performances at high vapour / low liquid qualities (c.f y_3 in Tab. 38) and is associated with partial dry-out [5]. More information about the two-phase kinetics of zeotropic mixtures as a function of

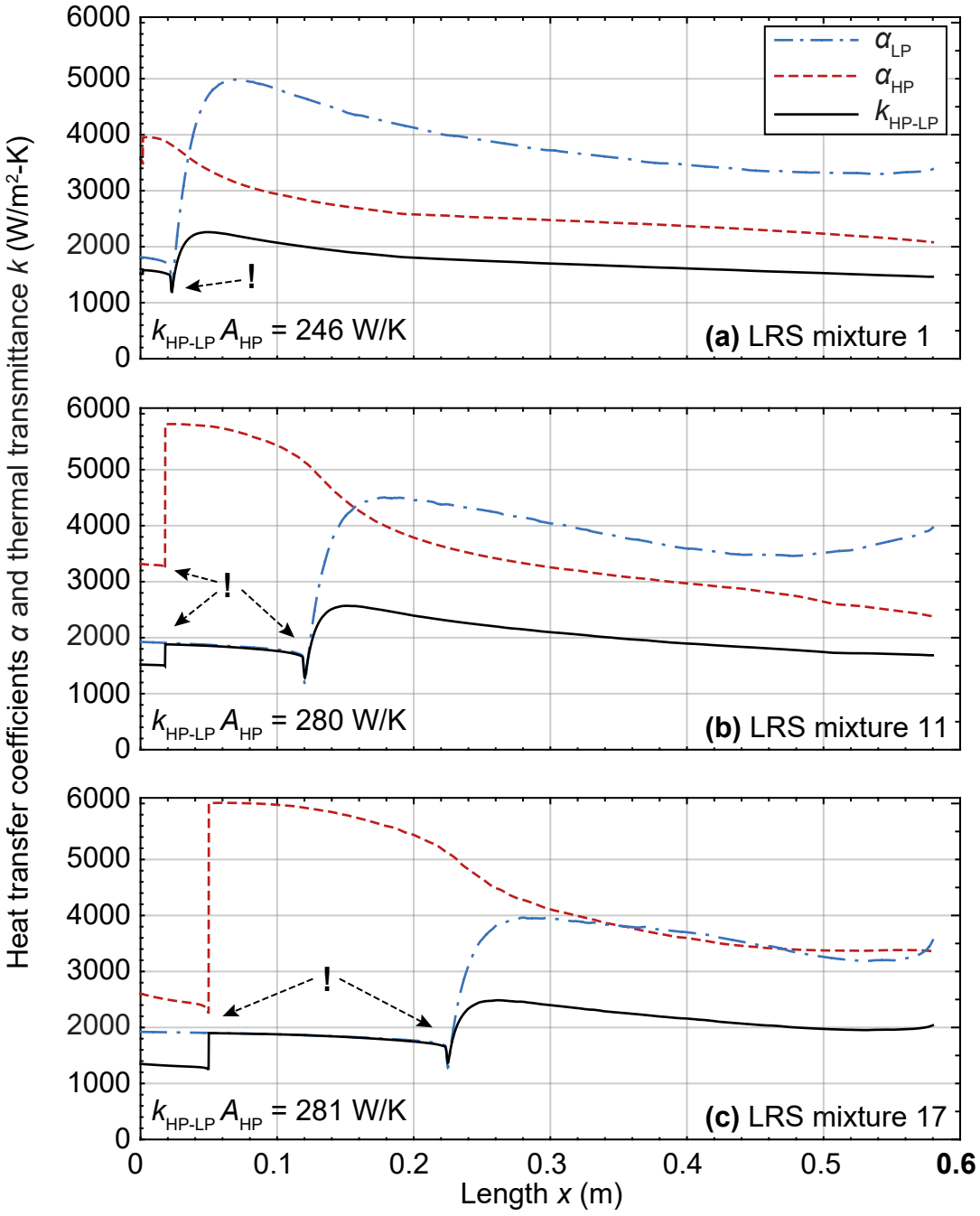

Figure 42: Heat transfer coefficients of the HP α_{HP} and LP α_{LP} streams and the thermal transmittance $k_{\mathrm{HP\text{-}LP}}$ between the streams as a function of the CL length for mixtures 1 (a), 11 (b) and 17 (c). Boundary conditions of the first parametric study are used. The thermal transmittance $k_{\mathrm{HP\text{-}LP}}$ is relative to the heat transfer area A_{HP} of the HP stream according to Tab. 17.

the vapour quality may be found in [5, 118].

The numerical results of the three mixtures 1, 11 and 17 that are examined in-depth are summarized in Tab. 21. In addition, two new parameters for the total energy consumption of the CMRC-CL system are included. The total energy consumption $P_{\mathrm{2xCL,total,el}}$ of the

CMRC-CL test stand (c.f. Sec. 4.2) with two 10 kA current leads, defined as

$$P_{\mathrm{2xCL,total,el}} = 2 \cdot \left(P_{\mathrm{comp}} + P_{\mathrm{el,1}} + P_{\mathrm{el,2}}\right) + P_{\mathrm{AL600}} \tag{4.26}$$

with the electric power consumption of the AL600 cryocooler $P_{\mathrm{AL600}} = 11.5\,\mathrm{kW}$ that is planned for the test stand. The second parameter $P_{\mathrm{1xCL,total,el}}$ describes the total power consumption of one 10 kA CMRC-CL system and is calculated as

$$P_{\mathrm{1xCL,total,el}} = P_{\mathrm{comp}} + P_{\mathrm{el,1}} + P_{\mathrm{el,2}} + P_{\mathrm{AL300}} \tag{4.27}$$

and would require a cryocooler with less cooling power, like the AL300 with a power consumption of about $P_{\mathrm{AL300}} = 7.0\,\mathrm{kW}$. The cooling power and the efficiencies of the cryocoolers are given in Tab. 11. The total power $P_{\mathrm{1xCL,total,el}}$ that is needed for one 10 kA CMRC-CL system is about 800 W/kA for all three mixtures 1, 11 and 17. It is smaller compared to a pure conduction cooled system with a AL600 cryocooler that requires 1190 W/kA. Compared to other cooling options for a 10 kA CL that are presented in Tab. 15, comparable results of about 770 W/kA and 650 W/kA are obtained with a PCL system in combination with a AL300 cryocooler or a forced-flow VCCL system, respectively. However, significantly smaller specific power consumptions are archived only with a self-sufficient gas cooled system. The overall power consumption $P_{\mathrm{1xCL,total,el}}$ of a CMRC-CL system can be further reduced by increasing the inlet pressure of the HP

Table 21: Summary of numerical results of the investigated mixtures 1, 11 and 17. Boundary conditions of the first parametric study are used.

Parameter	Unit	LRS mixture 1	LRS mixture 11	LRS mixture 17
$P_{\mathrm{2xCL,total,el}}$	(W/kA)	1310	1337	1364
$P_{\mathrm{1xCL,total,el}}$	(W/kA)	780	793	807
T_6	(K)	161	142	148
$\dot{Q}_{\mathrm{c}}$	(W/kA)	30.2	24.9	27.6
$\dot{Q}_{\mathrm{h}}$	(W/kA)	66.2	28.8	11.6
$P_{\mathrm{el,1}}$	(W/kA)	28.9	28.0	31.0
$P_{\mathrm{el,2}}$	(W/kA)	7.2	6.4	6.8
$\dot{Q}_0$	(W/kA)	73.1	36.5	18.7
P_{comp}	(W/kA)	43.9	58.9	69.4
$\dot{Q}_{\mathrm{a}}$	(W/kA)	117.0	95.4	87.7
$\tilde{\eta}_1$	%	54.8	25.2	10.3
$\tilde{\eta}_2$	%	13.8	21.0	17.8
err	%	-0.41	0.86	1.76
Δp_{HP}	(bar)	5.2	7.6	8.7
Δp_{LP}	(bar)	0.5	0.7	1.1

stream, which results in a larger specific refrigeration power of the CMRC cycle according to Fig. 23 . The magnitude of this increase depends on the mixture composition and is analysed in the second parametric study in the following.

4.5 Study with increased high-pressure level

The following boundary conditions are used in the second parametric study:

1. same boundary conditions that are used in the first parametric study, except for
2. fluid high pressure of $p_3 = 30\,\text{bar}$
3. fluid low pressure p_6 is ranging from 3 bar to 5 bar
4. the mixtures 1, 11 and 17 are investigated

The numerical results of the second parametric study are summarized in Fig. 43 and the corresponding tabulated data are given in the appendix Sec. B. The numerical values of a CMRC-CL with mixture 1 at a LP of $p_6 = 5\,\text{bar}$ are excluded from the following studies, due to the relative high LP boiling point temperature T_6. In Fig. 43a the compression power P_{comp} is presented for the mixtures 1, 11 and 17 as a function of the low pressure p_6. Generally, P_{comp} decreases with increasing LP, because of the smaller pressure ratio that is needed for the compression. Compared to the results of the first parametric study, P_{comp} is larger due to the larger HP of the fluid. Further, the correlation that was found in the first parametric study between the amount of high boilers in the mixture and the compression power is also confirmed in this study, yielding smaller values for mixtures with a larger amount of high boilers. The minimum value for the thermal load at the cold end of $\dot{Q}_{\text{c}} = 15.4\,\text{W/kA}$ is found with the mixture 17 at a LP of 3 bar, yielding a 64 % reduction compared to a conventional CCCL and is presented in Fig. 43b. Compared to the mixture 1 and 11, a CMRC-CL that is operated with mixture 17 shows smaller thermal loads $\dot{Q}_{\text{c}}$ at the same pressures p_6. Further, the maximum efficiency of $\tilde{\eta}_2 = 27\,\%$ (c.f. Tab. 40) is found with this mixture at $p_6 = 3\,\text{bar}$. The minimum temperature after the throttling device of 108 K is found with mixture 17 at a LP of $p_6 = 3\,\text{bar}$ and is presented in Fig. 43d. Generally, the temperature of the LP stream T_6 is decreasing with decreasing LP p_6 for all three mixtures. It should be noted that the refrigeration power $\dot{Q}_0$ of mixture 1 is about a factor of two larger compared to mixture 17 at 3 bar (c.f. Tab. 39), but shows a larger temperature T_6 and yields a larger thermal load $\dot{Q}_{\text{c}}$ at the cold end. The benefit of a larger refrigeration power at higher temperatures of mixture 1, however, is almost completely used for the thermal load $\dot{Q}_{\text{h}}$ at the warm end of the CL, which in turn is a function of the temperature gradient at the warm end and therefore, a function of $\dot{Q}_0$. The refrigeration power of mixtures with a larger amount of high boilers may become more usable, if the warm end of the CL can be thermally isolated from the ambience at 300 K, e.g with a combination of Peltier elements and a

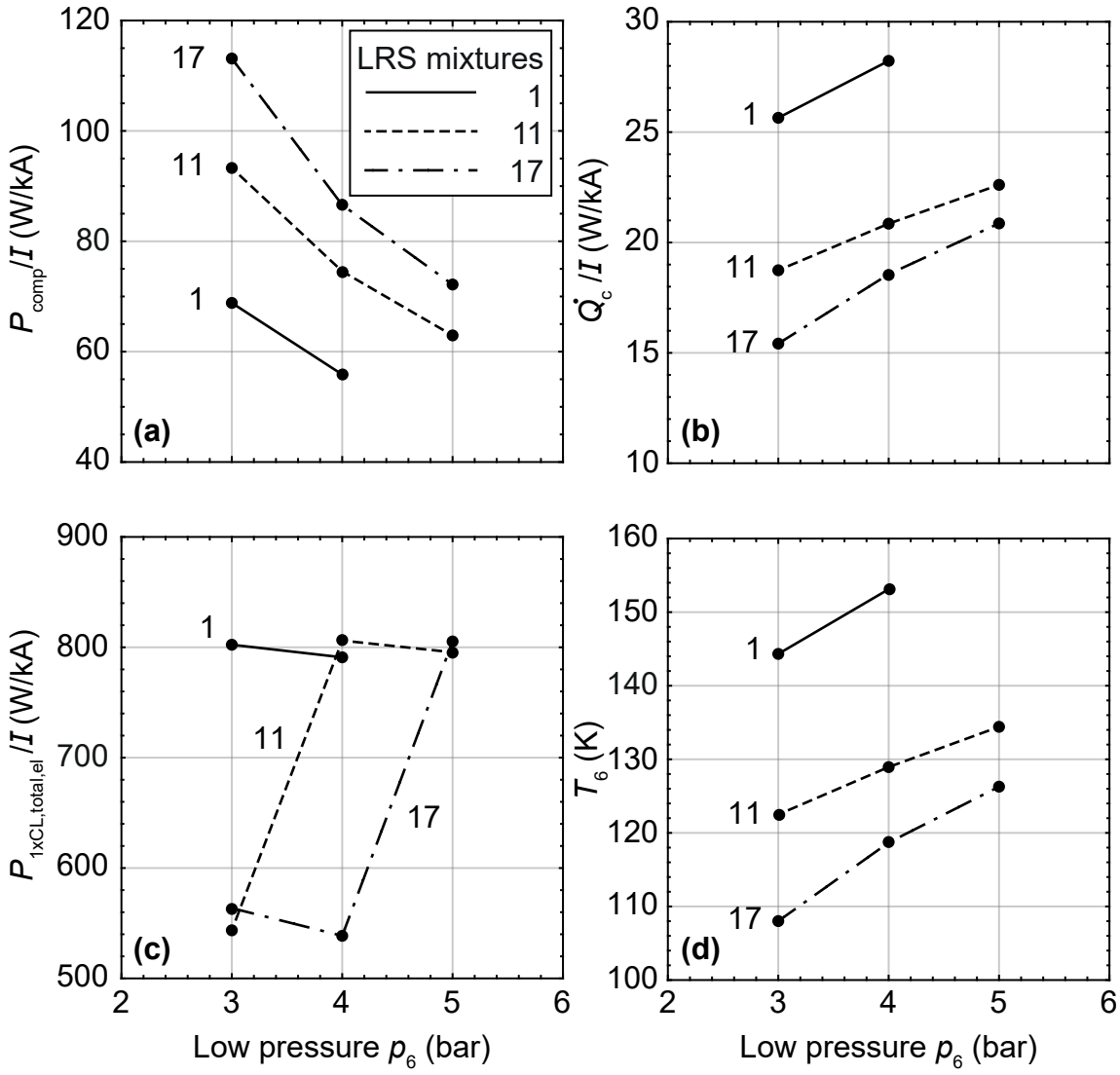

Figure 43: Power input of the compressor P_{comp} (a), thermal load at the cold end of the CL $\dot{Q}_{\mathrm{c}}$ (b), total power consumption of one CMRC-CL $P_{\mathrm{1xCL,total,el}}$ and the temperature after the throttling device T_6 (d) as a function of the low pressure p_6 for mixtures 1, 11 and 17. Boundary conditions of the second parametric study are used. The tabulated results are given in the appendix Tab. 39. $P_{\mathrm{1xCL,total,el}}$ is calculated according to (4.28).

CMRC-CL [119]. However, instead of an additional refrigeration cycle like it is presented in [119], a preconnected heat exchanger may be necessary to cool down the mixture to the intersection temperature of the PCL.

The total power consumption of one CMRC-CL $P_{\mathrm{1xCL,total,el}}$ is presented in Fig. 43c and is given by the following expression

$$P_{\mathrm{1xCL,total,el}} = P_{\mathrm{comp}} + P_{\mathrm{el},1} + P_{\mathrm{el},2} + \begin{cases} P_{\mathrm{AL300}} = 7.0\,\mathrm{kW} & \text{for} \quad 190\,\mathrm{W} < \dot{Q}_{\mathrm{c}} \leq 320\,\mathrm{W} \\ P_{\mathrm{AL200}} = 4.2\,\mathrm{kW} & \text{for} \quad \dot{Q}_{\mathrm{c}} \leq 190\,\mathrm{W} \end{cases} \tag{4.28}$$

taking into account that for thermal loads at the cold end of the CL below 190 W the crycooler AL200 (c.f. Tab. 11) with a smaller power consumption may be used in combination with the CMRC cycle. The minimum value of $P_{\mathrm{1xCL,total,el}} = 539\,\mathrm{W/kA}$ is found with the mixture 17 at $p_6 = 4\,\mathrm{bar}$. Compared to other cooling options in Tab. 15, only the self-sufficient gas cooled system archive smaller specific power consumptions. This means that this CMRC-CL system is the most efficient closed cooling system for high amperage current leads, compared to the systems that are presented in this work. However, this minima is restricted to the time of this publication available refrigeration machines at the relevant cooling power and temperature level and therefore, does not represent the physically possible minima of this concept. Furthermore, it should be noted that there is a realistic possibility to develop a CMRC without the need of an additional cryocooler system.

4.6 Study on the influence of mass flow

In the third parametric study, the influence of the mass flow is investigated and the following boundary conditions are used

1. same boundary conditions that are used in the second parametric study, except for
2. the fluid mass flow $\dot{m}$ is ranging from 2.5 g/s to 3.5 g/s

The numerical results of the third parametric study are summarized in Fig. 44 and the corresponding tabulated data are given in the appendix Sec. B. Generally, the compression power P_{comp} decreases with decreasing mass flow as well as the refrigeration power of the CMRC cycle $\dot{Q}_0$, yielding a larger thermal load at the cold end of the CL. In Fig. 44a this thermal load $\dot{Q}_{\mathrm{c}}$ and in Fig. 44b the temperature after the throttling device T_6 are presented for the mixtures 1, 11 and 17 as a function of the low pressure p_6 and as a function of the mass flow. This parameters are decreasing with increasing mass flow, yielding smaller thermal loads and temperatures at the cold end of the CL and the heat exchanger, respectively. The minimum values $\dot{Q}_{\mathrm{c}} = 14\,\mathrm{W/kA}$ and $T_6 = 105\,\mathrm{K}$ are found with the mixture 17 at a LP of $p_6 = 3\,\mathrm{bar}$ and a mass flow of $\dot{m} = 3.5\,\mathrm{g/s}$, yielding the maximum efficiency of $\tilde{\eta}_2 = 29\,\%$ (c.f. Tab. 48). The corresponding temperature profile of the CMRC-CL is presented in Fig. 45. Here, the two-phase to gaseous change of state of the LP streams takes place at a temperature of about 240 K, yielding a steep and linear decrease of the CL temperature down to this point.

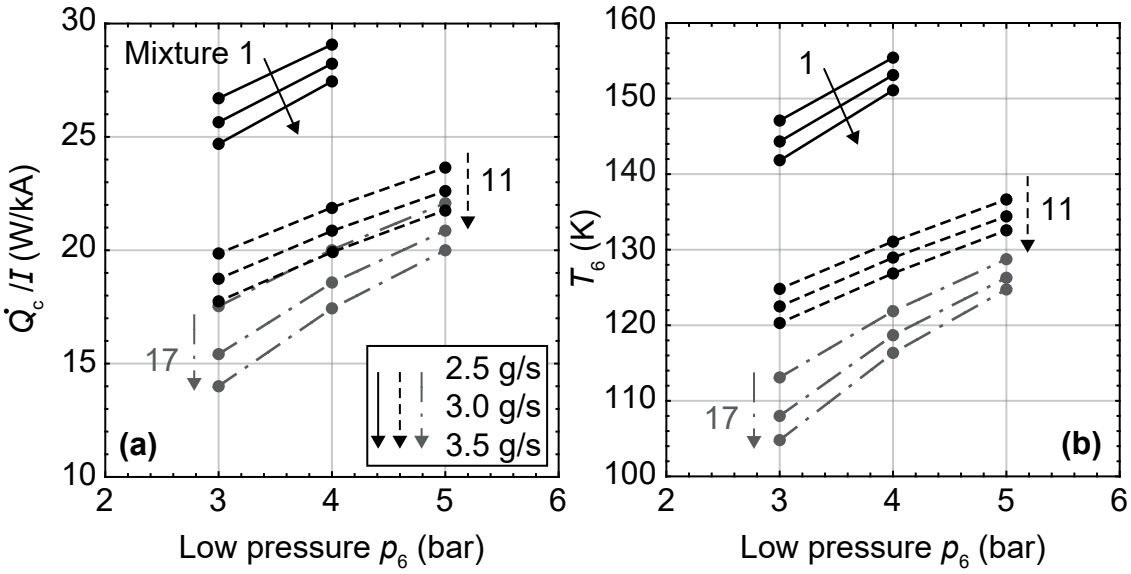

Figure 44: Thermal load at the cold end of the CL $\dot{Q}_c$ (a)and the temperature after the throttling device T_6 (b) as a function of the low pressure p_6 and the mass flow of the fluid $\dot{m}$ for mixtures 1, 11 and 17. Boundary conditions of the third parametric study are used. The tabulated results are given in the appendix Sec. B.

As a summary, the numerical results of the developed 10 kA CMRC-CL for the case of a

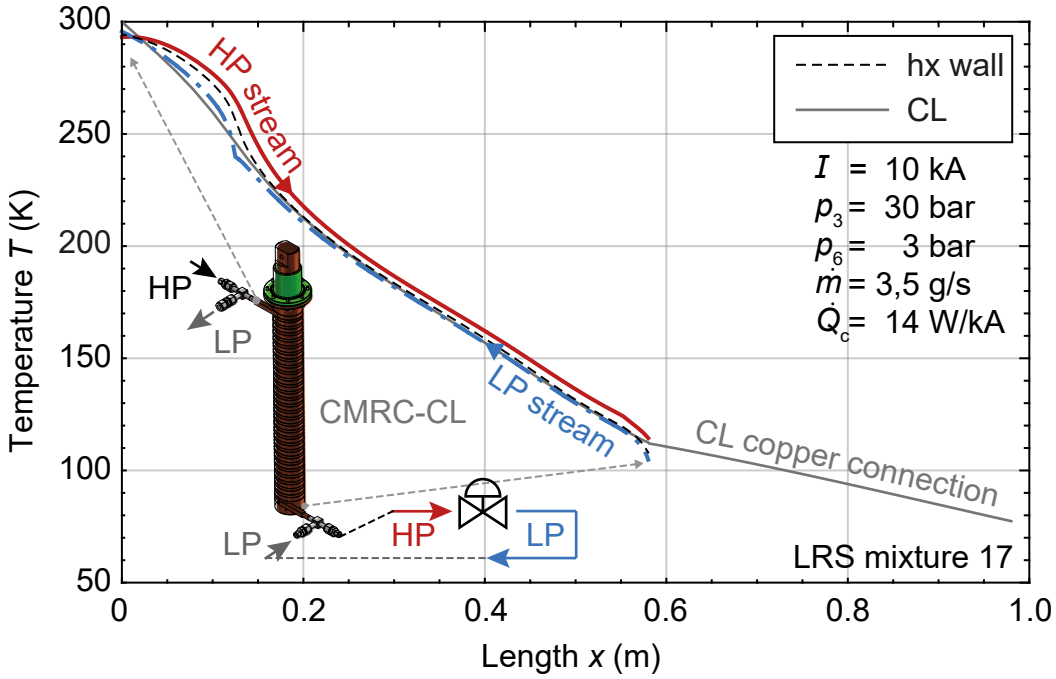

Figure 45: Temperature profiles of a CMRC-CL working with the mixture 17 at a LP of $p_6 = 3$ bar as a function of the current lead coordinate x. Boundary conditions of the third parametric study with the mass flow of 3.5 g/s are used.

Table 22: Summary of numerical results of the developed 10 kA CMRC-CL in combination with a AL200 GM cryocooler.

Parameter	Unit	$\dot{Q}_{\mathrm{c,min}}$	$P_{\mathrm{1xCL,total,el,min}}$
T_6	(K)	105	113
$\dot{Q}_{\mathrm{c}}$	$\left(\mathrm{W/kA}\right)$	14.0	17.5
$P_{\mathrm{1xCL,total,el}}$	$\left(\mathrm{W/kA}\right)$	598	539
$\tilde{\eta}_1$ (4.24)	%	225	128
$\tilde{\eta}_2$ (4.25)	%	29	25
Mixture	$(-)$	LRS mixture 17	
$\{p_{\mathrm{HP}}\ ,\ p_{\mathrm{LP}}\}$	(bar)	$\{30\ ,\ 3\}$	
Δp_{HP}	(bar)	8.15	4.31
Δp_{LP}	(bar)	1.65	0.87
$\dot{m}$	$\left(\mathrm{g/s}\right)$	3.5	2.5

minimal thermal load at the cold end $\dot{Q}_{\mathrm{c,min}}$ and for the case of a minimal overall power consumption of a system with one CMRC-CL $P_{\mathrm{1xCL,total,el,min}}$, are presented in Tab. 22. From the seventeen investigated mixtures that are depicted in Tab. 20, the LRS mixture 17 leads to minimum values for the parameters of interest. Mixture 17 has a small molar concentration of high boilers butane and propane and a larger concentration of low boilers, especially methane.

4.7 Study with increased heat transfer area

In the fourth and the last parametric study, a numerical thought experiment of a larger internal heat transfer area between the fluid streams and between the LP stream and the CL are investigated. The following boundary conditions are used

1. same boundary conditions and geometries of the heat exchanger and of the current lead that are used in the second parametric study, except for
2. the fluid mass flow $\dot{m}$ is fixed at 3.5 g/s
3. the heat transfer areas between the HP and LP stream (c.f Tab. 17) are increased from 100 %, with $A_{\mathrm{HP}} = 0.1414\,\mathrm{mm}^2$ and $A_{\mathrm{LP}} = 0.2063\,\mathrm{mm}^2$, to 120 % and 140 %
4. the heat transfer area between between the CL and the LP stream is increased from 100 % with $A_{\mathrm{CL\text{-}LP}} = 0.139\,\mathrm{mm}^2$ to 120 % and 140 %

The numerical results of the thermal loads at the cold end of the CL $\dot{Q}_{\mathrm{c}}$ and of the temperatures after the throttling device T_6 are presented in Fig. 46, as a function of p_6 and of the above mentioned heat transfer areas. Both, $\dot{Q}_{\mathrm{c}}$ and T_6 are decreasing with increasing internal heat transfer area between the streams and between the CL and the LP stream, for the investigated mixtures 1, 11 and 17. Minimum values are found with the mixture 17 at a LP of 3 bar with the largest internal heat transfer areas, with

$\dot{Q}_c = 10.8\,\mathrm{W/kA}$ and $T_6 = 97\,\mathrm{K}$. Further, due to the significant lower thermal load at the cold end of the CL, a crycooler with a smaller cooling power could be used, e.g. the AL125 (c.f Tab. 11) with a cooling power of 120 W at 80 K and a power consumption of 3300 W. Expanding (4.28) with the cryocooler AL125, yield a minimization of the overall power consumption to $P_{1\mathrm{xCL,total,el}} = 503\,\mathrm{W/kA}$ for the mixture 17 at $p_6 = 3\,\mathrm{bar}$.

To increase the heat transfer area of the classical tubes-in-tube heat exchanger and the CL in contact with the LP stream practically, it may be necessary to implement fins along the HP capillaries and the outer walls of the copper tube and/or increasing the length of the heat exchanger. The increase of the hx length would be possible with an increase of the CL diameter or the length of the CMRC part. However, according to the shape factor of the CMRC part of the CL that is given in Tab. 18 and due to its definition in (2.10), an increase in the length of the CMRC part would lead to an increase of the core diameter of the CL as well. An increase of the heat exchanger length by 40 %, yields an increase in the length L_1 and the cross section area A_1 for the electric current of the CMRC part by 26 % and is calculated by the geometric relation between the CL and the hx that is presented in (4.1). Therefore, the overall CL length increases to $L_{\mathrm{CL}} = 1.11\,\mathrm{m}$ and the outer diameter of the CMRC part to $D_1 = 90\,\mathrm{mm}$. This adjustment of the CL, however, leads to an increase of the pressure drop of the streams and therefore, the pressure of the LP stream has to be adjusted to a larger pressure, e.g. 4 bar instead of the intended 3 bar for the case of mixture 17. Applying this changes to the numerical CMRC-CL model, yields to significant larger values of $\dot{Q}_c = 16.3\,\mathrm{W/kA}$ and $T_6 = 113\,\mathrm{K}$ in comparison to

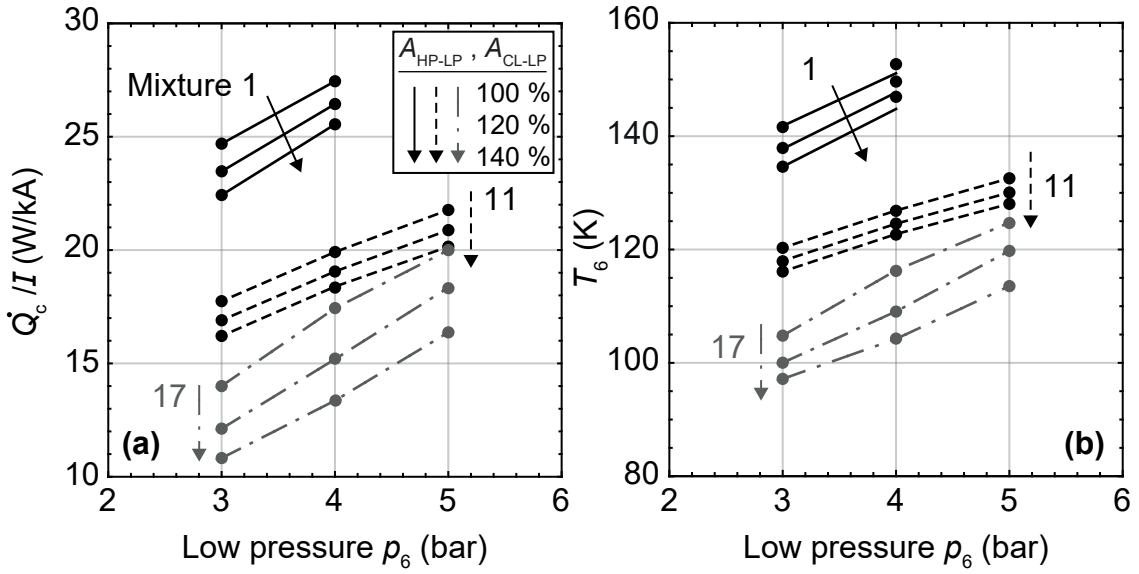

Figure 46: Thermal load at the cold end of the CL $\dot{Q}_c$ (a)and the temperature after the throttling device T_6 (b) as a function of the low pressure p_6 and the heat transfer areas between the HP and LP stream, and between the CL and the LP stream for mixtures 1, 11 and 17. Boundary conditions of the forth parametric study are used.

the minimum values that are found in this numerical thought experiment.

One of the main objectives for further optimizations of CMRC-CLs may be the increase of internal heat transfer area between the fluid streams and between the streams and the CL, without the increase of the fluid pressure drop. Further, the investigated concept of the classical tubes-in-tube heat exchanger leads to a relative large length and diameter of the CL, yielding to large geometric dimensions of the vacuum chamber.

4.8 Conclusion on the CMRC-CL with the classical heat exchanger

The cryogenic mixed refrigerant cooled current lead (CMRC-CL) show a significant reduction of the overall power consumption $P_{\mathrm{1xCL,total,el}}$, compared to other state-of-the-art closed cycle cooling systems that are presented in Tab. 23. A conventional conduction cooled system (CCCL) leads to an overall power consumption of 1190 W/kA and therefore, a factor 2.2 larger value compared to the optimal CMRC-CL with 539 W/kA, which is a reduction to 45 %. Considerable smaller values are archived only with an optimized self-sufficient vapour cooled current lead (ss-VCCL) with 280 W/kA, however, comes with the disadvantage of an open system that requires a continuous supply of LN_2. Nevertheless, because of the reduction of the thermal load at the cold end $\dot{Q}_{\mathrm{c}}$ with a CMRC-CL by about 67 % compared to a CCCL, it is possible to use a refrigeration system with a small power consumption at the 78 K temperature stage compared to single stage CCCLs, hereby reducing the overall power consumption of the system. In this work this reduction is presented for a 10 kA CL, however, the CMRC cycle is a scalable technology and can be adjusted to larger currents by increasing the heat transfer area in the recuperative heat exchanger and by increasing the circulating mass flow. However, the adjustment of the

Table 23: Cooling systems for a 10 kA current lead at 77 K. Cryocooler description refers to the refrigeration machines presented in Tab. 11. The power consumption $P_{\mathrm{total,el}}$ corresponds to $P_{\mathrm{1xCL,total,el}}$ in the case of the CMRC-CL. $\dot{Q}_{\mathrm{ex}}$ is the excess cooling power at the cold end of the CL.

Cooling system	Description	Current lead type	$\dot{Q}_{\mathrm{c}}$ W	$\dot{Q}_{\mathrm{ex}}$ W	$P_{\mathrm{total,el}}$ kW	$P_{\mathrm{total,el}}/I$ W/kA
GM cryocooler	AL600	CCCL	425	175	11.9	1190
GM cryocooler	AL300	PCL	310	10	7.7	770
PT cryocooler	PTC 330	ss-VCCL[a]	262[b]	4	12.4	1240
	PTC 330	ss-VCPCL[c]	206	12.6	31	3100
Reversed-Stirling	SPC-1	ss-VCCL[a]	246	717	10.7	1070
	SPC-1	ff-VCCL	90[a]	495	10.7	1070
	SPC-1	ss-VCPCL[c]	206	977	10.7	1070
Cryocoolers	[1]	MCCL	335	-	17.6	1760
LN_2	(3.7)	ss-VCCL[a]	246	-	2.8	280
LN_2	(3.16)	ff-VCCL	90	-	6.5	650
CMRC+GM(AL200)	$\left\{\dot{Q}_{\mathrm{c,min}}, T_{\mathrm{6,min}}\right\}^{\mathrm{d}}$	CMRC-CL	140	50	6.0	600
CMRC+GM(AL200)	$P^{\mathrm{d}}_{\mathrm{1xCL,total,el,min}}$	CMRC-CL	170	15	5.4	540

[a] with the heat transfer area multiplier $f = 100$
[b] with the mass flow of $\dot{m} = 0.396\,\mathrm{kg/(h\,kA)} < \dot{m}_{\mathrm{VCCL,ss}}$
[c] presented in the appendix (A) - VCPCL $f = \infty$ copper
[d] according to Tab. 22

heat transfer area of the classical tubes-in-tube heat exchanger leads to larger hx lengths and therefore, to larger pressure drops of the fluid streams, in particular the LP stream. Further, larger CL lengths and diameters are needed for this adjustment making the CL not a compact system. In combination with a larger mass flow, it may be necessary to adjust the LP to larger values, due to the larger pressure drop, however, as investigated in the second parametric study, the increase of the LP will lead to larger thermal loads at the cold end of the CL. Consequently, the heat transfer area has to be increased to archive lower thermal loads and is shown in the fourth parametric study. To overcome the disadvantage of a larger pressure drop, it is necessary to increase the hydraulic diameters of the streams, especially of the LP stream. However, larger hydraulic diameters of the LP stream in the classical hx design will lead to a smaller amount of hx windings and therefore, the length and the diameter of the CL has to be adjusted as well.

The author suggests to follow a different heat exchanger design concept for CMRC-CLs that comprises a larger internal heat transfer area at low pressure drops of the fluid streams, making the the CL automatically more compact. A possible solution to this design problem is the use of a micro-structured heat exchanger as the counterflow heat exchanger in the CMRC cycle, which has exactly the above mentioned qualities. Without the problematic relations between the pressure drop, the heat transfer area and the CL geometries, a micro-structured CMRC-CL that is built out of several layers [5] may be the solution for a fully scalable CMRC-CL technology. Providing that this technology is technically visible, an optimization to larger low pressures and therefore, to smaller technical work of the CMRC cycle may become relevant. The design and the numerical results of the micro-structured CMRC-CL prototype III are presented in the following Sec. 4.9. Experiments on the micro-structured heat exchanger prototype II at a CMRC test stand are presented in Sec. 5.

Finally, the temperature profiles of the investigated state-of-the-art 10 kA current leads (c.f. Sec. 3.4) are presented in Fig. 47 as a function of the individual current lead lengths L_{CL} and the coordinate x. As can bee seen from the temperature profiles at the cold end at $x = 0\,\mathrm{m}$, the temperature gradient and therefore, the thermal load at the cold end is minimal for the CMRC-CLs compared to other systems, however, larger CL lengths are needed. Depending on the boundary conditions of the refrigeration cycle, it was found that the LRS mixture 17 can lead to a minimal overall power consumption or to a minimal thermal load at the cold end. Compared to other mixtures that are given in Tab. 20, mixture 17 has a larger composition of low boilers, especially methane. Nevertheless, further investigations are needed to overcome the need of an additional cryocooler at the cold end at 78 K and develop a cascade solution with a second CMRC cycle that is connected to the lower and colder part of the CL. Consequently, the mixture in the second CMRC part needs a larger amount of low boilers, such as oxygen, nitrogen, argon, neon,

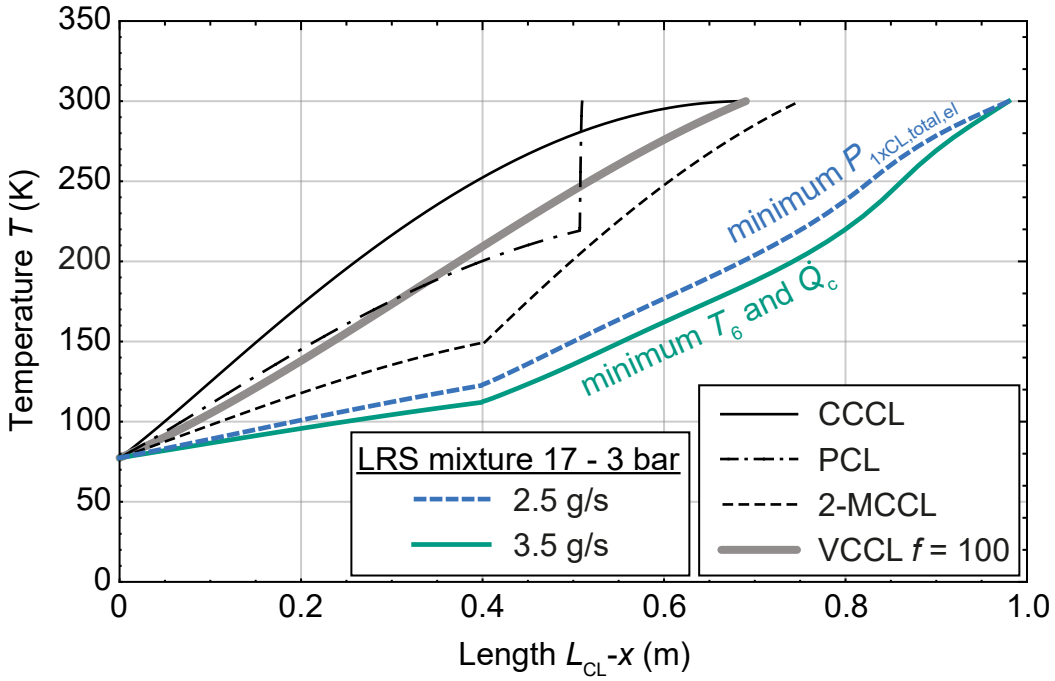

Figure 47: Temperature profiles of 10 kA conduction (CCCL), multi-stage (2-MCCL), self-sufficient vapour (VCCL $f = 100$), Peltier (PCL), according to Sec. 2.6, and two different cryogenic mixed refrigerant cycle (CMRC) cooled current leads.

hydrogen and helium [120].

4.9 Conceptual design with micro-structured heat exchanger

In order to overcome the disadvantages of the small heat transfer area, the large pressure drop of the fluid streams and the relative large geometries of the current lead in combination with the classical heat exchanger design, a new current lead prototype (III) is developed, manufactured and patented [121] in the frame of this work and is depicted in Fig. 48. The manufacturing process was conducted at the Institute for Micro Process Engineering - Institut für Mikroverfahrenstechnik (IMVT). It is a micro-structured heat exchanger (MHE) made of copper Cu-OFE (CW009A) that consists of similar micro-structured sheets like in the previous stainless steel prototypes I and II. The first MHE prototype I is investigated experimentally by Gomse in [5]. Experiments on the second prototype II are conducted in the frame of this work and are presented in the following Sec. 5. The geometries of the copper prototype III are given in Tab. 24 and in Fig. 49. It is built out of several micro-structured sheet layers of 0.5 mm thickness, each comprises 50 etched micro channels for the fluid flow. In total, ten sheets for the HP stream and 20 sheets for the LP stream are used and stacked together in the order according to Fig. 50

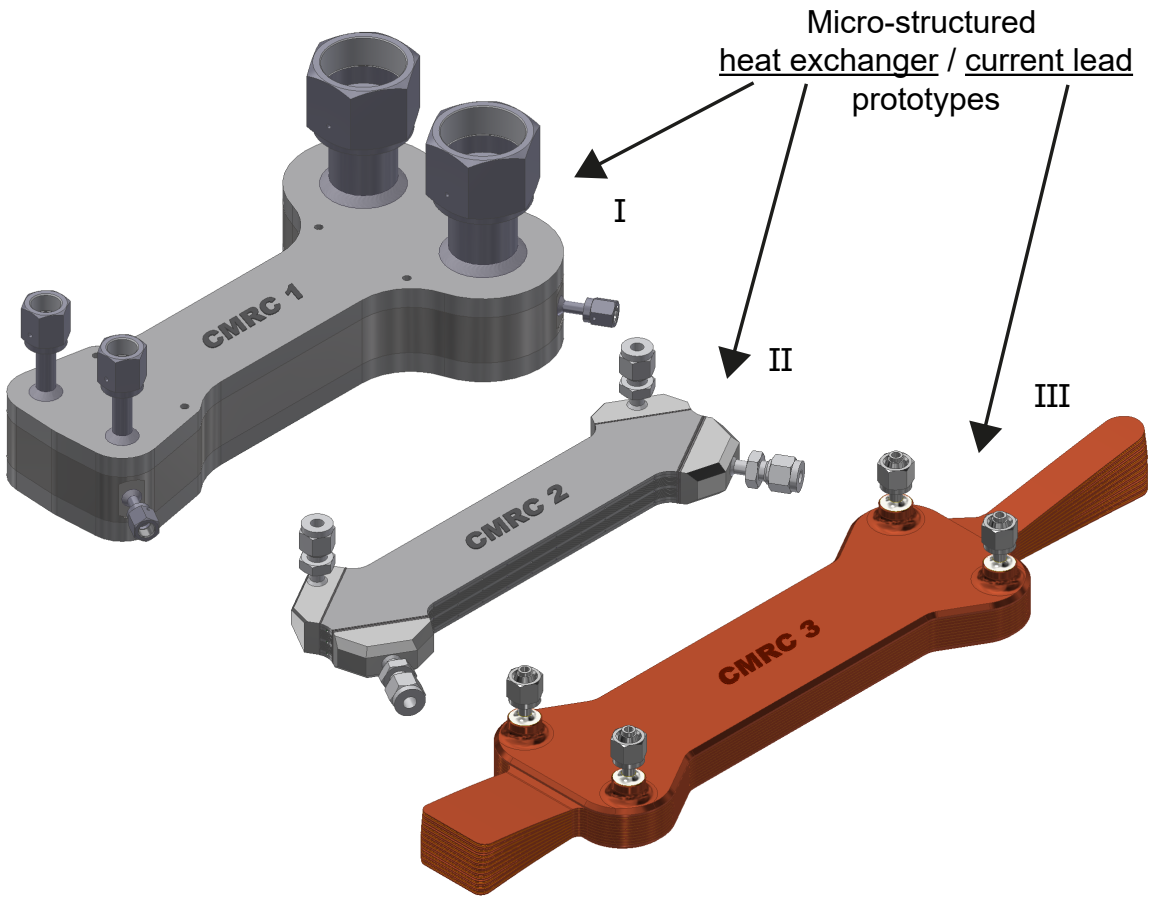

Figure 48: CAD-models of the first I (left), the second II (middle) and the third III (right) micro-structured heat exchanger prototypes.

Table 24: Overview of the MHE prototype I and II geometries.

Parameter	Prototype III
Sheets	
Thickness	0.5 mm
No of channels	50
Channel width	0.4 mm
Channel depth	0.2 mm
Channel length	227 mm
Heat exchanger	
No of sheets for HP stream	10
No of sheets for LP stream	20
Stacking pattern	face-to-back
Hydraulic diameter HP channel	0.24 mm
Hydraulic diameter LP channel	0.24 mm
Total height	21 mm
Total width	36 mm
Total length	264 mm
Volume of HX wall	1.6×10^{-4} m^3
Cross section of HX wall	6.9×10^{-4} m^2
Cross section of HX wall for current	4.8×10^{-4} m^2
Heat transfer area HP stream	0.086 m^2
Heat transfer area LP stream	0.171 m^2

with the so-called face-to-back stacking pattern. All sheets are covered by one top and bottom plate and irreversibly connected in a diffusion furnace at IMVT. The protruding

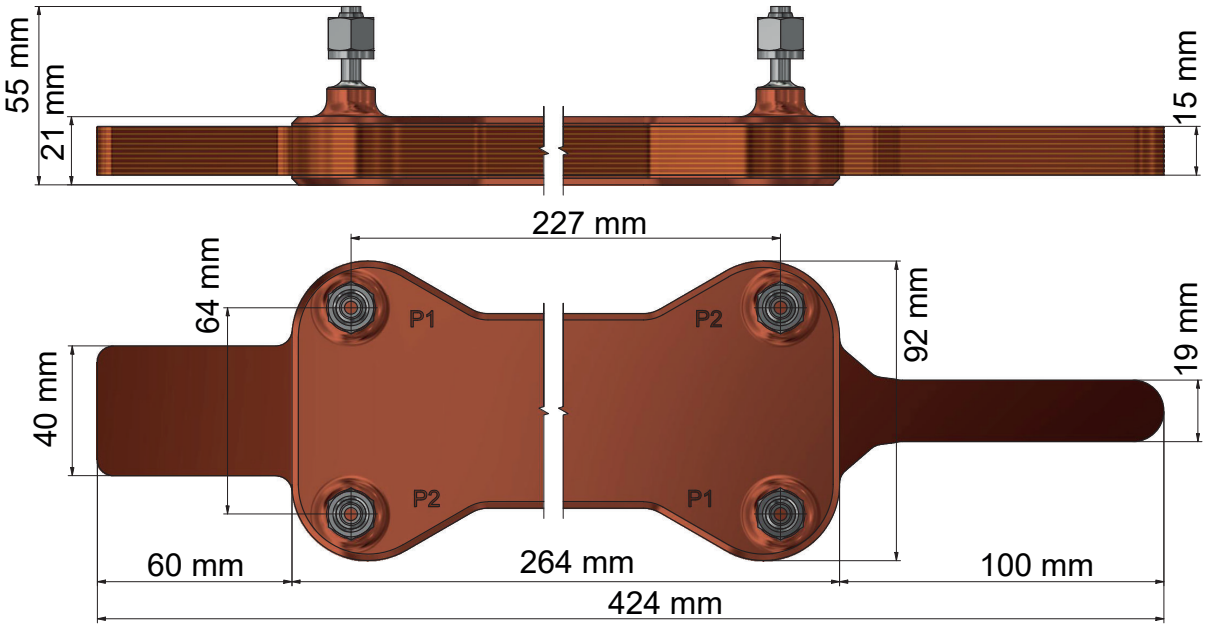

Figure 49: Design of the micro-structured heat exchanger prototype III.

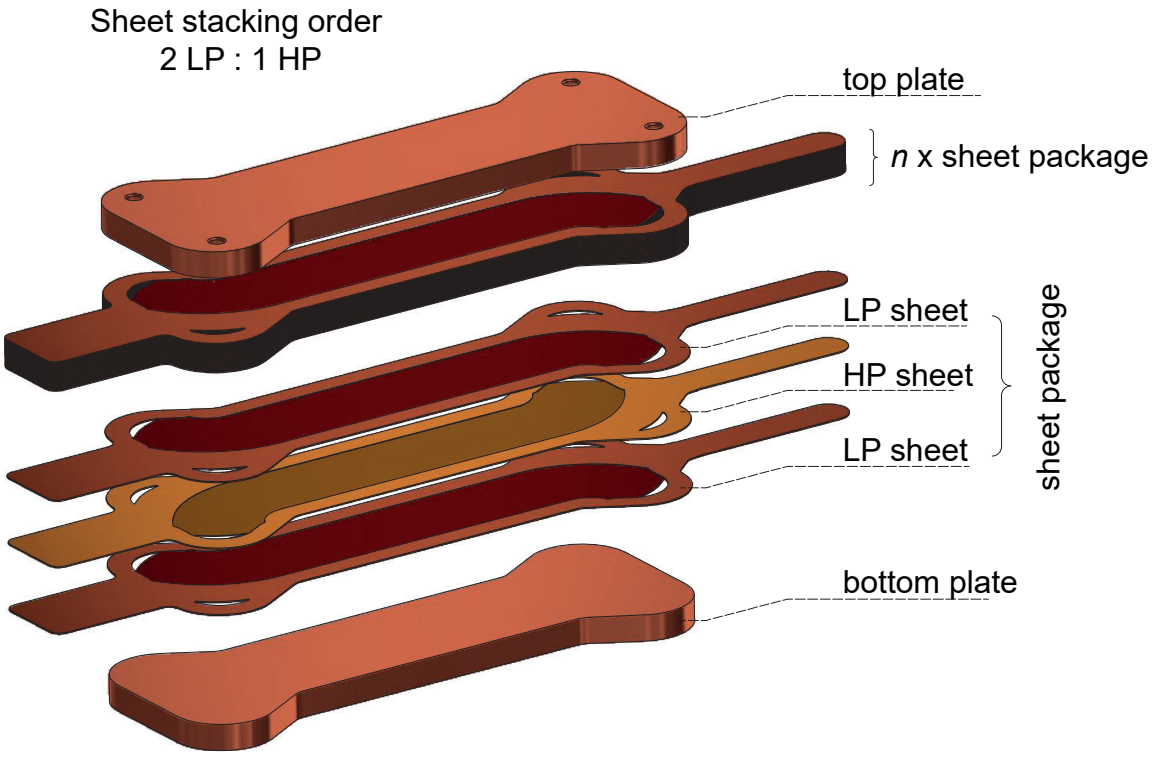

Figure 50: Sheet stacking order of the micro-structured heat exchanger prototype III.

parts of the copper sheets that are not covered by the top and bottom plates, may be used for the electric connection with a current clamp at the warm end (wide part) and with a high-temperature superconducting tape at the cold end (thin part). It is to denote that the top and bottom plates are not used for the determination of the optimal electric current flow and exclusively the total cross section of the sheets is considered. Several cylindrical flow distributing elements are implemented at both ends (inlet and outlet) of the micro-channels that should reduce the flow-maldistribution (cold bypass) of the parallel micro-channels at cryogenic temperatures. More information about this effect is found in [5] and in the following experimental investigations of the second prototype II in Sec. 5.

In the following, the computation results of the micro-structured CMRC-CL numerical model are presented for the refrigerant mixtures 17 (c.f. Tab. 20) at different mass flow rates. In contrast to the presented model in Sec. 4.3, the additional coordinate system x is not needed in the micro-structured CMRC-CL model. Therefore, no additional differential equations for the current lead, like (4.7) and (4.8), are needed and the respective contribution to the Joule heating is implemented into the cell method [5] of the wall temperature calculation. Hereby, the heat flux from ambience $\dot{q}'_{\mathrm{a}}$ which is used to implement the thermal load due to thermal radiation as a parasitic heat load into the recuperative heat exchanger [5], is extended with the specific $\left(\mathrm{W/m}\right)$ term for the Joule heating,

yielding

$$\dot{q}'_{\mathrm{a}} = \dot{q}'_{\mathrm{rad}} + \dot{q}'_{\mathrm{el}} = \dot{q}'_{\mathrm{rad}} + \frac{\rho\,(T)}{A} \cdot I^2 \tag{4.29}$$

Further, the hot end temperature of the wall/current lead is fixed at 300 K, analogous to the classical design. The respective cold end temperature is considered as an open end as defined in [5]. The following current lead types are numerically investigated:

A The manufactured micro-structured CMRC-CL prototype III (according to the geometries given in Tab. 24) at an electric current of $I = 10\,\mathrm{kA}$, yielding a shape factor of $\left(I \cdot L/A\right) = 4768\,\mathrm{kA/m}$. The inlet pressures of the HP and LP streams are set to 30 bar and 2 bar, respectively. The inlet temperature of the HP stream is set to 293.15 K. The isentropic efficiency of the compressor is set to 0.7.

B Analogous boundary conditions to **A**, however, the amount of HP and LP sheets is changed to 15 and 30, respectively. Consequently, the shape factor is reduced to 3179 kA/m.

C Analogous boundary conditions and shape factor to **A**, however, the length of the current lead and the numbers of the HP and LP sheets are doubled.

D A CMRC-CL that is designed for an electric current of 20 kA and requires a length analogous to **C** and a four times larger number of sheets compared to **A**.

In the following Fig. 51 the cold end temperatures T_6 (c.f. Fig. 21b), the thermal loads at the cold end $\dot{Q}_{\mathrm{c}}$ (b), the total power consumptions $P_{\mathrm{total,el}}$ (c) and the $k_{\mathrm{HP\text{-}LP}} \cdot A_{\mathrm{HP}}$ values (d) as a function of the mass flow $\dot{m}$ are presented for the 10 kA micro-structured CMRC-CL designs **A**, **B** and **C**. These CLs are investigated in the mass flow range of 3-7 g/s. The minimum mass flow is limited to the required cooling power (c.f. Fig. 23) that is needed to absorb the thermal load due to the Joule heating along the CL and the thermal load due to thermal conduction from the warm end. The maximum possible mass flow is limited in this study to the maximum possible pressure drop in the LP stream of 1 bar, to avoid pressures below the atmospheric pressure in the system. The manufactured CMRC-CL prototype III (here **A**) archives a minimum temperature of about $T_6 = 105\,\mathrm{K}$ and a thermal load at the cold end of $\dot{Q}_{\mathrm{c}} = 14.6\,\mathrm{W/kA}$ at a mass flow of 5 g/s and at a total specific power consumption (compressor + electric power dissipation of the CL) of about $P_{\mathrm{total,el}} = 290\,\mathrm{W/kA}$. To increase the mass flow in the current lead, it is possible to increase the amount of HP and LP sheets, decreasing hereby the sheet specific mass flow and therefore, the pressure drop of the LP stream and is investigated in the CMRC-CL **B**. With **B** it is possible to increase the mass flow to 7 g/s, yielding a larger product of overall thermal transmittance and heat transfer area $k_{\mathrm{HP\text{-}LP}} \cdot A_{\mathrm{HP\text{-}LP}}$. Consequently, the cold end temperature reduces to $T_6 = 97\,\mathrm{K}$, however, yielding a thermal load at the cold

end that is comparable to the CMRC-CL design **A**. Therefore, by increasing the amount of sheets it is possible to increase the maximum mass flow and the heat transfer area between the fluids, yielding a further reduction of the cold end temperature. A further increase of the heat transfer area is possible by increasing the current lead length and adjusting the amount of sheets to keep the CL shape factor constant and is investigated in the design **C**. With a mass flow of 6 g/s the cold end temperature is further reduced to $T_6 = 85\,\mathrm{K}$, yielding a thermal load of $\dot{Q}_\mathrm{c} = 6.5\,\mathrm{W/kA}$ and a total specific power consumption of 315 W/kA. This thermal load is smaller compared to the state-of-the-art CL design solutions (c.f. Tab. 14). However, a further device or adjustment of the CMRC cycle is needed to absorb the remaining thermal load at the cold end. Further tabulated

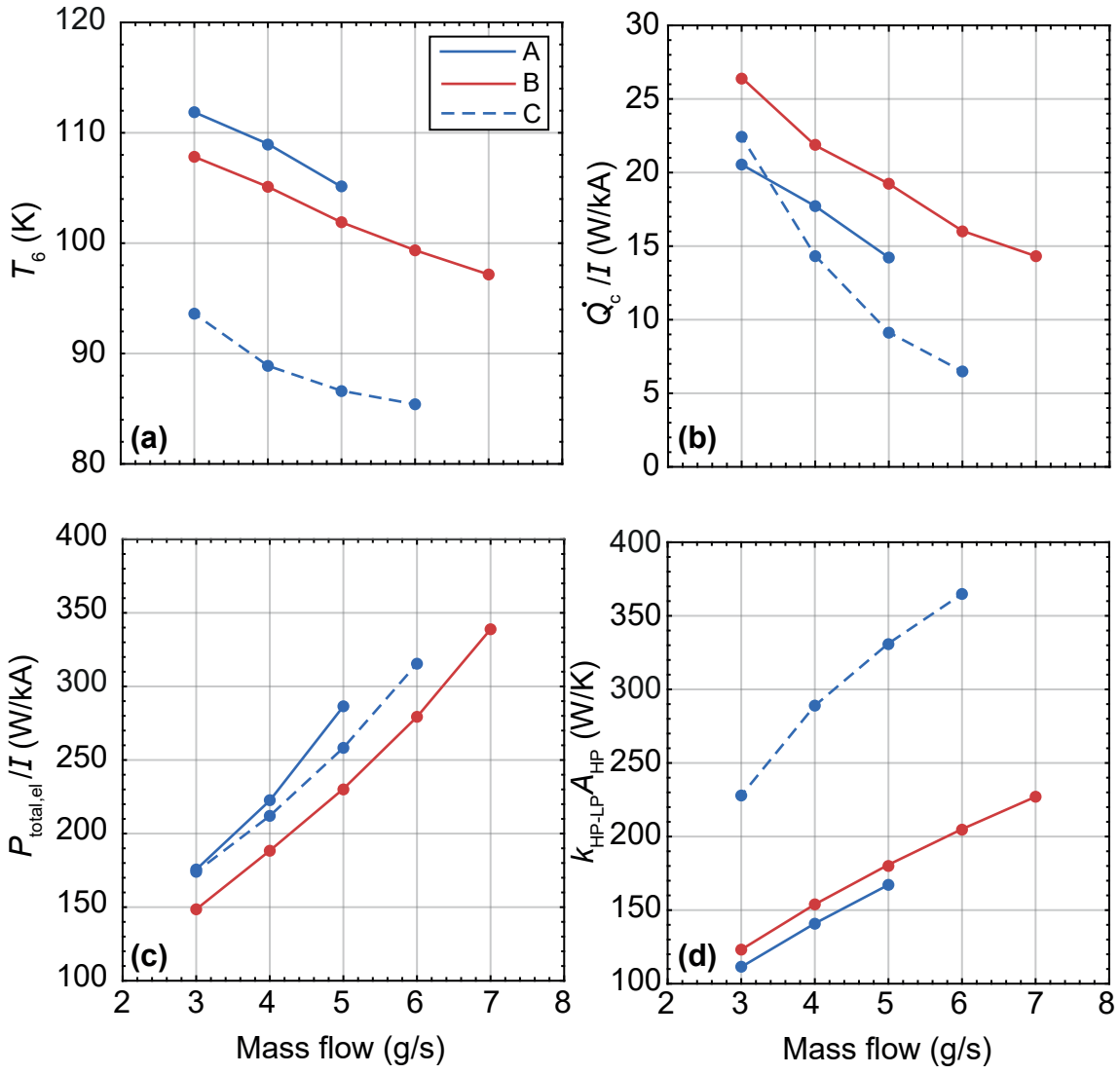

Figure 51: Temperature after the throttling device T_6 (a), thermal load at the cold end of the CL $\dot{Q}_\mathrm{c}$ (b), total power consumption $P_\mathrm{total,el}$ (c) and the $k_\mathrm{HP\text{-}LP} \cdot A_\mathrm{HP}$ value (d) as a function of the mass flow $\dot{m}$ of the 10 kA micro-structured CMRC-CL prototypes **A**, **B** and **C**.

results of the numerical investigations are given in the appendix Sec. C.

The temperature profiles of the micro-structured CMRC-CLs **A** (prototype III) and of the design **C** are presented in Fig. 52. The temperature profiles show a similar characteristic to the classical CMRC-CL design, however, smaller CL lengths are required to archive cryogenic temperatures. The pressure drops in the case **C** are 0.3 bar for the HP stream and 0.9 bar for the LP stream. Compared to the classical CMRC-CL system that leads to a minimal thermal load at the cold end (c.f. $\dot{Q}_{\mathrm{c,min}}$ in Tab. 22), the pressure drop of the HP stream in the design **C** is 27 times smaller at a 70 % larger mass flow. Consequently, the entropy production in the heat exchanger due to the HP stream pressure drop in the form of work $l_{\Delta p,\,\mathrm{HP}}$, is low as shown in Tab. 53. Further, it is interesting to denote that analogous to the classical CMRC-CL, the entropy production due to the concentration gradients $l_{\Delta c}$ is the largest contribution to the process work of the heat exchanger.

Finally, the micro-structured CMRC-CL temperature profiles are compared with the two profiles of the classical design that lead to minimal thermal load at the cold end and to minimal total power consumption (c.f. Tab. 22) in Fig. 53. As can be seen from the results, the micro-structured CMRC-CL **C** archive almost the temperature of liquid nitrogen at atmospheric pressure and offers a more compact solution compared to the classical design. The characteristics of the micro-structured CMRC-CL temperature profiles are similar to the theoretical concept of a CL with an infinite amount of refrigeration stages of the 3rd optimization method that is shown in Fig. 7. It is to denote that the classical CMRC-CLs are connected to an additional conduction cooled CL in the range of 0-0.4 m which is connected to a GM cryocooler at the cold end, while no further cold stage is considered for the micro-structured CMRC-CLs. The additional cryocooler is preliminary installed in the classical CMRC-CL system development, however, according to the results of the micro-structured CMRC-CL design **C** it is realistic to develop a system that does not need an additional cryocooler. Therefore, a further optimization has to be performed in subsequent work to determine the optimal shape factor, heat transfer area, LP and HP stream pressures and the mass flow per sheet of the new micro-structured CMRC-CL design.

To show that the micro-structured CMRC-CL technology is a scalable CL technology, a further 20 kA **D** CL design is investigated, which numerical results and geometric dimensions are given in Tab. 25. To increase the electric current of a micro-structured CMRC-CL, it is necessary to adjust the amount of sheets and/or the amount of channels per sheet and the mass flow of the fluid such, that the CMRC cycle has enough cooling power to absorb the electric power dissipation and to keep the pressure drop of the LP stream above atmospheric pressure. The 20 kA CMRC-CL requires a four times larger amount of sheets than the manufactured prototype III (**A**). However, the design **D** in comparison to the design **C** is not optimized, as can be seen from the larger thermal loads

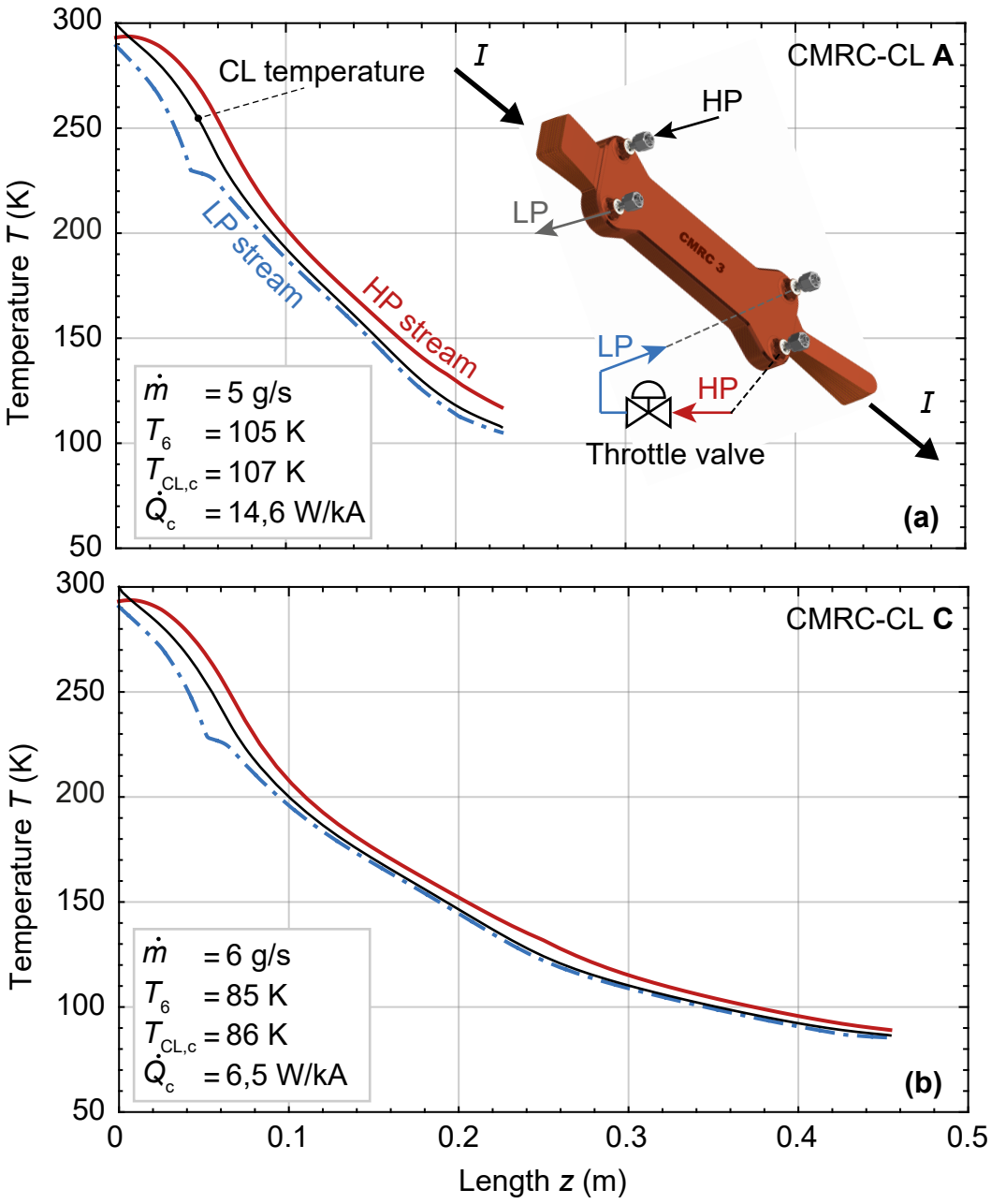

Figure 52: Temperature profiles of 10 kA micro-structured CMRC-CLs working with the mixture 17 ($T_3 = 293.15\,\mathrm{K}, p_3 = 30\,\mathrm{bar}, p_6 = 2\,\mathrm{bar}$) as a function of the current lead coordinate z. In (a) are the temperature profiles of the manufactured copper prototype III (here **A**) and in (b) are the profiles of a theoretically longer heat exchanger **C**.

at the cold end $\dot{Q}_c$ and an optimization method should be developed in the subsequent work. The development of micro-structured CMRC-CLs for larger current (e.g. 200 kA) may be possible by a similar adjustment of the number of sheets and channels, however, the length of the CL should be increased as well to reduce the thermal load at the warm end.

In conclusion, the new micro-structured cryogenic mixed refrigerant cooled current lead (micro-CMRC-CL) design shows a significant improvement over the classical CMRC-CL,

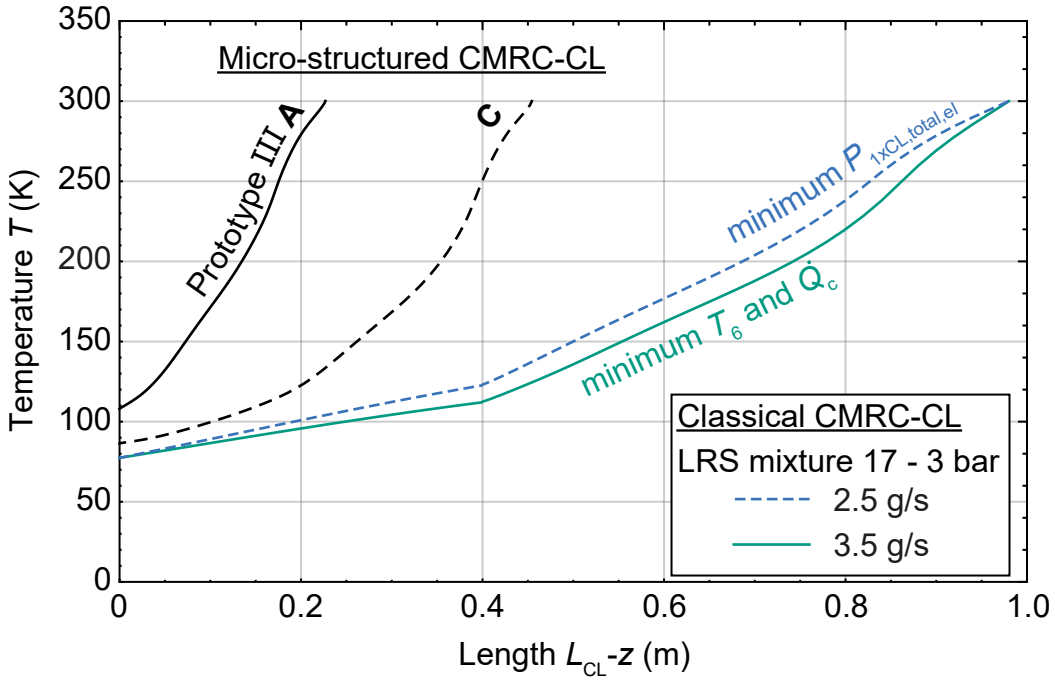

Figure 53: Temperature profiles of two classical and two micro-structured CMRC cooled current leads at an amperage of 10 kA. The classical CMRC-CLs are additionally connected to a GM cryocooler.

Table 25: Summary of the parameters and geometries of the investigated micro-structured CMRC-CLs. The respective tabulated results of the numerical investigation are given in the appendix Sec. C.

Parameter	Micro-structured CMRC-CL designs			
	A	**B**	**C**	**D**
Current (kA)	10	10	10	20
Mass flow (g/s)	5	7	6	8
T_6 (K)	105	97	85	87
$k_{\text{HP-LP}} \cdot A_{\text{HP-LP}}$ (W/K)	167	227	365	567
$\dot{Q}_c/I$ (W/kA)	14.2	14.3	6,5	11,3
$P_{\text{total,el}}/I$ (W/kA)	286	339	315	219
No of sheets for HP stream	10	15	20	40
No of sheets for LP stream	20	30	40	80
No of channels	50			
Total height (mm)	21	29	36	66
Total width (mm)	36			
Channel length (mm)	227	227	528	
Heat transfer area HP stream (m^2)	0.086	0.128	0.342	0.685
Heat transfer area LP stream (m^2)	0.171	0.257	0.685	1.370

due to the enhanced heat exchanger performance of the micro-structured sheets. The numerical results of the manufactured CMRC-CL prototype III (design **A**) show that it is not fully optimized for the electric current of 10 kA, however, it already shows the smallest thermal load at the cold end $\dot{Q}_c$ compared to the state-of-the-art CL solutions that are summarized in the following Tab. 26. Further, the successfully diffusion bonding manufacturing process of the copper prototype is an important milestone in the micro-structured CMRC-CL development. It was not possible to investigate the new prototype experimentally, during the time frame of this work. Therefore, experiments in the CMRC setup that is introduced in section Sec. 5, should be conducted to investigate the cool down behaviour of the copper prototype III with different refrigerants, especially with LRS mixtures.

In the ensuing numerical investigation of possible CL designs, it was found that it is possible to archive cryogenic temperatures down to 85 K with the hydrocarbon based mixture 17 with the 10 kA CMRC-CL design **C**, yielding a thermal load at the cold end as low as 6.5 W/kA. Compared to a CCCL that is working in this temperature range, this is a 85 % reduction of the thermal load and therefore, the largest reduction compared to the state-of-the-art solutions. Furthermore, it is possible to adjust the amount of LP and HP sheets, the number of channels per sheet, the length and also the fluid mass flow for a required electric current without the geometric problems that occur with the classical design (c.f. Sec. 4.8). In the frame of this work, the geometric dimensions and the mass flow for a 20 kA CMRC-CL are found, however, the design has potential for further optimization. To follow the concept of the CL comparison in this work that is presented in Tab. 26, the CMRC-CL design **C** is extended by an additional cooling machines (GM-AL60) at the cold end to absorb the remaining thermal load $\dot{Q}_c$. With a total power consumption (compressors + electric power dissipation) of 490 W/kA, the micro-structured CMRC-CL system is the most efficient closed-cycle system. Considerable smaller values are archived only with an optimized self-sufficient vapour cooled current lead (ss-VCCL) with 280 W/kA, however, comes with the disadvantage of an open system that requires a continuous supply of LN_2. However, it is to denote that it is realistic to develop CMRC-CL systems that do not need an additional cryocooler and temperatures below 85 K are possible by an adjustment of the refrigerant mixture and/or the refrigerant cycle and is discussed in the following section Sec. 5.

Table 26: Cooling systems for a 10 kA current lead at 77 K. Cryocooler description refers to the refrigeration machines presented in Tab. 11. The power consumption $P_{\mathrm{total,el}}$ corresponds to $P_{\mathrm{1xCL,total,el}}$ in the case of the classical CMRC-CL. $\dot{Q}_{\mathrm{ex}}$ is the excess cooling power at the cold end of the CL.

Cooling system	Description	Current lead type	$\dot{Q}_{\mathrm{c}}$ W	$\dot{Q}_{\mathrm{ex}}$ W	$P_{\mathrm{total,el}}$ kW	$P_{\mathrm{total,el}}/I$ W/kA
GM cryocooler	AL600	CCCL	425	175	11.9	1190
GM cryocooler	AL300	PCL	310	10	7.7	770
PT cryocooler	PTC 330	ss-VCCL[a]	262[b]	4	12.4	1240
	PTC 330	ss-VCPCL[c]	206	12.6	31	3100
Reversed-Stirling	SPC-1	ss-VCCL[a]	246	717	10.7	1070
	SPC-1	ff-VCCL	90[a]	495	10.7	1070
	SPC-1	ss-VCPCL[c]	206	977	10.7	1070
Cryocoolers	[1]	MCCL	335	-	17.6	1760
LN_2	(3.7)	ss-VCCL[a]	246	-	2.8	280
LN_2	(3.16)	ff-VCCL	90	-	6.5	650
CMRC+GM(AL200)	$\left\{\dot{Q}_{\mathrm{c,min}}, T_{6,\mathrm{min}}\right\}^{\mathrm{d}}$	CMRC-CL[e]	140	50	6.0	600
CMRC+GM(AL200)	$P^{\mathrm{d}}_{\mathrm{1xCL,total,el,min}}$	CMRC-CL[e]	170	15	5.4	540
CMRC+GM(AL60)	Design **C**	CMRC-CL[f]	65	-5	4.9	490

[a] with the heat transfer area multiplier $f = 100$
[b] with the mass flow of $\dot{m} = 0.396\,\mathrm{kg/(h\,kA)} < \dot{m}_{\mathrm{VCCL,ss}}$
[c] presented in the appendix (A) - VCPCL $f = \infty$ copper
[d] according to Tab. 22
[e] CMRC-CL with a classical heat exchanger
[f] CMRC-CL with a micro-structured heat exchanger

5 Experimental investigation of the micro-structured heat exchanger

In this chapter, the experimental framework of this work and the preceding results of the first micro-structured heat exchanger (MHE) prototype I that were conducted by Gomse et al. [5] are introduced. This is followed by the presentation of the performance and the operation characteristics of the MHE second prototype II, which is experimentally investigated in the frame of this work. The CAD models of the first and the second prototype are given in Fig. 54. These MHE prototypes were produced by diffusion bonding of several micro-structured sheets made of stainless steel (1.4571), which have 50 etched micro channels each. The corresponding experimental data are analysed and compared with the heat exchanger model of Gomse [5], which is adapted and modified for the second prototype II. Further, the analysis of the process work of the refrigeration cycle and the entropy production rates inside the MHE are presented.

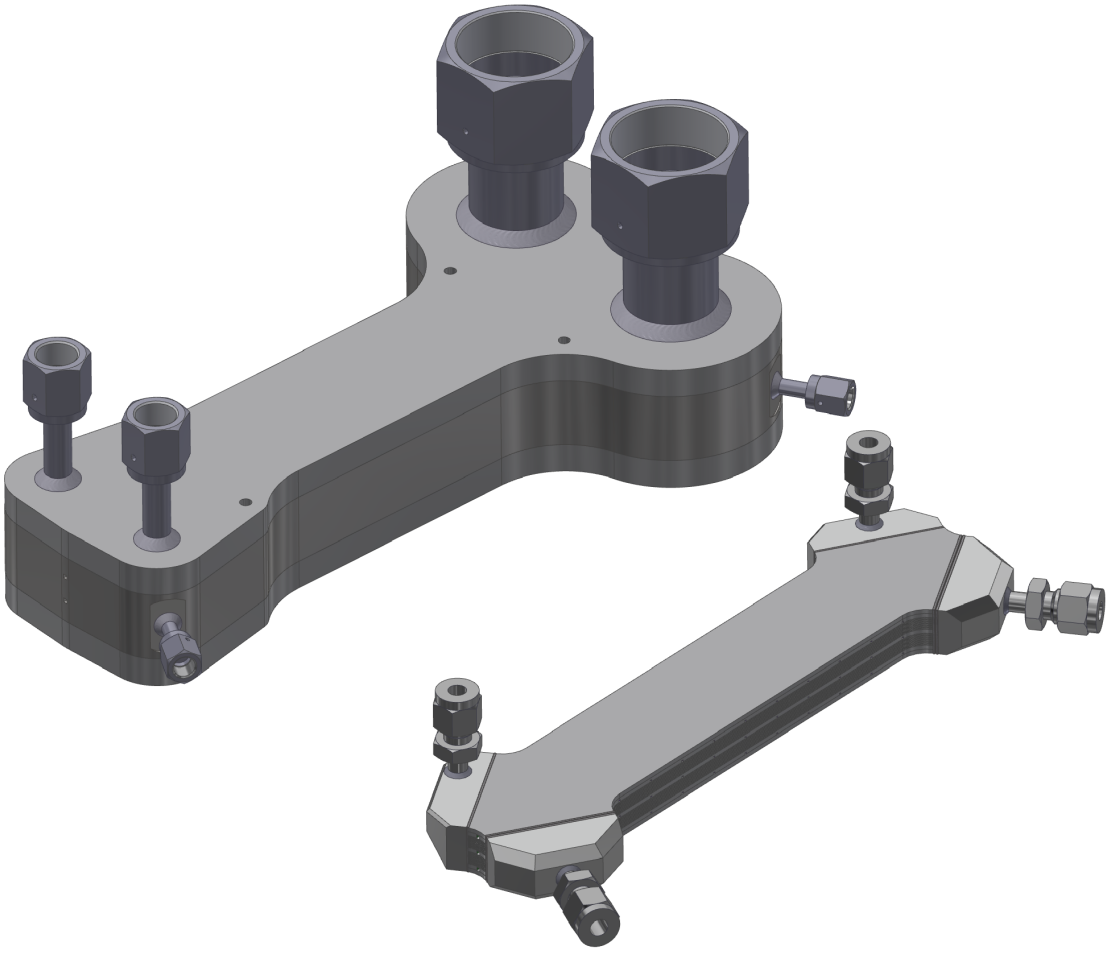

Figure 54: CAD-models of the first I (left) and the second II (right) micro-structured heat exchanger prototypes, taken from [5].

5.1 Experimental framework

The experimental studies of both MHE prototypes I and II are conducted in the CMRC test stand at the Institute of Technical Thermodynamics and Refrigeration - Institut für Technische Thermodynamik und Kältetechnik (ITTK). The experimental setup is originally build by Kochenburger [4] and is already well described in his work, as well as in [5, 122]. Therefore, the schematic representation of the CMRC setup that is shown in Fig. 55 is only briefly described here.

The P&ID of the CMRC test stand is shown in Fig. 55 and consists of a warm section that contains an air cooled compressor, an aftercooler, an oil-separation system, a buffer management system, a filling and sampling system and a cold section which is installed in a vacuum chamber. The cold section contains the three inner heat exchangers (HX1, HX2 and HX3), a throttling device and an evaporator. The heat exchanger HX 2 is connected to the R404a cooling cycle, which may be used for the pre-cooling or the temperature control of the HP stream inlet to the main heat exchanger HX 3, however, the pre-cooling cycle is not used in the experiments with the second prototype II. The investigated MHE prototypes I and II are installed at the position of the HX 3.

The fluid temperatures and pressures at the inlet and outlet of the HX 3 (c.f. point 5,6,10 and 11 in Fig. 55) are measured with Pt100 $^1/_{10}$ class B and Danfoss AKS32 sensors, respectively. Additionally, Fibre Bragg Grating (FBG) temperature sensors are used to measure the temperature profile along the MHE I and II, which have 19 measurement points each. In the case of prototype I, initially two FBG sensors were used [5], however, due to a damage of one sensor some results are presented with one FBG sensor only. The investigated MHE prototyp II in this work, has two FBG sensors installed that are placed inside the MHE at the top and bottom plates, however, one sensor showed negative temperature values on the Kelvin scale and therefore, the corresponding values are excluded from the experimental results. The details on the calibration process of the FBG sensors and their basic working concept, as well as further information of the instrumentation shown in Fig. 55, are given in [5].

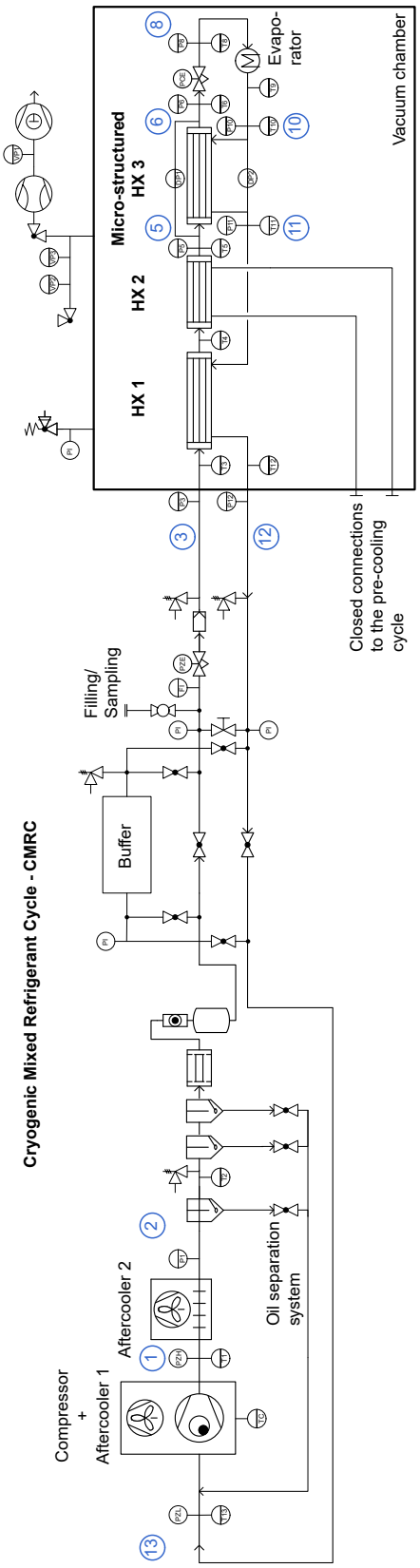

Figure 55: Piping and instrumentation diagram (P&ID) of the CMRC test stand, adapted from [4]. The test stand volume is about $8.13 \pm 0.06\,\mathrm{L}$ [122].

Table 27: Molar compositions and the LP stream inlet temperatures T_{10} (c.f. Fig. 55) after the throttling of the most important experimentally investigated refrigerant mixtures in prototype I by Gomse et al. [5] . The designation nomenclature of the experiments and of the refrigerant mixtures refer to [5]. A detailed summary on the respective test conditions are found in Tab. 8.2 in [5].

Experiment	Mixture	Nitrogen	Methane	Ethane	Propane	$T_{\mathrm{LP,in}}\,(T_{10})$
		mole - % charged mixture				(K)
Run 21	1	30	25	15	30	202.5
Run 23	3	**0**	30	30	40	133.0
Run 25	4	14	26	26	34	106.0

5.2 Preceding experimental results of prototype I

In this subchapter, three important preceding experiments of the MHE prototype I (c.f. Fig. 54) that were conducted by Gomse et al. [5] are briefly introduced. The molar compositions of these experiments, as well as the corresponding LP fluid temperatures after the throttling device $T_{\mathrm{LP,in}}$ are given in Tab. 27. The temperature profiles on the MHE prototype I for the first two experiments, Run 21 and Run 23, are presented in Fig. 56. In the first experiments (Run 21 - Mix 1) that is shown in Fig. 56a, the LP inlet temperature is at about 200 K. First, it is about 70 K higher than intended operating temperature and second, the measured wall temperatures show higher temperatures than the HP fluid outlet temperature. This indicates that the MHE prototype I is not cooled homogeneously in this experiment and implies a fluid flow-maldistribution over the heat

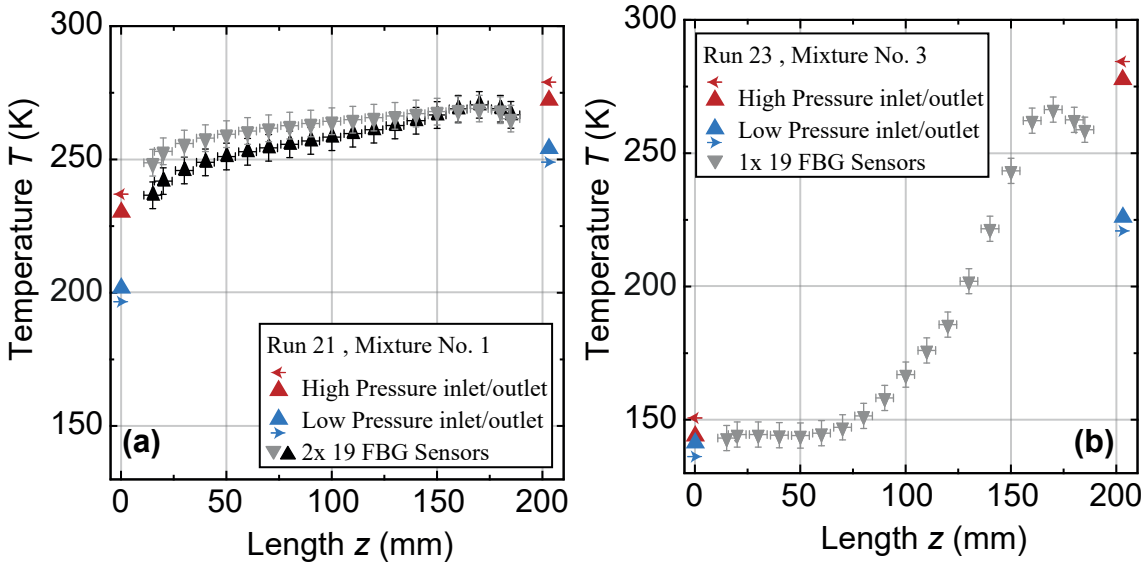

Figure 56: Experimental data of the MHE prototype I, conducted by Gomse et al. [5]. The molar compositions of the investigated mixtures in (a) and in (b) are depicted in Tab. 27.

exchanger height [5]. This effect is a common problem in cryogenic systems with parallel passages and is also referred to as cold bypass. The main reasons for a cold bypass are the different pressure drop characteristics of the liquid and vapour flow in combination with the heat flux dependency of the boiling pressure drop, yielding higher flow rates through colder channels of the MHE. A large thermal mass and a low thermal conductivity of the MHE favour the development of this flow-maldistribution. A more detailed analysis of this effect is given in [5].

In Fig. 56b the MHE temperatures of the second experiment (Run 23) are presented, however, with a nitrogen free mixture 3, which has a larger specific refrigeration power and a larger liquid fraction at higher temperatures during the cool-down, compared to the mixture 1. In this experiment, no flow-maldistribution is observed and LP fluid temperatures down to $T_{\mathrm{LP,in}} = 133\,\mathrm{K}$ are archived. In the third subsequent experiment (Run 25), nitrogen is filled into the running CMRC system that is operating with the mixture 3, yielding a new mixture 4 with a different composition according to Tab. 27. Hereby, a further cool-down of the LP stream down to a temperature of 106 K is achieved. The measured pressure drop of the HP and LP streams in Run 25 at a mass flow of about $1.12\,\mathrm{g/s}$ is equal to $8.5 \times 10^{-3}\,\mathrm{bar}$ and $0.06\,\mathrm{bar}$, respectively. In these experiments, no heat load in the evaporator is applied. It is interesting to denote, that after the warm up of the system with the mixture 4 and a repeated cool down (Run 27 [5]), a LP stream temperature of only 157 K is reached. Therefore, a specific cool-down procedure is needed for the first MHE prototype I to achieve cryogenic temperatures. Based on that, an invention disclosure [123] was submitted that generally describes an automatic liquid cool-down of mixed-refrigerant cycles (ALC-MRC).

5.3 Experimental results of prototype II

In order to overcome the disadvantages of the flow-maldistribution and the relative large mass of the first prototype, a new MHE prototype II (c.f. Fig. 54) was designed by Gomse [5] and is experimentally investigated in the frame of this work. The main differences in the geometry parameters between the two prototypes are listed in Tab. 28. The geometries of the micro-structured sheet are the same in both prototypes, however, the stacking pattern and the amount of used sheets are different. In the prototype I, a face-to-face stacking pattern is used in the manufacturing process, yielding round channels for the fluid flow. The second prototype II was build with a face-to-back pattern that yields half round channels and therefore, a smaller hydraulic diameter. Generally, the cross section area of the heat exchanger wall is about one order of magnitude smaller for the prototype II, due to the smaller amount of sheets and an additional mill off process, and results in a considerable smaller longitudinal heat conduction along the MHE. Consequently, the mass of the second prototype II is about 60 % smaller compared to the prototype I. However, the heat transfer area of the HP stream in the case of prototype II is reduced by about

Table 28: Overview of the MHE prototype I and II geometries.

Parameter	Prototype I	Prototype II
Sheets		
Thickness	0.3 mm	
No of channels	50	
Channel width	0.4 mm	
Channel depth	0.2 mm	
Channel length	203 mm	
Heat exchanger		
No of sheets for HP stream	30	10
No of sheets for LP stream	30	20
Stacking pattern	face-to-face	face-to-back
Hydraulic diameter HP channel	0.324 mm	0.240 mm
Hydraulic diameter LP channel	0.322 mm	0.240 mm
Total height	43 mm	16.5 mm
Total width	50 mm	36 mm
Total length	261 mm	234 mm
Volume of HX wall	$4.2 \times 10^{-4}\,\mathrm{m}^3$	$1.1 \times 10^{-4}\,\mathrm{m}^3$
Cross section of HX wall	$2.1 \times 10^{-3}\,\mathrm{m}^2$	$5.3 \times 10^{-4}\,\mathrm{m}^2$
Heat transfer area HP stream	$0.155\,\mathrm{m}^2$	$0.076\,\mathrm{m}^2$
Heat transfer area LP stream	$0.155\,\mathrm{m}^2$	$0.153\,\mathrm{m}^2$

the half, whereby the heat transfer area of the LP stream is approximately the same. Further, the MHE fluid inlet headers of the prototype II are redesigned in order to align the incoming fluid flow with the channels, i.e a 90° bend of the inlet headers compared to the first prototype (c.f. Fig. 54).

In the frame of this work and of Arnsberg [122], in total ten cool-down (CD-0 to CD-4.3) experiments are conducted, whereby the most important experiments are listed in Tab. 29 with the respective investigated mixture compositions. The respective experimental data are summarized in the appendix Sec. D. Further information about the uncertainty calculations are found in the appendix B in [5]. The designation nomenclature of the experiments and of the refrigerant mixtures, as well as the molar compositions of the circulating mixture that are given in brackets, refer to the work of Arnsberg [122]. In [122], the gravimetrically determined mixture compositions are further analysed in a gas chromatograph. This investigation is necessary, because of the mixture composition shift during the CMRC operation, due to a possible leakage, liquid hold-up in some parts and the different solubilities of the mixture components in the compressor oil [122]. The experiments are carried out without the activation of the evaporator. The first experiment CD-0, which is also published in [124], the prototype II was in operation at temperatures down to 85 K, without an adjustment of the cool-down procedure like it was done with the prototype I. Unfortunately, the mixture composition that is stated in [124] is not correct

Table 29: Molar compositions of the experimentally investigated hydrocarbon-based refrigerant mixtures and the corresponding LP stream inlet temperatures T_{10} (c.f. Fig. 54) after the throttling. The designation nomenclature of the experiments and of the refrigerant mixtures, as well as the molar compositions of the circulating mixture that are given in brackets, refer to the work of Arnsberg [122]. The respective experiential data are summarized in the appendix Sec. D.

Experiment	Mixture	Neon	Nitrogen	Methane	Ethane	Propane	$T_{\mathrm{LP,in}}\,(T_{10})$
	mole - % charged mixture (mole - % circulating mixture)						(K)
CD-0 [124]	CMR-1	0	22 (25)	28 (30)	17 (16)	33 (29)	85.66 ± 1.43
CD-3	CMR-1	0	23 (24)	28 (30)	16 (16)	33 (30)	88.89 ± 1.41
CD-3-1	CMR-1.1	4	22	27	16	31	-
CD-3-2	CMR-1.1	4	22	27	16	31	90.71 ± 1.40
CD-4-1	CMR-1	0	22	28	17	33	89.42 ± 1.40
CD-4-2	CMR-1.1	4	22	27	16	31	95.24 ± 1.40

and the valid values for CD-0 are given in this work and in [122]. After a warm-up of the test stand and a new refilling of the mixture CMR-1 for a repetition of the experiment CD-0, in CD-3 a slightly higher temperature of the LP stream inlet to the MHE of 89 K is achieved. Comparing the results of CD-3 with the prototype I experiment Run 25, a significant smaller temperature is achieved with the second prototype II. The measured pressure drop of the HP and LP streams in CD-0 at a mass flow of about 0.38 g/s is equal to 0.43 bar and 0.05 bar, respectively. This is about two orders of magnitude larger pressure drop in the HP stream at about the thirds of the mass flow, compared to the Run 25 of the first prototype I. That is mainly based on the considerable smaller amount of sheets for the HP stream and a reduced hydraulic diameter of the channels in the second prototype II.

The purpose of the experiments CD-3-1 to CD-4-2, is the investigation of a further cool-down of the fluid to temperatures down to about 65 K, through the addition of neon into the mixture. This further temperature decrease is based on the reduction of the evaporation temperature, due to the reduction of the partial pressures of the other components in the mixture. Experimental investigations of hydrocarbon mixtures in combination with neon in CMRCs, are already made by Wilke [120], Walimbe et al. [125], Vineed et al. [126] and Mostytskyi et al. [127] and achieved temperatures down to 65 K with a neon mole fraction of below 10 % in their experimental test stands.

In the first neon experiment CD-3-1, the gas is added into the operating system with a standard ball valve, right after the experiment CD-3. After a short period, the pressure of the HP stream started to increase and of the LP stream to decrease. Consequently, the pressure switch has shut down the compressor. It is suggested that neon formed a gas bubble in the HP stream without mixing with the other components and blocked the

throttling valve that was opened to about 6 %. After a warm-up of the test stand and a new cool-down with the neon mixture CMR-1.1, temperatures down to 91 K are achieved.

In next experimental runs CD-4-1 and CD-4-2, the standard valve is changed to a fine control valve for a more controlled neon filling procedure. After the initial cool-down in CD-4-1 to about 90 K, neon is filled in portions into the system in the experiment CD-4-2. During the addition of neon, strong mass flow fluctuations and no blockage of the throttling valve have been observed. Further, the mass flow has slightly increased from about 0.48 g/s to 0.52 g/s (c.f. Tab. 58). Contrary to the expectation of a further temperature decrease of the mixture like it is observed in [120], the temperature of the LP stream inlet increased to about 95 K. Arnsberg [122] found out that the specific cooling power of the mixture reduces after the addition of neon, this effect is also described in [96]. Consequently, the heat load into the system due to heat radiation and longitudinal thermal conduction, that remained approximately constant, and the larger mass flow from CD-4-1 to CD-4-2, yield inevitable to larger temperatures at the cold end. Arnsberg [122] performed further experiments (CD-5 to CD-7) with neon and slightly different mixture compositions, however, without a further temperature decrease below 87 K. The author suggest to conduct further neon experiments with a mixture that includes an additional high-boiling component isobutane, like it is used in the experiment 2 in [127] where a temperature decrease in the range of 65-75 K is observed. The corresponding molar compositions of the refrigeration mixture that is investigated by Mostytskyi et al. [127], are given in Tab. 30. However, a butane mole fraction of 40 % leads to a high risk of a freeze-out of this component and can lead to a blockage of the throttling device. Therefore, it may be necessary to implement an additional phase separator for butane after the first internal heat exchanger HX 1 in the current test stand or additional components for an automatic cool-down that can reduce the concentration of the high boilers during the cool-down automatically [123] without the need of additional heat exchangers in the cycle.

Table 30: Molar compositions of the refrigeration mixture with neon investigated by Mostytskyi et al. [127], yielding a temperature decrease in the range of 65-75 K.

Exp.	Neon	Nitrogen	Methane	Ethane	Propane	Butane	p_{HP}	p_{LP}
			mole - %				(bar)	
2 [127]	5	20	15	10	10	40	18-20	1.0-1.5

Table 31: Correlations used in the numerical calculation of the micro-structured heat exchanger. The correlations are valid for hydrocarbon-based mixtures.

Mechanism	Correlation
Single phase heat transfer	
Laminar	VDI Heat Atlas - G1 (3.2.1) [109]
Turbulent	Dittus-Boelter equation
Two-phase heat transfer	
Pure boiling (modified Little)	Gomse [5, 118]
Nucleat boiling correction factor F_c	Thome and Shakir [111]
Mixture boiling (modified Little)	Gomse [5, 118]
Mixture condensation (modified Little)	Gomse [5, 118]
Pure condensation	Cavallini [113]
Frictional pressure drop	
Single phase flow $f\,(Re)$	VDI Heat Atlas - L1.2 (1.1-1.2) [109]
Two-phase flow $f\,(Re)$	Lockhart and Martinelli [114]
Void fraction	
Separated flow	Baroczy [128]

Re - Reynolds number

In the following, the measured temperature data along the MHE prototype II of the experiment CD-3 are compared with the modified numerical model of Gomse [5]. Heat transfer, pressure drop and void fraction correlations used in the computation of the micro-structured heat exchanger are listed in Tab. 31. The hot and cold ends of the wall within the cell method are considered as adiabatic ends, as defined in [5]. The corresponding experimental data and numerical temperature profiles are presented in Fig. 57. The calculated temperature profiles of the HP and LP streams, as well as the wall temperature, are given in Fig. 57a with the composition of the charged mixture and in Fig. 57b with the composition of the circulating mixture, according to CMR-1 in Tab. 29. The fluid inlet and outlet temperatures are measured with Pt100 sensors and the temperature distribution along the MHE with one FBG sensor which has 19 measurement points (gratings). Despite the small difference in the mixture composition of CMR-1 between the charged (a) and the circulating (b) mixture (c.f. Tab. 29), a significant shift of the calculated temperature profiles in axial direction z is evident in Fig. 57b. Consequently, the temperature profiles that are calculated with the circulating mixture in (Fig. 57b) show a good agreement with the measured data of the FBG sensor in the range of about 270-170 K. Below 170 K the numerical results predict considerable smaller temperature values, as well as a significantly different gradients. The numerical model predicts the phase change of the component methane at an axial position of about 110 mm, which is typically indicated by the temperature gradient change in the range of 100-120 K, whereby the FBG sensors show a slope between the 18th and 19th grating at

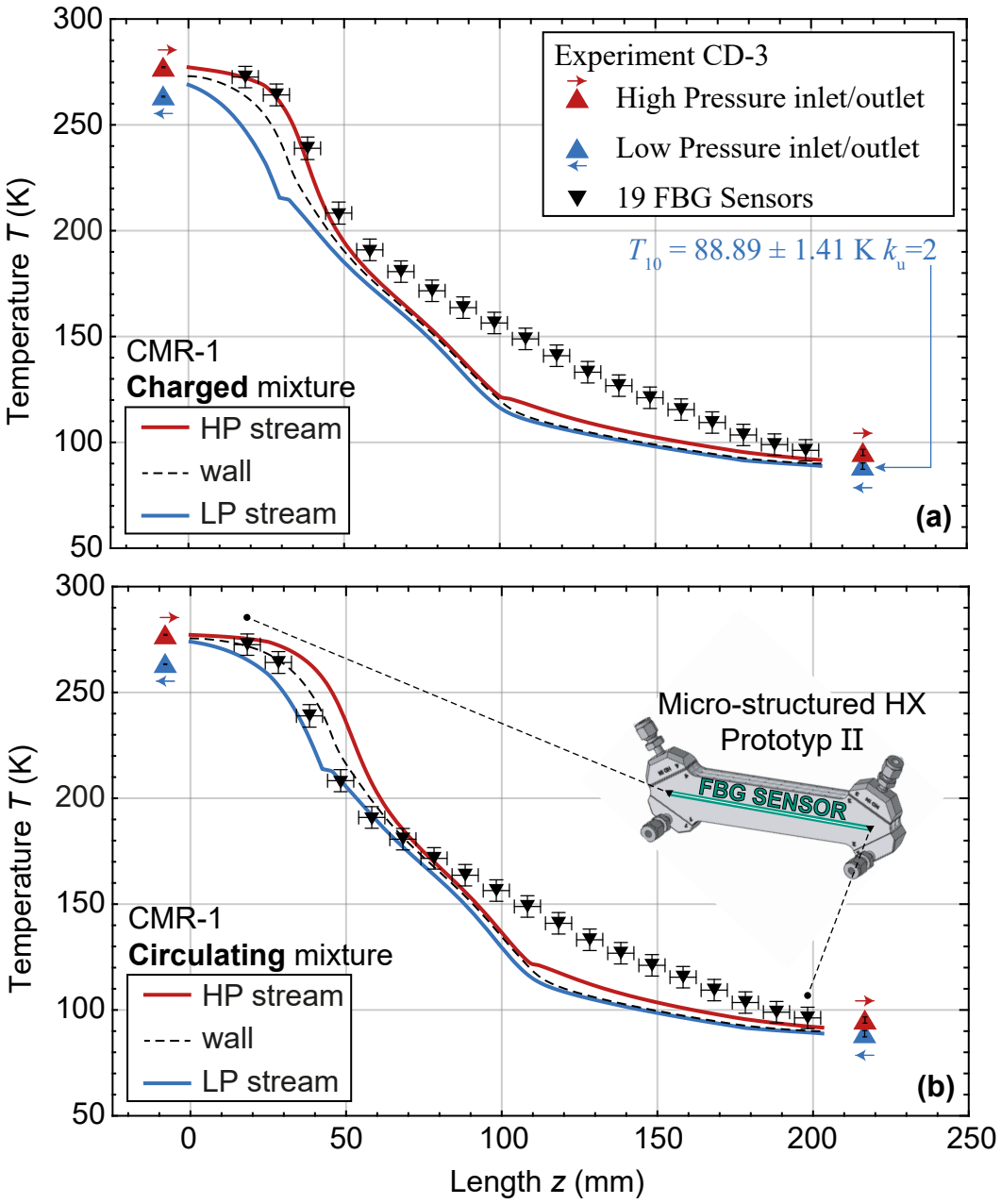

Figure 57: Temperature data of the experiment CD-3 and numerical temperature profiles of the micro-structured heat exchanger prototyp II. The calculations of the temperature profiles of the HP and LP streams, as well as the wall temperature, are performed in (a) with the composition of the charged mixture and in (b) with the composition of the circulating mixture, according to CMR-1 in Tab. 27.

the end of the MHE. Further, the linear dependence of the FBG sensor temperature data with z, between 50 mm and 200 mm, is obvious and indicates to an inefficient cooling by the fluid. The FBG sensor is placed directly between the top plate of the MHE and the first LP stream sheet. Therefore, the FBG sensor mainly measures the temperature profile of the top plate, which is mainly cooled by only one LP stream sheet. A strong cooling effect is observed in the range of 30-90 mm, due to the evaporating refrigerant in the LP

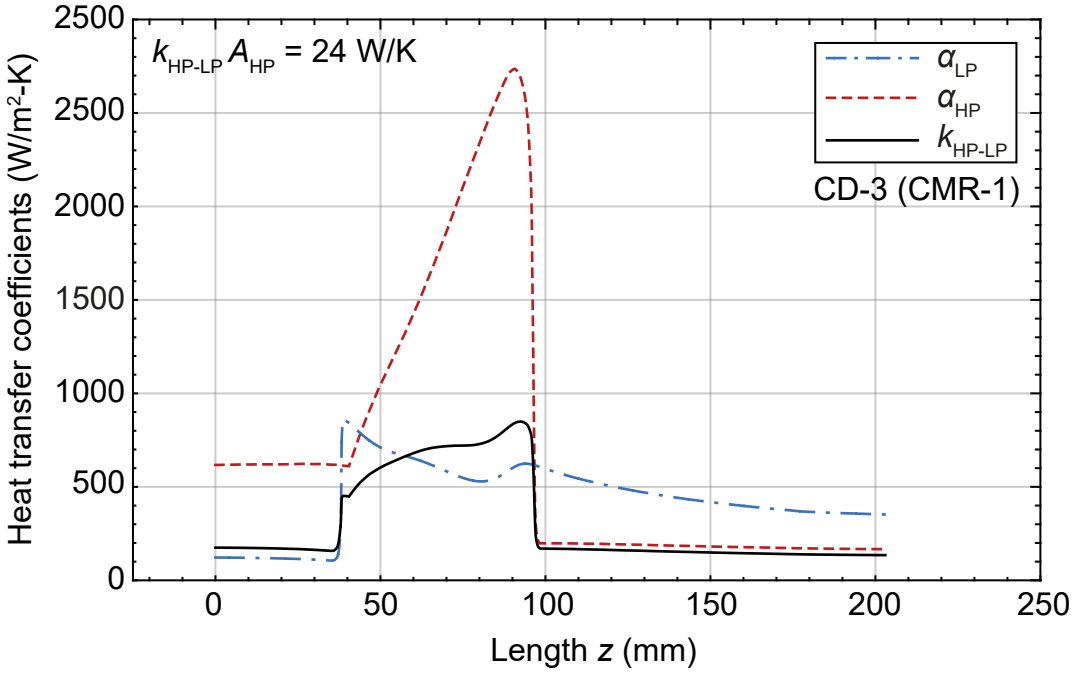

Figure 58: Heat transfer coefficients of the HP α_{HP} and LP α_{LP} streams and the thermal transmittance $k_{HP\text{-}LP}$ between the streams as a function of the MHE length for the mixture CMR-1 in the experiment CD-3. The thermal transmittance $k_{HP\text{-}LP}$ is relative to the heat transfer area A_{HP} of the HP stream according to Tab. 28.

stream. However, in the range of 90-200 mm the measured temperature values of the top plate show a strong deviation to the model and indicates a considerable worse cooling along the top plate. The heat transfer coefficients in the HP α_{HP} and LP α_{LP} stream, as well as the overall thermal transmittance $k_{HP\text{-}LP}$ that are shown Fig. 58 support this argumentation. The largest $k_{HP\text{-}LP}$ values are found in the range of about 40-90 mm. This explains the steep temperature decrease of the numerical profiles and the FBG gratings until $z = 90$ mm. At larger lengths z the thermal transmittance drops to relative small values of about 150 W/(m^2 K), which is a typical value for forced convection in gases [58]. Furthermore, the developed numerical model in [5] considers the overall heat exchanger wall area (both top plates and all sheets) to be in-between the streams and no distinction between the sheets and the top plates is implemented. Hence, the measured temperature data of the FBG sensors indicates to a thermal load from the top plates perpendicular into the LP sheets. This effect should close the temperature gap between the model and the measurement and has to be implemented into the model in subsequent work.

A comparison of the calculated and measured temperatures and pressures, as well as the thermal load due to thermal radiation, of the MHE streams is presented in Tab. 32. According to the already discussed top plate effect, the calculated outlet temperatures of the HP stream $T_{HP,out}$ and the LP stream $T_{LP,out}$ show smaller values and the model

Table 32: Comparison of measured and calculated temperatures, pressures and thermal loads of the MHE in the experiment CD-3.

Parameter	Experiment	Model
$T_{\mathrm{HP,in}}$ (K)	277.22 ± 0.14	277.22
$T_{\mathrm{HP,out}}$ (K)	95.18 ± 1.38	**91.68**
$p_{\mathrm{HP,in}}$ (bar)	21.02 ± 0.32	21.02
$p_{\mathrm{HP,out}}$ (bar)	20.59 ± 0.32	**20.99**
$T_{\mathrm{LP,in}}$ (K)	88.89 ± 1.41	88.89
$T_{\mathrm{LP,out}}$ (K)	263.29 ± 0.16	**274.00**
$p_{\mathrm{LP,in}}$ (bar)	1.48 ± 0.32	1.48
$p_{\mathrm{LP,out}}$ (bar)	1.43 ± 0.32	**1.43**
$\dot{Q}_{\mathrm{rad}}$ (W)	6.71	**6.48**
$\dot{m} \cdot \Delta h_{\mathrm{HX\text{-}3}}$ (W)	6.71	**10.11***

* Num. error 3.63 W (2.6 % $^{\Delta h_{\mathrm{HX\text{-}3}}}/_{\Delta h_{\mathrm{LP}}}$)

therefore, over predicts the effectiveness of the MHE. While the LP stream outlet pressure is predicted well by the model, a large deviation is observed in the outlet pressure of the HP stream. However, because of the relative large expanded uncertainty of the used pressure sensors of ±0.32 bar [5] (with a coverage factor of $k_{\mathrm{u}} = 2$), a further discussion on the pressure drop along the streams is not expedient. The numerically calculated thermal radiation heat load show a slightly smaller value to the experiment. However, according to the first law of thermodynamics the model yields a numerical error of about 3.6 W, which is 2.6 % referred to the transferred heat to the LP stream.

In order to evaluate the efficiency of the refrigeration cycle, an analysis of the thermodynamic work functions is performed for the experiment CD-3 in the following. According to (3.21), the sum of all process work in a thermodynamic cycle is equal to the technical work l_{t} that is necessary to preserve its stationary energy transformation, yielding for the CMRC test stand

$$l_{\mathrm{t}} = \sum l_{\mathrm{i\text{-}j}} = l_{13-1} + l_{1-2} + l_{2-3} + l_{3-12} + l_{12-13} \stackrel{!}{=} (h_1^{\star} - h_{13}) \tag{5.1}$$

$$l_{\mathrm{t}} = \left(l_{\mathrm{comp}} + l_{\mathrm{af.cool\text{-}1}}\right) + l_{\mathrm{af.cool\text{-}2}} + l_{\mathrm{HP\text{-}pipe}} + l_{\mathrm{cold\text{-}box}} + l_{\mathrm{LP\text{-}pipe}} \tag{5.2}$$

$$l_{\mathrm{t}} = 2 \cdot l_{\mathrm{cold\text{-}box}} = 2 \cdot \left[(h_3 - h_{12}) - T_{\mathrm{a}} \cdot (s_3 - s_{12})\right] \tag{5.3}$$

$$l_{\mathrm{cold\text{-}box}} = l_{\mathrm{HX\text{-}1}} + l_{\mathrm{HX\text{-}2}} + l_{\mathrm{HX\text{-}3}} + l_{\mathrm{thr}} + l_{\mathrm{evap}} \tag{5.4}$$

with the individual terms $l_{\text{i-j}}$ that describe the process work of each component in the refrigeration cycle and are calculated with the thermodynamic work function (3.20). The numbering of $l_{\text{i-j}}$ refer to the test stand cycle points that are depicted in Fig. 55. The results of the above work functions are given in Tab. 33a-c, as well as the thermal loads in Tab. 33d that are absorbed by the fluid inside the vacuum chamber. The evaluated technical work l_{t} of this cycle corresponds to a compressor input power of about 165 W, yielding an isentropic efficiency of about 65 %. The largest contribution to the technical work is the process work that is accomplished by the fluid in the vacuum chamber (cold box) $l_{\text{cold-box}}$, whereby the micro-structured heat exchanger is the component with the largest process work $l_{\text{HX-3}}$ within the cold box. It is interesting to denote that the process work of the evaporator in Tab. 33b, which is in-between the throttling device and the HX-3, shows a negative value for the process work. Negative values in the process work are only possible in the case of an extraction of energy from the fluid flow and its conversion into useful work, like the work that is produced by a turbine. However, no turbines or similar mechanical components are installed in the test stand. Also a temperature decrease along the evaporator from $T_8 = 90.20\,\text{K}$ to $T_{10} = 88.89\,\text{K}$ (c.f. Tab. 56) is

Table 33: Results of the efficiency analysis of the test stand in the experiment CD-3.

(a) Work function according to (5.2)

$\left(l_{\text{comp}} + l_{\text{af.cool-1}}\right)$	$l_{\text{af.cool-2}}$	$l_{\text{HP-pipe}}$	$l_{\text{cold-box}}$	$l_{\text{LP-pipe}}$	l_{t}
		$\left(\text{kJ/kg}\right)$			
212.52 90.46 122.06	5.25	0.14	217.97	0.07	435.95

(b) Work function according to (5.3)

$(l_{\text{HX-1}} + l_{\text{HX-2}})$	$l_{\text{HX-3}}$	l_{thr}	l_{evap}	$l_{\text{cold-box}}$
	$\left(\text{kJ/kg}\right)$			
6.59	165.80	54.70	-9.12	217.97

(c) Work function according to (5.3) **+** $\boldsymbol{T_8}$ **correction**

$(l_{\text{HX-1}} + l_{\text{HX-2}})$	$l_{\text{HX-3}}$	l_{thr}	l_{evap}	$l_{\text{cold-box}}$
	$\left(\text{kJ/kg}\right)$			
6.59	165.80	17.35	28.23	217.97

(d) Thermal loads into the cold box

$\left(\dot{Q}_{\text{HX-1}} + \dot{Q}_{\text{HX-2}}\right)$	$\dot{Q}_{\text{HX-3}}$	$\dot{Q}_{\text{thr}}$	$\dot{Q}_{\text{evap}}$	$\sum Q_{\text{i-j}}$
	(W)			
2.15	6.71	0	4.52	13.38

measured, however, can not be explained by a further Joule-Thomson cooling effect due to the fluid pressure drop in evaporator and pipes. Furthermore, the temperature after the throttling device should be at $T_8^\star = 85.47\,\mathrm{K}$, according to the isenthalpic change of state in the throttling device and the corresponding fluid property data [97, 98]. Therefore, the temperature sensor in the cycle point 8 shows most likely incorrect values. Consequently, the measured temperature value T_8 is replaced by the calculated value $T_8^\star$ in the following analysis of the work functions, which are given in Tab. 33c. Additionally, the respective percentage compositions of the process work are presented in Fig. 59. The corrected work function, yields a positive value for the process work in the evaporator which is reasonable, because of the thermal loads due to thermal radiation and thermal conduction of about 4.5 W. It is suggested that the relative large thermal load at the evaporator is mainly due to thermal conduction from the motor of the throttling device, which has a temperature of about 230 K during the experiment CD-3. Because of the T_8 correction, this thermal load is implemented in the process work of the evaporator and not in the throttling device. With the corrected process work l_{evap} and the corresponding thermal load in the evaporator $\dot{Q}_{\mathrm{evap}}$ it is possible to calculate the Carnot efficiency $\tilde{\eta}_{\mathrm{C}}$ (c.f. (2.20)) of the CMRC cycle, yielding

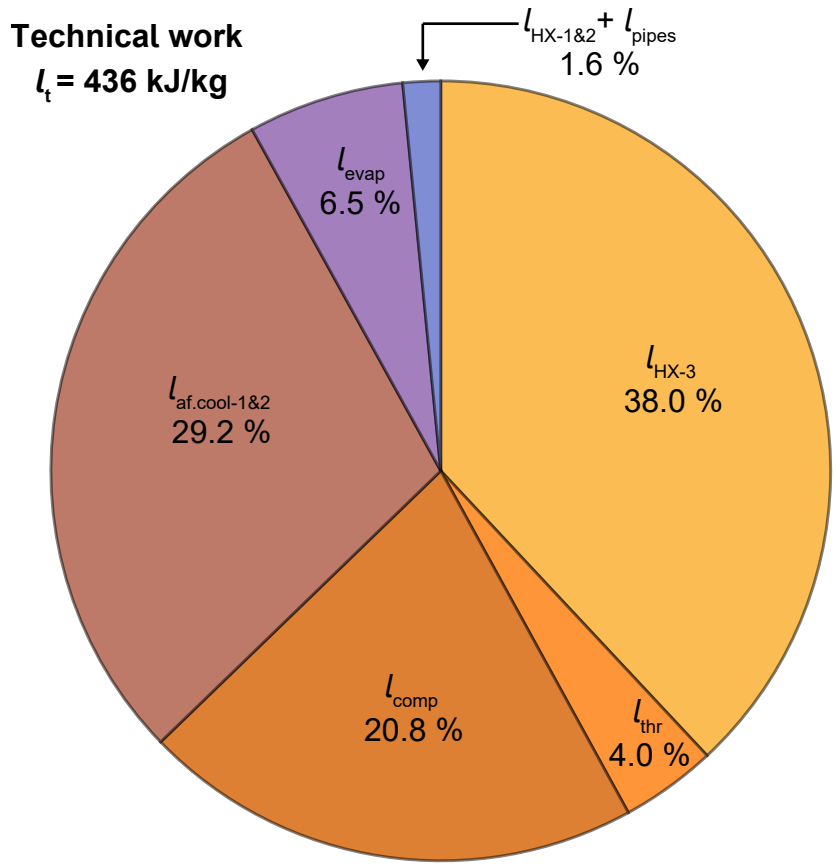

Figure 59: Percentage compositions of the process work in the CMRC test stand of the experiment CD-3, according to Tab. 33a and Tab. 33c.

$$\tilde{\eta}_{\mathrm{C}} = \frac{COP_{\mathrm{exp}}}{COP_{\mathrm{Carnot}}} = \frac{\dot{Q}_{\mathrm{evap}} \cdot \left(\frac{T_{\mathrm{a}}}{T_{10}} - 1\right)}{\dot{m} \cdot l_{\mathrm{t}}} = 6.3\% \tag{5.5}$$

In conclusion, in the experiments of the micro-structured heat exchanger prototype II temperatures at the LP inlet of about 85-88 K are archived with hydro-carbon refrigerant mixtures. In the experiment CD-3 a thermal load of about 4.5 W is absorbed in the evaporator, resulting in a LP inlet temperature of about 88 K. This corresponds to a compressor input power of about 165 W, yielding a Carnot efficiency of the CMRC system of $\tilde{\eta}_{\mathrm{C}} = 6.3\%$ which is comparable to GM cryocoolers that are depicted in Tab. 11. However, the CMRC test stand is not an optimized refrigerant system and therefore, its efficiency is not further discussed here.

According to the very small pressure drop it is possible to operate the MHE prototype II at significant larger mass flows, providing by that a larger cooling power with a simultaneous increase of the heat transfer performance, due to higher heat transfer coefficients. Further, once an optimal mass flow for a particular application is determined, the number of HP and LP sheets can be adjusted to increase the heat transfer area or to keep a constant specific mass flow per sheet. In addition, it is possible to increase the specific refrigeration power by an order of magnitude in future investigations by using LRS mixtures (c.f. Fig. 23) instead of a GRS mixtures that are used in this experiments.

The prediction of the temperature profiles inside the heat exchanger is a strong function of the mixture composition and the exact composition of the circulating mixture is needed for a correct investigation. The model shows a good prediction of the temperature profiles in the temperature range of 293-170 K, however, shows a considerable deviation to the FBG sensor below 170 K. Further, the model over predicts the heat exchanger performance, yielding larger LP stream and smaller HP stream outlet temperatures. This may be the result of the incorrect implementation of the heat exchanger top plates into the model and a respective modification should be considered in subsequent work.

Experiments with mixture containing neon showed no further cool down of the system and the temperature at the cold end increased instead, because of the reduced specific cooling power of this mixture with neon [122]. Further experiments with LRS mixtures, that have a considerable larger specific cooling power (e.g. Tab. 30), may be performed to overcome this effect.

6 Conclusions

The aim of this work is the development of a 10 kA cryogenic mixed refrigerant cooled current lead (CMRC-CL). In order to enable a detailed investigation of the CL design, the existing numerical heat exchanger model [5] is modified and implemented in the resistive current lead model that is developed in the frame of this work. Prior to that implementation, a literature review on the state-of-the-art CL solutions and cooling systems are conducted, numerically investigated and compared with each other. Based on this, a classical multi-tubes-in-tube CMRC-CL and a micro-structured CMRC-CL are developed and investigated numerically in this work.

In order to identify an optimal refrigerant mixture, several parametric studies are performed with the classical CMRC-CL design. It was found that the LRS mixture 17 can lead to a minimal overall power consumption or to a minimal thermal load at the cold end. Compared to other mixtures that are given in Tab. 20, mixture 17 has a larger composition of low boilers, especially methane. In general, the classical CMRC-CL shows a significant reduction of the thermal load at the cold end and of the overall power consumption, compared to other state-of-the-art closed cycle cooling systems that are presented in Tab. 26. The classical CMRC-CL designs in combination with a cryocooler at the cold stage, yields a specific thermal load at the 80 K cold stage of 14 W/kA at an overall power consumption of about 600 W/kA. Compared to a conventional conduction cooled current lead (CCCL) that is cooled by one cryocooler, this is a 67 % reduction of the thermal load at a 50 % reduced overall power consumption. Considerable smaller values are archived only with an optimized self-sufficient vapour cooled current lead (ss-VCCL) with a thermal load of 9 W/kA at a power consumption of 280 W/kA, however, comes with the disadvantage of an open system that requires a continuous supply of LN_2.

The classical heat exchanger design leads to several scalability problems and the adjustment of this design to larger electric currents is related to relative large CL lengths and diameters. Therefore, a new micro-structured CMRC-CL design is developed, manufactured by IMVT and patented in the frame of this work. It consists of several micro-structured copper sheets of 0.5 mm thickness that comprise a certain amount of etched channels for the fluid flow. The total amount of the sheets depends on the electric current and the refrigerant mass flow that is needed to absorb a certain amount of Joule heating, thermal radiation and thermal load due to thermal conduction from the ambience. All sheets are stacked together by a specific stacking pattern, then covered by the top and bottom plates and irreversibly connected in a diffusion bonding process. The new design, allows a simple adjustment of the amount of sheets, the amount of channels per sheet, the CL length and the refrigerant mass flow for a desired electric current. The respective numerical model is developed and CLs for electric currents of 10 kA and 20 kA are designed and numerically investigated. The investigated CMRC-CL design **C**, yields a thermal load of 6.5 W/kA

at a temperature of 85 K. Compared to a CCCL that is working in this temperature range, this is an 85 % reduction of the thermal load and therefore, the largest reduction compared to the state-of-the-art solutions. To follow the concept of the CL comparison that is shown in Tab. 26, the CMRC-CL design **C** is extended by an additional cooling machines (GM-AL60) at the cold end to absorb the remaining thermal load. With a total power consumption of 490 W/kA, the micro-structured CMRC-CL system is the most efficient closed-cycle system. However, it is to denote that it is realistic to develop CMRC-CL systems that do not need an additional cryocooler and temperatures below 85 K are possible by an adjustment of the refrigerant mixture and/or the refrigerant cycle (e.g. [123]).

An optimal mixture may be found in the analysis of vapour-liquid-equilibrium, vapour-liquid-liquid-equilibrium and solid-liquid-equilibrium measurements that are possible in the Cryogenic Phase Equilibria Test Stand (CryoPHAEQTS) [129] in the temperature range of 15-300 K and at pressures up to 150 bar. In conclusion, the developed and manufactured micro-structured CMRC-CL is a solid and important design milestone in the development of future CL types. Therefore, an optimization process for the above mentioned parameters is needed to be conducted in subsequent work.

The conducted experiments on the micro-structured heat exchanger prototype II in the CMRC test stand showed a temperature decrease of about 85 K with a thermal load of 4.5 W and at a power consumption of about 165 W. The respective Carnot efficiency is comparable to GM cryocoolers, however, the CMRC test stand is not an optimized refrigerant system and therefore, its efficiency is not further discussed in this work. The numerical model showed a good agreement with the measured temperature data along the heat exchanger at temperatures above 170 K, however, a significant deviation of the temperature gradients is present at lower temperatures. The main reason for this is the present implementation of the heat exchanger top and bottom plates into the calculation method and should be corrected in the subsequent work. Further, a significant difference in the HP stream outlet pressure is identified, however, due to the relative large measurement uncertainties, it is not possible to have a further discussion on this effect. Therefore, the inlet and outlet pressure sensors should be changed to sensors that lead to smaller uncertainties. Further experiments with mixtures containing neon showed no further cool down of the system and the temperature at the cold end increased instead, because of the reduced specific cooling power of this mixture with neon [122]. Further experiments with LRS mixtures, that have a considerable larger specific cooling power (e.g. Tab. 30), may be performed to overcome this effect.

In conclusion, the numerical and experimental results on the micro-structured heat exchanger designs provide evidence that it is possible to develop a CMRC system that can cool down a superconducting application at least to the temperature of liquid nitrogen

without the need of additional cryocoolers as the last cold stage. Furthermore, the new micro-structured CMRC-CL design allows a simple adjustment of its geometric and hydraulic parameters for a predefined electric current and it may be possible to design CLs even for the large electric currents of aluminium plants that are typically operated at 200-500 kA.

References

[1] F. Schreiner. *Design of a three-stage cooled Current Lead for Superconducting High Current DC Busbars in Industrial Applications*. Berlin, Heidelberg: Shaker-Verlag, 2020. ISBN: 978-3-8440-7307-2.

[2] M. Stemmle et al. "AmpaCity project - update on world's first superconducting cable and fault current limiter installation in a German city center". In: *23rd International Conference on Electricity Distribution, Lyon, F, June 15-18, 2015 Paper publ.online Paper 0678*. 37.06.02; LK 01. 2015.

[3] E. Shabagin et al. "Modelling of 3D temperature profiles and pressure drop in concentric three-phase HTS power cables". In: *Cryogenics* 81 (2017), pp. 24–32. URL: https://doi.org/10.1016/j.cryogenics.2016.11.004.

[4] Thomas Kochenburger. *Kryogene Gemischkältekreisläufe für Hochtemperatursupraleiter-Anwendungen*. Verfahrenstechnik. München: Verlag Dr. Hut, [2019]. ISBN: 9783843939874.

[5] D.J. Gomse. "Development of heat exchanger technology for cryogenic mixed refrigerant cycles". KITopen-ID: 1000119417. PhD thesis. Karlsruher Institut für Technologie (KIT), 2020. 155 pp.

[6] Y. Iwasa. *Case Studies in Superconducting Magnets*. 2nd ed. Boston, MA: Springer-Verlag US, 2009. URL: https://doi.org/10.1007/b112047.

[7] R. McFee. "Optimum input leads for cryogenic apparatus". In: *Review of Scientific Instruments* Vol. 30 (1959), pp. 98–102. URL: https://doi.org/10.1063/1.1716499.

[8] F. Wiedemann and Franz B. "Ueber die Wärme-Leitfähigkeit der Metalle". In: *Annalen der Physik und Chemie* Vol. 165, Issue 8 (1853), pp. 497–531. URL: https://doi.org/10.1002/andp.18531650802.

[9] L. Lorenz. "Bestimmung der Wärmegrade in absolutem Maasse". In: *Annalen der Physik und Chemie* Vol. 223, Issue 11 (1872), pp. 429–52. URL: https://doi.org/10.1002/andp.18722231107.

[10] Jack Ekin. *Experimental techniques for low-temperature measurements: cryostat design, material properties and superconductor critical-current testing*. Oxford Scholarship Online, 2016. URL: https://doi.org/10.1093/acprof:oso/9780198570547.001.0001.

[11] N. Gust, Kozlowski K, and et al. "Multichannel temperature regulation for SIS100 HTS current leads". In: *Cryogenics 2019 Proceedings of the 15th IIR International Conference* (2019). 30025809. URL: http://dx.doi.org/10.18462/iir.cryo.2019.0039.

[12] B. Hongyu, William S.M., and et. al. "Current leads cooling for the series-connected hybrid magnets". In: *AIP Conference Proceedings* Vol. 1574 (2014), pp. 1707–12. URL: https://doi.org/10.1063/1.4860913.

[13] W.S. Marshall, Bai H., and et. al. "Design of N2 cooled Bi-2223 HTS current leads for use in 0.4T field for the NHMFL series-connected hybrid magnet". In: *AIP Conference Proceedings* Vol. 1573 (2014), pp. 1018–25. URL: https://doi.org/10.1063/1.4860817.

[14] A. Ballarino, Bauer P., and et. al. "Design of the HTS Current Leads for ITER". In: *IEEE Transactions on Applied Superconductivity* Vol. 22, Issue 3 (2012). 4800304. URL: https://doi.org/10.1109/TASC.2011.2175192.

[15] T. Zhou, Lu K., and et. al. "Design and Development of 16-kA HTS Current Lead for HMFL 45-T Magnet". In: *IEEE Transactions on Applied Superconductivity* Vol. 25, Issue 4 (2015). 4802906. URL: https://doi.org/10.1109/TASC.2015.2409194.

[16] H.M. Chang and Kim M.J. "Optimization of conduction-cooled current leads with unsteady operating current". In: *Cryogenics* Vol. 49, Issue 5 (2009), pp. 210–16. URL: https://doi.org/10.1016/j.cryogenics.2009.01.006.

[17] S. Jeong and Smith J.L. "Optimum temperature staging of cryogenic refrigeration system". In: *Cryogenics* Vol. 34, Issue 11 (1994), pp. 929–33. URL: https://doi.org/10.1016/0011-2275(94)90078-7.

[18] H.M. Chang and Van Sciver S.W. "Thermodynamic optimization of conduction-cooled HTS current leads". In: *Cryogenics* Vol. 38, Issue 7 (1998). URL: https://doi.org/10.1016/S0011-2275(98)00043-5.

[19] H.M. Chang, Choi Y.S.C., and et al. "Optimization of operating temperature in cryocooled HTS magnets for compactness and efficiency". In: *Cryogenics* Vol. 42, Issue 12 (2002). URL: https://doi.org/10.1016/S0011-2275(02)00147-9.

[20] H.M. Chang, Lee G.H., and et al. "Two-Stage Cryocooling Design for Hybrid Superconducting Fault Current Limiter". In: *IEEE Trans. Appl. Supercond.* Vol. 20, Issue 3 (2010), pp. 2047–50. URL: https://doi.org/10.1109/TASC.2009.2039862.

[21] L. Bromberg, Michael P.C, and et al. "Current lead optimization for cryogenic operation at intermediate tempeatures". In: *AIP Conf. Proc.* 1218 (2010), pp. 577–84. URL: https://doi.org/10.1063/1.3422405.

[22] S. Yamaguchi, Emoto M., and et al. "A proposal of multi-stage current lead for reduction of heat leak". In: *Physics Procedia* 27 (2012), pp. 448–51. URL: https://doi.org/10.1016/j.phpro.2012.03.508.

[23] S. Yamaguchi, Emoto M., and et al. "Refrigeration Process to Realize a Multistage and Gas-Cooled Current Lead". In: *IEEE Trans. Appl. Supercond.* Vol. 23, Issue 3 (2013). 4802304. URL: https://doi.org/10.1109/TASC.2013.2243896.

[24] L. Bromberg. "Efficient and lightweight current leads". In: *AIP Conference Proceedings* Vol. 1573 (2014), pp. 1034–41. URL: https://doi.org/10.1063/1.4860819.

[25] P.C. Michael, Bromberg L., and et al. “Design and Test of a Prototype 20 kA HTS DC Power Transmission Cable”. In: *IEEE Trans. Appl. Supercond.* Vol. 25, Issue 3 (2015). 5401005. URL: https://doi.org/10.1109/TASC.2014.2373824.

[26] C. Hanebeck, S. Huwer, and et al. *Cryogenics in high-current busbars and multistage cooled current leads*. Vortrag gehalten auf 2nd International Workshop on Cooling Systems for HTS Applications (IWC-HTS), Karlsruhe, Germany, 13th - 15th September 2017. 37.06.02; LK 01. 2017. URL: https://publikationen.bibliothek.kit.edu/1000075563.

[27] F. Schreiner, Gutheil B., and et al. “Design and manufacturing of a multistage cooled current lead for superconducting high current DC busbars in industrial applications”. In: *IEEE Trans. Appl. Supercond.* Vol. 27, Issue 4 (2017). 4802405. URL: https://doi.org/10.1109/TASC.2017.2655108.

[28] D. Goloubev. “Kühlung eines resistiven HTSL-Kurzschlussstrombegrenzers mit einer Gemisch-Joule-Thomson-Kältemaschine”. PhD thesis. Technische Universität Dresden, Dresden, 2004. URL: https://nbn-resolving.org/urn:nbn:de:swb:14-1095838519812-78347.

[29] R. Agsten. “Thermodynamic optimization of current leads into low temperature regions”. In: *Cryogenics* Vol. 13, Issue 3 (1973), pp. 141–46. URL: https://doi.org/10.1016/0011-2275(73)90280-4.

[30] S.C. Kaushik, S.K. Tyagi, and P. Kumar. *Finite Time Thermodynamics of Power and Refrigeration Cycles*. New Delhi, India: Springer International Publishing, 2017. ISBN: 978-3-319-62812-7. URL: https://doi.org/10.1007/978-3-319-62812-7.

[31] L. Decker. *Overview on cryogenic refrigeration cycles for large scale HTS applications*. International Workshop on Cooling System for HTS Applications (IWC-HTS), Matsue, Japan, 14th - 16th October 2016.

[32] M. Hilal. “Optimization of current leads for superconducting systems”. In: *IEEE Transactions on Magnetics* Vol. 13, Issue 1 (1977), pp. 690–93. URL: https://doi.org/10.1109/TMAG.1977.1059320.

[33] J.R. Hull. “High-temperature superconducting current leads”. In: *IEEE Transactions on Applied Superconductivity* Vol. 3, Issue 1 (1993), pp. 869–75. URL: https://doi.org/10.1109/77.233839.

[34] K.R. Efferson. “Helium vapor cooled current leads”. In: *Review of Scientific Instruments* Vol. 28, Issue 12 (1967), pp. 1776–1779. URL: https://doi.org/10.1063/1.1720670.

[35] Q.S. Shu, J. Demko, and et al. “Thermal optimum analyses and mechanical design of 10-kA, vapor-cooled power leads for SSC superconducting magnet tests at MTL”. In: *IEEE Transactions on Applied Superconductivity* Vol. 3, Issue 1 (1993), pp. 408–12. URL: https://doi.org/10.1109/77.233735.

[36] A. Ballarino. “Current leads for the LHC magnet system”. In: *IEEE Transactions on Applied Superconductivity* Vol. 12, Issue 1 (2002), pp. 1275–1280. URL: https://doi.org/10.1109/TASC.2002.1018635.

[37] R. Heller, G. Friesinger, and et al. “Test of a forced-flow cooled 30 kA/23 kV current lead for the POLO model coil”. In: *IEEE Transactions on Magnetics* Vol. 30, Issue 4 (1994), pp. 2387–90. URL: https://doi.org/10.1109/20.305757.

[38] R. Heller, G. Friesinger, and et al. “Development program of a 60 kA current lead using high temperature superconductors”. In: *IEEE Transactions on Applied Superconductivity* Vol. 7, Issue 2 (1997), pp. 692–95. URL: https://doi.org/10.1109/77.614598.

[39] R. Heller, S.M. Darweschsad, and et al. “Experimental results of a 70 kA high temperature superconductor current lead demonstrator for the ITER magnet system”. In: *IEEE Transactions on Applied Superconductivity* Vol. 15, Issue 2 (2005), pp. 1496–99. URL: https://doi.org/10.1109/TASC.2005.849145.

[40] R. Heller, W.H. Fietz, and et al. “Overview of JT-60SA HTS Current Lead Manufacture and Testing”. In: *IEEE Transactions on Applied Superconductivity* Vol. 28, Issue 3 (2018). 4800105. URL: https://doi.org/10.1109/TASC.2017.2768166.

[41] R. Heller, H. Bau, and et al. “Operation Experience of the Wendelstein 7-X High-Temperature Superconductor Current Leads”. In: *IEEE Transactions on Applied Superconductivity* Vol. 29, Issue 6 (2019). 4200105. URL: https://doi.org/10.1109/TASC.2019.2891163.

[42] R. Heller, A. Class, and et al. “Modelling of the fin type heat exchanger for the HTS current leads of W7-X and JT-60SA”. In: *Cryogenics* Vol. 50, Issue 3 (2010). URL: https://doi.org/10.1016/j.cryogenics.2009.08.006.

[43] E. Rizzo. “Simulations for the optimization of High Temperatur Superconductor current leads for nuclear fusion applications”. PhD thesis. Karlsruhe Institute of Technology, Karlsruhe, 2014. URL: http://dx.doi.org/10.5445/KSP/1000037132.

[44] H.J. Kim, T.S. Lee, and et al. “Design and Experimental Evaluation on kA-Class HTS Binary Superconducting Current Lead Using a Liquid Nitrogen Bath Under Short-Term Current Test”. In: *IEEE Transactions on Applied Superconductivity* Vol. 24, Issue 3 (2014). 4802005. URL: https://doi.org/10.1109/TASC.2013.2292516.

[45] J.R. Miller, G.E. Miller, and et al. “Design and development of a pair of 10 kAHTS current leads for the NHMFL 45 hybrid magnet system”. In: *IEEE Transactions on Applied Superconductivity* Vol. 15, Issue 2 (2005). 1492-95. URL: https://doi.org/10.1109/TASC.2005.849140.

[46] W.S. Marshall, H. Bai, and et al. “Design of N2 cooled Bi-2223 HTS current leads for use in 0.4T field for the NHMFL series-connected hybrid magnet”. In: *AIP*

Conference Proceedings Vol. 1573 (2014). 1018-25. URL: https://doi.org/10.1063/1.4860817.

[47] J.A. Demko, W.E. Schiesser, and et al. "Thermal Optimization of the Helium-Cooled Power Leads for the SSC". In: *Supercollider 4*. Springer US, 1992, pp. 635–642. URL: https://doi.org/10.1007/978-1-4615-3454-9_78.

[48] J.A. Demko, W.E. Schiesser, and et al. "A method of lines solution of the transient behavior of the helium cooled power leads for the SSC". In: SSCL-Preprint-107 (1995). URL: https://doi.org/10.2172/80734.

[49] R. Heller. "Numerical calculation of current leads for fusion magnets". In: *Kernforschungszentrum Karlsruhe* 4608 (1989). URL: https://services.bibliothek.kit.edu/primo/start.php?recordid=KITSRC018751830.

[50] R. Wesche and A.M. Fuchs. "Design of superconducting current leads". In: *Cryogenics* Vol. 34, Issue 2 (1994), pp. 145–54. URL: https://doi.org/10.1016/0011-2275(94)90037-X.

[51] J.R. Hull, A. Unal, and M.C. Chyu. "Analysis of self-cooled binary current leads containing high temperature superconductors". In: *Cryogenics* Vol. 32, Issue 9 (1992), pp. 822–28.

[52] A. Ballarino. "Current Leads, Links and Buses". In: *CAS - CERN Accelerator School: Course on Superconductivity for Accelerators* CERN-2014-005 (2013), pp. 547–58. URL: http://dx.doi.org/10.5170/CERN-2014-005.547.

[53] R. Heller, G. Friesinger, and et al. "Development of a 20 kA high temperature superconductor current lead". In: *Cryogenics* Vol. 41, Issue 8 (2001), pp. 539–47. URL: https://doi.org/10.1016/S0011-2275(01)00101-1.

[54] H.M. Chang, Y.S Choi, and et.al. "Optimization of current leads cooled by natural convection of vapor". In: *AIP Conference Proceedings* Vol. 710, Issue 1 (2004), pp. 944–51. URL: https://doi.org/10.1063/1.1774775.

[55] H.M. Chang, J.J Byon, and H.B. Jin. "Effect of convection heat transfer on the design of vapor-cooled current leads". In: *Cryogenics* Vol. 46, Issue 5 (2006), pp. 324–32. URL: https://doi.org/10.1016/j.cryogenics.2005.04.001.

[56] E. W. Lemmon et al. *NIST Standard Reference Database 23: Reference Fluid Thermodynamic and Transport Properties-REFPROP, Version 10.0, National Institute of Standards and Technology*. 2018. DOI: http://dx.doi.org/10.18434/T4JS3C. URL: https://www.nist.gov/srd/refprop.

[57] R. Span, Lemon E.W., and et. al. "A Reference Equation of State for the Thermodynamic Properties of Nitrogen for Temperatures from 63.151 to 1000 K and Pressures to 2200 MPa". In: *Journal of Physical and Chemical Reference Data* Vol. 29, Issue 6 (2000), pp. 1361–1433. URL: https://doi.org/10.1063/1.1349047.

[58] *VDI Heat Atlas*. Berlin, Heidelberg, 2010.

[59] *Numerical Solution of Boundary Value Problems (BVP)*. URL: https://reference.wolfram.com/language/tutorial/NDSolveBVP.html (visited on 10/24/2020).

[60] N.M. Oezisik. *Heat Conduction*. 2nd. John Wiley & Sons, Inc., 1993.

[61] A. Saggion, Faraldo R., and Perno M. *Thermodynamics - Fundamental principles and applications*. Springer, 2019.

[62] H. Okumura and S. Yamaguchi. "One dimensional simulation for peltier current leads". In: *IEEE Transactions on applied superconductivity* Vol. 7, Issue 2 (1997), pp. 715–18. URL: https://doi.org/10.1109/77.614604.

[63] K. Sato, Okumura H., and Yamaguchi S. "Numerical analysis of Peltier current lead". In: *Proceedings ICT2001. 20 International Conference on Thermoelectrics (Cat. No.01TH8589)* (2001), pp. 491–94. URL: https://doi.org/10.1109/ICT.2001.979938.

[64] K. Sato, Okumura H., and Yamaguchi S. "Numerical calculations for Peltier current lead designing". In: *Cryogenics* Vol. 41, Issue 7 (2001), pp. 497–503. URL: https://doi.org/10.1016/S0011-2275(01)00117-5.

[65] J. Hasegawa, Oike T., and et. al. "Thermoelectric property measurement for a Peltier current lead". In: *Proceedings ICT2001. 20 International Conference on Thermoelectrics (Cat. No.01TH8589)* (2001), pp. 507–10. URL: https://doi.org/10.1109/ICT.2001.979942.

[66] K. Fujii, Fukuda S., and et. al. "Thermoelectric property dependence and geometry optimization of Peltier current leads using highly electrically conductive thermoelectric materials". In: *Journal of Electronic Materials volume* Vol. 40, Issue 5 (2011), pp. 691–95. URL: https://doi.org/10.1007/s11664-011-1513-4.

[67] T. Yamaguchi, H. Okumura, and et. al. "Multi-stage Peltier current lead system for liquid helium free magnets". In: *IEEE Transactions on Applied Superconductivity* Vol. 13, Issue 2 (2003), pp. 1914–17. URL: https://doi.org/10.1109/TASC.2003.812945.

[68] M. Moriguchi, S. Mizutani, and et. al. "Polarity change switch for Peltier current lead". In: *IEEE Transactions on Applied Superconductivity* Vol. 14, Issue 2 (2004), pp. 1786–89. URL: https://doi.org/10.1109/TASC.2004.831096.

[69] T. Yamaguchi, H. Okumura, and et. al. "Characteristics of Peltier current lead system for alternating current mode". In: *IEEE Transactions on Applied Superconductivity* Vol. 13, Issue 2 (2003), pp. 1910–13. URL: https://doi.org/10.1109/TASC.2003.812944.

[70] S. Yamaguchi, T. Yamaguchi, and et. al. "Peltier current lead experiment and their applications for superconducting magnets". In: *Review of Scientific Instruments* Vol. 75, Issue 1 (2004), pp. 207–12. URL: https://doi.org/10.1063/1.1633987.

[71] T. Yamaguchi, S. Mizitani, and et. al. "Experimental and numerical characteristics of Peltier current lead for direct current mode". In: *IEEE Transactions on Applied*

Superconductivity Vol. 14, Issue 2 (2004), pp. 1719–22. URL: https://doi.org/10.1109/TASC.2004.831052.

[72] M. Hamabe, A. Sasaki, and et. al. "Test of Peltier Current Lead for Cryogen-Free Superconducting Magnet". In: *IEEE Transactions on Applied Superconductivity* Vol. 16, Issue 2 (2006), pp. 465–68. URL: https://doi.org/10.1109/TASC.2006.873326.

[73] F.K. Gehring, M.E. Hüttner, and R.P. Huebener. "Peltier cooling of superconducting current leads". In: *Cryogenics* Vol. 41, Issue 7 (2001), pp. 521–28–500. URL: https://doi.org/10.1016/S0011-2275(01)00124-2.

[74] S. Yamaguchi, M. Hamabe, and et. al. "Research activities of DC superconducting power transmission line in Chubu University". In: *Journal of Physics: Conference Series* Vol. 97 (2008), p. 012290. URL: https://doi.org/10.1088%2F1742-6596%2F97%2F1%2F012290.

[75] S. Yamaguchi, Y. Ivanov, and et. al. "Construction and 1st experiment of the 500-meter and 1000-meter DC superconducting power cable in Ishikari". In: *Physics Procedia* Vol. 81 (2016), pp. 182–86. URL: https://doi.org/10.1016/j.phpro.2016.04.046.

[76] S. Yamaguchi, Y. Ivanov, and et. al. "Multi-channel data acquisition system for a 500 m DC HTS power cable in Ishikari". In: *Physics Procedia* Vol. 81 (2016), pp. 187–90. URL: https://doi.org/10.1016/j.phpro.2016.04.047.

[77] S. Yamaguchi, Y. Ivanov, and et. al. "Testing of Peltier current leads used in real electrical superconducting network". In: *Materials Today: Proceedings* Vol. 8, Issue 2 (2019), pp. 607–12. URL: https://doi.org/10.1016/j.matpr.2019.02.060.

[78] P.C. Michael, C.A. Galea, and L. Bromberg. "Cryogenic Current Lead Optimization Using Peltier Elements and Configurable Cooling". In: *IEEE Transactions on Applied Superconductivity* Vol. 25, Issue 3 (2015), p. 4801805. URL: https://doi.org/10.1109/TASC.2014.2373512.

[79] K. Raczka. "Untersuchungen zu Peltier-Stromzuführungen für Anwendungen der Supraleitung". Bachelor's Thesis. KIT Department of Chemical and Process Engineering at Karlsruhe Institute of Technology (KIT), 2018.

[80] C. Enss and S. Hunklinger. *Low-Temperature Physics*. Springer, 2010. URL: https://doi.org/10.1007/b137878.

[81] *CryoComp*. 5.0. Eckels Engineering.

[82] R. Heller, Fink S., and et. al. "Development of forced flow cooled current leads for fusion magnets". In: *Cryogenics* Vol. 41, Issue 3 (2001), pp. 201–11. URL: https://doi.org/10.1016/S0011-2275(01)00093-5.

[83] R. Feldman, L. Talley, and et. al. "Upper limit for magnetoresistance in silicon bronze and phosphor bronze wire". In: *Cryogenics* Vol. 17, Issue 1 (1977), pp. 31–32. URL: https://doi.org/10.1016/0011-2275(77)90303-4.

[84] Milind D. Atrey. "Cryocooler technology: The path to invisible and reliable cryogenics". In: *Cryocoolers, International Cryogenics Monograph Series*. Ed. by Milind D. Atrey. 6330 Cham, Switzerland: Springer Nature Switzerland AG 2020, 2020. Chap. 1, pp. 1–46. URL: https://doi.org/10.1007/978-3-030-11307-0_1.

[85] K.A. Gschneidner, A.O. Pecharsky, and V.K. Pecharsky. "Low temperature cryocooler regenerator materials". In: *Cryocoolers* Vol. 12 (2003), pp. 457–465. URL: https://doi.org/10.1007/0-306-47919-2_61.

[86] *Leybold COOLPOWER cold heads*. https://www.leyboldproducts.de/en. [Online; accessed 25-November-2020]. 2020.

[87] *Cryomech Gifford-McMahon cryocoolers*. https://www.cryomech.com. [Online; accessed 25-November-2020]. 2020.

[88] *cryo.TransMIT Lambda Line Pulse Tube crycoolers*. https://cryo.transmit.de/. [Online; accessed 25-November-2020]. 2020.

[89] *Cryogenic Buyer's Guide - Cryocoolers*. https://csabg.org/cryocoolers/. [Online; accessed 28-November-2020]. 2020.

[90] Ronald G. Jr. Ross. "Refrigeration systems for archieving cryogenic temperatures". In: *Low temperature materials and mechanism*. Ed. by Yoseph Bar-Cohen. Boca Raton: CRC Press, 2016. Chap. 6, pp. 109–181. URL: https://doi.org/10.1201/9781315371962.

[91] *AFCryo - STC1500 PT crycooler*. https://af-cryo.com/. [Online; accessed 28-November-2020]. 2020.

[92] *Stirling Cryogenics - SPC-4 Cryogenerator*. https://www.stirlingcryogenics.eu/. [Online; accessed 28-November-2020]. 2020.

[93] *SHI Cryogenics Group*. http://www.shicryogenics.com/. [Online; accessed 28-November-2020]. 2020.

[94] *RIX Industries - Thermoacoustic Stirling Cryocooler*. https://www.rixindustries.com/. [Online; accessed 28-November-2020]. 2020.

[95] *Prozessdetails: Xtra-generischN2 (flüssig)*. https://www.probas.umweltbundesamt.de/php/index.php. [Online; accessed 05-December-2020]. 2020.

[96] G. Venkatarathnam. *Cryogenic mixed refrigerant processes*. International cryogenics monograph series. Springer, 2008. URL: https://doi.org/10.1007/978-0-387-78514-1.

[97] D.Y. Peng and D.B. Robinson. "A new two-constant equation of state". In: *Industrial & Engineering Chemistry Fundamentals* Vol. 15, Issue 1 (1976), pp. 59–64. URL: https://doi.org/10.1021/i160057a011.

[98] Aspen Plus V10. *Aspen Technology*.

[99] M. Ruhemann. *The separation of gases*. 2nd. The international series of monographs on physics. Oxford University Press, 1949.

[100] Steffen Grohmann. *Vorlesung - Kältetechnik B.04: Energiebedarf in Prozessen zur Gasverflüssigung*. lecture notes. 2021.

[101] F. Keppler, G. Nellis, and S.A. Klein. "Optimization of the Composition of a Gas Mixture in a Joule-Thomson Cycle". In: *HVAC&R Research* 10.2 (2004), pp. 213–230. URL: https://doi.org/10.1080/10789669.2004.10391100.

[102] *Edwards - Polycold® PCC cooler*. https://www.edwardsvacuum.com/de/our-markets/semiconductor-and-electronics/cryogenics/cryochillers/pcc-compact-coolers. [Online; accessed 27-February-2021]. 2021.

[103] G.F Nellis, J.M Pfotenhauer, and S.A. Klein. "Actively cooled current leads for superconducting electronics using mixed-gas Joule-Thomson refrigeration". In: *Proceedings of the ASME 2004 International Mechanical Engineering Congress and Exposition* (2004), pp. 339–346. URL: https://doi.org/10.1115/IMECE2004-60284.

[104] G.F. Nellis. "A heat exchanger model that includes axial conduction, parasitic heat loads, and property variations". In: *Cryogenics* 43.9 (2003), pp. 523–538. URL: https://doi.org/10.1016/S0011-2275(03)00132-2.

[105] J.M. Pfotenhauer et al. "Progress towards a low power mixed-refrigerant Joule-Thomson cryocooler for electronic current leads". In: *Cryocoolers* 14 (2007), pp. 443–452. URL: http://digital.library.wisc.edu/1793/21652.

[106] K. Weckemann. "Untersuchungen zum Betriebsverhalten und Modifikation eines Gemisch-Joule-Thomson-Kleinkühlers". Diplomarbeit. Universität Karlsruhe, 2003.

[107] S.S.H. Kruthiventi. "Studies on coiled wire finned heat exchangers and expansion capilary used in mixed refrigerant J-T refrigerator". PhD thesis. Madras: IITM, 2017.

[108] E. Shabagin and S. Grohmann. "Development of 10 kA current leads cooled by a cryogenic mixed-refrigerant cycle". In: *IOP Publishing* 502 (2019), p. 012138. URL: https://doi.org/10.1088/1757-899x/502/1/012138.

[109] *VDI Heat Atlas*. Berlin, Heidelberg, 2010.

[110] Z. Liu and R. Winterton. "A general correlation for saturated and subcooled flow boiling in tubes and anulli, based on a nucleate pool boiling equation". In: *International Journal of Heat and Mass Transfer* 34.11 (1991), pp. 2759–66. URL: https://doi.org/10.1016/0017-9310(91)90234-6.

[111] J.R. Thome and S. Shakir. "New correlation for nucleate pool boiling of aqueous mixtures". In: *AIChE Symposium Series* 83.257 (1987), pp. 46–51.

[112] R.G. Sardesai, R.A.W. Shock, and D. Butterworth. "Heat and mass transfer in multicomponent condensation and boiling". In: *Heat Transfer Engineering* 3.3-4 (1982), pp. 104–114. URL: https://doi.org/10.1080/01457638108939589.

[113] A. Cavallini, D. Del Col, and et. al. “Condensation in horizontal smooth tubes: A new heat transfer model for heat exchanger design”. In: *Heat Transfer Engineering* 27.8 (2006), pp. 31–38. URL: https://doi.org/10.1080/01457630600793970.

[114] R.W.. Lockhart and R.C. Martinelli. “Proposed correlation of data for isothermal two-phase, two-component flow in pipes”. In: *Chemical Engineering Progress* 45.1 (1949), pp. 39–48.

[115] D. Chrisholm. “An equation for velocity ratio in two-phase flow”. In: *NEL Report* 535 (1972), p. 13.

[116] O. Kunz and W. Wagner. “The GERG-2008 Wide-Range Equation of State for Natural Gases and Other Mixtures: An Expansion of GERG-2004”. In: *Journal of Chemical & Engineering Data* 57.11 (2012), pp. 3032–3091. URL: https://doi.org/10.1021/je300655b.

[117] *Mathematica*. 11.0. Wolfram Research. 2016.

[118] D. Gomse and S. Grohmann. “Heat transfer and pressure drop in the main heat exchanger of a cryogenic mixed refrigerant cyclce”. In: *IOP Conference Series: Materials Science and Engineering* 502 (2019), p. 012027. URL: https://doi.org/10.1088/1757-899x/502/1/012027.

[119] E. Shabagin, K. Raczka, and S. Grohmann. “Investigation of cryogenic mixed-refrigerant cooled current leads in combination with peltier elements”. In: *IOP Conference Series: Materials Science and Engineering* Vol. 755 (2020), p. 012138. URL: https://doi.org/10.1088%2F1757-899x%2F755%2F1%2F012138.

[120] F.B. Wilke. “Untersuchungen zu einem Gemisch-Joule-Thomson-Kleinkühler”. Diplomarbeit. Universität Karlsruhe, 2002.

[121] S. Grohmann et al. “Microstructured current leads for applications of superconductivity (Micro-CL)”. KIT19026DE ST/GS 102020205184.4. 23.04.2020.

[122] J. Arnsberg. “Eperimentelle Untersuchung eines kompakten mikrostrukturierten Wärmeübertragers in einem kryogenen Gemischkältekreislauf”. Master’s thesis. Karlsruhe Institute of Technology (KIT), 2020.

[123] S. Grohmann, E. Shabagin, and D. Gomse. “Automatic liquid cool-down of mixed refrigerant cycles (ALC-MRC)”. KIT19025DE ST/GS 102020205183.6. 23.04.2020.

[124] E. Shabagin and S. Grohmann. *Einsatz eines kompakten, mikrostrukturierten Wärmeübertragers im kryogenen Gemischkältekreislauf*. German. Vortrag gehalten auf Jahrestagung des Deutschen Kälte- und Klimatechnischen Vereins (2019), Ulm, 20.–22. November 2019. 37.06.02; LK 01. 2019. URL: https://doi.org/10.5445/IR/1000105188.

[125] N.S. Walimbe, K.G. Narayankhedkar, and M.D. Atrey. “Experimental investigation on mixed refrigerant Joule-Thomson cryocooler with flammable and non-flammable refrigerant mixtures”. In: *Cryogenics* 50.10 (2010), pp. 653–59. URL: https://doi.org/10.1016/j.cryogenics.2010.06.002.

[126] N. Vineed and G. Venkatarathnam. "Experimental investigation on mixed refrigerant cryocooler operating at 70 K for cooling high temperature superconductors". In: *IOP Conference Series: Materials Science and Engineering* 171 (2017), p. 012073. URL: https://doi.org/10.1088/1757-899x/171/1/012073.

[127] V.V. Miklashevich and A.V. Mostytskyi. "Cold aggregat (in Russian)". Soviet patent SU 1 054 400 A1. 15.11.1983. URL: https://patenton.ru/patent/SU1054400A1.

[128] C.J. Baroczy. "Systematic correlation for two-phase pressure drop". In: *Chem. Eng. Prog. Symp. Ser.* 62.64 (1966), pp. 232–49. URL: https://www.osti.gov/biblio/4300603.

[129] J. Tamson, M. Stamm, and S. Grohmann. "Set-up of the cryogenic phase equilibria test stand CryoPHAEQTS". In: *IOP conference series / Materials science and engineering* 502.1 (2019), p. 012087. DOI: https://doi.org/10.1088/1757-899x/502/1/012087.

[130] T. Kawahara, M. Emoto, and et. al. "Possibility of a gas-cooled Peltier current lead in the 200 m-class superconducting direct current transmission and distribution system of CASER-2". In: *Physics Procedia* Vol. 27 (2012), pp. 380–83. URL: https://doi.org/10.1016/j.phpro.2012.03.490.

[131] S. Miyata, Y. Yoshiwara, and et. al. "Evaluation of thermoelectric performance of Peltier current leads designed for superconducting direct-current transmission cable systems". In: *IEEE Transactions on Applied Superconductivity* Vol. 26, Issue 3 (2016), p. 5401604. URL: https://doi.org/10.1109/TASC.2016.2541686.

[132] S. Yamaguchi, Y. Nakamura, and et. al. "Peltier current leadexperiments with a thermoelectric semiconductor near 77 K". In: *XVI ICT '97. Proceedings ICT'97. 16th International Conference on Thermoelectrics (Cat. No.97TH8291)* Vol. 26, Issue 3 (2016), pp. 657–60. URL: https://doi.org/10.1109/ICT.1997.667615.

A Vapour cooled Peltier current leads

The thermal load at the cold end of a Peltier current lead (PCL) with 31.0 W/kA that is presented in (Sec. 2.5), compared to the thermal load of an ideal vapour cooled current lead (VCCL) with 24.5 W/kA (see Tab. 5), is about 26 % larger. However, the implementation of Peltier elements into a vapour cooled current lead, can further reduce the thermal load at the cold end. This idea was first mentioned, and theoretically investigated by Kawahara in [130], yielding a reduction of the thermal load to about 25 W/kA.This thermal load is higher in comparison to an ideal vapour cooled current lead, and leads to the conclusion that the combination of a PCL and VCCL is unnecessary. However, in [130] the Peltier effect was implemented in the differential equation for the temperature profile of the Peltier elements, and not in the boundary condition at the cold metal-semiconductor junction, like in (2.55). Hereby, the Peltier effect is erroneously described as an integrated effect over the whole length of the element. In this work, the Peltier effect is implemented as a boundary effect at the cold junction. In the following, the calculated results for vapour cooled Peltier current leads (VCPCL) are presented.

The temperature profile of a VCPCL can be described by a system of two differential equations, according to

$$\frac{\partial}{\partial x}\left(\lambda_{\mathrm{PE}}\left(T\right)\cdot A_{\mathrm{PE}}\cdot\frac{\partial T}{\partial x}\right)+I_{\mathrm{PE}}^{2}\cdot\frac{\rho_{\mathrm{PE}}\left(T\right)}{A_{\mathrm{PE}}}=0 \tag{A.1}$$

$$\frac{\partial}{\partial x}\left(\lambda\left(T\right)\cdot A\cdot\frac{\partial T}{\partial x}\right)+I^{2}\cdot\frac{\rho\left(T\right)}{A}-\dot{m}\cdot c_{\mathrm{p}}\left(T\right)\cdot\frac{\partial T}{\partial x}=0 \tag{A.2}$$

with the equation (A.1) for the temperature profile of one Peltier element, and the equation (A.2) for the vapour cooled metal part. The differential equation system is connected with four boundary conditions, analogous to (2.53−2.56). The temperature profiles of two VCPCLs with copper and aluminium, as the lower part of the lead, are shown in Fig. 60 in comparison to the respective PCLs without vapour cooling. The VCPCL with copper, reduces the thermal load to about 20.6 W/kA, and with aluminium to 18.4 W/kA. This is more than a 50 % reduction of the thermal load at the cold end, compared to a conventional conduction cooled current lead. This difference is based on the corresponding material properties of the metals and their deviation from the Wiedermann-Franz-Lorenz law [8, 9], which is discussed in Sec. 2.7. In comparison to the temperature profile of the PCL with copper, a temperature drop of about 15 K at the cold junction of the corresponding VCPCL is observed, whereby in the respective comparison with aluminium, the junction temperature does not change. The reason in the temperature drop difference, between copper and aluminium, is not fully understood yet, and may be discussed in future works.

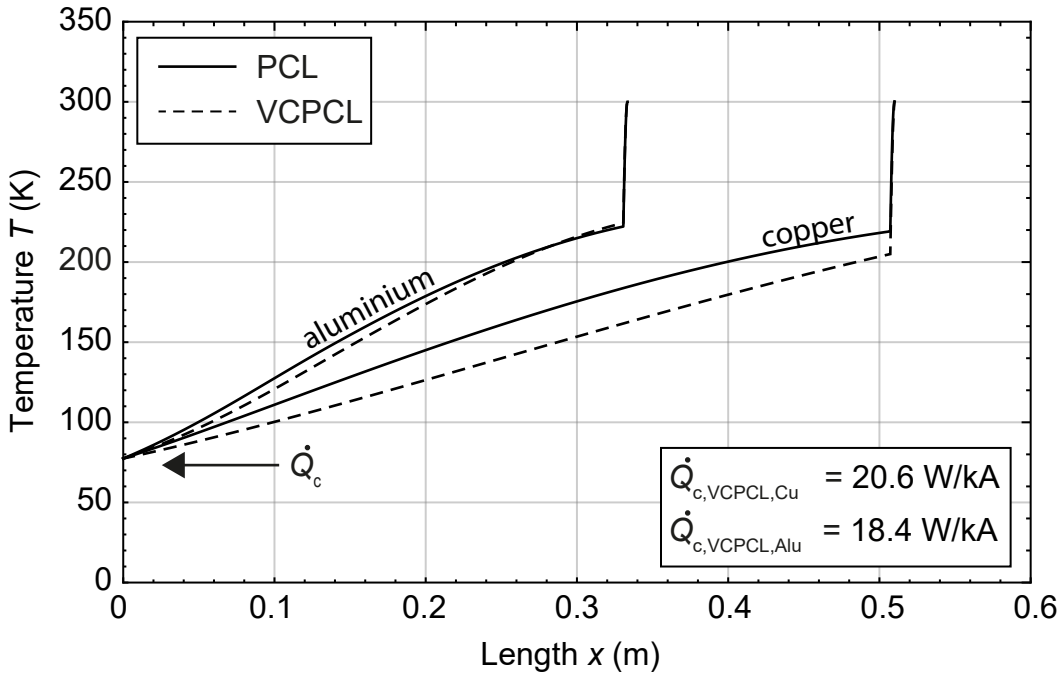

Figure 60: Temperature profiles of two conduction and two vapour cooled Peltier current leads. The metal parts of the current leads on the left-hand side, are made of aluminium.

The calculated results for the thermal loads, electric power dissipations and overall power consumptions of the PCL and VCPCL current leads are presented in Tab. 34. Compared to an ideally vapour cooled current lead VCCL, the specific minimal liquefaction work P_{total}/I of a VCPCL is lower, because of the reduced thermal load at the cold end, yielding in a smaller evaporating mass flow. However, the specific electric power dissipation P_{el}/I is about two times larger, due to the three orders of magnitude higher specific electrical resistance of the Peltier elements, compared to the corresponding metallic conductors. Therefore, the overall power consumptions $P_{\mathrm{total,el}}/I$ of the VCPCLs are larger compared

Table 34: Numerical results of two conduction and two vapour cooled Peltier current leads VCPCL in comparison to an ideal VCCL.

Current lead design	$\dot{m}$ kg/(h kA)	$\dot{Q}_{\mathrm{c}}/I$ W/kA	P_{total}/I W/kA	P_{el}/I W/kA	$P_{\mathrm{total,el}}/I$ W/kA
VCCL $f = \infty$	0.443	24.5	94.7*	35.7	130.5
PCL copper	0	31.0	89.3⋆	66.1	155.4
VCPCL $f = \infty$ copper	0.373	20.6	79.7*	61.7	141.5
PCL aluminium	0	28.9	83.1⋆	65.6	148.7
VCPCL $f = \infty$ aluminium	0.333	18.4	71.2*	70.8	142.0

⋆ Carnot power
* Minimal liquefaction work (Sec. 3.2)

to an ideal VCCL.

The combination of a PCL and a self-suifficient VCCL can clearly lead to a reduction of the thermal load below 20 W/kA, but comes with the main disadvantage of an open system. However, this open system can be substituted by an appropriate closed cryogenic mixed refrigerant cycle (CMRC) and was already demonstrated theoretically in [119], with the result of a thermal load at the cold end of 20.5 W/kA. For further studies in the field of Peltier current leads, it will be important also to investigate the third thermoelectric effect, the so-called Thomson effect. Likewise the Joule heating effect, the Thomson effect generates a certain heat load inside a thermoelectric cooling device, however, this effect yield to a negligible contribution to the heat generation and is often ignored in the design process of thermoelectric coolers. However, in a resent study [131] it was found that the Thomson effect could be as influential as the other two thermoelectric effects, and may lead to a further understanding and improvement of heat control in Peltier current leads.

The Peltier elements Bi_2Te_3 used in this work, perform well in the temperature range between 200 K and 300 K. An another material, BiSb, also exhibits a significant Peltier effect and is known as a good semiconductor near 77 K. With a BiSb Peltier cooling device, it is possible to generate a temperature difference of about 12 K [132], with regard to 77 K. Interesting fact about BiSb is that it can further increase the temperature difference in transverse magnetic fields [62]. Hereby, the galvanomagnetic Ettinghausen effect may be utilized to explain this phenomenon.

B Numerical results - classical CMRC-CL

Table 35: Specific thermal loads and temperatures T_6 of a 10 kA CMRC-CL for the investigated mixtures in the first parametric study.

Refrigerant mixture	T_6 (K)	P_{comp}/I	$\dot{Q}_{af.cool}/I$	$\dot{Q}_0/I$	$P_{el,1}/I$	$P_{el,2}/I$	$\dot{Q}_h/I$	$\dot{Q}_c/I$	*err* %
					(W/kA)				
1	161	43.95	116.98	73.12	28.89	7.19	66.22	30.24	-0.41
2	158	46.11	115.47	69.67	28.43	7.05	62.61	29.49	-0.42
3	154	48.74	109.78	61.21	27.91	6.84	53.64	28.04	-0.37
4	160	50.77	107.93	57.02	28.99	7.14	50.54	30.10	-0.19
5	156	53.30	104.46	51.17	28.61	6.99	44.42	29.07	-0.10
6	152	54.79	101.78	47.06	28.42	6.83	40.19	28.02	0.16
7	150	56.42	99.11	42.87	28.37	6.72	35.55	27.29	0.23
8	152	56.15	98.75	42.65	28.43	6.83	35.73	28.00	0.16
9	159	57.46	99.00	41.71	29.24	7.11	34.51	29.86	-0.33
10	149	58.00	95.94	38.10	28.45	6.68	30.64	27.01	0.33
11	142	58.94	95.36	36.54	28.00	6.37	28.79	24.94	0.86
12	157	59.02	96.51	37.69	29.22	7.04	30.25	29.25	-0.21
13	155	60.86	94.27	33.57	29.38	6.95	25.81	28.79	-0.11
14	155	62.74	90.97	28.36	29.79	6.96	20.40	28.91	-0.07
15	144	63.43	88.74	25.41	29.37	6.45	16.85	25.47	0.99
16	145	66.22	86.58	20.57	30.39	6.56	12.89	26.19	1.71
17	148	69.41	87.72	18.74	31.06	6.77	11.64	27.58	1.76

Table 36: Technical work, efficiencies and the work functions of the CMRC cycle for the investigated mixtures in the baseline study.

Refrigerant mixtures	l_{t}	l_{comp}	$l_{\mathrm{af.cool}}$	l_{hx}	l_{thr}	$\tilde{\eta}_1$	$\tilde{\eta}_2$
			$\left(\mathrm{kJ/kg}\right)$			%	
1	146.49	34.35	38.83	61.25	12.05	55	14
2	153.71	35.79	37.49	68.45	11.97	51	15
3	162.45	37.47	36.57	77.09	11.32	45	17
4	169.23	38.61	40.00	71.78	19.84	38	14
5	177.67	40.17	38.40	79.81	19.29	33	16
6	182.64	41.08	38.61	83.51	19.44	31	17
7	188.06	42.07	39.10	87.63	19.26	28	17
8	187.18	41.87	38.31	87.15	19.84	28	17
9	191.54	42.44	40.66	80.57	27.87	25	14
10	193.34	43.00	39.35	91.72	19.27	25	18
11	196.34	43.90	39.14	101.88	11.54	25	21
12	196.74	43.34	40.97	84.37	28.06	22	15
13	202.88	44.36	42.02	88.76	27.74	19	15
14	209.13	45.40	42.99	92.61	28.13	16	16
15	211.45	46.57	42.06	111.16	11.66	16	21
16	220.74	48.21	44.34	115.00	13.18	12	21
17	231.36	49.63	47.77	108.39	25.57	10	18

Table 37: Process work of the heat exchanger and the required work due to the entropy production rates that are caused by gradients for the investigated mixtures in the baseline study.

Refrigerant mixtures	l_{hx}	$l_{\Delta c}$	$l_{\Delta T,\ \mathrm{HP\text{-}LP}}$	$l_{\Delta T,\ \mathrm{CL\text{-}LP}}$	$l_{\Delta p,\ \mathrm{HP}}$	$l_{\Delta p,\ \mathrm{LP}}$
			$\left(\mathrm{kJ/kg}\right)$			
1	61.25	41.84	10.45	4.37	3.02	1.58
2	68.45	46.69	12.87	3.76	3.22	1.92
3	77.09	52.44	15.71	2.57	3.83	2.55
4	71.78	47.98	10.63	2.42	7.46	3.30
5	79.81	52.26	13.11	2.05	8.30	4.09
6	83.51	54.29	14.43	1.83	8.31	4.66
7	87.63	56.30	15.55	1.66	8.74	5.38
8	87.15	54.35	16.91	2.04	8.54	5.31
9	80.57	51.83	11.31	1.56	9.85	6.02
10	91.72	57.13	17.35	1.71	9.28	6.25
11	101.88	61.66	24.04	2.04	7.78	6.37
12	84.37	52.96	12.62	1.54	10.37	6.88
13	88.76	54.58	13.32	1.44	11.39	8.02
14	92.61	54.29	14.71	1.52	12.50	9.59
15	111.16	61.40	26.99	2.00	10.84	9.93
16	115.00	58.14	28.84	2.48	13.47	12.08
17	108.39	54.65	22.04	2.02	15.46	14.22

Table 38: Heat exchanger temperature and pressure differences and the inlet and outlet liquid fractions according to the numbering in Fig. 21 for the investigated mixtures in the baseline study.

Refrigerant mixtures	T_6	ΔT_{HD}	ΔT_{ND}	Δp_{HD}	Δp_{ND}	kA	y_3	y_4	y_6	y_7
		(K)			(bar)	(W/K)			(−)	
1	161	127	133	5.15	0.49	246	0.68	0.94	0.90	0
2	158	130	136	5.26	0.49	250	0.63	0.94	0.90	0
3	154	134	141	5.66	0.53	255	0.55	0.94	0.90	0
4	160	128	136	8.38	0.74	264	0.52	0.82	0.80	0
5	156	131	139	8.73	0.75	270	0.45	0.82	0.79	0
6	152	135	143	8.50	0.77	272	0.41	0.82	0.79	0
7	150	137	146	8.53	0.79	275	0.36	0.83	0.79	0
8	152	135	143	8.49	0.77	273	0.35	0.82	0.79	0
9	159	129	137	8.63	0.90	262	0.36	0.72	0.70	0
10	149	138	147	8.60	0.81	277	0.31	0.82	0.79	0
11	142	144	154	7.63	0.74	280	0.27	0.93	0.88	0
12	157	131	139	8.66	0.91	264	0.31	0.72	0.69	0
13	155	133	141	8.87	0.94	267	0.27	0.71	0.69	0
14	155	132	141	8.94	0.96	269	0.21	0.71	0.68	0
15	144	143	153	8.19	0.84	285	0.15	0.93	0.88	0
16	145	141	152	8.90	0.92	289	0.10	0.91	0.85	0
17	148	138	149	8.67	1.05	281	0.09	0.77	0.73	0

Table 39: Specific thermal loads and temperatures T_6 of a 10 kA CMRC-CL for the investigated mixtures in the study with increased high-pressure level.

Refrigerant mixture	T_6	P_{comp}/I	$\dot{Q}_{\mathrm{af.cool}}/I$	$\dot{Q}_0/I$	$P_{\mathrm{el},1}/I$	$P_{\mathrm{el},2}/I$	$\dot{Q}_{\mathrm{h}}/I$	$\dot{Q}_{\mathrm{c}}/I$	err
	(K)				(W/kA)				%
1 - 3 bar	144	68.83	152.56	83.73	27.02	6.48	77.28	25.65	0.46
1 - 4 bar	153	55.86	138.20	82.34	28.21	6.86	75.69	28.23	0.07
11 - 3 bar	122	93.29	152.81	59.53	24.84	5.45	50.69	18.74	1.00
11 - 4 bar	129	74.56	133.42	58.86	25.78	5.77	50.44	20.85	0.90
11 - 5 bar	134	62.94	121.17	58.22	26.54	6.03	50.44	22.61	0.90
17 - 3 bar	108	113.12	152.07	38.95	25.57	4.97	50.44	15.42	3.05
17 - 4 bar	119	86.58	124.97	38.38	26.58	5.43	31.49	18.56	2.64
17 - 5 bar	126	72.17	110.03	37.86	27.33	5.77	30.60	20.86	2.37

Table 40: Technical work, efficiencies and the work functions of the CMRC cycle for the investigated mixtures in the study with increased high-pressure level.

Refrigerant mixtures	l_t	l_{comp}	$l_{af.cool}$	l_{hx}	l_{thr}	$\tilde{\eta}_1$	$\tilde{\eta}_2$
			(kJ/kg)			%	
1 - 3 bar	229.44	48.61	76.66	86.25	17.92	433	15
1 - 4 bar	186.20	41.22	62.24	66.22	16.51	477	13
11 - 3 bar	310.95	61.91	87.33	146.91	14.80	287	24
11 - 4 bar	248.53	52.24	64.98	117.81	13.49	331	22
11 - 5 bar	209.81	45.77	52.29	99.22	12.54	366	21
17 - 3 bar	377.07	70.67	107.92	177.16	21.32	180	27
17 - 4 bar	288.60	58.24	73.40	133.69	23.27	207	24
17 - 5 bar	240.57	50.78	56.48	110.37	22.94	226	22

Table 41: Process work of the heat exchanger and the required work due to the entropy production rates that are caused by gradients for the investigated mixtures in the study with increased high-pressure level.

Refrigerant mixtures	l_{hx}	$l_{\Delta c}$	$l_{\Delta T,\,\mathrm{HP\text{-}LP}}$	$l_{\Delta T,\,\mathrm{CL\text{-}LP}}$	$l_{\Delta p,\,\mathrm{HP}}$	$l_{\Delta p,\,\mathrm{LP}}$
			(kJ/kg)			
1 - 3 bar	86.25	62.45	13.74	6.16	0.99	2.91
1 - 4 bar	66.22	47.13	10.62	6.01	1.10	1.36
11 - 3 bar	146.91	102.85	28.58	3.81	2.04	9.63
11 - 4 bar	117.81	83.73	24.63	3.01	2.17	4.27
11 - 5 bar	99.22	70.04	21.80	2.61	2.30	2.47
17 - 3 bar	177.16	109.83	35.59	4.82	5.14	21.78
17 - 4 bar	133.69	86.77	29.17	3.42	5.54	8.79
17 - 5 bar	110.37	71.88	24.98	2.64	5.88	4.99

Table 42: Heat exchanger temperature and pressure differences and the inlet and outlet liquid fractions according to the numbering in Fig. 21 for the investigated mixtures in the study with increased high-pressure level.

Refrigerant mixtures	T_6	ΔT_{HD}	ΔT_{ND}	Δp_{HD}	Δp_{ND}	kA	y_3	y_4	y_6	y_7
		(K)		(bar)		(W/K)		(−)		
1 - 3 bar	144	142	149	2.53	0.57	222	0.80	0.99	0.91	0
1 - 4 bar	153	134	139	2.77	0.46	226	0.80	0.98	0.91	0
11 - 3 bar	122	165	173	3.39	0.83	242	0.50	1.00	0.92	0
11 - 4 bar	129	158	166	3.64	0.64	244	0.50	1.00	0.92	0
11 - 5 bar	134	153	161	3.87	0.54	246	0.50	1.00	0.92	0
17 - 3 bar	108	175	188	6.03	1.20	246	0.28	1.00	0.84	0
17 - 4 bar	119	163	177	6.50	0.89	251	0.28	0.97	0.82	0
17 - 5 bar	126	156	170	6.85	0.74	255	0.28	0.92	0.81	0

Table 43: Specific thermal loads and temperatures T_6 of a 10 kA CMRC-CL for the investigated mixtures in the study on the influence of mass flow at 2.5 g/s.

Refrigerant mixture	T_6	P_{comp}/I	$\dot{Q}_{af.cool}/I$	$\dot{Q}_0/I$	$P_{el,1}/I$	$P_{el,2}/I$	$\dot{Q}_h/I$	$\dot{Q}_c/I$	err
	(K)				(W/kA)				%
1 - 3 bar	147	55.70	125.77	70.07	27.72	6.63	63.98	26.70	0.59
1 - 4 bar	155	45.91	115.16	69.25	28.81	7.00	62.97	29.07	0.18
11 - 3 bar	125	74.43	124.12	49.69	25.78	5.62	41.73	19.86	1.55
11 - 4 bar	131	60.58	109.74	49.16	26.61	5.92	41.66	21.88	1.44
11 - 5 bar	137	51.51	100.16	48.65	27.33	6.18	41.53	23.65	1.30
17 - 3 bar	113	87.29	119.76	32.47	26.79	5.28	25.62	17.53	3.63
17 - 4 bar	122	69.39	101.39	32.00	27.53	5.64	25.47	20.02	3.41
17 - 5 bar	129	58.56	90.15	31.58	28.17	5.95	25.26	22.08	3.11

Table 44: Technical work, efficiencies and the work functions of the CMRC cycle for the investigated mixtures in the study on the influence of mass flow at 2.5 g/s.

Refrigerant mixtures	l_{t}	l_{comp}	$l_{\mathrm{af.cool}}$	l_{hx}	l_{thr}	$\tilde{\eta}_1$	$\tilde{\eta}_2$
			(kJ/kg)			%	
1 - 3 bar	222.80	47.44	74.93	81.78	18.65	302	14
1 - 4 bar	183.64	40.64	62.24	63.56	17.21	331	12
11 - 3 bar	297.74	59.92	82.67	139.56	15.59	203	23
11 - 4 bar	242.30	51.17	63.14	113.66	14.33	231	21
11 - 5 bar	306.06	45.08	51.32	96.17	13.48	254	20
17 - 3 bar	349.18	66.88	96.80	159.77	25.73	128	25
17 - 4 bar	277.56	56.55	69.53	125.32	26.15	145	23
17 - 5 bar	234.26	49.73	54.49	104.44	25.60	157	21

Table 45: Process work of the heat exchanger and the required work due to the entropy production rates that are caused by gradients for the investigated mixtures in the study on the influence of mass flow at 2.5 g/s.

Refrigerant mixtures	l_{hx}	$l_{\Delta c}$	$l_{\Delta T,\ \mathrm{HP\text{-}LP}}$	$l_{\Delta T,\ \mathrm{CL\text{-}LP}}$	$l_{\Delta p,\ \mathrm{HP}}$	$l_{\Delta p,\ \mathrm{LP}}$
			(kJ/kg)			
1 - 3 bar	81.78	61.44	12.15	5.26	0.74	2.19
1 - 4 bar	63.56	47.02	9.55	5.11	0.82	1.06
11 - 3 bar	139.56	101.71	25.24	4.00	1.64	6.97
11 - 4 bar	113.66	83.38	22.12	3.15	1.73	3.28
11 - 5 bar	96.17	70.10	19.70	2.61	1.82	1.95
17 - 3 bar	159.77	104.87	31.55	5.43	3.68	14.23
17 - 4 bar	125.32	84.58	26.45	3.99	3.90	6.40
17 - 5 bar	104.44	70.42	23.10	3.07	4.08	3.76

Table 46: Heat exchanger temperature and pressure differences and the inlet and outlet liquid fractions according to the numbering in Fig. 21 for the investigated mixtures in the study on the influence of mass flow at 2.5 g/s.

Refrigerant mixtures	T_6	ΔT_{HD}	ΔT_{ND}	Δp_{HD}	Δp_{ND}	kA	y_3	y_4	y_6	y_7
		(K)		(bar)		(W/K)		(−)		
1 - 3 bar	147	139	148	1.87	0.40	197	0.80	0.99	0.91	0
1 - 4 bar	155	131	139	2.04	0.33	200	0.80	0.98	0.91	0
11 - 3 bar	125	162	171	2.69	0.61	213	0.50	1.00	0.91	0
11 - 4 bar	131	155	165	2.85	0.48	215	0.50	1.00	0.91	0
11 - 5 bar	137	150	159	3.02	0.40	216	0.50	1.00	0.91	0
17 - 3 bar	113	168	183	4.31	0.87	214	0.28	1.00	0.83	0
17 - 4 bar	122	159	174	4.57	0.66	218	0.28	0.96	0.81	0
17 - 5 bar	129	153	168	4.77	0.55	221	0.28	0.92	0.80	0

Table 47: Specific thermal loads and temperatures T_6 of a 10 kA CMRC-CL for the investigated mixtures in the study on the influence of mass flow at 3.5 g/s.

Refrigerant mixture	T_6	P_{comp}/I	$\dot{Q}_{\mathrm{af.cool}}/I$	$\dot{Q}_0/I$	$P_{\mathrm{el,1}}/I$	$P_{\mathrm{el,2}}/I$	$\dot{Q}_{\mathrm{h}}/I$	$\dot{Q}_{\mathrm{c}}/I$	err
	(K)				(W/kA)				%
1 - 3 bar	142	83.66	180.90	97.24	26.36	6.33	90.69	24.69	0.42
1 - 4 bar	151	66.48	161.48	95.00	27.67	6.74	87.59	27.45	-0.14
11 - 3 bar	120	114.85	184.18	69.33	23.97	5.31	59.88	17.75	0.67
11 - 4 bar	127	89.47	157.98	68.51	25.01	5.63	59.61	19.92	0.63
11 - 5 bar	133	74.89	142.65	67.76	25.87	5.90	59.42	21.77	0.61
17 - 3 bar	105	148.93	194.42	45.49	24.61	4.77	37.16	14.01	2.33
17 - 4 bar	116	105.96	150.70	44.74	25.76	5.26	36.36	17.43	2.03
17 - 5 bar	125	86.88	130.99	44.11	26.62	5.64	36.15	20.00	1.81

Table 48: Technical work, efficiencies and the work functions of the CMRC cycle for the investigated mixtures in the study on the influence of mass flow at 3.5 g/s.

Refrigerant mixtures	l_t	l_{comp}	$l_{af.cool}$	l_{hx}	l_{thr}	$\tilde{\eta}_1$	$\tilde{\eta}_2$
			(kJ/kg)			%	
1 - 3 bar	293.03	50.31	79.30	92.18	17.25	579	16
1 - 4 bar	189.94	42.05	62.44	69.51	15.94	644	13
11 - 3 bar	328.14	64.47	93.56	156.32	13.80	378	24
11 - 4 bar	255.62	53.42	67.18	122.29	12.73	447	23
11 - 5 bar	213.97	46.52	53.40	102.27	11.79	497	22
17 - 3 bar	425.51	76.93	128.20	202.23	18.15	225	29
17 - 4 bar	302.74	60.36	78.46	143.25	20.67	275	25
17 - 5 bar	248.22	52.03	58.91	116.50	20.77	303	23

Table 49: Process work of the heat exchanger and the required work due to the entropy production rates that are caused by gradients for the investigated mixtures in the study on the influence of mass flow at 3.5 g/s.

Refrigerant mixtures	l_{hx}	$l_{\Delta c}$	$l_{\Delta T,\,\mathrm{HP\text{-}LP}}$	$l_{\Delta T,\,\mathrm{CL\text{-}LP}}$	$l_{\Delta p,\,\mathrm{HP}}$	$l_{\Delta p,\,\mathrm{LP}}$
			(kJ/kg)			
1 - 3 bar	92.18	64.43	15.48	7.06	1.26	3.95
1 - 4 bar	69.51	47.41	11.75	6.90	1.41	1.75
11 - 3 bar	156.32	104.80	31.96	3.80	2.44	13.31
11 - 4 bar	122.29	84.07	27.15	3.04	2.63	5.39
11 - 5 bar	102.27	69.99	23.72	2.68	2.82	3.05
17 - 3 bar	202.23	115.04	39.01	4.40	7.12	36.65
17 - 4 bar	143.25	89.13	31.36	2.98	7.83	11.95
17 - 5 bar	116.50	72.95	26.44	2.27	8.38	6.46

Table 50: Heat exchanger temperature and pressure differences and the inlet and outlet liquid fractions according to the numbering in Fig. 21 for the investigated mixtures in the study on the influence of mass flow at 3.5 g/s.

Refrigerant mixtures	T_6	ΔT_{HD}	ΔT_{ND}	Δp_{HD}	Δp_{ND}	kA	y_3	y_4	y_6	y_7
		(K)		(bar)		$\left(\mathrm{W/K}\right)$		(−)		
1 - 3 bar	142	145	151	3.23	0.78	246	0.80	0.99	0.91	0
1 - 4 bar	151	136	139	3.55	0.62	250	0.80	0.98	0.91	0
11 - 3 bar	120	168	174	4.11	1.07	268	0.50	1.00	0.92	0
11 - 4 bar	127	161	168	4.45	0.82	272	0.50	1.00	0.92	0
11 - 5 bar	133	155	162	4.79	0.69	274	0.50	1.00	0.92	0
17 - 3 bar	105	179	191	8.15	1.65	277	0.28	1.00	0.85	0
17 - 4 bar	116	166	179	8.94	1.16	284	0.28	0.97	0.83	0
17 - 5 bar	125	159	171	9.49	0.96	289	0.28	0.92	0.82	0

C Numerical results - micro-structured CMRC-CL

The heat transfer, pressure drop and void fraction correlations used in the computation of the micro-structured heat exchanger made out of copper are listed in Tab. 31.

Table 51: Specific thermal loads of the investigated micro-structured CMRC-CLs. Mixture 17 is used as the refrigerant. The inlet pressures of the HP and LP streams are set to 30 bar and 2 bar, respectively. The inlet temperature of the HP stream is set to 293.15 K. The isentropic efficiency of the compressor is set to 0.7.

CMRC-CL design	I (kA)	$\dot{m}$ (g/s)	P_{comp}/I	$\dot{Q}_{\text{af.cool}}/I$	$\dot{Q}_0/I$	P_{el}/I	$\dot{Q}_{\text{h}}/I$	$\dot{Q}_{\text{c}}/I$	err %
					(W/kA)				
A	10	5	237.59	297.56	59.97	48.82	36.57	14.22	2.55
B	10	7	310.21	383.84	73.63	28.55	85.12	14.31	4.53
C	10	6	278.76	352.03	73.27	36.58	58.06	6.48	2.96
D	20	8	174.80	227.33	52.53	43.82	22.34	11.29	0.7

Table 52: Technical work, efficiencies and the work functions of the investigated micro-structured CMRC-CL cycles. Mixture 17 is used as the refrigerant. The inlet pressures of the HP and LP streams are set to 30 bar and 2 bar, respectively. The inlet temperature of the HP stream is set to 293.15 K. The isentropic efficiency of the compressor is set to 0.7.

CMRC-CL design	l_{t}	l_{comp}	$l_{\text{af.cool}}$	l_{hx}	l_{thr}	$\tilde{\eta}_1$	$\tilde{\eta}_2$
			(kJ/kg)			%	
A	475.18	83.60	145.59	216.49	29.50	27	15
B	443.16	80.79	125.19	213.65	23.53	31	15
C	464.60	82.20	141.86	225.71	14.83	36	19
D	437.00	78.23	133.79	208.36	16.62	35	22

Table 53: Process work of the micro-structured heat exchanger of the investigated CMRC-CLs and the required work due to the entropy production rates that are caused by gradients. Mixture 17 is used as the refrigerant. The inlet pressures of the HP and LP streams are set to 30 bar and 2 bar, respectively. The inlet temperature of the HP stream is set to 293.15 K.

CMRC-CL design	l_{hx}	$l_{\Delta c}$	$l_{\Delta T,\ \mathrm{HP\text{-}Wall}}$	$l_{\Delta T,\ \mathrm{Wall\text{-}LP}}$	$l_{\Delta p,\ \mathrm{HP}}$	$l_{\Delta p,\ \mathrm{LP}}$
			$\left(\mathrm{kJ/kg}\right)$			
A	216.49	91.78	53.55	44.84	0.21	26.11
B	213.65	84.98	64.28	49.21	0.16	15.03
C	225.71	135.56	43.52	33.35	0.14	13.14
D	208.36	134.85	36.27	27.66	0.10	9.49

Table 54: Heat exchanger inlet and outlet temperatures, pressures and liquid fractions of the investigated micro-structured CRMC-CLs. Mixture 17 is used as the refrigerant. The inlet pressures of the HP and LP streams are set to 30 bar and 2 bar, respectively. The inlet temperature of the HP stream is set to 293.15 K. The isentropic efficiency of the compressor is set to 0.7.

CMRC-CL design	T_6	ΔT_{HD}	ΔT_{ND}	Δp_{HD}	Δp_{ND}	kA	y_3	y_4	y_6	y_7
		(K)		(bar)		$\left(\mathrm{W/K}\right)$		(−)		
A	105	176	184	0.27	0.96	167	0.28	1.00	0.83	0
B	97	187	183	0.22	0.79	227	0.28	1.00	0.86	0
C	85	204	205	0.26	0.86	365	0.28	1.00	0.93	0
D	87	201	209	0.16	0.55	567	0.28	1.00	0.91	0

D Experimental data

Table 55: Experimental fluid data of the experiment CD-0. The numbering of process state points refer to Fig. 55. The mass flow is equal to $\dot{m} = 0.49 \pm 0.01\,\mathrm{g/s}$. The thermodynamic properties are calculated with the Peng-Robinson equation of state [97, 98]. The expanded uncertainty of the measured values are calculated with a coverage factor of $k_\mathrm{u} = 2$. The filling quantity amounts to 5.56 mol.

Process state points	Temperature (K)	Pressure (bar)	Liquid fraction (−)	Enthalpy $\left(\mathrm{J/kg}\right)$	Entropy $\left(\mathrm{J/(kg\,K)}\right)$
1	338.04 ± 0.25	18.07 ± 0.32	0	$-2.22413 \cdot 10^6$	-4749.09
2	293.89 ± 0.18	18.07 ± 0.32	0	$-2.30421 \cdot 10^6$	-5002.85
3	292.67 ± 0.17	18.02 ± 0.32	0	$-2.30632 \cdot 10^6$	-5009.30
5	272.75 ± 0.14	18.00 ± 0.32	0.06	$-2.36141 \cdot 10^6$	-5206.31
6	92.45 ± 1.39	16.38 ± 0.32	1	$-3.02230 \cdot 10^6$	-8853.90
8	87.62 ± 1.42	1.72 ± 0.32	0.85	$-3.01056 \cdot 10^6$	-8677.22
10	85.66 ± 1.43	1.71 ± 0.32	0.87	$-3.01807 \cdot 10^6$	-8763.96
11	264.81 ± 0.16	1.64 ± 0.32	0	$-2.32670 \cdot 10^6$	-4439.12
12	292.00 ± 0.17	1.53 ± 0.32	0	$-2.28321 \cdot 10^6$	-4262.21
13	294.34 ± 0.17	1.53 ± 0.32	0	$-2.27939 \cdot 10^6$	-4249.20

Table 56: Experimental fluid data of the experiment CD-3. The numbering of process state points refer to Fig. 55. The mass flow is equal to $\dot{m} = 0.38 \pm 0.01\,\mathrm{g/s}$. The thermodynamic properties are calculated with the Peng-Robinson equation of state [97, 98]. The expanded uncertainty of the measured values are calculated with a coverage factor of $k_\mathrm{u} = 2$. The filling quantity amounts to 5.68 mol.

Process state points	Temperature (K)	Pressure (bar)	Liquid fraction (−)	Enthalpy $\left(\mathrm{J/kg}\right)$	Entropy $\left(\mathrm{J/(kg\,K)}\right)$
1	336.10 ± 0.26	21.06 ± 0.32	0	$-2.23120 \cdot 10^6$	-4810.04
2	296.47 ± 0.18	21.06 ± 0.32	0	$-2.30416 \cdot 10^6$	-5041.04
3	295.26 ± 0.18	21.03 ± 0.32	0	$-2.30631 \cdot 10^6$	-5047.88
5	277.22 ± 0.14	21.02 ± 0.32	0.06	$-2.35825 \cdot 10^6$	-5231.15
6	95.18 ± 1.38	20.59 ± 0.32	1	$-3.01566 \cdot 10^6$	-8788.81
8	90.20 ± 1.40	1.49 ± 0.32	0.82	$-2.99971 \cdot 10^6$	-8547.80
10	88.89 ± 1.41	1.48 ± 0.32	0.83	$-3.00376 \cdot 10^6$	-8592.73
11	263.29 ± 0.16	1.43 ± 0.32	0	$-2.32866 \cdot 10^6$	-4409.16
12	299.28 ± 0.27	1.34 ± 0.32	0	$-2.27106 \cdot 10^6$	-4184.11
13	296.86 ± 0.18	1.34 ± 0.32	0	$-2.27503 \cdot 10^6$	-4197.44

Table 57: Experimental fluid data of the experiment CD-3-2. The numbering of process state points refer to Fig. 55. The mass flow is equal to $\dot{m} = 0.38 \pm 0.01$ g/s. The expanded uncertainty of the measured values are calculated with a coverage factor of $k_u = 2$.

Process state points	Temperature (K)	Pressure (bar)
1	356.21 ± 0.29	21.46 ± 0.32
2	295.74 ± 0.18	21.46 ± 0.32
3	294.28 ± 0.18	21.32 ± 0.32
5	264.50 ± 0.15	21.02 ± 0.32
6	98.44 ± 1.36	20.40 ± 0.32
8	93.89 ± 1.38	2.69 ± 0.32
10	90.71 ± 1.40	2.67 ± 0.32
11	224.37 ± 0.22	2.60 ± 0.32
12	293.81 ± 0.18	2.42 ± 0.32
13	295.00 ± 0.18	2.42 ± 0.32

Table 58: Experimental fluid data of the experiments CD-4-1 and CD-4-2. The numbering of process state points refer to Fig. 55. The mass flows in CD-4.1 and CD-4.2 are equal to 0.48 ± 0.01 g/s and 0.52 ± 0.01 g/s, respectively. The expanded uncertainty of the measured values are calculated with a coverage factor of $k_u = 2$. The filling quantity in CD-4.2 amounts to 5.68 mol.

CD-4-1			CD-4-2		
Process state points	Temperature (K)	Pressure (bar)	Process state points	Temperature (K)	Pressure (bar)
1	344.71 ± 0.27	19.70 ± 0.32	1	345.95 ± 0.27	20.08 ± 0.32
2	298.23 ± 0.18	19.70 ± 0.32	2	296.84 ± 0.18	20.08 ± 0.32
3	297.00 ± 0.18	19.65 ± 0.32	3	295.90 ± 0.17	20.02 ± 0.32
5	276.54 ± 0.14	19.64 ± 0.32	5	275.26 ± 0.14	20.00 ± 0.32
6	99.01 ± 1.35	19.23 ± 0.32	6	104.54 ± 1.32	19.47 ± 0.32
8	92.48 ± 1.39	1.74 ± 0.32	8	98.31 ± 1.36	1.87 ± 0.32
10	90.80 ± 1.40	1.72 ± 0.32	10	96.56 ± 1.37	1.86 ± 0.32
11	267.09 ± 0.15	1.66 ± 0.32	11	267.13 ± 0.15	1.79 ± 0.32
12	299.17 ± 0.18	1.55 ± 0.32	12	299.02 ± 0.18	1.67 ± 0.32
13	298.41 ± 0.18	1.55 ± 0.32	13	297.07 ± 0.18	1.67 ± 0.32

Table 59: FBG temperature data of the experiments. The uncertainty of the FBG temperature measurement data of all gratings and of all experiments is approximately ±5 K [5].

FBG grating	CD-0	CD-3	CD-3.2	CD-4.1	CD-4.2
	Temperature (K)				
1	270.52	272.58	258.26	273.17	273.15
2	269.78	264.14	248.18	267.16	271.86
3	265.38	238.93	226.14	248.16	265.92
4	255.03	208.32	208.23	219.48	250.84
5	239.57	190.95	196.94	199.65	226.71
6	219.35	180.67	188.08	187.07	205.97
7	203.17	171.61	179.69	177.11	190.83
8	190.94	163.65	172.40	168.95	179.31
9	180.81	156.40	166.00	162.15	170.82
10	172.20	148.89	159.61	155.37	163.53
11	164.16	140.94	152.63	148.21	156.58
12	155.80	133.15	144.12	140.76	149.51
13	146.73	126.81	136.03	133.90	142.48
14	137.58	121.08	128.32	128.29	135.73
15	128.73	115.48	121.65	122.92	129.28
16	120.43	109.38	114.96	116.46	122.62
17	112.12	103.51	108.49	109.68	116.25
18	104.54	98.95	102.60	103.26	110.40
19	98.67	96.24	98.46	99.16	105.30

Eugen Shabagin

Publikationsliste 2. April 2022

✉ *eugen.shabagin@gmail.com*

Veröffentlichungen und Abschlussarbeiten

Konferenz Paper

A European collaboration to investigate Superconducting Magnets for Next Generation Heavy Ion Therapy
Autoren: L. Rossi, A. Ballarino, D. Barna, E. Benedetto, C. Calzolaio, G. Ceruti, E. De Matteis, A. Echeandia, T. Ekelof, S. Farinon, E. Felcini, M. Gehring, G. Kirby, T. Lecrevisse, J. Lucas, S. Mariotto, J. Munilla, R. Musenich, A. Pampaloni, K. Pepitone, D. Perini, D. Popovic, M. Pullia, L. Quettier, S. Sanfilippo, C. Senatore, **E. Shabagin**, M. Sorbi, M. Statera, D. Tommasini, F. Toral, D. Veres, M. Vieweg
Veröffentlicht: IEEE Transactions on Applied Superconductivity 2021 (wird noch veröffentlicht)

Konferenz Paper

Environmental Life Cycle Assessment of a 10 kV High-Temperature Superconductor Cable System for Energy Distribution
Autoren: A. Buchholz, M. Noe, D. Kottonau, **E. Shabagin**, M. Weil
Veröffentlicht: IEEE Transactions on Applied Superconductivity Vol. 31 Issue 5, Aug. 2021
DOI: 10.1109/TASC.2021.3070703

Vortrag

Environmental Life-Cycle Assessment of a 10 kV High-Temperature Superconductor Cable System for Energy Distribution
Autoren: A. Buchholz, M. Noe, D. Kottonau, **E. Shabagin**, M. Weil
Veröffentlicht: Applied Superconductivity Conference (ASC 2020), Juni 2020, Tampa, FL, USA
KITopen ID: 1000126996

Journal Paper

An open-source 2D finite difference based transient electro-thermal simulation model for three-phase concentric superconducting power cables
Autoren: W.T.B. de Sousa, **E. Shabagin**, D. Kottonau, M. Noe
Veröffentlicht: Superconductor Science and Technology Vol 34 Nr. 1 (2020) 015014
DOI: 10.1088/1361-6668/abc2b0

Forschungsbericht

Evaluation of the Use of Superconducting 380 kV Cable
Autoren: D. Kottonau, **E. Shabagin**, et. al.
Veröffentlicht: KIT Scientific Publishing, 2019, Karlsruhe, Deutschland
DOI: 10.5445/KSP/1000117918

Vortrag *Wirtschaftlichkeit von HTSL Kabeln am Beispiel einer 380 kV Teilerdverkabelung*
Autoren: M. Noe, D. Kottonau, **E. Shabagin**, W.T.B. de Sousa, J. Geisbüsch, H. Stagge, S. Fechner, H. Woiton, T. Küsters
Veröffentlicht: Zukunft und Innovation der Energietechnik mit Hochtemperatur-Supraleitern VII. Ziehl, Mrz., 2020, Berlin, Deutschland
LINK: https://ivsupra.de/vii-ziehl-vortraege/

Vortrag *Einsatz eines kompakten, mikrostrukturierten Wärmeübertragers im kryogenen Gemischkältekreislauf*
Autoren: **E. Shabagin**, S. Grohmann
Veröffentlicht: DKV Tagung, Nov., 2019, Ulm, Deutschland
DOI: 10.5445/IR/1000105188

Forschungsbericht *Bewertung des Einsatzes supraleitender 380-kV-Kabel*
Autoren: D. Kottonau, **E. Shabagin**, et. al.
Veröffentlicht: KIT Scientific Publishing, 2019, Karlsruhe, Deutschland
DOI: 10.5445/KSP/1000093864

Konferenz Paper *Investigation of cryogenic mixed-refrigerant cooled current leads in combination with Peltier elements*
Autoren: **E. Shabagin**, K Raczka, S. Grohmann
Veröffentlicht: IOP Conference Series: Materials Science and Engineering 502, 2020, Hartford CT, US
DOI: 10.5445/IR/1000121281

Vortrag *Investigation of cryogenic mixed-refrigerant cooled current leads in combination with Peltier elements*
Autoren: **E. Shabagin**, K Raczka, S. Grohmann
Veröffentlicht: Cryogenic Engneering Conference, July, 2019, Hartford CT, US
LINK: C1Or2B-07

Vortrag *Influence of mixture composition on the performance of cryogenic mixed refrigerant cooled current leads*
Autoren: **E. Shabagin**, S. Grohmann
Veröffentlicht: 15th Cryogenics, Apr., 2019, Prag, Tschechische Republik

Konferenz Paper *Development of 10 kA current leads cooled by a cryogenic mixed refrigerant cycle*
Autoren: **E. Shabagin**, S. Grohmann
Veröffentlicht: ICEC27-ICMC 2018, Sep. 3-7, 2018, Oxford, England
DOI: 10.1088/1757-899X/502/1/012138

Vortrag *E-10: 017 - Development of 10 kA current leads cooled by a cryogenic mixed refrigerant cycle*
Autoren: **E. Shabagin**, S. Grohmann
Veröffentlicht: ICEC27-ICMC 2018, Sep. 3-7, 2018, Oxford, England
KITOPEN-ID: 1000087308

Vortrag *Modellierung des instationären Wärme- und Stofftransports eines Neutronenmoderators aus festem Deuterium zur Erzeugung ultrakalter Neutronen*
Autoren: **E. Shabagin**, D. Gomse, S. Grohmann
Veröffentlicht: Thermodynamik-Kolloquium, Sep. 27-29, 2017, Dresden, Deutschland

Vortrag *Calculation of temperature profiles and pressure drop in concentric three-phase HTS power cables*
Autoren: **E. Shabagin**, C. Zoller, S. Strauß, S. Grohmann
Veröffentlicht: 2nd International Workshop on Cooling Systems for HTS Applications, Sep. 13-15, 2017, Karlsruhe, Deutschland
DOI: 10.5445/IR/1000075575

Masterarbeit *Modeling of Transient Heat and Mass Transfer of a Solid Deuterium Neutron Moderator for the Generation of Ultra-Cold Neutrons*
Referent: Prof. Dr.-Ing. Steffen Grohmann ; Note: 1,0

Journal Paper *Modelling of 3D temperature profiles and pressure drop in concentric three-phase HTS power cables*
Autoren: **E. Shabagin**, C. Heidt, S. Strauß, S. Grohmann
Veröffentlicht: Cryogenics 81 (2017) 24-32
DOI: 10.1016/j.cryogenics.2016.11.004

Konferenz Paper *Opportunities for High-voltage AC Superconducting Cables Part of New Long-distance Transmission Lines*
Autoren: D. Kottonau, **E. Shabagin**, M. Noe, S. Grohmann
Veröffentlicht: IEEE Transactions on Applied Superconductivity (Volume: 27, Issue: 4, June 2017)
DOI: 10.1109/TASC.2017.2652856

Vortrag *Opportunities for High-voltage AC Superconducting Cables Part of New Long-distance Transmission Lines*
Autoren: D. Kottonau, **E. Shabagin**, M. Noe, S. Grohmann
Veröffentlicht: Applied Superconductivity Conference (ASC 2016), Denver, CO, September 4-9, 2016)
KITopen ID: 1000054650

Poster *Comparison of superconducting cables with conventional high-voltage power transmission lines*
Autoren: J. Geisbüsch, D. Kottonau, **E. Shabagin**, M. Noe
Veröffentlicht: 608. Heraeus Seminar, Bad Honnef (18.02-20.02.2016)
KITopen ID: 1000054564

Vortrag *Untersuchungen zum Druck- und Temperaturverhalten supraleitender Kabel*
Autoren: **E. Shabagin**, C. Zoller, S. Strauß, S. Grohmann
Veröffentlicht: DKV-Tagung, Nov. 19-21, 2014, Düsseldorf, Deutschland
ISBN: 9781510800014

Bachelorarbeit *Untersuchungen zum Druck- und Temperaturverhalten supraleitender Kabel*
Referent: Prof. Dr.-Ing. Steffen Grohmann ; Note: 1,0